

Advanced Non-Destructive Testing of Blade Manufacturing Defects

Euan Duernberger

Department of Electronic and Electrical Engineering

University of Strathclyde

A thesis submitted for the degree of

Doctor of Philosophy

2023

Copyright Declaration

This thesis is the result of the author's original research. It has been composed by the author and has not been previously submitted for examination which has led to the award of a degree.

The copyright of this thesis belongs to the author under the terms of the United Kingdom Copyrights Acts as qualified by the University of Strathclyde Regulation 3.50. Due acknowledgement must always be made of the use of any material contained in, or derived from, this thesis.

Signed:

A handwritten signature in black ink, appearing to read "Sean Neenan". The signature is written in a cursive style with a prominent flourish at the end.

Date:

16/01/2023

Acknowledgements

Firstly, I would like to extend a heartfelt thank you to supervisor Charles Macleod for his regular and continued help and guidance throughout the highs and lows of the last three years. I greatly appreciate the relaxed and yet professional nature of his supervision, allowing me to take ownership of the work and steer the PhD in my preferred direction.

Thanks also goes to second supervisor James Carroll of the Wind Energy Centre (WEC) for both academic support and providing a useful link between my research group and the Centre for Doctoral Training (CDT), through which this PhD was made possible.

Numerous members of the Centre for Ultrasound Engineering (CUE) have given their time and effort into explaining the operation of necessary hardware and software. However, some must be mentioned here for special praise. In the first year, Carmelo Mineo for providing the robot training courses as well as answering my countless follow-up questions. Knowledge of how to operate and program these robots was vital for practical work conducted. Therefore, I would also like to thank Harris Loukas for sharing his extensive knowledge of KUKA robotics and for always being willing to troubleshoot the latest issue.

The expertise of David Lines in ultrasonic transducer operation, data analysis and presentation has also been invaluable. It has been a pleasure working with an expert in the field and I thank him for his patience and feedback when frowning at my work.

Regular and reliable contact with members of industrial partner, Siemens Gamesa Renewable Energy (SGRE), has been very useful in keeping the project on track and implementing the aims, first discussed during an introductory visit to Denmark. I would like to thank the members of the Non-Destructive Testing (NDT) team at the SGRE Aalborg Plant: Georgios Martakos, Lars Heskjaer, Per Nielsen, Cristiani Demetrio and Alexis Detroyat. Thanks also to Chris Briggs, Regional Innovation Manager at SGRE, for being a point of contact as well as organising a very informative visit to the SGRE plant in Hull during my final year.

A note of appreciation also goes to the UKRI COVID-19 Doctoral Extension Funding Scheme for granting me an additional three month's funding in which to complete and submit my PhD. This has reduced the inevitable pressure which comes at the end of such a project and removed the risk of completing a thesis whilst in other employment.

Table of Contents

Copyright Declaration.....	2
Acknowledgements	3
Table of Contents	5
List of Figures.....	9
Abbreviations.....	17
Abstract	19
1 Introductory Chapter	21
1.1 Introduction.....	21
1.2 Background.....	23
1.3 Contributions to Knowledge.....	29
1.3.1 Practical Inspections and Ultrasonic Inspection System.....	29
1.3.2 Adaptive and Autonomous MA Beamforming.....	30
1.3.3 FVF Determination Theory	31
1.4 Publications	32
1.5 Thesis Structure	33
2 Review of Relevant Topics	35
2.1 Wind Turbine Design	35
2.1.1 Overview	35
2.1.2 Blade Design	39
2.1.3 Blade Materials	40
2.1.4 Pultruded CFRP Panel Uncoiling.....	42
2.2 Composite Materials	44
2.2.1 Introduction.....	44
2.2.2 Defects in Composites.....	46
2.2.3 Defects in Wind Turbine Blades	50
2.3 Non-Destructive Testing and Evaluation	52
2.3.1 Introduction.....	52
2.3.2 NDT Techniques	53
2.3.3 Defect Detection	57

2.3.4	Robotic Automated NDT	58
2.4	Ultrasound	61
2.4.1	Introduction.....	61
2.4.2	Historical Context	63
2.4.3	Sound Propagation	64
2.4.4	Ultrasonic Inspection	69
2.4.5	Ultrasonic Data Presentation	81
2.4.6	Signal Processing Techniques.....	88
2.5	Ultrasonic NDT in Composites	99
2.5.1	Introduction.....	99
2.5.2	Frequency Tuning Methods	100
2.5.3	Defect Detection Considerations	103
2.5.4	Composite Defect Signatures.....	105
2.5.5	Ultrasonic NDT of Wind Turbine Blades.....	109
2.6	Conclusion	116
3	Phased Array Ultrasonic Inspection.....	117
3.1	Introduction.....	117
3.2	Theory.....	119
3.2.1	PAUT Inspection Parameters	119
3.2.2	PA Calibration Work	126
3.2.3	Data Processing	139
3.2.4	Ultrasonic NDT Modelling	144
3.3	Practical Set-Up	149
3.3.1	KUKA Robotics and Force-Torque Sensor	151
3.3.2	Olympus Phased Array Wheel Probe	153
3.3.3	Phased Array Data Acquisition.....	155
3.3.4	LabVIEW Integration	157
3.3.5	Samples	159
3.4	Results and Discussion.....	165
3.4.1	Defect-free Panel Scans	165
3.4.2	Artificial Defect Panel Scans.....	166
3.4.3	Defective Panel Scans.....	168
3.4.4	Practical Limitations	172

3.5	In-process Ultrasonic Inspection System.....	181
3.5.1	Introduction.....	181
3.5.2	Components	181
3.5.3	Samples	186
3.5.4	Inspection Procedure	188
3.5.5	Results and Discussion	190
3.5.6	Future Work	192
3.6	Conclusion	196
4	Adaptive MA Beamforming	197
4.1	Introduction.....	197
4.1.1	Linear Scanning and MA Beamforming.....	197
4.1.2	MA in Medicine	200
4.1.3	Defect Sizing Techniques.....	200
4.2	Autonomous Multi-Aperture Theory	201
4.3	Experimental Procedure	203
4.3.1	Hardware.....	203
4.3.2	Resolution Definitions	204
4.3.3	Inspection Scenarios	204
4.4	Calibration and Validation Samples.....	206
4.5	Results and Discussion.....	208
4.5.1	Sizing and Location of Calibration Defects.....	209
4.5.2	MA Gap Determination	210
4.5.3	Validation Scans	216
4.5.4	PAC Firmware Update	222
4.6	Conclusions and Future Work	225
5	FVF Screening and Fibre Directionality.....	227
5.1	Introduction.....	227
5.1.1	Composite Material Structure and FVF Definition.....	228
5.1.2	FVF Effect on Properties.....	230
5.1.3	Conventional FVF Measurement.....	231
5.2	Ultrasonic FVF Measurement Theory.....	233
5.3	Experimental Hardware.....	241

5.4	Ray Tracing Simulations.....	243
5.5	Results and Discussion.....	245
5.5.1	Glass Block Validation	245
5.5.2	CFRP Panel Characterisation	247
5.5.3	FVF Investigations	248
5.5.4	Repeatability of Results.....	249
5.5.5	Generation of Screening Curves.....	251
5.5.6	Blind Tests	252
5.6	T/R Reduction Concept.....	256
5.7	FVF Determination with Linear Imaging.....	260
5.8	Fibre Directionality	262
5.8.1	Theory	262
5.8.2	Initial Results and Discussion	264
5.9	Future Work.....	269
5.10	Conclusions.....	271
6	Concluding Chapter.....	273
6.1	Conclusions.....	273
6.2	Future Work.....	276
6.2.1	In-process Ultrasonic Inspection System	276
6.2.2	Adaptive MA Beamforming.....	276
6.2.3	Advanced Defect Identification.....	278
6.2.4	GFRP Inspection	278
6.3	General Overview	280
6.4	References	281

List of Figures

Figure 1.1. Necessary emission pathways alongside actions and policies [4].	24
Figure 1.2. European wind resource, both onshore and offshore [13].	25
Figure 1.3. Total European installed wind capacity by country [11].	26
Figure 1.4. LCoE both fossil-fuel based and renewable [21].	27
Figure 2.1. Schematic highlighting main components of the 'Danish Concept'.	35
Figure 2.2. Example of a wind turbine power curve with the cut-in, cut-out and rated-wind speeds labelled.	38
Figure 2.3. Blade design schematic highlighting the changing cross-sectional shape from root to tip.	39
Figure 2.4. Schematic illustrating the pultrusion process to manufacture a single-ply panel.	41
Figure 2.5. Blade internal structure incorporating both pultruded CFRP panels and GFRP with various layup orientations.	42
Figure 2.6. Schematic highlighting the stages of the pultruded CFRP uncoiling and gridding processes.	43
Figure 2.7. Material use as weight percentage in a Boeing 787 passenger jet [34].	45
Figure 2.7. Example images of phased array robotic ultrasonic inspection hardware, similar to that used in referenced works.	60
Figure 2.8. Schematic highlighting mode conversion and the presence of first and second critical angles as the angle of incidence is varied.	67
Figure 2.9. Schematic highlighting pulse-echo, pitch-catch, and through-transmission ultrasonic inspection modalities.	73
Figure 2.10. Phased array focal laws used to steer and focus a beam [67].	74
Figure 2.11. MATLAB simulation using of focal laws and the principles of acoustic interference to show beam focussing on a chosen location.	75

Figure 2.12. FMC matrix generated by reception and transmission using all possible combinations of elements.....	76
Figure 2.13. Example of reflection and transmission coefficients using ultrasonic immersion test of steel.	79
Figure 2.14. Example of an A-scan in raw RF format.	82
Figure 2.15. Example of prenatal scan [73].....	83
Figure 2.16. Example of amplitude and ToF C-scans.....	85
Figure 2.17. Reference sample schematic to illustrate TVG explanation.	89
Figure 2.18. Schematic showing a TVG curve modifying the amplitude of features in an A-scan.	90
Figure 2.19. Example of wind turbine blade inspection process.	113
Figure 2.20. Image of the P-scan system by Force Technologies [115].	115
Figure 3.1. Schematic illustrating linear beamforming with $A=4$, $S=1$, $C=64$	120
Figure 3.2. Screenshot, highlighting inputs and outputs of an Excel-based tool used to demonstrate the relationship between inspection parameters.	124
Figure 3.3. Images, including dimensions, of a glass calibration block used for FMC data collection and subsequent phased array characterisation.....	128
Figure 3.4. Example plot highlighting the calculation and presentation of the median waveform.	129
Figure 3.5. Example spectrum taken from the same example median waveform as in previous figure.....	130
Figure 3.6. Example spectrum displaying the two separate definition of the centre frequency.	131
Figure 3.7. Bandwidth calculation using the same example spectrum.	132
Figure 3.8. Waveform plot with various dB levels to define the pulse width.....	133
Figure 3.9. Graphic highlighting the sensitivity definition.	134
Figure 3.10. Graphic highlighting the definition of element crosstalk taken from first and second off-diagonals in the calibration FMC matrix.	135
Figure 3.11. Phased array characterisation hardware	137

Figure 3.12. Output datasheet for an Olympus 64-element, 5 MHz probe.....	137
Figure 3.14. Example A-scan highlighting which region is used for each type of C-scan.....	141
Figure 3.15. Example RF and corrected A-scans demonstrating the gating procedure.....	143
Figure 3.15. Example of CIVA model view as well as ultrasonic phased array probe composite material parametrisation.	147
Figure 3.16. System block diagram illustrating the connections between each of the practical component referred to an image of the experimental set-up.....	150
Figure 3.17. Images of the probe and associated hardware attached to the KR6 robot flange. The second image shows a clean section of the pultruded sample	150
Figure 3.18. Example images of KUKA KR6 robot and Shunk FT sensor used throughout.	152
Figure 3.19. Labelled image of disassembled phased array ultrasonic wheel probe.	154
Figure 3.20. Image of the fully assembled wheel probe.....	154
Figure 3.21. Examples of PAC units as manufactured by PEAK NDT.....	155
Figure 3.22. Annotated VI controls used for robot path execution and array control	158
Figure 3.24. Image of a defect-free pultruded CFRP sample	161
Figure 3.25. Images of a pultruded CFRP sample with artificial defects machined.	162
Figure 3.26. Dimensions and positions of artificial defects in CFRP panel.	163
Figure 3.27. Defect panel 3 photographs with defects highlighted.....	164
Figure 3.28. Defect Panel 4 photographs with defects highlighted.....	164
Figure 3.29. Example of A, B-scan taken from a clean pultruded CFRP panel. The A-scan is located at the indicated position on the B-scan.....	166
Figure 3.30. A and B-scans taken at a hole position from the artificial defect panel. The A-scan is taken from the indicated position on the B-scan.	167

Figure 3.31. Amplitude profile taken from the internal section of the sample across the B-scan. Used for 6 dB hole sizing.	167
Figure 3.32. C-Scans taken from a section of the artificial defect panel.	168
Figure 3.33. B and C-scans taken for the RoI in Defect Panel 1.	169
Figure 3.34. B and C-scans taken for the RoI in Defect Panel 2.	169
Figure 3.35. B and C-scans taken for the RoI in Defect Panel 3.	170
Figure 3.36. ToF C-scan taken from Defect Panel 4.	170
Figure 3.37. 6 dB sizing technique, across five lateral positions, applied to an internal defect found in Defect Panel 1.	171
Figure 3.38. Schematic defining pitch and roll axis for the wheel probe	172
Figure 3.39. Schematic demonstrating the pitch and roll limits for ultrasonic wheel probe phased array imaging	173
Figure 3.40. Impact of pitch angle on C-scans of 10 mm artificial defect holes. .	175
Figure 3.41. Effect on increasing pitch angle on ToF and backwall amplitude in each A-scan.	175
Figure 3.42. Impact of roll angle on the artificial defect sample C-scans.	176
Figure 3.43. Impact of force variation on artificial defect sample C-scans.	178
Figure 3.44. Wheel probe and transducer overlapping the side of the sample. .	179
Figure 3.45. Impact of tyre overlap on artificial defect sample C-scans.	180
Figure 3.46. AutoCAD assembly of an ultrasonic inspection system design.	182
Figure 3.47. Images of the completed inspection with key components labelled.	185
Figure 3.48. Image detailing encoder components and the mounting point.	185
Figure 3.49. Defect panel 7 with surface defect indications highlighted.	186
Figure 3.50. Defect panel 9 with surface defect indications highlighted.	187
Figure 3.51. Defect panel 10 with surface defect indications highlighted.	187
Figure 3.52. Schematic detailing positions of scan passes in relation to sample. .	189
Figure 3.53. Image detailing example of scan pass 1 in relation to sample.	189
Figure 3.54. Defect Panel 7, amplitude, and ToF C-scan.	191

Figure 3.55. Defect Panel 10, amplitude, and ToF C-scan.....	191
Figure 3.56. Defect Panel 11, amplitude, and ToF C-scan.....	192
Figure 3.57. Schematic of proposed single array and wheel probe set-up.	194
Figure 3.58. Screenshot, highlighting inputs and outputs of an Excel-based tool used to demonstrate achievable resolution for different custom probe configuration.	195
Figure 4.1. Schematic contrasting linear (top) to MA (bottom) beamforming for the first three pulses. In this example the aperture, step and MA gap size are three, one and two elements respectively.	198
Figure 4.2. Schematic of FMC matrix to illustrate algorithm procedure.	202
Figure 4.3. Flow chart describing the autonomous and adaptive MA algorithm.	202
Figure 4.4. Image of the of the probe and associated hardware attached to the KR6 robot flange.....	203
Figure 4.5. Image and specifications of calibration sample used to collect FMC data.	207
Figure 4.6. Decay curves observed by shifting receiving element incrementally away from the edge of each defect in calibration set 5. Data are obtained from three separate FMC acquisitions scanning four separate defects.	211
Figure 4.7. Schematic of focal laws written with algorithm-determined MA gap. Only the first two pulses of the necessary nine are shown.	213
Figure 4.8. B-scans obtained with both a linear and three MA beamforming cases. The focal law parameters in each are as follows. a) Linear firing with a four-element aperture. b) MA firing with a gap of five elements chosen by the adaptive MA algorithm as the op optimum size. c) MA firing with a decreased gap of three elements, chosen to be too small to prevent beam contamination. d) MA firing with an increased gap of seven elements, chosen to be unnecessarily large and thus wasting PRF for the same imaging quality. The results of defect sizing performed on each are presented in Table 5.5.’	214
Figure 4.9. Sample containing a series of 3 mm holes, used for the validation .	217

Figure 4.10. Validation C-scans from scenarios A-C. The inspection parameters for each image are as follows. a) The reference case, low speed using linear scanning. b) The high-speed case, using the same focal laws but a much higher scanning speed than in 'a'. c) Finally, the MA firing case with gap chosen by the autonomous MA algorithm. Both high resolution and reliable defect sizing is achieved at high scanning speed. The results of defect sizing for each scenario are presented in Figure 12..... 218

Figure 4.11. Comparison of amplitude profiles in both axis for 1.0 mm and 3.0 mm and spaced holes in the validation panel using each inspection scenario. 221

Figure 4.12. Schematic detailing the saving methodology applied during AMPS 3 and 13 commands, applied to both linear and MA beamforming. 223

Figure 4.13. Schematic detailing the desired hybrid saving methodology to optimise the PAC operation for MA beamforming..... 224

Figure 5.1. Schematic detailing a cross-sectional view of a composite showing fibres and the geometry calculations yielding the maximum FVFs. 228

Figure 5.2. Schematic of the phased array inspection set-up..... 234

Figure 5.3. Schematic illustrating the geometry of wheel probe and sample in a cross-sectional view. The interfaces analysed using Snell's law, for both ray propagation paths, are circled, and expanded. 235

Figure 5.4. Schematic illustrating Snell's Law for both propagation paths..... 236

Figure 5.5. FMC definition showing the structure of matrix containing A-scans from every possible transmit and receive combination. The angular variation is achieved by investigating the effect of shifting the reception element whilst transmission is constant..... 238

Figure 5.6. Example A-scan, highlighting the delay between front and backwall response as well as the envelope-detected using the Hilbert Transform. 239

Figure 5.7. Image showing the experimental hardware and CFRP sample used, highlighting the necessary array and fibre orientation 243

Figure 5.8. Validation of method using FMC data acquired from a isotropic material, a glass calibration block. Experimental data and CIVA simulated data are plotted on the same axis.....	245
Figure 5.9. Comparison of relative velocity as a function of angle to normal incidence. Three FVFs are plotted along with data from CIVA simulation. The increase in velocity is normalised and expressed as increase relative to that seen at normal interface.....	247
Figure 5.10. Relative velocity curves generated for six FMC datasets taken from each FVF panel.	250
Figure 5.11. Average curves generated from multiple FMC datasets. Lower and upper screening curves are formed based on the standard deviation from the mean for each FVF.....	251
Figure 5.12. Validation of method using FMC from a separate FVF 60.5% panel compared to the screening curves as well as the FVF 60.5% calibration panel. ...	252
Figure 5.13. Example A-scans from $T_{10}R_{15}$ and $T_{10}R_{35}$, highlighting the amplitude of echoes and thus the increased attenuation as propagation angle and distance are increase.	254
Figure 5.14. Geometry of inspection set giving the maximum propagation angle in the sample when transmission and reception elements are 25 apart.....	255
Figure 5.15. Schematic showing the active elements utilised in the first three pulses of a four-element linear scan. A 64-element array would require 61 pulses of this aperture size for complete one sweep.	256
Figure 5.16. Schematic illustrating the transmission and reception elements used for firstly a linear B-scan, and secondly to capture the additional data required for FVF screening.	258
Figure 5.17. Example A and B-scans obtained during phased-array inspection of defect-free samples alongside FVF screening implementation.....	261

Figure 5.18. Inspection implementation. Screening curves and average curves for each FVF calibration sample plotted alongside the point values of effective velocity increase at specific angles from the inspection	261
Figure 5.19. Image showing probe rotation angle at zero degrees. The array and fibre orientation are parallel.	262
Figure 5.20. Schematic highlighting angles and orientations regarding fibre directionality work.	263
Figure 5.21. Schematic highlighting post-processing steps to yield anisotropy quantification from FMC data.	265
Figure 5.22. Increased in velocity as a function of sample propagation angle for a 0-90 range of probe rotation angles. Plots for FVF = 60.5, 66.3 and 69.9% are shown.	266
Figure 5.23. Anisotropy quantification graph highlighting a subsection of sample propagation angles used to generate curves.	267
Figure 5.24. Effective velocity increase across the full rotation of probe rotation angle at a subsection of sample propagation angles. Curves are generated for three FVF values.	268

Abbreviations

ADC	Analogue to Digital Conversion
Bi-A	Bi-Axial
BVID	Barely Visible Impact Damage
CDT	Centre for Doctoral Training
CFRP	Carbon Fibre Reinforced Polymer
CoP	Conference of the Parties
CT	Computed Tomography
CUE	Centre for Ultrasound Engineering
DoF	Degree of Freedom
EMAT	Electromagnetic Acoustic Transducer
FMC	Full-Matrix Capture
FPS	Frames per Second
FT	Force-Torque
FT	Fourier Transform
FVF	Fibre Volume Fraction
GFRP	Glass Fibre Reinforced Polymer
HAWT	Horizontal Axis Wind Turbine
HT	Hilbert Transform
IPCC	Inter-Governmental Panel on Climate Change
LCoE	Levelized Cost of Electricity
MA	Multi-Aperture
ML	Machine Learning
MLT	Multi-Line Transmission

MRI	Magnetic Resonance Imaging
NDE	Non-Destructive Evaluation
NDT	Non-Destructive Testing
PA	Phased Array
PAC	Phased Array Controller
PAUT	Phased Array Ultrasonic Testing
POD	Probability of Detection
PRF	Pulse Repetition Frequency
RF	Radio Frequency
RoI	Region of Interest
RSI	Robot Sensor Interface
RT	Radon Transform
SGF	Savitzky-Golay Filter
SGRE	Siemens Gamesa Renewable Energy
SHM	Structural Health Monitoring
SNR	Signal to Noise Ratio
TFM	Total Focussing Method
TGC	Time Gain Compensation
ToF	Time-of-Flight
TRL	Technology Readiness Level
TVG	Time Varying Gain
UD	Uni-Directional
WAMESS	Wind and Marine Energy Systems and Structures
WEC	Wind Energy Centre

Abstract

In response to the international climate crisis, governments across the globe have set target dates by which they aim to achieve net zero greenhouse gas emissions. These targets range between the years 2040 to 2060 depending on a range of environmental, technological, and political factors at play in each nation. The necessity to decarbonise the electricity supply is key to this and due to its cost effectiveness, and technological maturity, wind power plays a major role. The size of installed wind capacity will continue to grow exponentially over the coming years thus making the manufacture of wind turbine blades a rapidly growing and developing sector [1].

Non-destructive testing (NDT) is used across a wide range of engineering fields to ensure a final component is defect-free and can be guaranteed to perform as certified in each application. In the framework of blade manufacture, NDT is often in the form of ultrasonic inspections that can identify faults and errors in the early production phase so to prevent failures and reduce the cost of operations and maintenance. This thesis reports on research carried out to develop future ultrasonic NDT techniques applied to composite turbine blades. To that end, three innovative developments to improve the manufacturing environment, resulting in significant overall benefits for clean energy production, are presented.

An in-process ultrasonic inspection system, using dry-coupled phased array inspection has been designed and tested for the inspection of Carbon Fibre Reinforced Polymer (CFRP) blade subcomponents.

Secondly, novel adaptive methods of ultrasonic phased array operation and data analysis, employed using a new Multi-Aperture (MA), ultrasonic beam transmission and reception strategy, have been shown to increase imaging frame rates, resulting in the ability for increased inspection speeds and/or resolutions. An adaptive and autonomous MA firing sequence generator has been designed, specific to the sample and target defect size, with frame rate increases by a factor of 6.7 reported.

Finally, the nature of an ultrasonic wave's interaction with a composite's non-homogenous and anisotropic internal structure has been used to determine both the Fibre Volume Fraction (FVF) as well as fibre orientation, in the third major contribution reported in this thesis. Data obtained was used as an effective screening technique to guarantee that these parameters, and thereby the mechanical performance of a composite, fall within the desired range. FVF values determined by this method were typically within 2 % of reference values, measured by a third party using conventional testing methods.

1 Introductory Chapter

1.1 Introduction

This three-year PhD project is concerned with advanced Non-Destructive Testing (NDT) of wind turbine blade defects. These are state-of-the-art blades, constructed from composite materials and are used in the latest generation of multi-megawatt offshore installations. For this, ultrasonic, dry-coupled phased array inspection is used, in combination with novel transmission/reception strategies and data analysis methods. Research proposed herein enables the industry to take steps in moving towards fully automated inspections in large-scale blade manufacturing.

The work is made possible via the Centre for Doctoral Training (CDT) in Wind and Marine Energy Systems at the University of Strathclyde. Following on from a year of taught courses, the project started in November 2019 and was carried out at the Centre for Ultrasound Engineering (CUE), also at Strathclyde. This was in collaboration with Siemens Gamesa Renewable Energy (SGRE), one of the world's leading wind turbine manufacturers. Regular communication as well as progress meetings, between the Glasgow-based team and NDT department at SGRE in Aalborg, Denmark, is established at the outset and continues to be important throughout the course of the project. SGRE supports the project by providing the current ultrasonic inspection benchmark and supplying material samples as well as technical engineering support.

The Centre for Ultrasonic Engineering (CUE), at the University of Strathclyde is a multi-disciplinary research group. Their expertise in ultrasonic transducer systems and NDT inspection range over a wide range of industrial sectors. These range from bioacoustics, looking towards the natural world to inspire innovations in acoustic and ultrasonic engineering, through transducer design involving precise machining of piezo electrics as well as industrial process control, metrology, and NDT automation. This last area makes the expertise of the group particularly suitable to this project. CUE work with the aerospace, energy, nuclear and oil and gas sectors to deliver novel robotic inspection solutions carried out in a range of physical environments and concerning a multitude of different materials, from in-process ultrasonic weld inspection to robot path planning for complex geometry composite components used in high-end aerospace. The combination of expertise in ultrasonic NDT of composites and robotic inspection allows for a PhD researching advanced ultrasonic inspection of composite wind turbine components to be successfully carried out.

1.2 Background

Despite the science behind man-made global warming, through the release of so-called ‘greenhouse’ gases, being well understood and published, since the 1980’s, it has taken the main historical emitters till late 2015, at the UN Climate Change Conference, Conference of the Parties (COP21) in Paris, to put in place any meaningful commitments on emission reductions. Such pledges, although not legally-binding, are hoped to limit global mean temperature rises to within 2 degrees Celsius, as compared to a pre-industrial benchmark taken from 1850-1900, and ideally to within 1.5 degrees [2]. Following this, the 2021 UN Climate Change Conference (COP26) in Glasgow, was seen as very much a last chance to take further steps to phase out the burning of fossil fuels as well as address other sources of CO₂ and CH₄ (methane), in food production and building materials. The potential scale of both ecological and humanitarian disaster, cannot be underestimated and is best detailed in the latest report, published by the Inter-governmental Panel on Climate Change (IPCC) [3]. Shown in Figure 1.1 are the global emission pathways necessary to limit warming, as compared to a pre-industrial benchmark, alongside current actions, and policies [4].

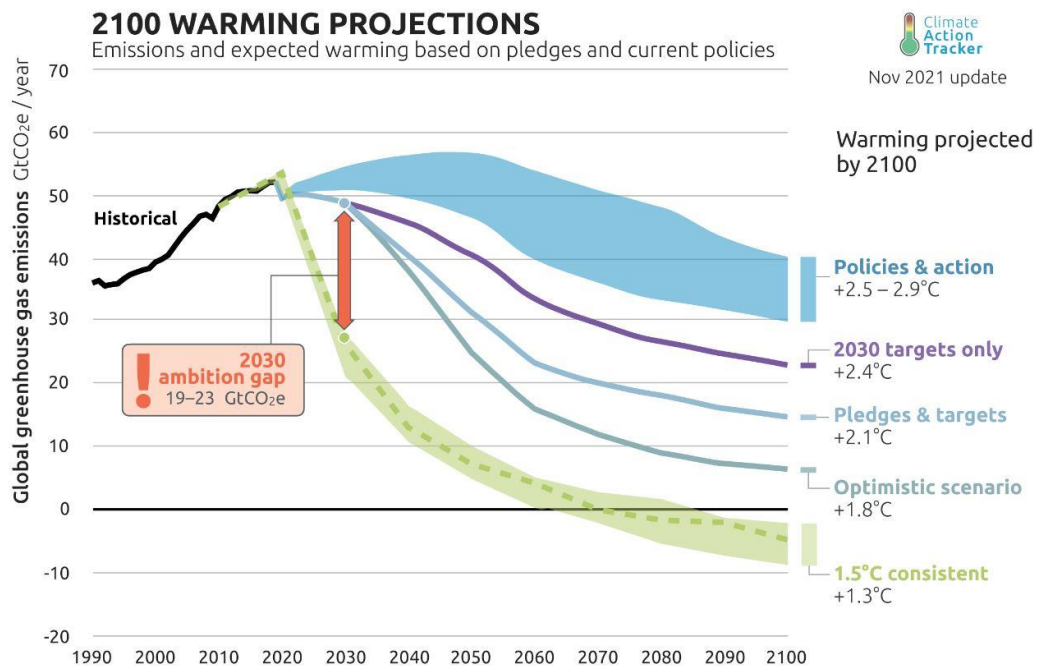


Figure 1.1. Necessary emission pathways alongside the impact of current actions and policies [4].

Consequently, renewable energy targets, now set by numerous European governments mean that there is a strive for clean energy sources to provide the world with low cost and low carbon energy sources. At their current levels of technological maturity, both wind and solar far eclipse wave or tidal technology [5][6][7]. Whilst solar energy has shown significant potential across more southern European nations, this form of renewable energy is of less relevance in the UK due to the more northerly latitude resulting in reduced solar irradiance. Therefore, wind energy will continue to play a leading role in UK electricity generation with the size of installed capacity expected to grow exponentially over the coming decades [1]. As of 2020, wind energy accounted for 24% of total electricity generation in the UK with a roughly even split between onshore and offshore installations [8]. The UK has the highest capacity of

installed offshore wind in Europe at over 10 GW, having grown rapidly over the last decade [9][10]. This can be seen in Figure 1.3, although if onshore is also considered the UK is in third place [11]. It is also in the fortunate position of having 40 % of Europe's wind resource [12]. This fact can clearly be seen on the map of average wind speed, both on and offshore, found across Europe that is shown in Figure 1.2 [13].

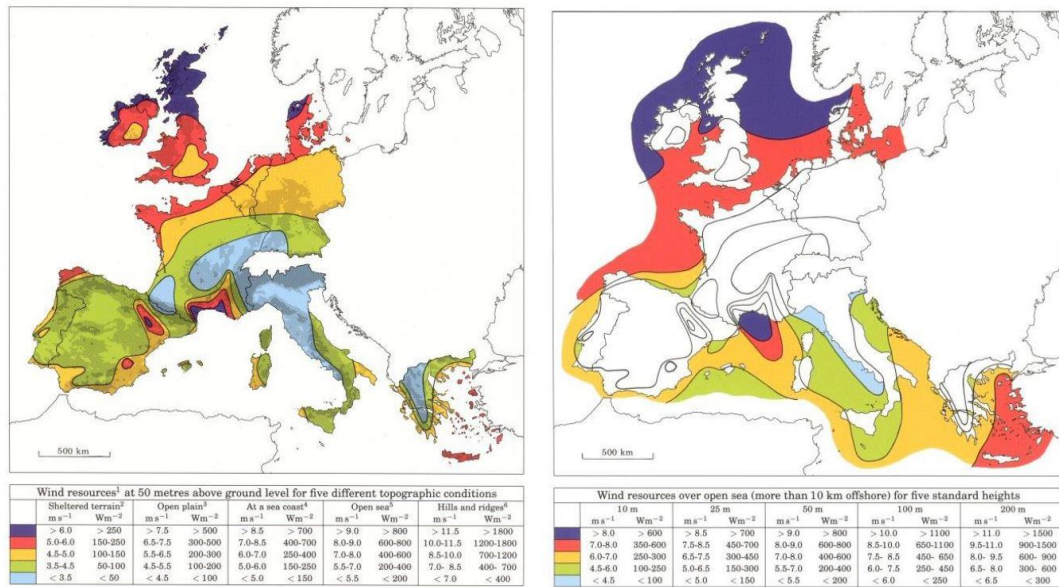


Figure 1.2. European wind resource, both onshore and offshore [13].

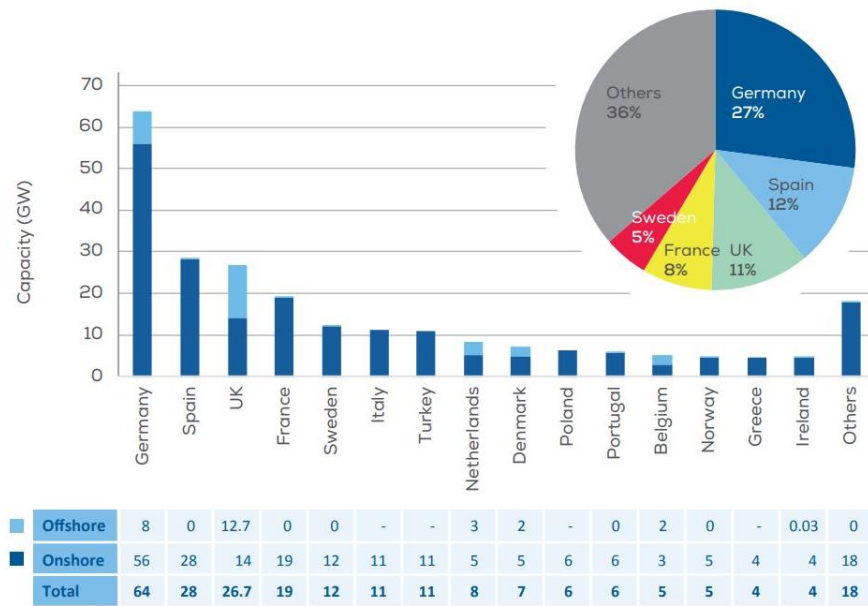


Figure 1.3. Total European installed wind capacity by country [11].

Offshore turbines tend to be larger than their onshore counterparts, taking advantage of fewer transport and regulatory limitations. In addition to this, greater, and more constant wind speeds are commonly found offshore. Wind-turbine blades are now approaching 100 metres in length with capacities exceeding 8 MW per turbine [14][15]. The proportion of electricity produced from these offshore installations is set to rise significantly faster than their onshore counterparts and it is predicted that nearly 40 GW installed capacity will be required by 2030 for the UK government to meet its legally binding targets of net zero greenhouse gas emissions by 2050 [8][9]. [16]

Cost effectiveness has also been the key driver in making both on and offshore wind power competitive compared to fossil fuel generation. The latest figures place offshore wind as having the lowest Levelized cost of Electricity (LCoE) of all sources at just above and below 40 £/MWh for on and offshore, respectively [17][18][19]. A separate example shows offshore wind power to be four times cheaper than new gas developments [20]. The graphic shown in Figure 1.4, is taken from a recent LCoE analysis and highlights the recent declining trend in the cost of wind energy [21].

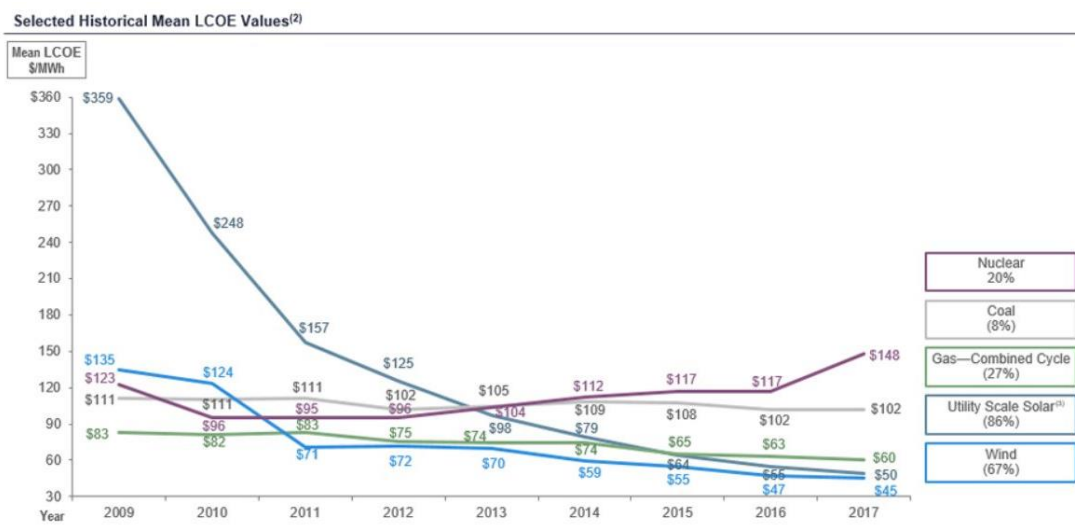


Figure 1.4. A LCoE analysis for both fossil-fuel based and renewable energy sources [21].

Since the earliest days of turbine blade design and construction, NDT methods have been utilized early in the production phase. Wind turbine blades are one of the most costly and complicated components of the wind turbine, their blades manufactured using carbon and glass fibre reinforced polymer (CFRP and GFRP) composites. NDT methods are utilized to identify any potential defects so to reduce potential asset outages as well as operational maintenance costs and extend lifetimes. Ultrasonic testing techniques are a promising NDT method for blade inspection, due to their volumetric inspection capability, but current uses are limited due to complexities with the data or image analysis typically performed by trained experts. The aerospace industry has pioneered NDT methods for complex geometry inspection of composite materials, coupled with detection algorithms and machine-learning techniques and thereby set the benchmark for fast and reliable fault detection in high end composite components. The investigation into and application of these methods to wind turbine blades will enable more efficient and cost-effective inspections resulting in overall advantages for clean energy production.

1.3 Contributions to Knowledge

The main achievements and contributions to knowledge of this PhD can be broadly split into three pieces of work. These form the main body of this thesis and are described in Chapters 3, 4 and 5, respectively.

1. Characterisation of the effectiveness of practical ultrasonic inspections leading to the development of an in-process ultrasonic inspection system for CFRP components.
2. Development of an adaptive and autonomous MA beamforming approach to increase frame rates, leading to increased inspection speed and/or resolution.
3. Fibre volume fraction and fibre directionality determination based on analysis of FMC data quantifying sample anisotropy.

1.3.1 Practical Inspections and Ultrasonic Inspection System

Firstly, hardware to perform small scale inspections of CFRP sample was set-up in a Strathclyde laboratory. The operation of this equipment and design of data analysis and imaging algorithms proved the effectiveness in relation to the project aims. Inspections could be optimised with the focus on achieving high scanning speeds and robust defect detection. The first half of Chapter 3 describes the work in detail and presents data acquired and results. This initial hardware led to the design of a prototype in-process ultrasonic inspection system, targeted at implementation in the

production line. Justification for this design, as well as initial tests, carried out on defect CFRP panels provided by the industrial partner, are detailed in the second half of Chapter 3.

1.3.2 Adaptive and Autonomous MA Beamforming

Secondly, novel work has been carried out on ultrasonic multi-aperture beamforming. This is the focus of Chapter 4. The technique has been shown to increase frame rates, and hence inspection speeds, when compared to traditional linear beamforming. Thereby, this has the potential to address any potential NDT bottlenecks caused by the recent rapid growth in demand for wind turbine installations. An adaptive MA, and spacing, concept is presented to autonomously optimise the MA focal laws for the sample in question as well as a critical defect size. For this, Full Matrix Capture (FMC) data from a calibration sample, designed specifically for the target defect size and spacing, is used to drive the resultant optimised inspection scenario. A 6.7-fold increase in scanning speed, with no degradation in resolution or defect sizing accuracy, was reported. Three inspection scenarios are presented using firstly linear beamforming at 3.0 mms^{-1} and 22.0 mms^{-1} before MA beamforming at 22.0 mms^{-1} . Resolutions of 0.8, 5.4 and 0.8 mm in the scan axis are recorded and consequently the optimum scenario, allowing for high resolution at the higher scanning speed, is presented. The concept is verified and validated by C-scan inspection of CFRP samples, at varying inspection parameters, commonly used in high-power blade construction.

1.3.3 FVF Determination Theory

A fibre re-enforced plastic composite is formed by the combination of load-bearing fibres and a resin matrix, holding these in a fixed structure. These fibres can be glass, carbon, or natural materials such as hemp or cotton, often arranged in layers with alternating orientation so that the final material's elastic properties are constant in at least one plane. Composites have become the material of choice in a wide range of manufacturing applications. The fibre volume fraction (FVF) is the percentage of the composite taken up by the fibres and typically in the range of 50-70 % and plays a key role in determining the final strength and stiffness of a part as well as influencing the ultrasonic bulk velocity.

A novel screening technique for FVF, based on the angular dependence of the sound velocity with respect to the composite fibre direction, is presented in Chapter 5. This method is introduced and validated by inspection of the same pultruded CFRP panels used in the previous two chapters. Full matrix capture (FMC) data acquired from a Phased Array (PA) ultrasonic probe is used to generate calibration data for samples ranging in FVF from 60.5 % to 69.9 %. These screening curves, of velocity as a function of angle, are used to estimate the FVF of samples and ensure they fall within the desired range. Experimental results of 61, 66 and 68 %, with accuracy estimation 1-2 %, compare favourably to the known values 60.5 ± 0.6 , 66.3 ± 1.3 and 69.9 ± 0.3 %, obtained by third-party, acid digestion, measurement. Again, results shown here offer significant potential in terms of the factory implementation of NDT procedures to ensure final parts satisfy standards and certification by ensuring any FVF inconsistencies are identified as early in the manufacturing process as possible.

1.4 Publications

Various aspects of the research conducted for this PhD have been published in reputable academic journals as well as presented at conferences. Details of these are listed chronologically below.

Conferences:

- 2nd Annual General Meeting of Scottish Ultrasound 28th February 2020
- Future Wind and Marine 2020 5th March 2020
- 3rd Annual General Meeting of Scottish Ultrasound 27th August 2021
- Future Wind and Marine 2022 17th February 2022

Journal Papers:

E. Duernberger, C. MacLeod, D. Lines, C. Loukas, and M. Vasilev, “*Adaptive optimisation of multi-aperture ultrasonic phased array imaging for increased inspection speeds of wind turbine blade composite panels,*” NDT E Int., vol. 132, no. May, p. 102725, 2022, doi: 10.1016/j.ndteint.2022.102725.

E. Duernberger and C. MacLeod, D. Lines “*Fibre volume fraction screening of pultruded carbon fibre reinforced polymer panels based on analysis of anisotropic ultrasonic sound velocity,*” Compos. Part B Eng. (***Under review***)

1.5 Thesis Structure

This thesis is formed of six chapters. An introduction to the topic areas, research group and contributions to knowledge is given in the first chapter. This introduces relevant concepts and justifies the research. A more in-depth explanation and literature review concerning, wind turbine blade construction, composite materials, and the use of ultrasound in NDT is given in Chapter 2. Chapter 3 details the initial inspection set-up, presenting ultrasonic data and results, the optimisation for high scanning speeds and the design and test of an in-process ultrasonic inspection system for factory implementation. This chapter is primarily focussed on the practical aspects of the PhD.

Chapters 4 and 5 are extended versions of the journal publications detailed in the ‘Publications’ Section 1.4. Additional data and figures are provided with more emphasis given to discussion of results and potential improvements in future work. Finally, Chapter 6 concludes the thesis, summarises what has been achieved and reiterates the importance of the work within the field of NDT of wind turbine blades.

This document follows a top-down approach. Starting with a high-level introduction to the relevant topics it outlines the path, taken by the author throughout the course of the work, to the chapters presenting novel research. Thereby, it is hoped that this thesis can fulfil multiple purposes. Initially, to educate a reader in NDT requirements, ultrasonic inspection techniques as well as wind turbine blade materials and manufacture. A person with no background in these fields should be able understand the premise of the work from the first two or three chapters without being confronted by unnecessary detail relating to specific aspects of experimental method or analysis.

Likewise, an expert can follow the flow of the thesis to the later chapters, whose content will hopefully add to their field of knowledge. Throughout these pages, clarity is the focus with detailed graphics and photos of experimental set-ups, results, and data analysis procedures, provided in each section.

2 Review of Relevant Topics

2.1 Wind Turbine Design

2.1.1 Overview

The modern industry standard is a three-bladed Horizontal Axis Wind Turbine (HAWT). This is commonly referred to as the ‘Danish Concept’. Over the course of the 1980s and 1990s the wind energy industry converged to this one design in a manner not seen by other renewable energy technologies, such as wave or tidal. The result is that wind energy possesses a level of technological maturity well ahead of other alternative renewable sources [22]. A rudimentary schematic, labelling the main components of a wind turbine, is shown in Figure 2.1.

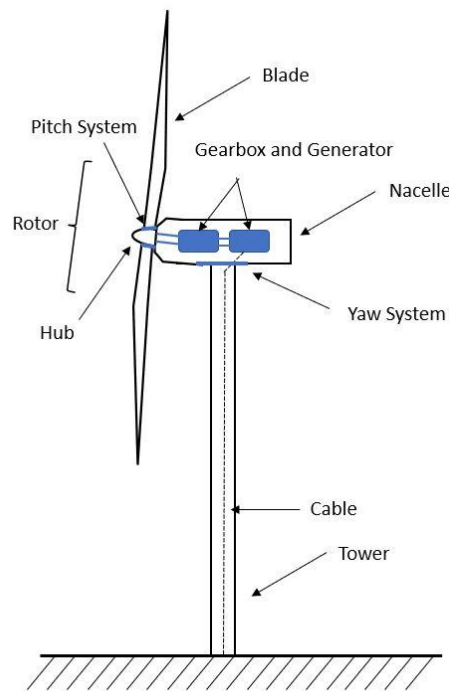


Figure 2.1. Schematic highlighting main components of the 'Danish Concept'.

The dominance of three-bladed HAWTs, over one, two or even five-bladed alternatives is the result of an optimum point between capital costs, energy capture and structural loading. Alongside the initial capital, as well as installation cost, the operational and maintenance expenses during the machine's lifespan must also be considered. A three-bladed turbine gives higher annual energy capture than a one or two-bladed alternative. It is, however, only very slightly ahead of a two-bladed design. One could argue that this small difference (approx. 5%) would be eclipsed by the lesser capital expenditure of having fewer blades. Two-bladed machines have cost and weight advantages and are easier to install. However, the three-bladed rotor has three sinusoidal loads which balance out and thus reduce cyclic fatigue loading. In short, the whole rotor is better balanced [10].

A five-bladed design would have a higher aerodynamic efficiency, albeit over a narrower range of tip-speed ratios. This can be explained by considering the energy lost to vortices at the blade tips, commonly modelled using a Prandtl correction. Moving towards an ideal rotor there would be no tip effects and aerodynamic efficiency would approach the Betz limit [23]. This is the physical maximum proportion of the energy extractable from a fluid flow, as first derived by German physicist Albert Betz. The Betz limit has a value of 0.593. Modern turbines are now achieving maximum efficiencies of around 0.53. However, the improvement offered by five blades over three is small and therefore does not justify the increased cost and weight of the two additional blades. The total tower-top mass, nacelle and rotor, is a very expensive part of the total capital cost of the turbine, as can be seen in [10].

Wind turbine blades are designed and orientated such that as much of the wind's momentum change as possible results in rotor torque. This optimisation applies at wind speeds below the rated value. The rated wind speed is that at which the turbine first reaches its rated power. For example, a typical offshore model may have a name plate capacity of 8 MW and a rated wind speed of 12 ms^{-1} [14]. At wind speeds beyond this value, but before the cut-out speed, power output must be curtailed, as best illustrated by Figure 2.2. During power curtailment, the rotor must become less aerodynamically efficient. In modern turbines this is achieved by pitch control, the principle of moving to less aerodynamically efficient operating regions, by rotating the blades, along their length axis, using motors located in the hub [12]. This reduces lift, by altering the angle of attack seen by each aerofoil section, and thus the total turning force supplying the shaft torque leading to the gearbox and/or generator. Therefore, we can say that the HAWT is a variable speed, pitch regulated machine. This control strategy, in contrast to the alternatives of fixed speed and/or stall regulation, offers the best balance between energy capture around rated power and structural loads experienced by the blades, bearings and drivetrain during normal operation and curtailment. Slight improvements in energy capture around the rated windspeed, offered by this control strategy, translate into significant increases in the annual energy capture once wind speed distribution, commonly described using a Weibull probability distribution of 10-minute mean wind speeds, is considered [22].

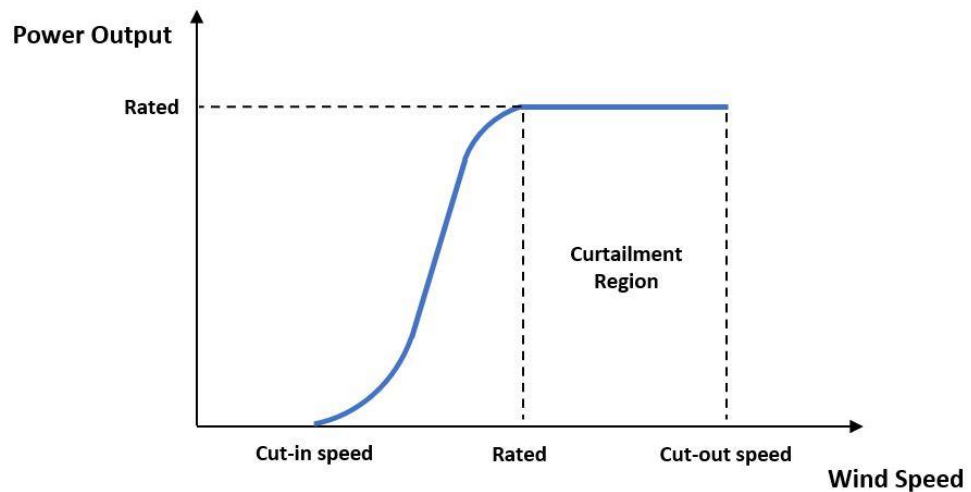


Figure 2.2. Example of a wind turbine power curve with the cut-in, cut-out and rated-wind speeds labelled.

Finally, the performance and lifetime of wind turbines is limited by cyclic loads, stimulated by stochastic aerodynamic forces, rather than any static ones. A turbine's lifespan is therefore fatigue-driven and is typically around 20-25 years. On their scale, turbines are considered 'flexible' structures, with multiple vibrational modes. It is of the utmost importance that the frequencies of these modes are avoided during normal operation, lest the turbine literally shake itself to pieces.

2.1.2 Blade Design

The blades are the single most expensive component of the turbine and can account for nearly a fifth of the capital cost. The basic design on a blade can be seen in Figure 2.3.

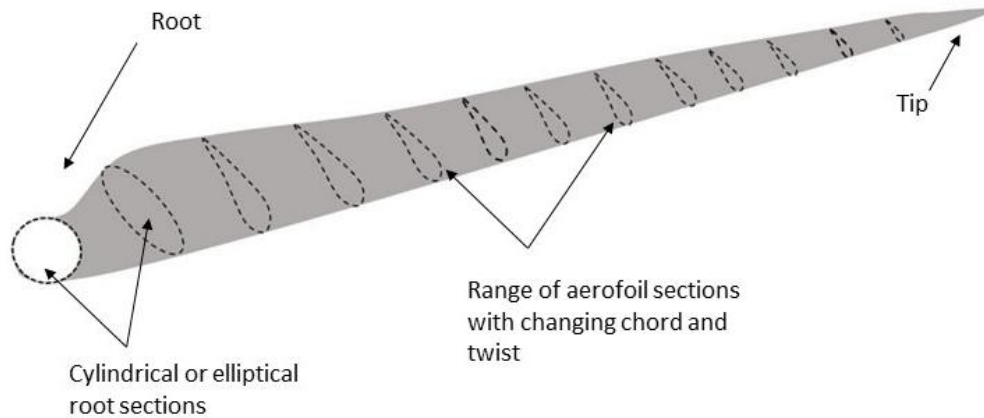


Figure 2.3. Blade design schematic highlighting the changing cross-sectional shape from root to tip.

The cross-sectional shape of a blade is complex and varies continuously between the root and tip. The root section tends to be cylindrical or elliptical with the design optimised for strength rather than aerodynamic performance. Comparatively low inflow speeds are experienced here due to the lesser radial distance from hub [24]. Moving towards the tip, the cross-section evolves into a range of different aerofoil shapes. These vary continuously in chord and twist to account for the increasing relative wind speed seen towards the outer sections of the rotor. The chord and twist distribution means that an optimum angle of attack, made to the inflow angle, and therefore lift, is maintained [22].

2.1.3 Blade Materials

The first wind turbine blades were constructed using simple wooden panels. However, these were found merely at the advent of such technology and composite materials have been employed since the 1990s, when wind energy became a viable industry, and the first UK windfarm was connected to the grid. This installation was built in Delabole, Cornwall, in 1991 [25]. The blades of today's turbines are manufactured using a combination of both Glass and Carbon Fibre Reinforced Polymers (GFRP and CFRP), possessing complex geometries, aerodynamically optimised to simultaneously increase efficiency, and reduce loading on the structure [26][27]. The largest turbine blades are now approaching 100 metres in length with turbine nameplate capacities exceeding 8-10 MW in commercial installations and prototypes in the 12-15 MW range [14][15]. Fibre composites are used since a high bending stiffness is required and blades need to be as light as possible to soften the requirements on the other turbine components, such as the tower, as well as pitch and yaw systems.

The impact on blade manufacture of this growth is that stiffer and lighter materials need to form load-bearing sections of the individual blades. Glass fibre alone is no longer able to handle the immense weight, 33-34 tons for 81.4 m models, and operational loading stresses experienced by this size of blade.

Carbon fibres are stronger and have a lower density than glass ones, but they do come at increased cost. An additional advantage of composites is the ability to manufacture large structures from far fewer individual parts than would be the case in an equivalent metal structure [28]. This is highlighted by the fact that modern blade

manufacturing techniques can now produce an entire blade within a single mould. The largest blades, used for offshore turbines, contain a main spar running down their length. As mentioned, the function of the inner section of the blade is mainly load bearing and therefore this spar is reinforced by a CFRP beam running within the GFRP sections. The spar is manufactured from pultruded CFRP, due to the superior strength and stiffness. Pultrusion is a low maintenance process during which carbon fibres are saturated by pulling them through a resin bath, as shown in Figure 2.4. The result is a single-ply panel.

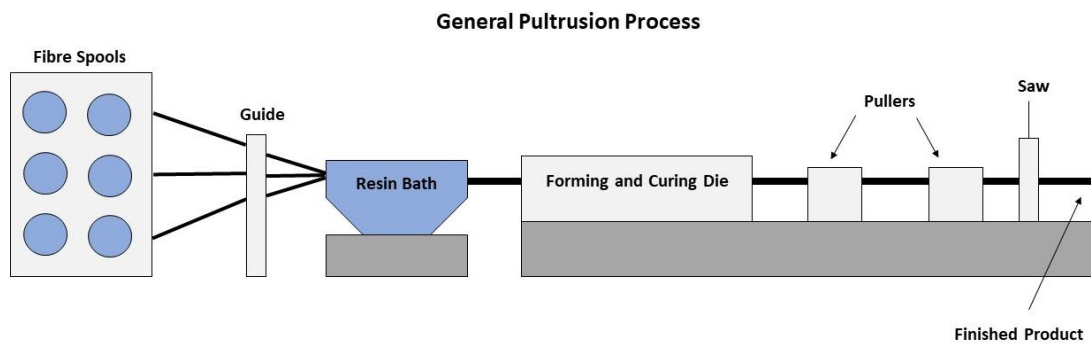


Figure 2.4. Schematic illustrating the pultrusion process to manufacture a single-ply panel.

Similar components are also found as reinforcement in steel and concrete structures [29][30]. CFRP main spar sections are assembled from these pre-manufactured elements. Planks are formed using layers of pultruded CFRP panels. The following graphics illustrate the blade structure. GFRP sections are manufactured from both Uni-Directional (UD) and Bi-Axial (Bi-A) orientated GFRP sections as illustrated in Figure 2.5.

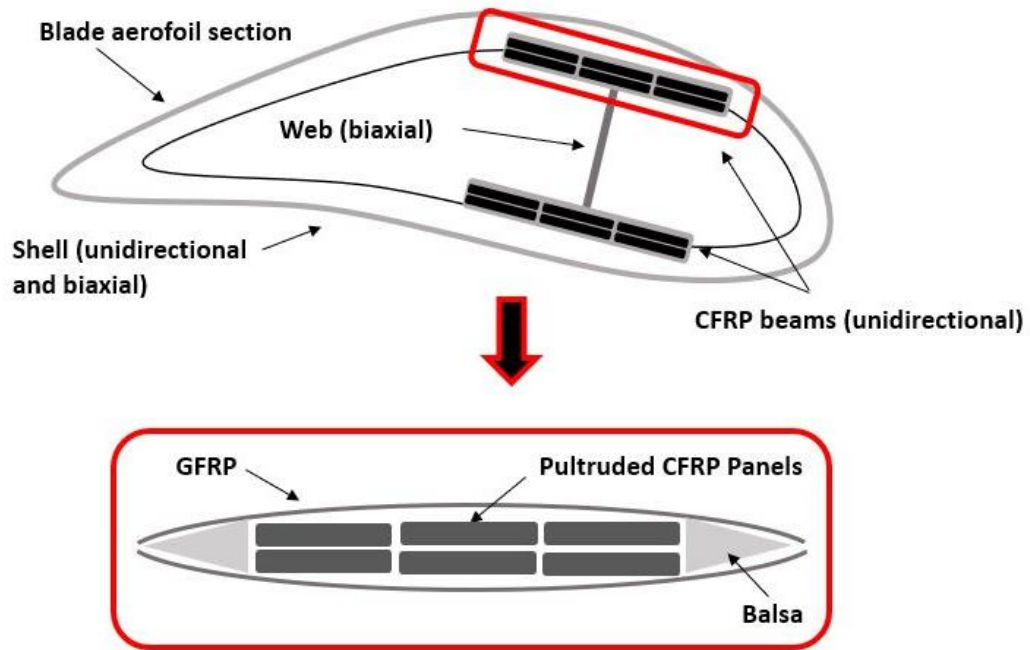


Figure 2.5. Blade internal structure incorporating both pultruded CFRP panels and GFRP with various layup orientations.

2.1.4 Pultruded CFRP Panel Uncoiling

For the research presented in this thesis, small sections of pultruded CFRP are acquired from the industrial partner. These are taken from a longer panel. used to form a load-bearing beam running within the GFRP aerofoil sections of the wind turbine blade. A more in-depth description of blade design, including schematics, was given in section 2.1.3. Such pultruded CFRP is delivered premanufactured to the SGRE blade factory and takes the form of a coil. This coil is unrolled onto a series of support rollers and processed within a container as can be seen in Figure 2.6. It is held vertical, axis parallel to the ground, whilst unrolled by a drive unit in stage one of the process. Panels are pushed through the entire system at speeds between 100

and 200 mms^{-1} , with the ambition of progressing towards 2 ms^{-1} within the coming years. Next, a protective film is removed before the edges are ground to shape and surfaces activated to allow panels to be bonded together. The procedure is performed in a container with brushes and a vacuum system removing CFRP dust as well as any other potential loose contaminants. Finally, the individual planks are lifted and placed into the precast beam mould before being incorporated into the GFRP layup process. Since there is no NDT performed throughout this procedure any defects present in the panels will not be identified until much later in the blade manufacturing workflow, once they are within the GFRP and the entire blade is at the NDT stage. The requirement for a form of in-process NDT, applicable at high pull-through rates is therefore clear to see. This demand motivates the practical inspections reported on throughout Chapter 3, the in-process ultrasound inspection system, Chapter 3, Section 3.5, and the scanning speed increases made possible by novel phased array acquisition approaches in Chapter 4.

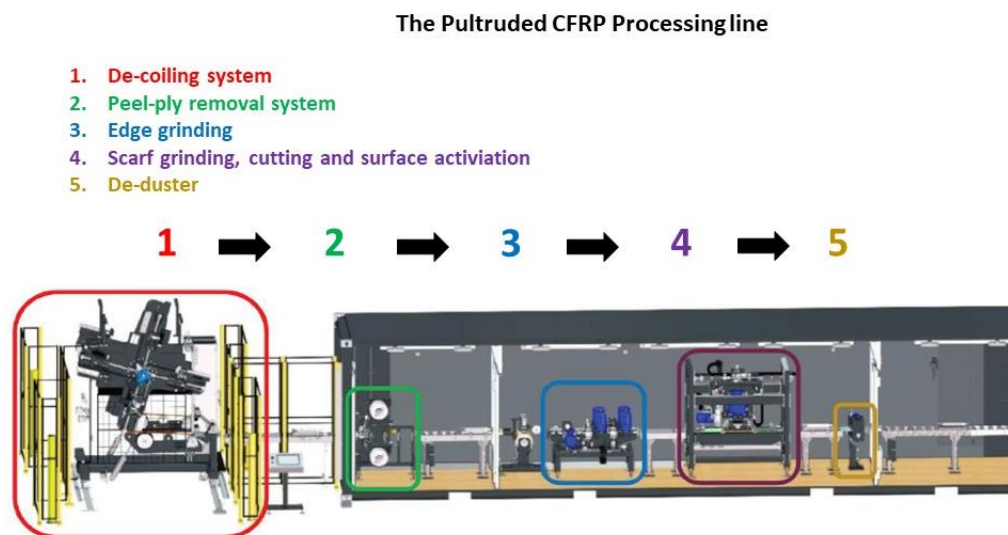


Figure 2.6. Schematic highlighting the stages of the pultruded CFRP uncoiling and griding processes.

2.2 Composite Materials

2.2.1 Introduction

Composite materials are formed of at least two key parts. Together, they exhibit physical properties far superior to those found in their individual constituents. Such materials are often lighter and stronger than any metals used for the same application [31]. A composite typically contains an internal matrix structure of fibres infused by a hardened polymer resin or epoxy to hold this matrix in a fixed position. Fibres can be natural, for example cotton or hemp, but more commonly are man-using glass or carbon strands. In combination with the polymer resin, the final material is referred to as Carbon/Glass Fibre Reinforced Polymer (G/CFRP). Fibres can be arranged either randomly or in very specific orientations and stacking sequences, and thereby can exhibit the desired mechanical stiffness and strength in a chosen orientation.

Composite materials are becoming increasingly prevalent in a variety of engineering and manufacturing applications demanding high-performance materials [32]. Driving factors behind this shift, away from more traditional metal alloys, are the high modulus and/or strength-to-weight ratios, improved fatigue performance, toughness and durability, as well as the ability to construct complex-geometry parts from fewer individual sections [33][34]. Additionally, one can design the component tailored to application with minimal excess material, further reducing weight and capital cost. A common example is a modern civilian aircraft where a weight percentage of between 25 % and 50 % is attributed to composite materials as shown in Figure 2.7 [35][36].



Figure 2.7. Material use as weight percentage in a Boeing 787 passenger jet [35].

The aerospace industry is leading the development of advanced composite materials as well as their application into high-value components that must fulfil stringent structural integrity and safety standards [37][38]. This field pioneers much design implementation and has long been at the forefront of NDT and defect detection. More recently, composites have become the material of choice in high-end automotive applications as well as in the maritime and renewable energy industry. The high strength to weight, and stiffness to weight ratios, make composites ideal for wind turbine blade manufacture, as was detailed in section 2.1.3.

2.2.2 Defects in Composites

The two-part make-up of a composite, and consequent inhomogeneous internal structure mean that the type of flaw present in such structures is also very different to those commonly found in metals. These anomalies include, but are not limited to, porosities or thickness changes in the laminate, voids, foreign object inclusion, trapped air, cracks, dry fibres, or areas of defective fibre alignment. All these flaws can ultimately lead to delaminations and separation of the composite's plies [39].

The focus of this thesis is on manufacturing defects. However, it should be noted that damage can also occur during a part's service-life. This can be caused either by impacts, the loading cycles causing fatigue, or drastic events of overloading. Examples and descriptions of manufacturing defect types are highlighted in the following paragraphs. At the end of this Chapter 2, after ultrasonic NDT has been introduced, the characteristics of the same defects under ultrasound inspection are detailed.

2.2.2.1 FVF, Voids and Porosity

Firstly, and most easily identifiable, are any voids or gaps within the material. These can be the result of trapped air, which is not removed from the vacuum curing process. Resin cannot impregnate all areas leaving gaps and leading to stress concentration sites. Voids tends to have a regular shape whilst porosity is more irregularly distributed throughout the structure.

Alongside the fibre matrix, this resin or epoxy makes up the second constituent of a composite and the ratio and distribution of the two can give rise to so called resin-rich or resin-starved areas, effecting local strength and stiffness. These can be the consequence of severe component geometries making resin extraction and distribution difficult. The volume fraction of fibre to resin is crucial in determining the mechanical as well as acoustic properties of the final product.

Porosity defects can range vastly in their characteristic size. At the smallest scale insufficient resin in a region leads to a matrix of tiny air bubbles or, pockets of ‘micro-air’. In such areas the ratio of fibre matrix to epoxy is not as intended. At the other end of the scale, as the size of air pockets increases, the porosity will develop into physical voids within the material. Voids and porosity are fundamentally the same flaw but on a continuous spectrum of characteristic size. Since there are areas of lower FVF, there will also be regions within the composite where there is too much epoxy compared to the fibre matrix. These can form resin drops or pools and are a weakness in the structure due to the absence of the load-carrying fibres in these areas.

2.2.2.2 Fibre Orientation

The alignment and lay-up sequence of the composite fibres is crucial in understanding not only the mechanical characteristics of the final component but also its response to any NDT technique. Fibres can be arranged in, for example, in +45, +90, 0, -90, -45 lay-up sequence with each ply angled with respect to the layer above and below. Any mis-orientation or mis-order, originating from the lay-up process mistakes, can severely affect the mechanical performance of the final structure in the form of greatly reduced strength or stiffness in a certain axis.

2.2.2.3 Delaminations

Delamination is a term meaning a separation of the plies, or layers, within composite structure. These can be present in a wide range of sizes and thus their effect on a component's strength can range from negligible to severe enough to cause catastrophic failure [40]. Of all those described, such a flaw is perhaps the most common. It is important to note that a delamination is often caused by different defects being present and creating a ply separation located far from original flaw. The delamination can thereby be the indication of a more fundamental underlying issue within the structure. Small flaws, can ultimately lead to the development of stress concentration sites and cause a delamination in a separate region of the composite [41]. Finally, if the plies are still in contact, but there is no transferral of strain, then the defect is referred to as a kissing dis-bond. The two surfaces of the ply are in close contact but transmit very little or zero tensile load [42].

2.2.2.4 Manufacturing Environment

Finally, the manufacturing environment can also present inherent problems and cause defects. There is always the risk of foreign object inclusion, which can occur during, for example, the stacking procedure of fibre glass cloths to form a GFRP component's layers. Composites can be very sensitive to impacts depending on their fibre layout and orientation. Even gentle ones can generate a matrix of cracking within, often not visible on the surface. This area of fractured fibres or matrix cracking is termed Barely Visible Impact Damage (BVID) and can lead to significant reductions in safe operational lifespan [43].

2.2.3 Defects in Wind Turbine Blades

The previously outlined composite defects also provide challenges in the wind turbine blade manufacturing industry. Defects may be divided into more specific types based on their characteristics and location within the blade structure. There can be poor cohesion between skin laminate and the epoxy as well as regions where the epoxy volume fraction used is either too high or low. Delaminations can also be present between the adhesive and the main spar or within the main spar itself [27].

The presence of material defects decreases the component's strength and thereby how well it can withstand typical loading conditions. For example, a delaminated component will further redistribute the fatigue loading in a manner not intended by the design. This can result in either an increasing area of the original delamination or the creation of a new one at a different location. The extent of damage can increase exponentially and quickly lead to catastrophic failure.

With most defects coming from the manufacturing process, even if failure or delamination occurs during service, but under normal loading, this can still be considered a manufacturing error. The defect was present at installation and will redistribute the fatigue loading under operation. Even when subjected to hurricane-force winds, the turbine will pitch its blades to reduce loading and therefore such conditions can still be described as 'normal' operational loads. An exception would be a 50-year gust, one sudden very high windspeed the turbine is not designed to ever experience. Blades also experience very complex loading sequences due to the stochastic nature of the wind field [27]. Additionally, the heterogeneous and

anisotropic nature of composites makes their fatigue behaviour complex, and several damage mechanisms can develop during the operational life.

A thorough understanding of the composite materials is therefore crucial. A statistical review looking at the failure mechanisms seen worldwide reported blade damage as the greatest single cause, at nearly 20% of all incidents [44]. More locally, blade failure was also reported as the most common accident cause in data obtained from a Caithness windfarm [45]. Composite materials possess much more complex failure modes than more homogenous materials and it can be difficult to reveal the relationships between micro and macroscopic characteristics, such as fibre arrangement and shape [41]. FEA models can be developed to investigate these relationships and thereby effectively predict the mechanical properties of complex internal structures.

2.3 Non-Destructive Testing and Evaluation

2.3.1 Introduction

Non-Destructive Testing and Evaluation (NDT/E) is a broad and interdisciplinary field. It aims to establish if structural components or systems are fit for purpose. The British Institute of Non-Destructive Testing defines NDT as “the branch of engineering concerned with all methods of detecting and evaluating flaws in materials”. The essential feature of these tests is that the component is unchanged by the inspection in that there is little incentive to identify flaws in a component’s structure if this itself has been altered or damaged by the test [46].

Non-Destructive Evaluation refers to measurements that are more quantitative than qualitative in nature, but the term is often used interchangeably with NDT. NDT concerns the physical mechanisms and procedures used to acquire data from a component. Subsequently the NDE would give information on the state of the components as compared to either a reference sample or certification standard. NDE establishes the link between the data collected and the physical state of the component. Not only would defects need to be identified but conclusions on their size, location and effect on the overall structure need to be drawn. Related to this process of evaluation is the field of defect detection and characterisation using NDT data. Defect detection utilises a vast array of different signal processing and data analysis techniques, which are discussed in this chapter. In recent years, machine learning, pattern recognition and smart data analysis algorithms are increasingly being used to enhance the speed, quality, and reliability of NDE and defect detection.

2.3.2 NDT Techniques

The contribution to knowledge presented in this thesis concerns ultrasound inspection and its use applied to composite materials used in the wind turbine blade manufacturing industry. The underlying principles and methods of application will be discussed later in this Chapter 2. Firstly, and considering NDT as a broader topic, there are a host of other techniques which can be applied and have their advantages/drawbacks over ultrasonic testing [47][48]. Several of these are also suitable for the inspection of the composites used in wind turbine blade construction. The range of different NDT techniques is introduced in the following sections.

2.3.2.1 Visual Inspections and Tap Tests

The first step in any NDT procedure is often the visual inspection of the component, either performed manually, by an operator trained in what to look for, or be camera-based and employ image analysis software. This type of inspection does mean that small flaws are difficult to detect, subsurface ones impossible, and BVID often goes unnoticed despite being the source of much more major component damage. Once visual inspection has been satisfactorily completed, other techniques can be employed. Historically, the tap test involved merely listening to the responses caused by impact at different surface locations. The modern equivalent employs spectral analysis of the vibrations caused to identify areas of different stiffnesses, potentially caused by the result of a delaminations, grain-boundaries, voids, or other defects. The duration, a loaded hammer is in contact with the surface, can also give a good

indication of any anomalies. Although limited in its application to metals, the tap test is widely used as a quick, low-cost test for composites [49].

2.3.2.2 Shearography

The basis for shearography are the speckle patterns produced as reflections from a component's surface under illumination by a coherent light source, such as a laser. The wavelength, on the scale of hundreds of nanometres, allows for the tiny surface deformations, caused by a difference in local strength, to be detected. The unstressed component represents a reference dataset. Using sound, vibration, heat, or other method a stress is applied and the distribution of this interfered with a reference pattern. The resultant interference fringes, and concentration of these, are used to identify any sub-surface anomalies [49]. Literature, comparing this to other NDT techniques, has shown that thermal loading tends not to be sufficient to show up delamination defects within composites [26]. The amount of stress necessary is also highly material dependent and by its very nature shearography is insensitive to high-thickness measurements and thus of limited use to blade inspection. Another point to note is that shearography can be very difficult to implement in practice since the component needs to be completely isolated. Vibrations caused by cranes, in factories during manufacture, can be the main issue here when applying this technique to blade inspection.

2.3.2.3 Thermography

Alongside ultrasound, thermography is the most applicable NDT technique when inspecting CFRP or GFRP components. This technique is based on the difference in thermal conduction properties, caused by material discontinuities. Heat transfer will be significantly slowed when a barrier is encountered. This boundary, for example a delamination or void, will acquire an elevated temperature detectable using infrared cameras. The temperature discontinuity caused by the type of flaw relevant to composites can, however, be too small to detect. Consequently, low impact damage, or small flaws, will go undetected, despite these potentially causing failures through damage evolution under fatigue loading. On the other hand, one advantage of thermography is the quicker inspection time since one of the main drawbacks of ultrasound inspection can be the acquisition time [26].

Despite both thermography and ultrasonic scanning being found to be very effective in inspecting GFRP sections, ultrasound does provide a more detailed evaluation, much improved volumetric performance, and on balance, does yield the best all-round inspection. This is especially true in terms of depth and size identification when working with multi-layered structures [43]. Thermography is limited since GFRP cannot be heated to temperatures even close to those applied to metals. This would cause the epoxy to melt. Consequently, the resultant temperature gradient is minimal and along with low sensitivity cameras means defects can be hard to detect. Kissing bonds will also be difficult to identify unless there is an airgap to create a temperature discontinuity. Due to these limitations, phased array ultrasound is used in the

aerospace industry to detect sub-surface defects, while IR thermography is applicable for near-surface ones [50].

2.3.2.4 X-ray Inspection

X-ray inspection forms the basis for computed tomography (CT) scans. Due to the comparatively low attenuation of this electromagnetic wavelength in composites, X-ray inspection offers a viable alternative to ultrasound. Effective inspection depends on the attenuation values of any defects in comparison to those of the surrounding material [26]. For example, Teflon inserts, often used to simulate delaminations, are difficult to detect due to their much higher attenuation in comparison with air [51]. There is potential to use X-ray based NDT on wind turbine blades, but the equipment quickly becomes large and expensive for the comparatively thick composite sections present in large blades. One example, quoted the minimum detectable defect size as 2 % of the entire thickness [31]. X-ray inspection also suffers from a poor sensitivity to defects aligned parallel to the beam propagation direction. Therefore, access from multiple directions is sometimes required which is not always practical. Finally, the effective positioning of the receptor plate presents a difficulty since the top and bottom surfaces of a blade have complex curved geometries.

2.3.3 Defect Detection

Defect detection identifies flaws or differences between the physical state of a component and the desired structure. Based on knowledge of the characteristics the component should possess, conclusions can be drawn on how well this is adhered to and therefore if it passes some previously defined standards of quality. Defect detection thereby relies on ability to distinguish the characteristic defect signals from both the generic response of the material to the chosen NDT technique, as well as any unwanted sources of noise originating either from the nature of the material, inspection technique or experimental procedure. The outcome is either that all is well or that repairs, or design alterations need to be performed. Should a component fail the NDT it can also be that case that it needs to be scrapped and the manufacturing process started afresh.

A calibration sample is used to determine how a given material responds to the chosen NDT technique. This can either be a section of the same material as the component under inspection containing defects of a known size, geometry, and location or a clean sample. In the former, a reference scan, generated from the calibration block, provides knowledge of flaw response and such signal can then be looked for in the actual inspection. In the latter, the reference scan acts like a 'perfect' component to which future ones can then be compared and allow for the classification of defective or clean areas [52].

As an example, in ultrasound NDT, the following paper describes a reference scan performed on a clean sample to calibrate the sample and inspection parameters as well as the location of the backwall [53]. In the paper in question, the probe is scanned

over a series of known defects, operating under a range of inspection parameters. The sound velocity, pulse width, gain, sampling rate and transducer distance from the specimen surface all need to be known before any classification algorithms can be applied [53]. In addition to this a 25 MHz sampling rate is used, greatly reducing the amount of data to deal with and maintaining the recommended five to eight times greater value than the transducer frequency. From an experimental point of view, since the ultrasonic response of a flaw is determined both by the flaw type and by the transducer characteristics, it is essential for effective defect characterisation that the inspection characteristics are kept as near to constant as possible [54]. These are procedures that must be carried out prior to the application of any defect detection algorithms. Once inspection parameters are optimal these must be maintained to both minimise the false positive rates and maximise the probability of detection.

2.3.4 Robotic Automated NDT

Automated NDT combines these basic principles described with the data collection, presentation, and processing approaches. Together with the hardware necessary to physically carry out such inspections these then form a final procedure which can be integrated into the entire manufacturing workflow [52]. The volume of data to be processed and the industrial application, in which the NDT is applied, leads to a requirement for some level of automation within the process [55]. Analysis of all the scans collected by a modern ultrasonic inspection system is time consuming due to the volume of data collected. Reducing these volumes and pinpointing the quantitative information also contributes to lighting the operator's decision-making

load. These issues are well described, with potential solutions when applied to composites, in [52]. There is also an increased demand for inspections to yield 3D material parameters, instead of merely NDT-specific ones such as attenuation or velocity. Again, for ease of analysis and conclusion drawing. The results presented in [52] were a significant breakthrough in this.

For the inspection of complex shaped parts, robot systems are increasingly used [56][57][58]. The uptake of complex-geometry composite components in the aerospace industry, since the early 21st century, leads to difficulties faced inspecting with traditional automated methods, such as gantry systems [59]. Industrial robots are able follow complex, pre-defined paths, and manipulate Phased Array Ultrasonic Testing (PAUT) acquisition systems, with six Degrees of Freedom (DoF) [55][60]. Additionally, scanning speeds of up to several meters per second are possible, preventing the implementation of such hardware leading to bottlenecks within a manufacturing environment [61]. These techniques can be implemented in combination with fast data collection, extraction, and analysis tools in the form of advanced defect detection algorithms and machine learning techniques.

The integration of phased array equipment with robotic platforms, to facilitate ultrasonic inspection of complex geometry composite components, can be seen in a laboratory set-up shown in Figure 2.8. This apparatus is used for research as well as demonstration purposes in the University of Strathclyde's SEARCH lab, made possible through SPIRIT AeroSystems.

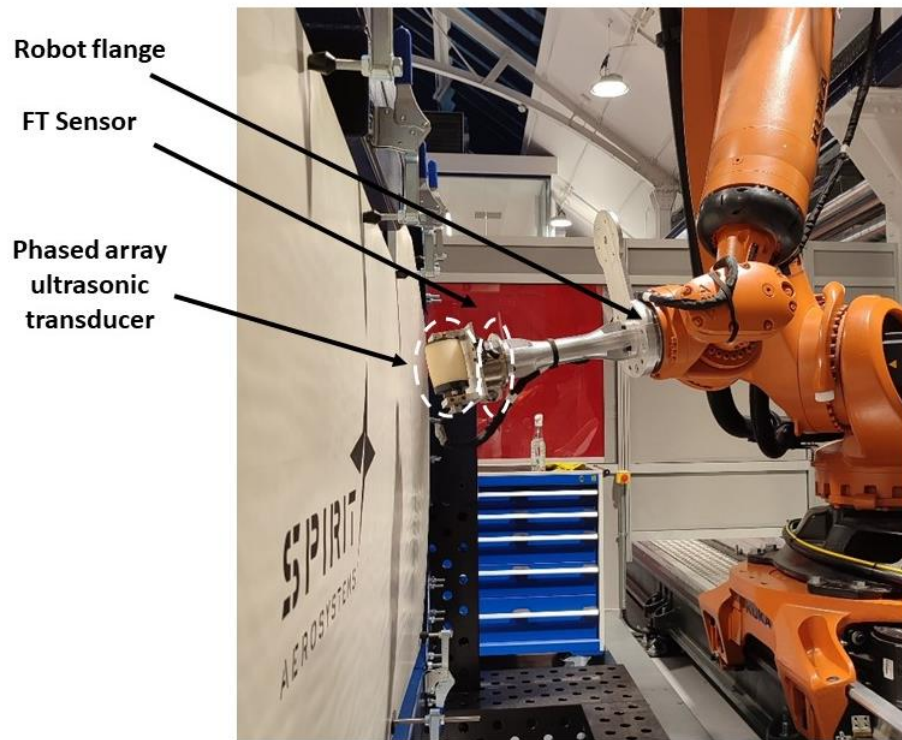
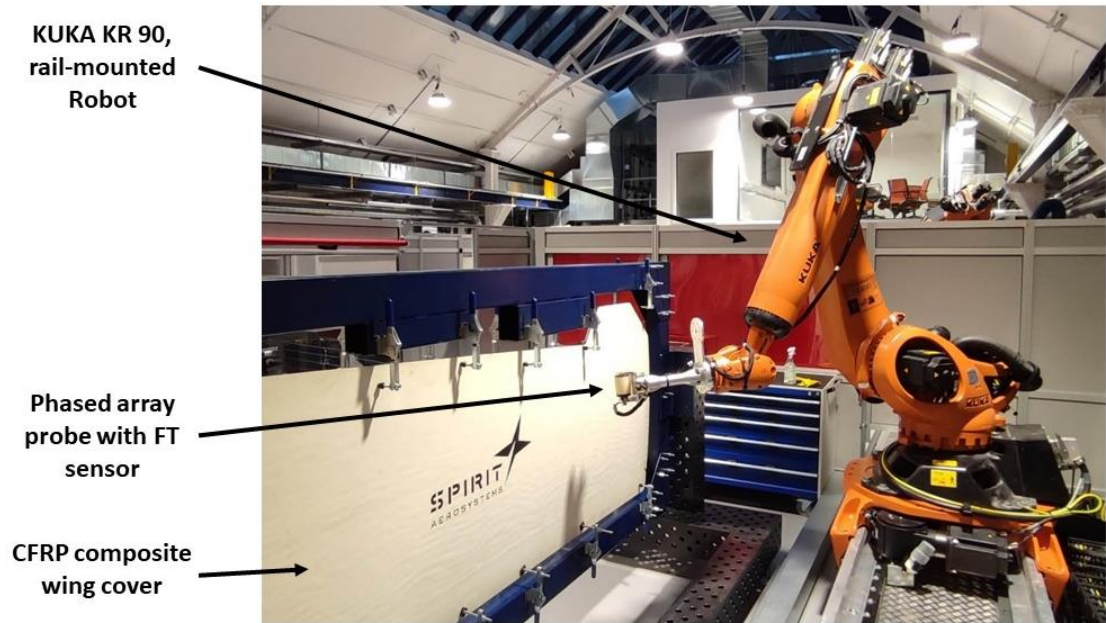


Figure 2.8. Example images of phased array robotic ultrasonic inspection hardware, similar to that used in referenced works.

2.4 Ultrasound

2.4.1 Introduction

The term ‘ultrasound’ refers to sound waves, a transient disturbance in the pressure of a substance, at a frequency beyond the human hearing range. Decreasing with age, our ears can detect sounds from 20 Hz to 20 kHz, sensitivity being much decreased at the boundaries of this range.

High frequency sound can be used to inspect materials and gauge distances by transmitting ultrasound pulses and collecting data on the reflected waves. Signal processing techniques, data analysis and imaging algorithms allow for these data to be presented so to give information on the shape and size of, as well as interfaces within, a sample. This allows the user to build a highly accurate representation of the internal structure of an object.

Ultrasound relies on acoustic physics and the theories of wave propagation. The laws of reflection, refraction, diffraction, and acoustic impedance profiles within, govern the nature of the received sound. Understanding these allows the ultrasonic response to be used to characterise materials, identify and inspect various Regions of Interest (RoI).

Dependent on application, ultrasound frequencies range from 100 kHz to 20 MHz. Lower values experience lesser attenuation and are therefore used in highly attenuating materials or when the propagation distance is to be maximised. By contrast the lower wavelengths of higher frequency waves allow for greater axial resolution and are utilised for higher quality imaging applications where attenuation

within the sample material is not the limiting factor. This trade-off between Signal to Noise Ratio (SNR) and resolution is a key consideration across ultrasound applications, be that medical, NDT/E, or maritime.

A background to the field of ultrasound, historical context and underlying physical principles will be described in these sections. The focus of this thesis is on ultrasonic NDT and therefore much of this section handles ultrasonic devices, their operation and the necessary signal processing and data presentation methods used to analyse the internal structure of a sample and detect flaws.

2.4.2 Historical Context

Perhaps the eldest and most well-known example of ultrasound is sonar. This is used in both civil and military naval applications. A vessel will send out pulses of sound that travel towards seabed. Based on both amplitude and Time-of-Flight (ToF) measurements, the depth and topography can be mapped. As is sadly often the case, nothing spurs innovation like conflict, and sonar technology was pioneered during the Second World War to detect the presence of submarines.

Following on from this, in the post-war 1950s, researchers were inspired to investigate the medical diagnostic potential of ultrasound. By now it is widely used in medical imaging to characterise tissue, identify potential cancers, and build highly detailed images, as well as live representations, of organs. Another well-known example would be the pre-natal scan, imaging a baby in its mother's womb.

Medical ultrasound technology tends to be easier to use and more readily available than the other forms of imaging used in the field: Magnetic Resonance Imaging (MRI) or Computed Tomography (CT) scanning. Much of the techniques and equipment first developed for medical applications are now cross-disciplinary and the cornerstone of the other main use of ultrasound in the 21st century: Non-destructive testing and evaluation.

2.4.3 Sound Propagation

2.4.3.1 Propagation Modes

Within a material, sound can propagate by the compression and relaxation of molecules in the propagation direction. This is known as a longitudinal wave. Deforming the molecular structure from its equilibrium position gives rise to restoring forces originating from the electromagnetic interactions between the atoms within. These, along with the inertia of the wave, lead to an oscillatory motion. Due to their crystalline structure, a solid will support the stable oscillation of different patterns of propagation apart from the standard longitudinal wave seen in fluids. These are known as wave modes. Longitudinal and shear waves are most common, with shear waves supported by a oscillation perpendicular to the propagation direction, but interfaces and surfaces allow for other types such as Lamb and Rayleigh, which are surface waves.

Surface waves have been found to be very useful for ultrasonic inspection and can be much more sensitive to certain defect types. When a Rayleigh wave is supported, the crystal centres propagate in an elliptical path. The major axis of the ellipse is perpendicular to the surface of the solid. As the depth of an individual from the surface increases the width of its elliptical motion decreases. Surface waves are generated when a longitudinal wave intersects the surface near at angle close to the second critical angle. Surface waves are useful since they exhibit great sensitivity to surface and/or shallow defects and can propagate around a component's curves, thus tackling coupling issues faced when working with complex geometries. Rayleigh waves can be produced in a relatively thick material and penetrate to a depth of one

wavelength. In contrast, plate waves can only be generated in materials a few wavelengths thick. Lamb waves are the most used plate waves in NDT. They propagate parallel to the test surface throughout the thickness of the material. Their propagation depends on the density and the elastic material properties of a component. They are also influenced greatly by the ultrasound frequency and material thickness. Lamb waves are generated at an incident angle in which the parallel component of the velocity of the wave in the source is equal to the velocity of the wave in the test material. Again, various modes of particle vibration are possible. The two most common are symmetrical and asymmetrical. Individual particles will follow similarly elliptical paths as with Rayleigh waves. Symmetrical Lamb waves are symmetrical in shape around a median plane of the plate. Wave motion in this mode is most efficiently generated when the exciting force from the transducer is parallel to the plate. By contrast, most of the motion is in the normal direction to the plate for the asymmetrical Lamb mode. In this mode, the body of the plate bends as the two surfaces move in the same direction.

Guided waves, such as Lamb waves, are fast and sensitive to various defect types [62]. They can propagate large distances in plate-like structures, such as composite laminates. Weak penetration into solids due to the acoustic mismatch can be tackled using acoustic mode conversion into guided waves [63].

2.4.3.2 Mode Conversion

Mode conversion is a phenomenon that will be observed when a sound wave encounters an interface between two acoustic impedances at an angle other than normal. Acoustic impedance, measured in 'Rayls', is defined as the speed of sound (ms^{-1}) multiplied by the material density (kgm^{-3}) and is responsible for the proportions of a wave that are reflected and transmitted at an interface. The unit of acoustic impedance is the pascal second per cubic metre, sometimes reference to as an acoustic Ohm. Acoustic discontinuities are the underlying principle allowing features to be detected using ultrasound. The parameter is analogous to the role of refractive index when studying electromagnetic waves.

Mode conversion can lead to the ultrasound signal received from within complex geometries being very difficult to analyse. Snell's law can also be applied to acoustics and gives rise to the first and second critical angles at an interface [64]. These are utilised in a wide range of NDT techniques and many of the modes of sound propagation described previously have been shown to be far more effective in the detection of certain defect types than a longitudinal wave entering at normal angle. Between normal incidence and the first critical angle there is a decreasing proportion of the energy travelling longitudinally. At the first critical angle the longitudinal one no longer exists and a shear wave is refracted into the specimen. There is also a 'creep' wave along the material interface, decaying rapidly in the same manner an electromagnetic evanescent one does. These are not used as often as Rayleigh waves in NDT but can be more useful since they are less sensitive to surface irregularities and the coarse material microstructure due to their longer wavelength. Beyond this

first critical angle, only the shear wave propagates into the material. The second critical angle is defined at the point where the shear wave has an angle of refraction of 90 degrees. Approaching this point the shear wave becomes weaker and as the second critical angle is reached all the energy is reflected at, or refracted into, the sample. Slightly beyond this angle, only surface waves will be generated. The principles described here are best visualised in the schematic shown in Figure 2.9 [65]. Since the critical angles are dependent the bulk and shear velocities in coupling and sample mediums, the materials used impact the shape and position of the curves shown. Figure 2.9 shows an example using Rexolite and stainless steel.

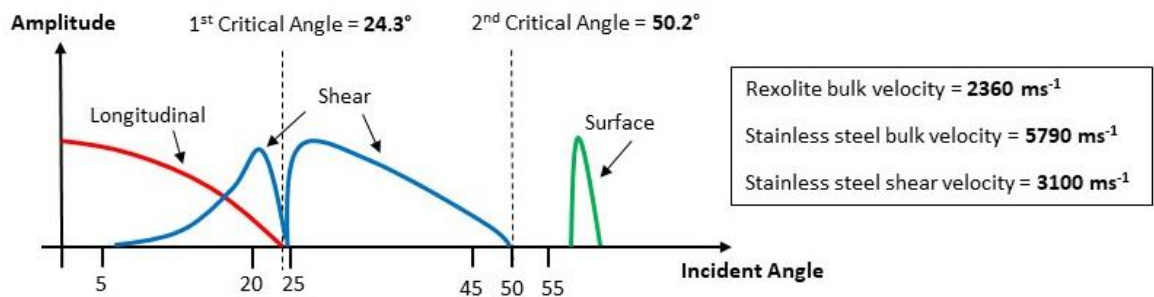


Figure 2.9. Schematic highlighting mode conversion and the presence of first and second critical angles as the angle of incidence is varied.

2.4.3.3 Attenuation

Attenuation combines the effects of absorption and scattering within a material. Both lead to a loss of energy, and ultimate demise, of an ultrasonic wave. Attenuation can be mathematically combined to be expressed as one exponential decay as a function of propagation distance.

Absorption converts acoustic energy into other forms, primarily heat. In an ideal, defect-free, material, attenuation would only be the consequence of the spreading of the wave in accordance with the Huygens principle. However, 'real-world' materials will scatter sound in other directions due to grain boundaries, voids, impurities, and the non-ideal crystalline structure. Materials will often exhibit non-linear properties, meaning attenuation and scattering effects are frequency dependent. This is origin of the SNR and resolution trade-off mentioned in the ultrasound introduction section. As a combined parameter, attenuation tends to be proportional to the square of the frequency. It is, however, highly dependent on material manufacturing processes and can vary significantly from sample to sample. For this reason, it is best practice to measure attenuation experimentally before each analysis along with the longitudinal and shear wave velocity. When performing an ultrasound inspection, any results obtained, in terms of dimensions, defect location and depth, are highly sensitive to both attenuation and sound velocities.

2.4.4 Ultrasonic Inspection

2.4.4.1 Introduction

Any ultrasonic inspection will require several basic components, primarily the ultrasonics transducer. A transducer is a device that converts a physical quantity, be that brightness or pressure, into an electrical signal and vice versa. Ultrasound transducers are utilised to both transmit and receive ultrasonic waves and commonly based on the piezoelectric effect. A single transducer can double up to act as both the transmitting and receiving element. Alternatively, dual crystal devices use two, acoustically isolated transducers, one to transmit and one to receive. An electrical pulse generator is required to trigger the transducer. This applies the required energy to form a wave. Finally, some form of data display for the received ultrasonic signal is necessary. In the simplest of set-ups this could be an oscilloscope. The physical mechanism employed for the generation and detection of signals can vary depending on the application. Examples include contact transducers, phased array, air-coupled, Electromagnetic Acoustic Transducers (EMATs) or laser ultrasonic set-ups. Hybrid systems also exist to capitalise on the advantages of these different approaches [39].

2.4.4.2 Piezoelectric Effect

The active element of an ultrasonic transducer is typically a thin disc of piezoelectric material. This converts the electrical energy into mechanical and thus produces ultrasound waves, to be transmitted into the sample. By the reverse effect, the same device will convert received ultrasound signal back into electrical waveforms and thus form the basis for imaging.

Dielectric materials can be polarized by the application of an electrical field. Piezoelectric materials are a subset of these, in which polarization can also be achieved by mechanical stress. These materials exist in nature but for ultrasonic transducers, man-made ceramics, for example lead zirconate, are commonly used. Recently, for health and environmental reasons, there has been a push to develop lead free piezoelectrics.

Under stress, a shifting of the positive and negative charge centres results in an external electrical field due to the imbalance of electric dipole moments. When reversed, an outer electrical field either stretches or compresses the piezoelectric material. The net electric field is the result of unbalanced electric dipole moments in that a force changes the position of the nuclei and average distribution of the electron cloud in each atom. Applying an alternating electric field to a piezoelectric will cause it to vibrate at given frequency determined by the field, given material and its dimensions. This generates ultrasonic waves and allows the device to be used as a transmitter. The reverse effect allows for received ultrasound waves to be converted back to electrical signals.

2.4.4.3 Ultrasonic Data Collection

Once the most suitable ultrasound transducer has been chosen, the characteristics of the specimen in question, as well as the type of inspection to be carried out, will determine the optimum data collection method. Factors to consider include sound attenuation within the material, step changes in acoustic impedance as well as more practical issues such as access to the component and the time and cost designated to a given inspection or imaging procedure. Several different configurations are outlined in this section. These are widely used throughout both ultrasonic NDT and medical applications and illustrated in Figure 2.10.

Perhaps the most well-established, and easiest to employ, technique is ultrasonic pulse-echo. Waves are coupled into a sample at a direction normal to the surface. Echoes will originate from the back surface of the material as well as any other acoustic impedance discontinuities found within. These waves then travel back towards the probe and are received at the same location as the original signal was transmitted. One clear advantage of this approach is that access is only required to one side of a sample. It does, however, rely on the attenuation being low enough that the sound can propagate twice the thickness and still possess a high enough SNR to register at the receiver. Pulse-echo mode can be performed by single-element acquisition or using a split crystal transducer. This second option would be advantageous when looking at a thin sample since the 'dead zone', distance from the probe which cannot be detected since it is either emitting a signal or reverberating, is greatly reduced. Phased arrays can also be operated in pulse-echo mode. These devices will be discussed in more detail in section 2.4.4.4.

Alongside pulse-echo, transducers can be operated either in through-transmission and/or pitch-catch modalities. Both require a minimum of two transducers, one acting as the receiver, one as the transmitter. Through-transmission set-ups place the sample between transducers. Therefore, alignment is crucial requiring careful calibration between the scanning paths associated with each transducer with transmitter and receiver probes secant or coaxial [66]. This can be especially difficult when working with complex geometries. Since sound waves only need to pass through the sample, through-transmission is often used when looking at highly attenuating structures or air-coupled ultrasound where low SNR values are already a challenge.

Pitch-catch ultrasound is performed with two separate transducers on the same side of the component. One to transmit the signal, one to receive. These two are held a fixed distance, and firing-angle, apart and can be moved as one across the sample surface. A pitch-catch configuration is often used for crack-tip diffraction where a crack on the bottom surface of the material will reflect sound waves in a different direction than a defect-free back wall. This change in reflection direction will be detected as a reduction in signal amplitude by the receiving transducer. Information can then be gained on the location and severity of the crack.

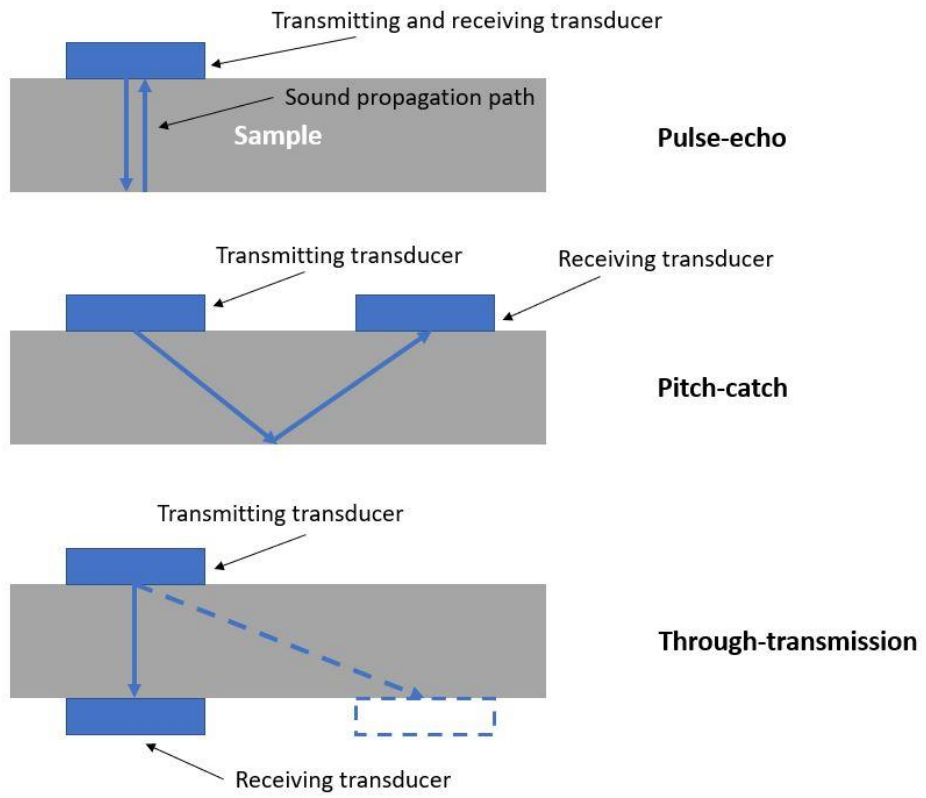


Figure 2.10. Schematic highlighting pulse-echo, pitch-catch, and through-transmission ultrasonic inspection modalities.

2.4.4.4 Ultrasonic Phased Arrays

Whilst ultrasonic inspection can be carried out using single element transducers, the use of Phased Array Ultrasound Testing (PAUT), offers a range of different acquisition and data presentation modalities [67]. Defect detection capabilities are also enhanced and a variety of imaging techniques and post-processing algorithms, which are not applicable to single-element probes, exist [50]. Phased Arrays (PA) contain many individual piezoelectric transducers, arranged in a linear or matrix fashion. PAs commonly comprise anywhere from 16 to 256 individual elements. These can be individually addressed in both transmission and reception with programmable, differential time-delays allowing the resulting ultrasound beams to be steered to and focussed at specific locations whilst the PA probe remains in a fixed position [68]. These differential time-delays are known as focal laws. Figure 2.11 illustrates this principle with the active elements used in each pulse forming the active aperture. Figure 2.12 shows the results of a MATLAB simulation using time delays, along with the physical principles governing the interference of waves of a given frequency, to yield a map of acoustic intensity within a test region [69].

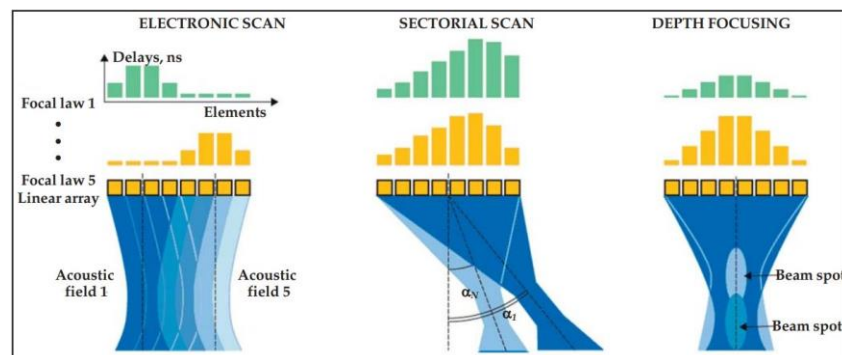


Figure 2.11. Phased array focal laws used to steer and focus a beam [69].

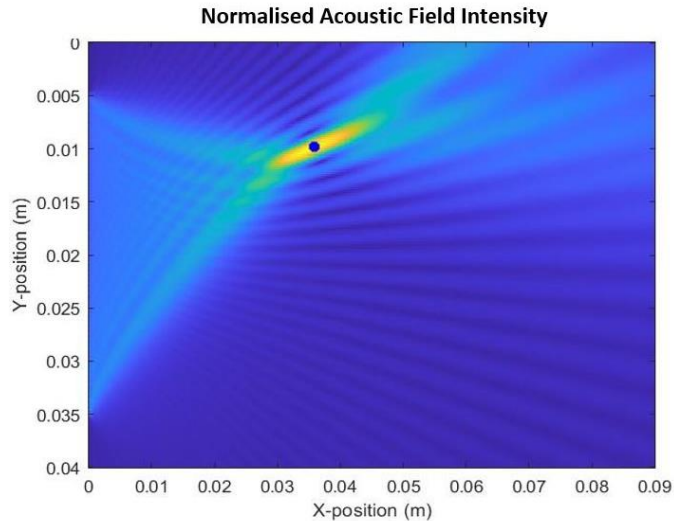


Figure 2.12. MATLAB simulation using of focal laws and the principles of acoustic interference to show beam focussing on a chosen location.

Inspection from a variety of angles without physical probe movement can thereby be achieved. This is used to greatly simplify the inspection of complex geometry components or those with limited access. Whereas standard pulse-echo mode can be very insensitive to defects orientated in the scanning direction PAUT allows anomalies to be analysed from a variety of angles. The ability to focus the beam at different depths also makes it much easier to size defects in volumetric inspections. PAUT allows for a variety of difference acquisition methods which cannot be achieved with single-element acquisition. An important example of this is Full Matrix Capture (FMC), the most comprehensive data collection mode available to PAUT systems. FMC acquisition collects data, in the form of amplitude as a function of time, on every receive channel whilst firing each element in turn. This results in a matrix of data acquired from all possible transmit and receive combinations, and

crucially, allows for decoupling of acquisition and data analysis stages [70][71]. A common analogy is a photograph of an object taken from every possible position.

FMC acquisition forms a 3D data set defined by T rows and R columns with the third dimension containing the number of samples in each time-sequence for each acquisition. This is shown in Figure 2.13. T_iR_j refers to transmission on phased array element 'i' and reception on element 'j'.

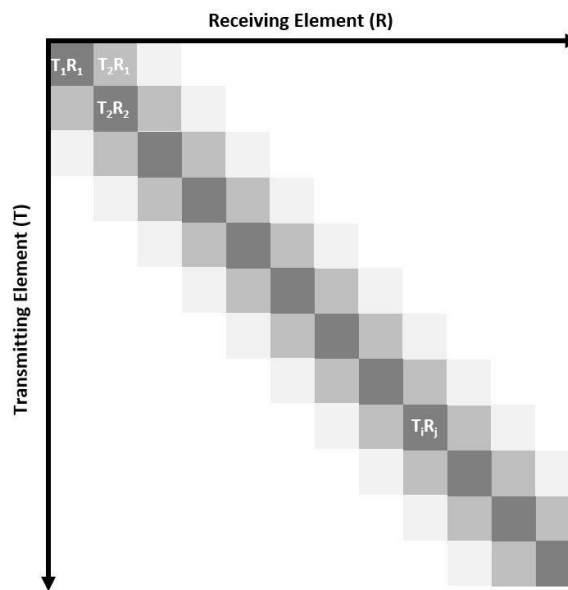


Figure 2.13. FMC matrix generated by reception and transmission using all possible combinations of elements.

It is important to note that coherence must be maintained over the entire frame and a wide dynamic range required to prevent receiver saturation making obtained numerical values meaningless. The amount of data produced per second, for even a modest number of individual transducers is immense and consequently fast communication links are required [72].

Finally, ultrasonic phased arrays allow also for both linear imaging, where an active aperture of a chosen size is moved incrementally across the array with a given step size, as well as multi-aperture firing. Multi-aperture acquisition simultaneously triggers several active apertures spaced across the array. This can be used to significantly increase imaging frame rate. The concept is discussed in more detail, and optimised for a particular application, in Chapter 4 of this thesis.

2.4.4.5 Coupling

Having outlined the basic components necessary for ultrasonic inspection, as well as the physical mechanisms by which such devices work, a note must be made on the role of coupling mediums. Alongside transducer positioning, and inspection modality, the role of coupling is an important practical consideration. The difference in acoustic impedance across an interface is responsible for the ratio of transmitted and reflected amplitude, as well as any phase shift imparted. Such differences can, for example, be found across different tissue types in medical ultrasound, weld passes in NDT, or varying composite layers. The reflections from each allow for the internal structure to be analysed.

Table 2.1 illustrates bulk, velocities, densities, and therefore acoustic impedance differences between common materials. Reflected and transmitted coefficients, R and T, are calculated by Equation 2.1 and Equation 2.2 where Z_1 and Z_2 are the acoustic impedances of the first and second material. A working example of percentages transmitted and reflected, as referred to the original pulse magnitude, is shown in Figure 2.14.

Material	Density (10^3 kgm^{-3})	Velocity (ms^{-1})	Acoustic Impedance (MRayl)
Air	0.0012	330	0.0004
Water	1	1450	1.45
Soft Tissue	1.1	1540	1.69
Aluminium	2.7	6420	17
Steel	7.85	5940	46.6
Glass	2.5	5900	14
CFRP	1.8	3000*	5.4

Table 2.1. Density, bulk velocities, and acoustic impedance of common materials used in medical and NDT ultrasound applications.

$$R = \left(\frac{Z_2 - Z_1}{Z_2 + Z_1} \right)^2$$

Equation 2.1

$$T = \frac{4Z_2Z_1}{(Z_2 + Z_1)^2}$$

Equation 2.2

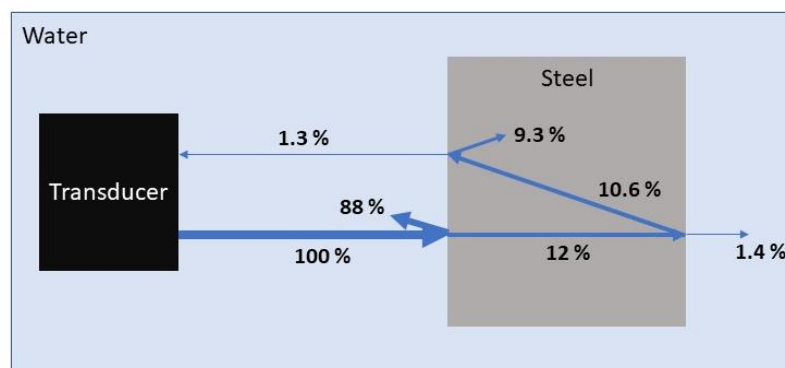


Figure 2.14. Example of reflection and transmission coefficients using ultrasonic immersion test of steel.

The greatest acoustic impedance difference observed tends to be the boundary between air and the sample under inspection. This must be overcome to couple ultrasound into a material in the first place. Various coupling mediums exist, the most commonly used are water or gel. Ultrasound inspections are often carried out within an immersion tank. This reduces the energy lost by adding another impedance step between transducer and sample. Similarly, transducers will often be manufactured using a matching layer on the front of the piezoelectric crystal with a lower impedance [73][74]. Forms of 'dry-coupling' also exist for applications where a liquid layer of water between sample and transducer is impractical or where the material could be damaged by moisture or water-ingress. The use of a phased array transducer, housed within an impedance matched, water-filled tyre is a good example of this. Such hardware is used extensively for the research presented in Chapters 3-5 of this thesis.

2.4.5 Ultrasonic Data Presentation

The data collected from the receiving elements can be displayed to the user in a variety of formats or complexities. Often these are combined to form new modalities or tailored for a given application. A number of these, found across all ultrasound applications, are discussed in the next sections to enhance the understanding of the ultrasound inspection, and form the basis of the work reported in subsequent chapters. More complex ways of post-processing and data presentation, made possible using PAUT, are also outlined.

2.4.5.1 A-Scan

An A-scan is the most straightforward way in which received ultrasound data can be presented. It is simply the energy received back, from the transmitted pulse, as a function of time. Most instruments presenting this scan allow for the signal to be displayed in its natural Radio Frequency (RF). Such a time-series will contain peaks, their position in time can be used to calculate the depth of features in the sample based on the propagation time and bulk velocity of the material. The amplitude will give information on the size, orientation, and nature of a reflector. A strong back-wall reflection will usually be the most prominent feature in an A-scan, if there are no defect present, since this is the source of the greatest acoustic impedance boundary. An example RF A-scan, with front and backwall response highlighted is shown in Figure 2.15.

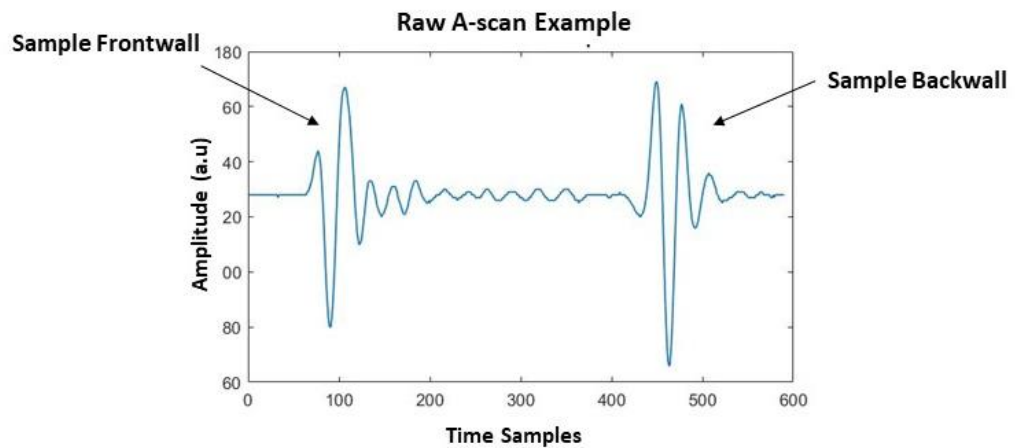


Figure 2.15. Example of an A-scan in raw RF format.

However, if a defect is large enough it may completely mask this back-wall reflection. As the sound waves bounce between front and back wall, within the sample, multiple echoes will be detected with exponentially decreasing amplitude. Therefore, it is best practice to allow the sound to decay sufficiently before the transducer is fired again, with a delay time of five to six round-trip times often used. Off-axis reflectors will act to scatter the waves and thus defect localisation can be difficult using a single A-scan at one position. The A-scan forms the basis for all, more complex, ultrasonic imaging modalities.

2.4.5.2 B-Scan

Aligning a series of A-scans along one axis results in a B-scan. Such an image presents a cross-sectional view of the specimen. A B-scan is a two-dimensional image at a plane orthogonal to the specimen's surface; a 'slice' through the material formed using a series of aligned A-scans [70]. Again, the position and approximate size of a discontinuity can then be determined. Applying a trigger gate, to each A scan, switched on at certain signal intensity, allows a B-scan to be produced. It is important to note that this display technique can lead to reflectors close to the surface masking ones deeper within the sample due to their increased amplitude. B-scan presentation is more intuitive to analyse, and the operator can quickly 'see' the internal structure. B-scans are a common imaging modality used in medical ultrasound with prenatal scans, exemplified in Figure 2.16, often presented as either a B-scan or sector scan [75].



Figure 2.16. Example of prenatal scan [75].

A D-scan or T-scan is very similar to a B-scan. However, the imaging plane is rotated by 90 degrees. Whereas the B-scan is parallel to the scanning direction, a D-scan is perpendicular to orientation as well as to the sample surface or scanning plane. Again, the amplitude received at each point is represented using a grey scale or colour palette.

2.4.5.3 C-Scan

A C-scan is a 2D image in a plane parallel to the sample surface or the inspection path plane of the transducer. C-scans are produced based on a matrix of individual A-scans, gated to give one value at a certain depth or range, and acquired at specific co-ordinates across the sample surface. Data collection is established on the A-scan and the amplitude, or time-of-flight of the signal, displayed at regular intervals as the transducer is scanned across the sample to generate many values at given points. This could be achieved using, for example a robot, following a given inspection path. Very high-resolution scans can produce detailed images with A-scan gating determining the depth and extent of each C-scan. Specific regions such as the backwall reflection or internal areas can be analysed [76][77]. It is then possible to image both the front, back and intermediate surfaces of a sample with each C-scan giving a 'slice' through the sample. Typically, C-scans map either amplitude or ToF data, as shown in Figure 2.17. A combination effectively utilises all the information available [78].

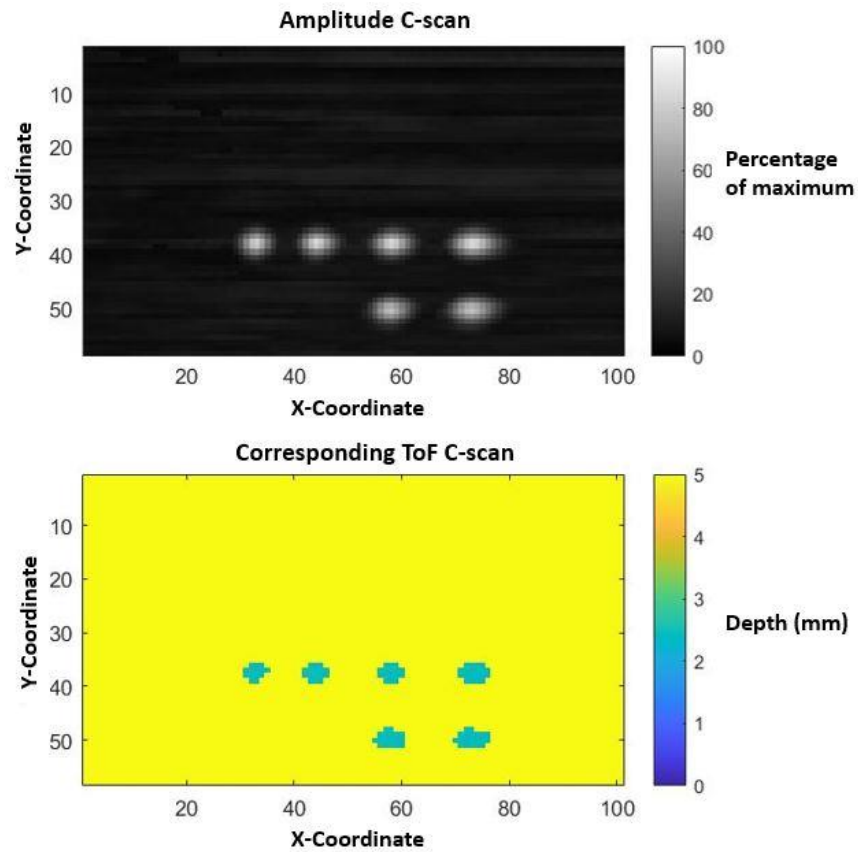


Figure 2.17. Example of amplitude and ToF C-scans.

2.4.5.4 PAUT Data Presentation

These basic presentation methods outlined, A, B and C-scans, apply to PAs as they do to single element inspection. However, the much greater flexibility offered by such devices mean several imaging techniques are available in addition to simple A, B and C-scans. Defects can be viewed from a variety of angles without the need for multiple transducers or mechanical movement of the probe. These can be used to generate phased array linear scans and create cross-sectional views, employing a different focal law at each active aperture. A pulse can be swept electronically across the array,

yielding a 2D image, perpendicular to the sample surface. This is a B-scan. To acquire a full C-scan the PA must be moved mechanically, generating multiple aligned B-scans, resulting in an image in a plane parallel to the sample surface. This is a C-scan. One of the main advantages of phased array, C-scan acquisition is the ability to re-analyse data by adjusting the gate to retrieve information on the different depths of defects [50].

A S-scan refers to sectorial (or sector) scan in a region of material. Whilst the other image formats discussed here can be achieved both with single and dual crystal transducers as well as phased arrays, sectorial scanning ability is unique to PAUT devices. In a linear scan B-scan all focal laws employed a fixed angle, and the aperture is moved across the array. By contrast S-scans employ a fixed aperture steered through a sequence of angles by adjusting the relative delays across the array elements [70].

Previously, FMC was highlighted as a particular benefit of PAUT. Since all ultrasonic waveform data is collected, across the entire array, all previously discussed data presentation methods and imaging formats can be applied at any inspection location. FMC allows for there to be a clear separation between the data capture procedure and the imaging algorithms used. Other advantages include, the ability to produce much higher resolution images through additional data processing, no precalculated focal law is necessary and there is the potential for larger inspection ranges [72].

Post-processing methods, unique to FMC datasets, such as the Total Focussing Method (TFM), can also be applied. This technique uses a ray-based model of ultrasonic wave propagation, utilising every pixel's ideal transmit and receive focal

point, and gives an image on which every pixel is generated by the ultrasonic response focussed on that point [70]. Instead of steering to the RoI, using focal laws, the focus is applied synthetically at the post-processing stage, having captured data from every combination of transmission and reception on the array. Additionally, using multiple ray paths to exploit direct and skip paths, many different views can be generated from one FMC dataset. This is known as multi-view TFM [79]. Often, for large defects this multi-view analysis is necessary. For example, one view may contain only a specular reflection whilst the characteristic of a crack-tip diffraction may be accessible from a second skip path [80].

2.4.6 Signal Processing Techniques

2.4.6.1 Introduction

Once a ultrasonic inspection has been carried out, a raw data set is to be analysed. There are several mathematical tools to consider before the final image, or other data presentation method, is generated. Received echoes from within components can often be difficult to interpret, contain high levels of noise, or be masked by features within the specimen other than those of interest. A range of techniques exist to make sense of these data and draw reliable conclusions. Various characteristics from the received signal can give information on the physical state of the component including the time-of-flight, amplitude, and frequency content. To identify the type of defect accurately, a range of signal and image processing algorithms, described in the following sections, are commonly applied.

2.4.6.2 Noise

To a certain extent, all data collected contains inherent noise [79]. During ultrasound inspection, a common example is structural, or grain, noise which tends to be zero mean valued [42]. Random noise can be suppressed through repeated capture and averaging. However, it must still be quantified reliably. This is known as incoherent and includes thermal noise as well as that caused by the electrical instrumentation. On the other hand, coherent noise, which is unevenly spectrally weighted, will persist and induces a limit on the defect detection capabilities [81]. Speckle noise is time-invariant and, since it is distributed irregularly over a wide range of frequencies,

cannot be eliminated by averaging or spectral filtering techniques. An additional complication to be tackled is when the noise has spectral characteristics similar to those expected as defect signatures [82][79].

2.4.6.3 Time Varying Gain

This technique can be applied either during acquisition or as a post processing technique. Time Varying Gain (TVG) can also be referred to as Time Gain Compensation (TGC) or time-corrected gain. All perform the same function and are a method to compensate for depth-dependent levels of attenuation. If a sample were to contain several defects at varying depths, and the inspection aimed to determine the size of these based on the magnitude reflected ultrasound pulses, then the material's attenuation would significantly degrade the returned signal amplitude. A schematic of such a sample is shown in Figure 2.18.

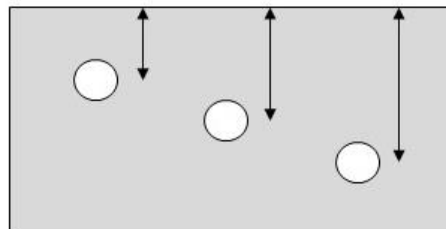


Figure 2.18. Reference sample schematic to illustrate TVG explanation.

Signals originating from deeper defects will be weaker since the sound travelled further to reach the reception transducer. It may then be wrongly assumed that these defects are smaller. TVG uses the amplitude of the back-wall echo and scales all the

signals between front and back wall reflection accordingly. This is achieved by fitting a varying gain curve, which is usually close to exponential in shape, defined such that the front and back wall amplitudes are equivalent in amplitude. The amplitude of all intermediate defect echoes is then modified to compensate for varying material attenuation. Consequently, accurate conclusions can be drawn on defect size and depth within the specimen. The process is shown in the schematic given in Figure 2.19.

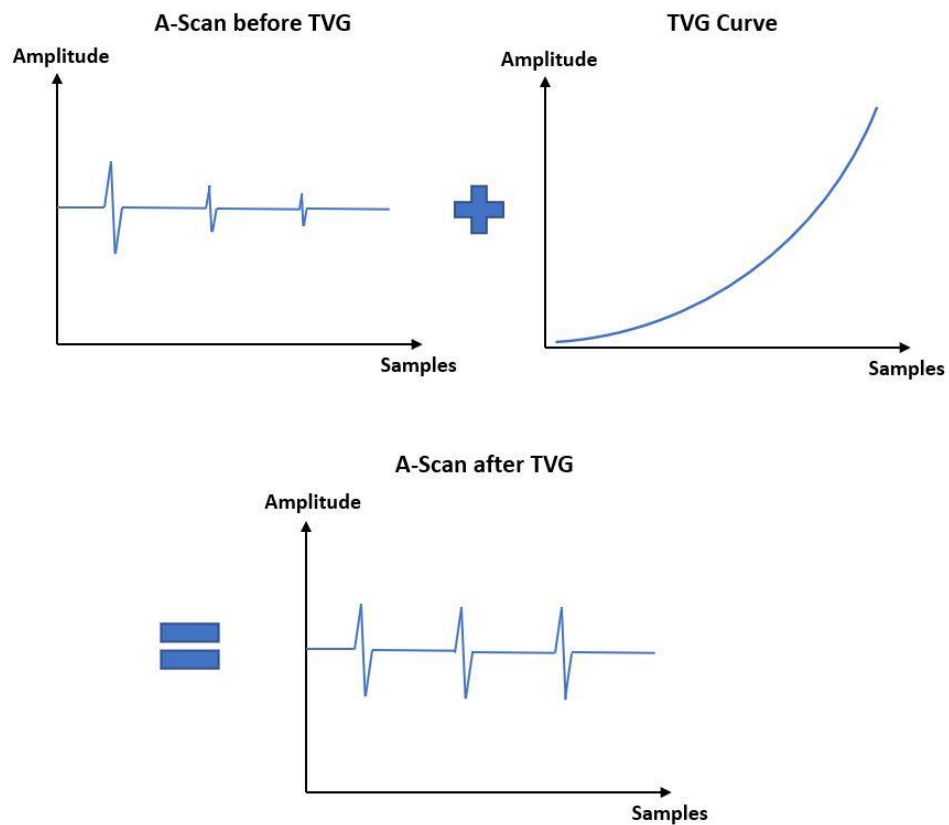


Figure 2.19. Schematic showing a TVG curve modifying the amplitude of features in an A-scan.

The TVG curve, based on front and backwall amplitude, is defined by and fitted to each A-scan. Similar curves can also be added across the dimensions of an FMC matrix, if the absolute amplitude values are to be used for defect characterisation. Reception on PA elements, or sub-aperture, other than those used for transmission will have lesser amplitude. This is a consequence of the geometry of the inspection set-up resulting in the sound having travelled further and is no longer at normal incidence to the transducer. A TVG curve, as a function of the difference between transmission and reception elements, can then be fitted across the FMC matrix. This concept is revisited in Chapters 4 and 5.

2.4.6.4 Fourier Series and Transform

The Fourier Transform (FT) is the cornerstone of any analysis concerning the spectral content of a signal. It decomposes a given periodic time-series into an alternative representation in the frequency domain using a linear sum of sinusoids. In the limit of the signal period approaching infinite, the Fourier series becomes an integral transform, shown in Equation 2.3, with sine and cosines taking their exponential representation based on Euler's formula.

$$F(T) = \int_{-\infty}^{\infty} f(x)e^{-i2\pi Tx} dx$$

Equation 2.3

Using these equations, one can transform from the time to the frequency domain allowing the frequency components, and their relative magnitude, to be determined. However, this method is not limited to time-domain signals and can be an effective analysis tool when applied to other Fourier-pair signals as well.

2.4.6.5 Wavelet Transform

Similar to the Fourier transform, the Wavelet Transform (WT) starts with a time varying signal and approximates it using a series of weighted components [40]. Wavelets are, however, known as ‘compact support’ signals, meaning they last for a finite time in contrast to the sinusoids comprising a Fourier series or transform [83]. There are an infinite number of possible wavelets, the integral of each being zero so that the energy is evenly disturbed. To process the WT, an analytical signal is multiplied by the wavelet analysing function. The output is then a matrix of the amplitudes and scale of the translation coefficients, defining the wavelet. These are in the time domain. Scale is effectively the pitch, how much each one is stretched and compressed while translation refers to the location in time. By definition, a high scale wavelet is stretched, thus low frequency and vice versa. High frequency wavelets will give better resolution in the time-domain but at the expense of depleted frequency-resolution. This in accordance with Heisenberg’s uncertainty principle. It is impossible to obtain an infinitely narrow distribution in both domains.

2.4.6.6 Hilbert Transform

The Hilbert Transform (HT) is a commonly applied mathematical operator when processing individual A-scans for imaging. This transform can be used to extract the magnitude and phase, of a time-varying signal, at every instant and thus the power in the signal. A function and its HT will therefore have the same amplitude spectrum. The HT is a linear operation and achieved by taking a convolution of the original signal with the function $1/\pi t$. Thereby, this transform imparts a $\pi/2$ phase shift on every Fourier component of the original function. In essence a FT, discussed earlier, is taken, the coefficients are rotated, and the inverse FT of these rotated coefficients gives the final HT. The original and transformed functions are orthogonal and thus, when used twice, the HT will yield the negative of the original function. Similarly, three Hilbert transforms can be used to give the inverse HT.

This is a mathematical tool that has been widely applied in the field of composite NDT and has been shown to solve the problem of closely time-spaced echoes [42]. Due to the lower frequencies employed for composites, flaw signals are often hidden in the tail of much stronger ones from the front and back surfaces as well as what is known as structural noise originating from the interface reflections from the composite's internal layers [82]. The HT can be used to resolve these. A combination of deconvolution followed by an adaptation of the HT, the Hilbert-Huang, has been employed to eliminate the strong echoes from interfaces, emphasize defect responses and thus and improve flaw visualisation [84].

Finally, the HT can be applied to any real-valued, band-limited signal for the estimation of instantaneous characteristics, used to express the rate of change of

signal energy [63]. Instantaneous frequency is most useful for characterization of disturbances for composite inspection. Often, only one part of the analytical signal is measured: the real part, such as acoustic pressure or particle velocity. In the complex plane, the signal follows a circular path with the phase representing how far around it has progressed [85]. Instantaneous frequency is defined as the rate of change of phase. The instantaneous parameters can be used in combination with the Radon transform, discussed next, to analyse the ply structure of CFRP [86]. The strength of reflections, from individual layers, can be enhanced by using an ultrasound probe with a frequency close to that of the ply's resonant one; the frequency that yields a 2π phase-shift per round trip.

2.4.6.7 Radon Transform

The Radon Transform (RT) is a 2D image transform used to reduce every 2D plane in a 3D data set to 2D image made up of 1D angular distributions. Consider the projection through the plane at every angle from zero to 180 degrees. At every point total amplitude, density, or absorption, is integrated along a line through this plane.

One of the most common uses of the Radon transform is in CT imaging which captures a series of X-ray images using a source and detector rotating around the patient. In this example, when a section of tissue is X-rayed, each pixel value is the sum of all the absorptivity values along one line at one projection angle. The imaging

bias, created by the varying absorption of different path lengths, can then be removed by dividing through by the number of pixels used to calculate each value.

The Radon Transform has also been applied to great effect in research conducted into the dominant fibre orientation within carbon fibre panels used in the aerospace industry [86]. The application yielded the ply direction at various depths within a composite laminate. The distribution created at every point in the 3D data was used to find the dominant orientation at that point. Thereby, a 3D set of ultrasonic data was transformed to a dataset representing the most likely fibre orientation, along with some confidence parameter. Contrast variation was highest when the projection was aligned with features in the image, or in this case the fibre orientation. Since the laminate is flat, it is enough to orientate the 2D images with the scanning plane. This would not be the case for the non-planar, or inclined plies one might find in tapered components [86].

2.4.6.8 Domain Sparsity Methods

There can be a large disparity between the information content within an ultrasound waveform, and the number of data points recorded in each time series. Due to the high frequencies involved in ultrasound inspection, high sample rates are required to capture waveforms, resulting in large quantities of data [87]. Signal compression can express the same NDT data, regarding health of a component, in a different domain. A signal may be dense in one domain but sparse in another. One of the most successful compression schemes is that of shrinkage, or thresholding in a transform domain using Fourier or Wavelet transforms [87]. Techniques such as auto-

correlation, cross-correlation with the time-domain reference pulse, as well as a comparison of features in the spectral domain can form ‘new’ A-scans, in a different domain. These are no longer amplitude signals as a function of time but rather 1D arrays indicating the ‘similarity’ of the received signal when compared to a reference one. It is possible to vastly reduce the total volume of data, data-rate requirements in inspection hardware as well as enhance the effectiveness of defect detection by showing up otherwise hidden defect signatures [87][88]. Such techniques are used in literature to compress data, whilst maintaining the information contained within, and identify defects close to interfaces. For example, a delamination signature that is ‘swamped’ by a much larger backwall echo can be resolved thereby increasing the probability of detection close to interfaces. This is final point is enforced by an increased Probability of Detection (PoD) at far side of a component in [89].

Two of these important features in an A-scan relate to their attenuation and TOF difference. The simplest, connection between TOF and material thickness is defined by the speed of sound of a material. By both auto-correlation and cross-correlation with a backwall signal, the ToF accuracy when looking at repetitions of the transducer’s transmitted pulse within the echo, can be improved. This was used for reconstruction of backwall shape, by subtraction of reference envelopes in [89].

2.4.6.9 Machine Learning

Machine Learning (ML) tools are becoming widely available in many data science applications. The term has very much become a buzzword in research across many different fields including the data obtained from wind-turbine inspections. As an example, neural network techniques have been applied to Structural Health Monitoring (SHM) of wind turbine blades to identify levels of mud coating or blade icing. An algorithm is trained to recognise patterns in data, provided by sensors imbedded in the blades [90]. Also, Gaussian processes have been applied, in a form a machine learning, to identify anomalies within blade edge frequency data and gain an insight into the structural health of this component [91].

In modern inspections, large volumes of inspection data are acquired in relatively short periods of time. This means that human analysis and defect detection in ultrasound data is becoming a bottleneck. In the past computing power and storage bandwidth put a limit on inspections [92]. It is now possible to access a whole host of models using, for instance, the MATLAB ML Toolbox, or inbuilt Python functionality [10]. These have great potential to analyse and simplify the vast size of ultrasonic inspection datasets. ML can filter out anomalous data and focus on those which are characteristic and unique to a certain type of flaw. However, the quality and homogeneity of the available data is crucial to the success of any ML technique. Data are often not properly labelled making both classification and segmentation challenging. These are two of the most common tasks performed. Classification would, for example, take a series of images and identify those containing a defect. Once this step had been performed, segmentation provides more detailed information

of the size and severity of anomalies as well as their potential impact on the entire structure [10].

An example, found in industry, concerns the Channel Inspection and Gauging Apparatus for Reactors (CIGAR) inspection of nuclear coolant delivery tubes. The machine learning algorithm presented is in the form of a two-stage clustering procedure. The healthy section is assumed to be larger than the sum of defects and therefore the group with the larger number of members is labelled as healthy. The remaining ones enter the second stage which aims to distinguish between potential defects areas and noise [93].

It is important when designing ML algorithms that the characteristics chosen can facilitate a non-system specific procedure. These can then prove effective when applied to a range of different datasets. In the above case, parameters include the variance, maximum and minimum value along with the index positions of these. These analyses are performed on single A-scans. On the other hand, it is also possible to compare numerous waveforms and use a statistical analysis to extract common features, thus making the algorithms more robust and reliable [81].

2.5 Ultrasonic NDT in Composites

2.5.1 Introduction

Previous sections of this chapter have outlined the basic structure of a composite material as well as the nature of flaws which may be present within. Nowadays, these materials are found in many high-end manufacturing applications, their mechanical characteristics making them particularly attractive to wind turbine blade construction. The concept of NDT and defect detection has been introduced giving justification for the use of a more automated approach to both physical inspections as well as subsequent data analysis procedures. Ultrasound has been introduced, the physical principles and necessary components for inspections described, and the common data analysis and presentation methods detailed.

The final section of this chapter aims to bring all these fields together and review the current state of ultrasonic NDT when applied to composite wind turbine blades. Firstly, the key characteristic signatures of various composite defects under ultrasound inspection will be described. This is necessary in understanding the results presented from the inspection of CFRP panels, used in blade construction, which are presented in Chapter 3. Next, defect detection methods in ultrasonic data are reviewed. Finally, the NDT currently utilised in wind turbine manufacture is summarised, with particular emphasis on the techniques employed by industrial partner SGRE.

2.5.2 Frequency Tuning Methods

A composite material's response to ultrasound inspection can be vastly different to that obtained from more traditional metal alloy, resulting in data being more difficult to link to the physical state of the component. Industries working with composites often rely on components with complex curved surfaces, variable thicknesses, and an anisotropic, multi-layered composition. This contributes to the complexity of inspections, far outweighing those concerning simpler, planar, metal-alloy components [27]. Process variability is another major issue when working with composites. Spring-back, when removing from the mould, can lead to deviations from the desired design dimensions.

Along with certain metal alloys and austenitic steels, composites exhibit an interaction with ultrasonic beams which is highly non-linear, potentially containing distinctive frequency-dependent properties. Enhanced signal processing is necessary due to the levels of scattering, reflection, refraction, attenuation and mode conversion occurring within [94]. Attenuation can be limited by using lower working frequencies, but this comes at the expense of lesser resolution and therefore a reduced defect detection capability [81]. As with all ultrasound inspection, the frequency versus resolution trade-off is key in terms of the achievable resolution and best SNR.

The complex nature of ultrasound reflections from composites had, in the past, led to the assumption that signal response from individual from plies was pretty much random and of little inspection use [95]. However, on the contrary, much post-processing work, reinforced by analytical models, has been published on this in the last decade. The Fourier, Hilbert and Radon transforms as crucial in obtaining

relevant information and building up a picture of the internal structure of the specimen. These allow for the parameters of instantaneous phase and frequency to be calculated. These parameters yield much more information on the internal structure of a composite and despite the underlying difficulties faced during the ultrasound inspection of composites, open the door to a whole host of techniques tailored to a composite's layered and varying structure to generate 3D profiles of porosity, resin layer thickness, ply spacing, and fibre orientation.

When only one part of the analytical signal is measured, for the example the real part, such as acoustic pressure or particle velocity, the complex plane will display the signal following a circular path with phase representing how far around it has progressed [85]. Instantaneous frequency is defined as the rate of change of phase. These instantaneous parameters can be used, in combination with the Radon transform, to analyse CFRP and show the significant impact porosity and resin layer thickness have on frequency response [86].

In example, tuning of the frequency of the transducer, to be optimal to the composite under inspection, is key to obtaining more accurate information on defects [85][86] [95][96]. A working frequency matched to that of the ply layer resonance, can be used to analyse the internal structure with changes in the response highlighting any variations in ply thickness [96]. This frequency yields a 2π phase-shift per round trip. Ply layers typically have thicknesses in the range of 0.01-0.03 mm, resulting in 3 and 9 MHz frequencies giving the correct round-trip phase-shift for resonance. Deviations from the ply resonant frequency also effect the instantaneous amplitude. The method has also been shown to be effective in ply-drop detection, areas within a

laminate where a fibre-termination, from the design geometry, cause a wedge-shaped region of resin richness. Adjacent plies will move together, to occupy the space dropped, and a stress-concentration site, major weakness in a component, can be formed [95].

The instantaneous phase has also been used to track the location of resin and ply layers, provided the input signal is sufficiently broadband and close to the fundamental resonant frequency. Deviation of an ultrasonic beam through resin wedges can be used to identify ply waviness. Using the RT, maps of in-plane fibre angle are generated in [86]. Taking cross-sections through this data then allows for the stacking sequence, of plies in the laminate, to be obtained. Depending on the plane orientation, at a given point, both in-plane waviness and out-of-plane wrinkling can be quantified. Any out-of-plane wrinkling is accompanied by changes in ply thickness and thus will yield a change instantaneous frequency as well as amplitude. Higher amplitudes will be observed when plies are squashed and vice versa [96]. Finally, instantaneous frequency has also been proposed to improve the distinction between different microstructures and classify defects within the specimen [86][96]. The effectiveness of the methods detailed here is partially owed to the well-structured and predictable layup CFRP. By contrast, GFRP is less ordered, in terms of internal structure, and therefore analysis is significantly more challenging.

2.5.3 Defect Detection Considerations

The characteristics of a composite's response to ultrasound inspections are of course also of consequence when any form of defect detection is carried out. Defect detection depends on the operator's ability to distinguish the characteristic defect signal from both the random and coherent noise within. This defect-signature is crucial in forming the link between data collected and the physical state of a component.

Performing defect detection, one is presented with the choice of analysis of the final images, or the raw A-scans used to form these images. The image processing approach is advantageous since images are relatively small compared to the data they are derived from. Therefore, quick and highly optimised algorithms can be written. This benefit must be compared to the issues created by having more layers of analysis before any form of defect classification is applied. It may well be the case that the information, corresponding to a flaw signal, is buried within A-scans, either in time, frequency, or other domain, and then lost depending on which methodology is used to form C-scans. C-scans also suffer from various sources of contamination which do not play a role when working in with raw A-scan data. Ultrasonic images are very sensitive to the optimal gating and gain settings being applied in the inspection procedure. Reliable and consistent coupling between transducer and sample is also necessary lest artefacts, which could be mis-classified as defective areas, be introduced to the final image. Alongside these factors, reliable front and backwall identification, chosen colourmap, sensor saturation and data fidelity, are all important when producing images which are representative of state of the sample. In simple

terms, there are more ways in which errors can be introduced and thus the probability of false positives is increased.

Therefore, analysis focussed on raw RF A-scans in the time domain, the ultrasonic data in its simplest form, is the most suitable for the inspection of composite components. All the available information is forehand before any defect detection techniques are applied. Using the full RF data also allows for more mathematically complex methods to be utilised and is the approach taken in most of reviewed literature on the subject.

2.5.4 Composite Defect Signatures

Alongside explanations of why and how each defect type becomes visible under ultrasound inspection brief descriptions and potential causes are also given in this section.

2.5.4.1 Foreign Object Inclusion

Firstly, the most obvious and easily avoidable manufacturing defect is foreign object inclusion which can occur during the stacking procedure of fibre glass cloth to form a GFRP component. Ultrasonically, these are detectable since the object tends to not bond to the laminate and will have a different acoustic impedance. If it does adhere, detection becomes much more difficult.

2.5.4.2 Voids and Porosity

Interlaminar voids and porosity are caused by trapped air which is not fully removed by the vacuum curing process. This creates blockages meaning the resin cannot impregnate all areas. An example of this in the wind turbine industry would be problem of so-called 'torpedo' defects where a blockage or slow flow in a 'resin highway' results in a large area of GFRP not receiving resin. Such defects can be metres or even tens of metres in length. Severe components geometries can also lead to difficulties in resin extraction with voids and porosity the result of the resin not reaching certain areas. The most severe voids or areas of porosity can often be found using visual inspections, provided they are close to any surface. If this is not the case

large difference in acoustic impedance between air and both constituents in surrounding matrix results in this type of defect showing up clearly as a strong reflection under ultrasound inspection. Voids tends to have a regular shape whilst porosity is more irregularly distributed through the structure. If individual void sizes are much smaller, they tend to be identified by higher attenuation level compared to the surrounding medium, since attenuation is lower in the resin material than the matrix. Provided the porosity is severe enough then one cluster can also appear as one large void.

2.5.4.3 Resin Rich/Starved Areas

Related to porosity is the potential issue of resin-starved or resin-rich areas within a composite. The ratio of fibre matrix to resin is crucial in determining the mechanical and acoustic properties of the final material and variations can be detected ultrasonically in a similar manner to voids or porosity. Acoustic attenuation is lower in the resin material than the matrix so any resin-rich areas will show up with higher transmitted intensity and vice versa. A downside of this detection technique is that it can make it difficult to detect other flaws since the amplitude threshold levels are adjusted for resin-starved areas. When variations in fibre volume fraction are very small, through transmission ultrasound is often used so that the amplitude differences experience less noise with the propagation-path halved.

2.5.4.4 Fibre Misorientation

Fibre mis-orientation or ply lay-up mis-order can originate during the lay-up process and severely effect the final mechanical performance. Ultrasonic C-scans from different depths allow for analysis of how well a given lay-up sequence (say: +45, +90, 0, -90, -45) has been executed. Gating at different depths allows for visualisation of the layup orientation. Deviations from the normal angular distribution could signify shear damage or stretching out of the composite [52]. An alternative method generates what is known as a polar C-scan with the ply orientation determined based on backscatter from a beam incident at oblique angle. Maximum energy is returned when the probe orientation is perpendicular to the fibres with depth determined based on the relative intensity of the reflection [28].

2.5.4.5 Fibre and Matrix Breakage

Related to mis-orientation is fibre fracture or breakage. This is most commonly a service-induced defect, originating from impact or fatigue loading. Fractured fibres or matrix cracking is often termed Barely Visible impact Damage (BVID) since nearly impossible to detect using a surface inspection. Ultrasonically, the presence of cracks can be detected by backscatter or crack tip-diffraction using an angle to the surface shifted from normal. Cracks will cause backscattered waves with a higher amplitude than those from fibres. Scanning through various angles can yield the crack-echo to fibre backscattered amplitude ratio, giving information on the severity and orientation of the crack. It can be difficult to detect this type of defect if structural

loading force the crack to close [97]. Various testing techniques, used to open the crack, whilst ultrasonic inspection is carried out, have been reported [94].

2.5.4.6 Delaminations and Kissing Bonds

Delaminations, or a separation of the plies, can be an inherent defect or originate from any of the previously mentioned fabrication defects. They can result over time or as the result of fatigue cycles or sudden changes in the operational loads. Such defects have nearly no strength in their thickness direction. In both GFRP and CFRP these dis-bonds are clearly detectable using pulse echo as well as through-transmission mode, provided there is some region of air between [26]. The acoustic impedance discontinuity within the sample allows delaminations to show up easily with their depth profile, location and geometry obtained from a combination of A-scans, B-scans and/or ToF data [98]. Such measurements are only possible when the thickness of the composite panel is several times the wavelength of the ultrasound which brings into consideration the previously described resolution and SNR trade-off to consider when choosing a working frequency. If the plies are still in contact, but there is no transferral of strain, then the defect is referred to as a kissing dis-bond. Kissing bonds are much more difficult to identify since there may not be an air or resin layer present to cause an impedance mismatch [26].

2.5.5 Ultrasonic NDT of Wind Turbine Blades

The source of typical defects within composites and their detection and characterisation under ultrasonic inspection have now been described. Using the basic structure of a modern turbine blade, a brief overview of ultrasonic NDT specific to these components will now be given. Procedures currently applied, by the industrial partner to this project, in their manufacturing facilities, are summarised, justifying the work presented in subsequent chapters.

The NDT of wind turbine components can be broadly split into two categories: inspections carried out at the manufacturing stage and those once the component is in-service [10]. Once in service, Structural Health Monitoring (SHM) is far more prevalent than any specific NDT inspections due to the associated cost [99][12]. SHM can be based on strain measurement, acoustic emission, ultrasound, or vibration analysis with sensors often embedded in the blades [100][101][102]. A very active area of research, concerning SHM of wind turbines and composite materials, is the data analysis, modelling and machine learning techniques often employed to link SHM data to the physical health of the component. The use of Gaussian processes, Bayesian modelling to quantify damage probabilities as well as machine learning techniques applied to data obtained from ultrasonic guided waves have been reported in [91][103][104][105]. Additionally, recent and very thorough reviews of damage detection techniques, applied once the blade it is in service can be found in [106][107].

Blades leave the manufacturing plant with their structural integrity ensured and guaranteed through company-specific standards whilst operating with no unexpected operational changes [106]. Once installed, general service procedures and maintenance schedules are carried out, but NDT only performed if a critical risk is found during SHM [99][12].

The work in this thesis focusses on techniques applied only at the manufacturing stage, whilst the blade is being laid up and still within the factory. The relative immaturity of the industry means that NDT at the blade manufacturing stage is not as well-developed as in the aerospace or nuclear sectors. These are often seen as being at the forefront of NDT development, with stringent standards and codes [38]. Consequently, the state of the art in a variety of methods and automation can be found in aerospace.

Within the non-destructive testing procedures, present at the turbine manufacturing stage, steel structures, such as the tower and nacelle, are inspected in accordance with European standards [10][108]. Different products sectors, have their own standards and there exists associated documentation on the various NDT methods. For example, EN ISO 17640: 2018, for ultrasonic testing of steel welded joints. By contrast, there are no overarching standards applied to the composite blades. DNV GL supply some guidance documentation, IEC 61400 for composite blade inspection, but in general turbine manufactures set their own 'in-house' standards [10][109]. The cross-industry agreements, found in oil and gas, are therefore not yet present. Each manufacturer's standards are designed to tackle common issues, unique to the wide range of blade manufacturing procedures that exist [109]. Such is the range of these, in terms of fibre

layup process and resin infusion techniques, that broad, industry-wide codes and standards have not yet been applied. Initially, some were based on ASMT in the late 1980's which are the earlier versions of today's ultrasound NDT standard practices [110]. Individual companies have since built on these and applied more stringent, and tailored measures to suit their own products and procedures.

When considering blade inspection, a key consideration is the higher penetration capability achieved using lower frequency ultrasound waves [27]. Values as low as 500 kHz are applied to GFRP parts. The largest blades manufactured today have root sections up to and beyond 90 mm in thickness and the high attenuation values in GFRP make acquiring adequate SNR a significant challenge [111]. Lower frequencies also come at the expense of reduced lateral resolution resulting in poorer defect detection capability and there is also a greater dead zone in front of the transducer face [26][50]. On the flipside, higher frequencies have been shown yield better results in detecting defects but this was restricted to inspections close to the outer surface of the blade [112].

Testing can be carried out on subcomponents or on the final blade. In the past, NDT was a procedure only performed at the end and not fully integrated into the manufacturing procedure [113]. This is now changing, and several blade subcomponents are already inspected at the pre-manufacturing stage. The increasing size of blades, and the complexity of their construction, drives this change. Finding potential flaws in pre-cast components is preferable since it is more cost efficient to scrap or repair parts at an earlier stage. An example, and the focus of the research presented here, is the inspection of pre-manufactured CFRP sections, for the

construction of load-bearing internal structures. These components are thinner, and with lower attenuation than the largest glass fibres sections, higher frequency ultrasound can be used. CFRP has a more ordered, or unidirectional, layup sequence, also resulting in more favourable ultrasound inspection characteristics.

Siemens Gamesa Renewable Energy is a world-leading manufacturer of wind turbines having added over 50 GW to their total worldwide installed capacity within the last decade [114][115]. State of the art fibre-layup and impregnation techniques are utilised to manufacture blades, with the most up to date models produced within one mould. This is a huge advantage in that there are no leading or trailing edge bond lines as potential points of weakness in the structure. Due to the rapidly growing size of installations, the manufacturing processes are also evolving. This has knock-on effects on NDT with a variety of procedures applied depending on application. These will vary but a blade would never leave the factory without a thorough NDT regime having been carried out.

After fibre layout and resin infusion the blade, there is an initial visual check concerning internal and external surfaces. In its most rudimentary form, this involves a team of trained operators inspecting the inside surface of the hollow blade using torches to check for any visible surface irregularities. Toward the tip, the narrowing cross-section makes access difficult, and lights and cameras mounted on extendable arms are employed. Based on this initial inspection, minor repairs are carried out and areas of glass fibre are cut and patched. Following this initial inspection, ultrasonic NDT is carried out using a series of single-element transducers, following a sinusoidal scanning path. The set-up is mounted on a flexible, forklift-mounted rig,

to allow for compliance to the contours of the blade surface, as shown in Figure 2.20. The entire blade length is scanned several times. A frequency of 500 kHz is used and coupled into the material using a water-delivery system. Again, based on analysis of the data collected, areas of the blade are cut and patched. Particular attention is given to the detection of impregnation errors, delaminations, and ply wrinkles due to their hugely detrimental impact on the composite strength [29]. Such procedures are now to be extended to the CFRP blade subcomponents.

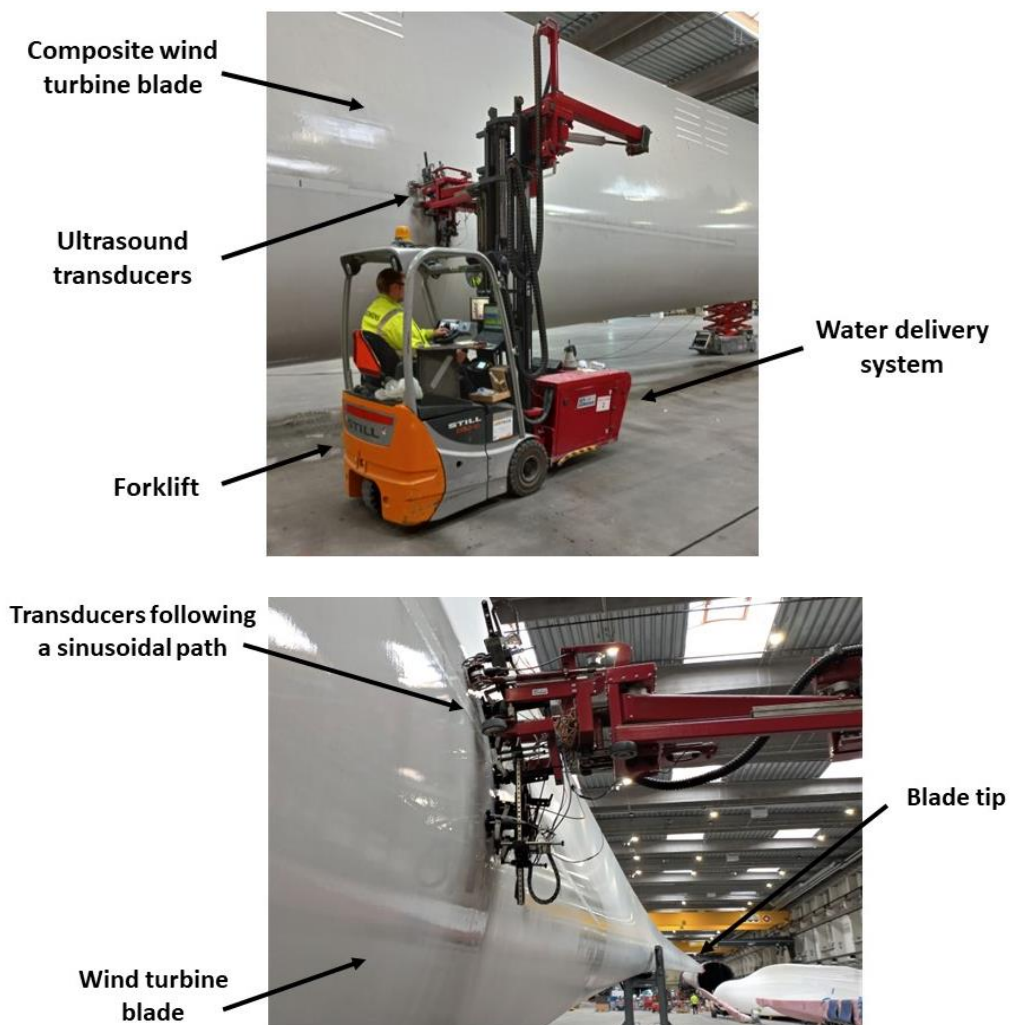


Figure 2.20. Example of wind turbine blade inspection process.

Several other NDT techniques are also employed as part of the entire process [109]. Examples include thermography testing on the leading-edge protection, as well as the lightning protection system. This consists of an electrical connection, between tip and root, running within the web to ensure any strikes are earthed and do not cause damage to the composite structure. A bond test of the copper terminals is carried out and the resistance of the electrical connection checked.

When considering additional NDT procedures, bottlenecks within the manufacturing procedure must be avoided. These can be due to the time taken to accurately inspect complex parts as well as subsequent data analysis procedures. For example, whilst the P-scan system from Force Technologies, shown in Figure 2.21, allows for scanning of GFRP blade sections at a rate of five metres per minute, the analysis can take three times as long [10][116]. Progressing to ultrasonic phased arrays can increase the volume of data by two orders of magnitude and thus this problem is exacerbated [10]. The P-scan inspection hardware employs a crawler system with couplant delivery and battery power unit to allow for mobile ultrasonic inspection of a range of materials and surface geometries. A range of different phased arrays, either linear or azimuthal with frequencies of 0.5 and 5 MHz available off the shelf and can be used in combination with the necessary delay wedge for a given application [117].

Similarly, NDT products by EVIDENT from Olympus offer a range of different industrial scanners, flaw detectors and ultrasonic thickness measurement hardware [118]. Again, phased array probes with frequencies ranging from 0.5 to 18 MHz, and a selection of wedges, allow for inspection of a range of components such as pipes,

pressure vessels and turbine components, both at the manufacturing stage as well as in-situ.



Figure 2.21. Image of the P-scan system by Force Technologies [116].

To conclude, the renewables sector is faced with the need to speed-up and reduce the time of inspections of critical components which will enable them to cope with future demand projections [1][119]. Advances such as the use of robotic cells, fast acquisition using ultrasonic phased arrays, automatic data analysis procedures and machine learning techniques have become standard practice across the aerospace industry [55]. Adaptive robot tool-paths, the development of high speed NDT data collection and surface metrology measurements have the potential increase inspection throughput [119][56]. These are flexible tools, quickly adaptable to a variety of environments, allowing them to be applied in the renewables industry [107]. Nevertheless, challenges are faced when dealing with composite material properties and the arbitrarily curved shapes often found in aerodynamically-tailored components [66].

2.6 Conclusion

These sections have served both to provide the necessary background for the results presented in the following chapters, as well as justify the entire body of research. The basic structure of a wind turbine blade, as well as how modern composite materials are used in a complex geometry design, has been introduced. The requirement for NDT, as well as a variety of techniques used today have been described. Next, ultrasound and ultrasonic NDT was introduced, starting with the basic physical principles of sound propagation, and finishing with complex beamforming and data analysis methods made possible using phased arrays. These relevant topics are all drawn on when the ultrasonic NDT of wind turbine blade materials is discussed in the final sections of Chapter 2. The defect responses of various anomalies present within composites were also outlined. The following chapters will draw on all these background topics when demonstrating phased array ultrasound NDT as well novel inspection and data analysis methodologies.

3 Phased Array Ultrasonic Inspection

3.1 Introduction

This chapter concerns the deployment of phased array ultrasound for the inspection of pultruded CFRP panels. These panels are used in the construction of a load bearing beam, incorporated into the GFRP lay-up process in the manufacture of wind turbine blades. The second half of Chapter 3 concerns an in-process ultrasonic inspection system for online factory inspection of CFRP. The panels inspected are the same as described in the first sections, which outlines the effectiveness of an automated phased array inspection set-up. High speed inspections are carried out and industrial requirements are shown to be well within the capabilities of the chosen hardware. Samples, used within a 81.4 m blade installed on offshore turbine with a nameplate capacity of 8 MW, are supplied by industrial partner, SGRE [14]. As detailed in section 2.1.3, these now incorporate lighter and stiffer CFRP subsections. Construction and quality assurance processes are therefore vital in driving the industry forward to meet increasing demand. Previous chapters have outlined the effectiveness of robotic phased array ultrasound inspection when applied to composite materials used in the aerospace sector. This can be seen both in research as well as more industrial settings. Similar hardware is now applied to these CFRP components with the aim of proving effectiveness as seen from a reliable defect detection and factory implementation standpoint. This final requirement calls for high speed inspections and therefore scanning velocity is a key consideration throughout the results presented here.

Following this introduction, the theory behind basic operational procedures, inspection parameters is discussed. Since the ultrasonic phased array is the key component of the experimental hardware, an additional section reports on a new calibration and characterisation tool, used to gain an important insight on the performance of the array. To aid the understanding of PAUT, computer simulations also play an important role in the generation of theoretical datasets for comparison purposes. General ultrasonic NDT modelling as well as the software package used for this application are discussed. Following the theory section, individual hardware and software tools used in the practical set-up are described and their use validated. The sample and its ultrasound inspection characteristics are also described in more detail, but the main impact of the chapter lies in the results presented as well as the defect characterisation carried out on rejected components from the industrial partner. Pultruded CFRP samples are inspected, defects identified, localised and their geometry determined by an amplitude-based method. A discussion, suggestions for future work and finally, concluding remarks close this chapter.

3.2 Theory

3.2.1 PAUT Inspection Parameters

In their simplest form, the phased array focal laws facilitate the acquisition of one B-scan during each sweep of the array. The number of beams comprising this scan is a function of the total array elements, aperture size and step size between adjacent apertures. Physical movement of the probe, achieved through robot motion, generates C-scans by stacking adjacent B-scans as the scan path is executed. To understand the theory behind phased array ultrasonic scanning, where the beam is swept electronically across the array and mechanically by robotics, several key parameters must be defined. The achievable image resolution, in all three axes, and therefore defect detection capability, can be calculated from these along with the corresponding file sizes and data rates. This aids the understanding of the physical principles behind ultrasonic inspection and subsequent image processing. There are both experimental and theoretical limits imposed on the inspection procedure, and it is important to operate well within these to allow for delays and margins imposed by physical equipment and connections.

3.2.1.1 Focal Law Parameters

Consider an array consisting of N total elements. In a pulse, triggering the transducers, the active aperture size is the number of elements used to transmit sound. The delays between elements firing results in the ability to focus or steer the beam. The operation of PAUT traditionally involves what is known as linear scanning. One aperture, consisting of a single or group of elements, is excited by each pulse of the phased array. The active aperture in each pulse steps along the array in a linear fashion with many positions contributing to one frame. The step size, S , is the number of elements between one pulse and next. The total number of beams or channels per B-scan is given by Equation 3.1, where $N=64$, $A=4$, $S=1$, resulting in $C=61$. Figure 3.1 exemplifies this. Each beam corresponds to a line in the B-scan image or C-scan coordinate as the probe is scanned.

$$C = \frac{(N - A)}{S} + 1$$

Equation 3.1

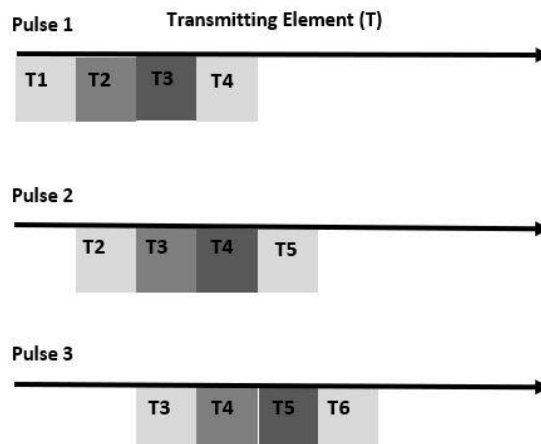


Figure 3.1. Schematic illustrating linear beamforming with $A=4$, $S=1$, $C=64$.

3.2.1.2 Number of Channels

The number of channels is the number of array elements transmitting and receive in each sweep of the transducer. For example, a 64-element array, pulsing and receiving on each single element incrementally, would result in 64 channels. The example in Figure 3.1 gives 61 channels due to the aperture and step size. FMC acquisition will yield N^2 channels, 4096 for a 64-element linear array. Consequently, the amount of data produced is significant and any data rate constraint imposes limitations on the maximum number of channels, or rate of inspection, a given inspection procedure can effectively utilise.

3.2.1.3 Pulse Repetition Frequency

The Pulse Repetition Frequency (PRF) is the number of times the array is pulsed per second. That is how many separate times ultrasound is emitted. The maximum value is determined by the internal architecture of the array controller but also limited by the sample, delay line thickness and speed of sound within each. In an inspection sound travels through the delay line, into the sample, reflecting off the sample backwall and back to the transducer array. The time taken for this imposes a limit on the PRF. It cannot exceed any value where which the transmitted signal has not returned and thus the PRF is naturally limited by the dimensions of both sample and delay line. The delay line also determines the maximum sample thickness that can be inspected. To prevent superposition of front and backwall echoes, and the requirement for the backwall echo to return before the second front wall reflection, a given thickness of water will determine a maximum sample thickness. Firing whilst receiving gives interference effects and such an operational mode is not considered.

3.2.1.4 Frames per Second

Frames per Second (FPS) is defined simply as the PRF divided by the number of channels, Equation 3.2. That is, how many times it is possible to perform an entire sweep of elements, using the chosen focal law and obtain one 'frame', in the timespan of one second.

3.2.1.5 Sampling Frequency

Sampling frequency is rate at which the amplitude of returning ultrasound signal is measured. Using this, along with the acquisition time, or length of A-scan, gives the number of data points making up each individual A-scan. Each point is sampled with a precision defined by the Analogue to Digital Conversion (ADC) rate to define the fidelity of the data.

3.2.1.6 Scanning Speed

The next consideration involves the fact that the array elements are also moving along the sample in an orthogonal direction to the electronic scan implemented on transducer array. Scanning at higher speed reduces the image resolution in the movement direction. This can be compensated by increased PRF. This scanning speed is also limited in that the receiving element is required to not have moved significantly during the time of flight of each ultrasound pulse so that it can still receive the reflected pulse. This upper limit has been found at 27 ms^{-1} , defined by the transducer element to have moved 10 % of its height of 10 mm during propagation time in delay line and sample. This value is much higher than any limitation imposed by maximum data acquisition rates available alongside the maximum robot

movement speed of 2 ms^{-1} . It can therefore be neglected since the array has only moved fractions of a percent of an element's height during the propagation time.

3.2.1.7 Achievable Resolution

Using these parameters, along with the acquisition time based on the thickness of samples it is possible to calculate the size of each frame acquired, Equation 3.4, and consequently the minimum required data transfer rate, Equation 3.5, at the chosen scanning speed. The resolutions of resulting C-scan images in both the array, Equation 3.3, and scanning direction as well, as the depth accuracy, can also be determined. These theoretical values serve to define the inspection parameters necessary for a given resolution at a given speed for a certain sample. Experimental Image resolution can then be compared to this. The following set of equations are used in these calculations [120], with nomenclature in Table 3.2.

$$FPS = \frac{PRF}{C}$$

Equation 3.2

$$R_s = \frac{FPS}{v_s}$$

Equation 3.3

$$fs = \frac{S.f.C}{8.1024}$$

Equation 3.4

$$tr = \frac{fs.FPS}{1024}$$

Equation 3.5

3.2.1.8 Data Rate and Resolution Examples

To consolidate this section, several hypothetical inspection scenarios are now presented in Table 3.1. These utilise various PRFs, channel numbers, scanning speeds and sampling frequencies. Using numerical values, the maximum achievable inspection rate, data rate and resolution, in each, has been calculated using Equation 3.2, Equation 3.3, Equation 3.4 and Equation 3.5. This acts to give an understanding of how the parameters relate and the limitations they impose. An Excel-based tool, shown in Figure 3.2, is designed to allow parameters to be quickly checked and the impact of one on the other seen. This is a useful aid throughout the work presented in this, as well as later, chapters. The following, Table 3.1, presents calculation results with the number of channels set to 61, the 4-element linear imaging sweep of a 64-element array shown in Figure 3.1.

Updated Scanning Parameters and Limitations Calculator			
Inputs (choose these)		Outputs	
Data Acquisition and Inspection Parameters			
Phased Array Channels	61	Frames per second (FPS)	125
Pulse Repetition Frequency (PRF) (kHz)	7.6	Frame Size (kB)	107.2
Sampling Frequency (MHz)	100	Minimum Required data transfer rate (MB/s)	13.0
Samples per beam, length of A-scan acquisition	1200		
		Resolution in scanning axis	0.80
ADC Rate (bits)	12	Resolution in array axis (mm)	0.8
Scanning speed (m/s)	0.1	Samples Expected	498
Element pitch (mm)	0.8		
Element height (mm)	10	Physical Limitations	
Aperture size (elements)	1		
Step Size (elements)	1	Total ToF (μ s)	38
		Maximum PRF (kHz)	26.6
Delay Line and Sample Parameters			
Delay line length	25	Consequent maximum FPS	436
Delay line bulk velocity	1480	Consequent maximum scanning axis resolution (mm)	0.23
Sample thickness	5.8		
Sample bulk velocity	3070	Percentage of array element moved per acquisition (%)	0.0
		Consequent maximum scanning speed (20% max) (ms^{-1})	53.2

Figure 3.2. Screenshot, highlighting inputs and outputs of an Excel-based tool used to demonstrate the relationship between inspection parameters.

Scenario	Acquisition (samples)	Scanning Speed (mms ⁻¹)	ADC (bits)	PRF (kHz)	Data Rate (MB/s)	Predicted Resolution (mm)
1	600	100	8	7.6	4.3	0.8
2	600	200	8	7.6	4.3	1.6
3	600	1000	8	19	10.9	3.2
4	1200	100	8	7.6	8.6	0.8
5	1200	100	12	7.6	13	0.8

Table 3.1. Examples of the effects of different parameters on the achievable resolution and necessary data export rates.

With the scanning speed and channels determined by the inspection requirements, the PRF value is adjusted to give a resolution in the scanning axis that matches the phased array pitch determining the array axis resolution. In example, Scenario 1, from Table 3.1 gives 0.8 mm scan axis resolution to suit the 0.8 mm pitch in a Olympus 5 MHz 64-element phased array and thus achieve square pixels in the final C-scans. Previous works, concerning the robotic inspection of composites, have looked into maximising the resolution or sample thickness within the boundaries imposed by the data link, to facilitate real-time inspection [55]. The application to thin planar CFRP panels, aims to maximize scanning speed, with detectable defect size being of lesser importance.

Scanning Parameter	Nomenclature
R_s	Scan axis resolution
v_s	Scan axis velocity (ms ⁻¹)
fs	Frame size (kB)
S	Number of samples
f	Analogue to digital conversion fidelity (bits)
tr	Data transfer rate (MB/s)

Table 3.2. Nomenclature used in Equations 3.2 to Equation 3.5.

3.2.2 PA Calibration Work

3.2.2.1 Introduction

It is standard practice for the manufacturers of phased transducer arrays to supply a datasheet in which the performance of the device is quantified. Such a document will contain a range of parameters relating to each element [121]. This gives a benchmark for the performance, taken when the array leaves the supplier. Characterisation of the array is also a useful tool for the consumer allowing them to firstly confirm the data supplied by the manufacturer as well as monitor the performance degradation over the device's lifetime. Using a standard reference sample, the quality of a probe before and after a series of inspections can be checked. Based on these, maintenance schedules or replacement strategies can be designed.

Modern phased arrays can be used for highly accurate imaging and defect detection applications. For example, the TFM imaging method applied to FMC data. Arrays must be carefully calibrated in order to utilise these data as effectively as possible [122]. In addition to this, it is beneficial if the time delays within the inspection hardware are also quantified. Variation in hardware leads to uncertainty in the images and it has been shown that these time offsets are the most significant factor in degradation when constructing TFM images from FMC data. By firstly quantifying the speed of sound accuracy and secondly the decoupling of transmit and receive peak time error these errors can be significantly reduced, as reported in [123].

Such a calibration tool has been previously designed using both a FIToolbox (Diagnostic Sonar Ltd, Livingston, UK) as well as Dynaray 6 (Zetec, Quebec,

Canada) as the phased array controller. Each was operated to acquire FMC data. Data analysis, yielding array parameters and hardware delays, was carried out using open-source Python coding [123]. The delays were then included in the TFM imaging algorithm and shown to enhance the accuracy of the TFM image, produced when inspecting a block of steel with three side-drilled holes [123][124].

The work presented in this section applies the same theory for use with PEAK NDT phased array controllers [125], alongside LabVIEW integration and MATLAB data analysis procedures. Application using these hardware and software allows for the same parameters to be obtained using equipment relevant during this PhD.

These results of this are not integrated into the data analysis and imaging work since the imaging algorithms generate A, B and C-scans. TFM imaging is not used and therefore hardware delays need not be integrated. However, this work does allow for confirmation of the satisfactory performance of all array elements and comparison between arrays. The tool is a useful contribution to aid a variety of related ultrasonic NDT projects carried out within the research group. In sections 3.2.2.3 and 3.2.2.4, array parameters are first discussed before the results of characterisation, applied to a Olympus 5 MHz wheel probe phased array, are presented.

3.2.2.2 Calibration Block

Data is acquired from an FMC dataset using a glass calibration block with dimensions 305 x 152 x 50 mm, as shown in Figure 3.3. Glass is commonly used as a calibration sample for ultrasonic imaging due to its low attenuation, high acoustic velocity, and isotropic nature, meaning the resultant A-scans have as high a SNR as achievable from a ‘real world’ inspection.

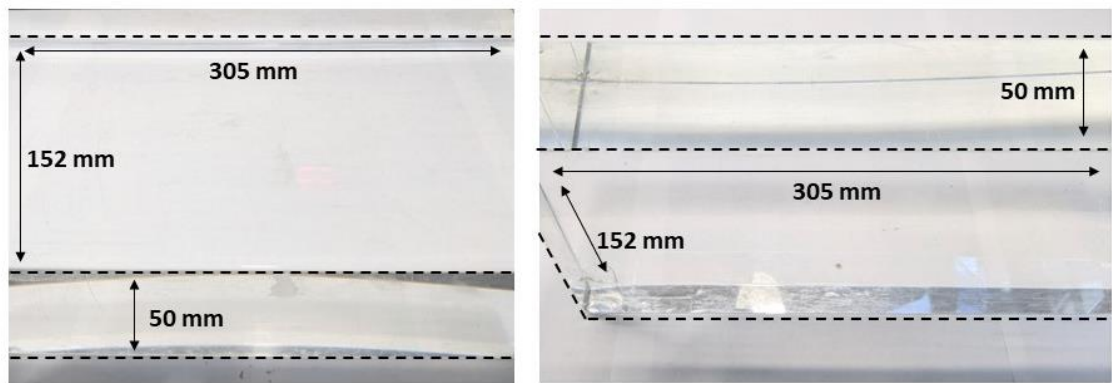


Figure 3.3. Images, including dimensions, of a glass calibration block used for FMC data collection and subsequent phased array characterisation.

3.2.2.3 Array Parameters

Median Waveform

This is defined as the amplitude as a function of time received by pulse-echo testing of a typical test target on the median element. Since it is a median value, half the returning pulses will have a peak to-peak voltage greater than this value and half lesser. All received pulses must therefore be ordered by ascending amplitude [126].

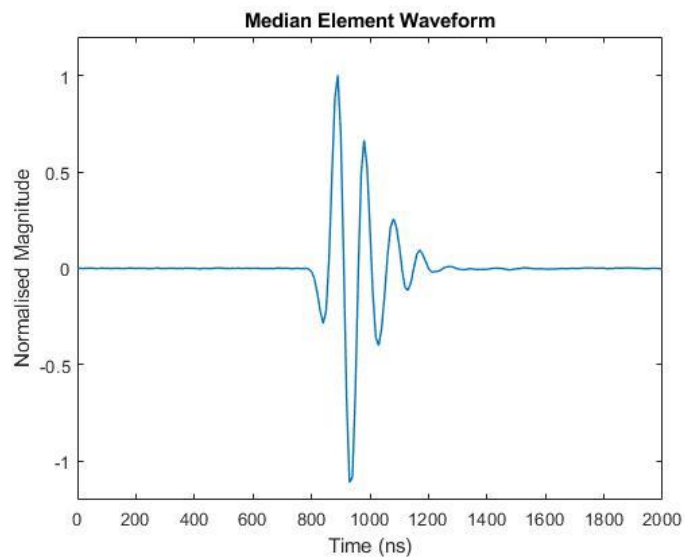


Figure 3.4. Example plot highlighting the calculation and presentation of the median waveform.

Medium Waveform Spectrum

This parameter is defined as the FFT of the median waveform. Only the positive real-valued part of this transform is displayed, giving information on the spectral content within the pulse. A range of zero MHz to twice the transducer's nominal frequency is commonly used [126].

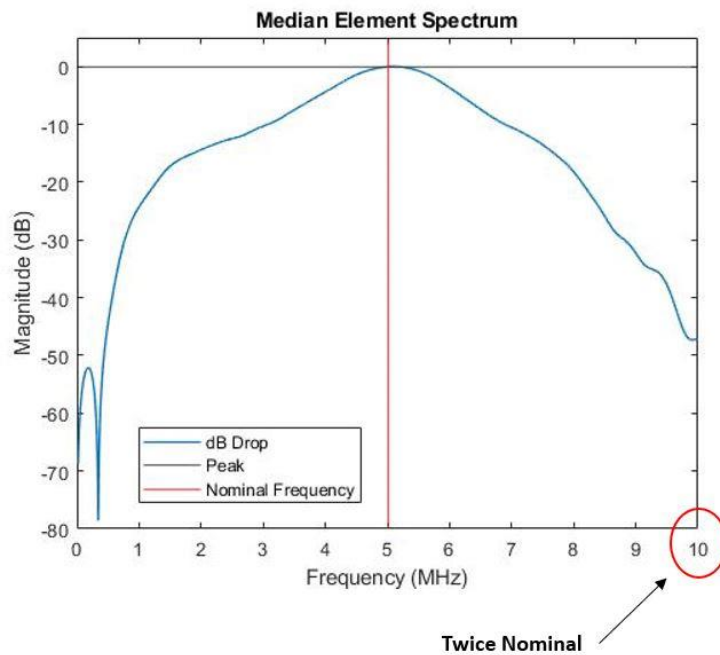


Figure 3.5. Example spectrum taken from the same example median waveform as in previous figure.

Centre Frequency

Whilst the medium waveform spectrum gives only one parameter for the entire array, the centre frequency is calculated for each element. There are two definitions of the centre frequency using the positive, real-valued part of the FT. Firstly, the point on the frequency axis when the spectrum has a maximum amplitude. The value used in most standards documents is, however, defined as the -6 dB centre frequency and found from the mid-point of -6 dB decay either side of the amplitude peak. This considers the fact that the waveform will not decay equally either side of its peak value.

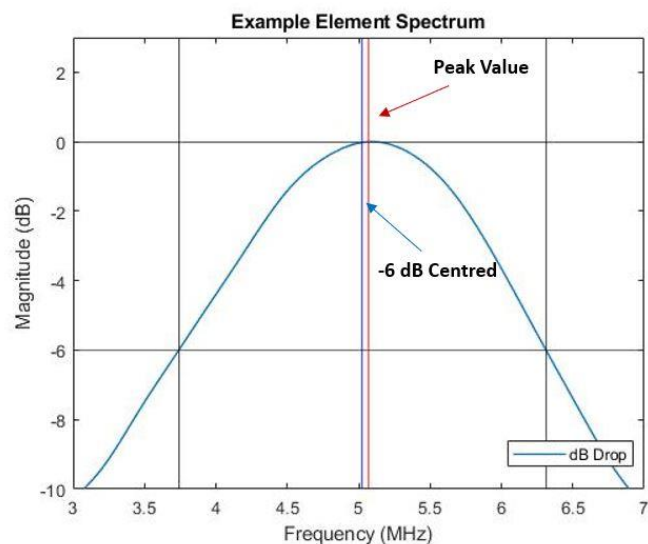


Figure 3.6. Example spectrum displaying the two separate definition of the centre frequency.

Bandwidth

A measure how quickly the amplitude of the FT decays either side of the peak frequency. This value is determined by using the length of a line intersecting a given element's spectrum at the -6 dB level. Bandwidth is expressed as a percentage of the centre frequency with an average value across all elements also displayed.

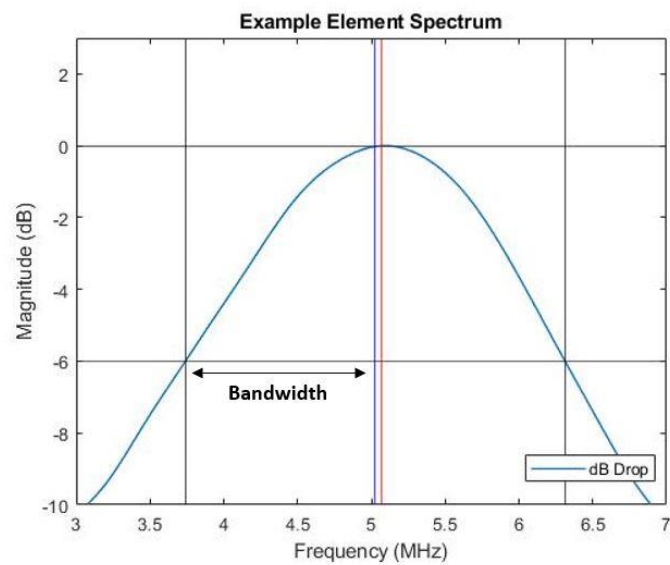


Figure 3.7. Bandwidth calculation using the same example spectrum.

Pulse Width

This parameter is calculated in the time domain and gives the length, usually in nanoseconds of a returning pulse from a calibration target. Pulse width is expressed as either the -20, -30 or even -40 dB level, for every element and as an average across the array.

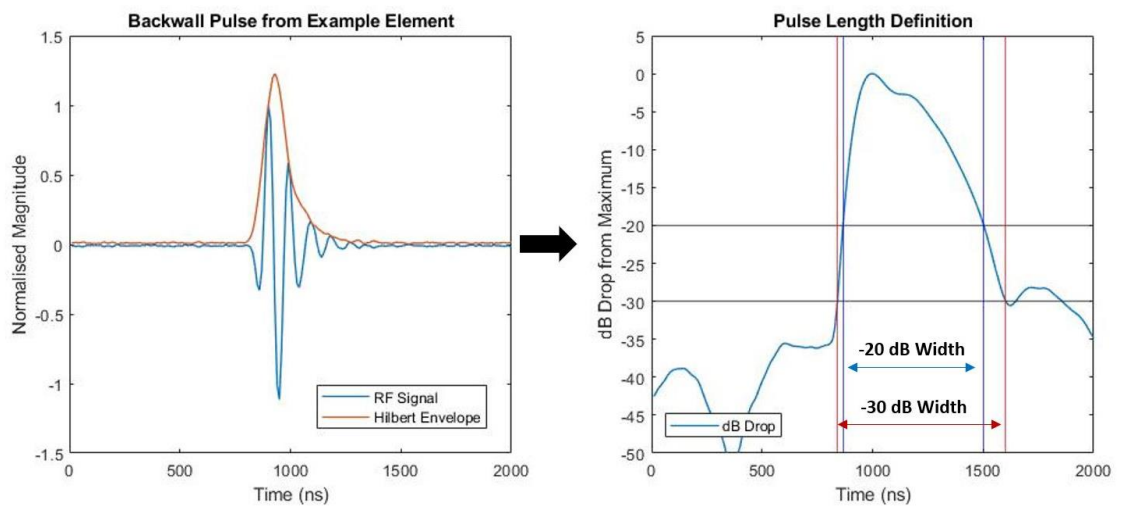


Figure 3.8. Waveform plot with various dB levels to define the pulse width.

Sensitivity

The peak-to-peak sensitivity represents the sensitivity of the individual transducers. The ratio between the magnitude of the excitation pulse, sent to each element, and the peak-to-peak voltage of the pulse-echo return from a suitable test target is used. The value is then -20 multiplied by the log of the ratio of these two values giving both individual element sensitivities as well as an average value.

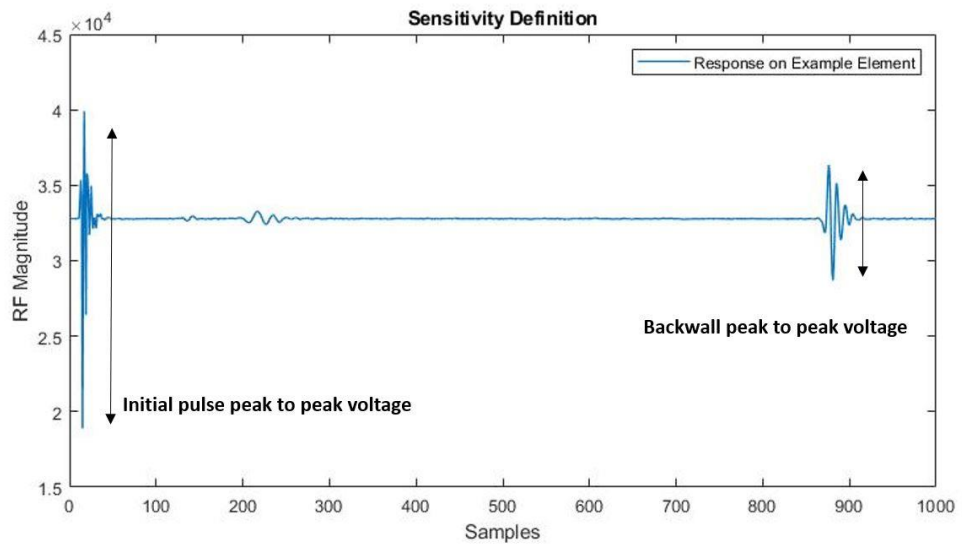


Figure 3.9. Graphic highlighting the sensitivity definition.

Crosstalk

Crosstalk is a measure of how effectively the individual elements are isolated from each other. The proximity of the piezoelectrics, and their associated electrical connections, can cause capacitive effects as well as the transmission of vibrational modes whilst transducers are firing [127]. For each element, the response to the initial ‘big bang’, the electrical impulse triggering the transducer, is measured on the 1st adjacent and 2nd adjacent element. These data are extracted from the off-diagonals of the FMC matrix, expressed as a dB drop compared to the peak-to-peak size of the initial pulse, and presented for each element as well as an array-average.

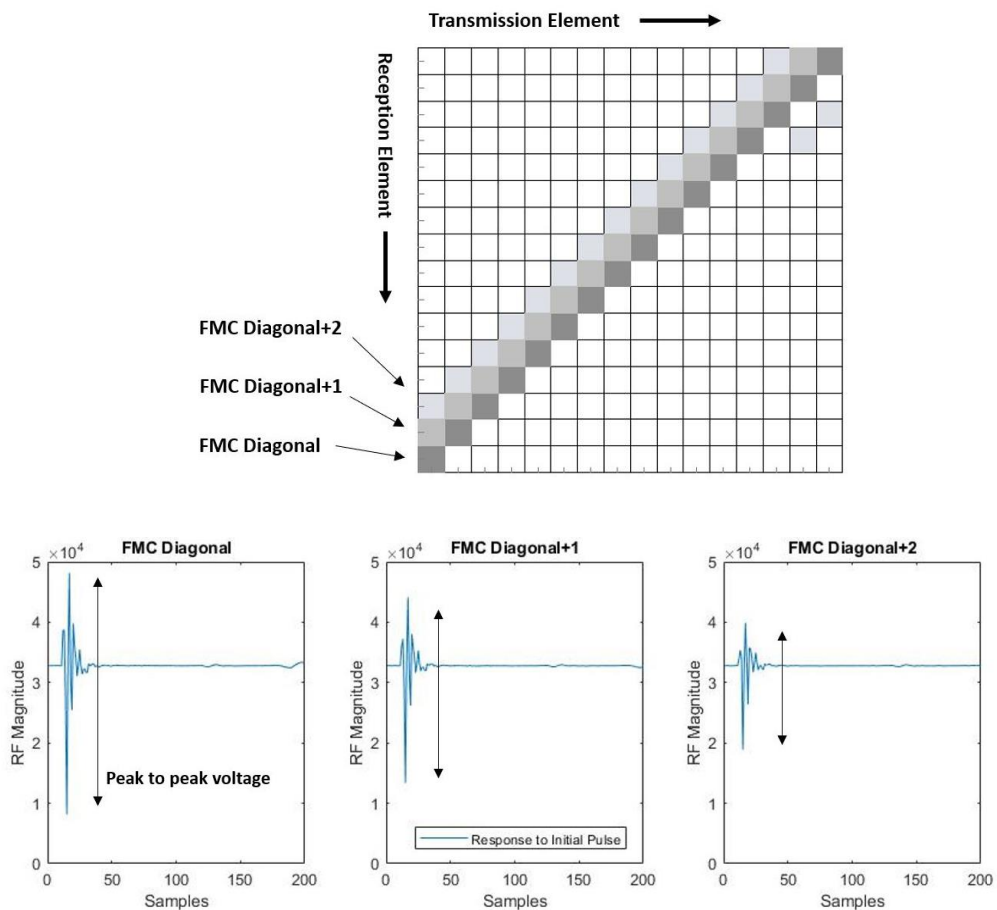


Figure 3.10. Graphic highlighting the definition of element crosstalk taken from first and second off-diagonals in the calibration FMC matrix.

Hardware Delays

This section is the most mathematically complex and can be used separately from the characterisation described by the previous parameters. Initially, the speed of sound is taken using the first and second backwall reflections. The calibration theory is then based on FMC data with time delay errors taken to be the difference between an empirical and theoretical value. For the FMC diagonals, the time between front wall and back wall reflection, for each element and adjacent element, can be extracted. The total error is assumed to be the sum of the error on reception by the same element, transmitting on element $T_x = n$ and receiving on element $R_x = n$, and reception on the adjacent one, transmitting on element $T_x = n$ and receiving on element $R_x = n + 1$. A theoretical time delay, based on the geometry and speed of sound in the material, is then subtracted from this total error to leave only the delays from the associated hardware. Necessary equations and a full mathematical description are reported in section 2.5 of the published work as well as Chapter 3 of the lead author's thesis [123][124].

3.2.2.4 Olympus Wheel Probe Phased Array

Since TFM imaging is not used for the practical work described here, only the array characterisation parameters are given for this array. Data is acquired from the described calibration block and performed before the probe is used for CFRP inspection. Hardware can be seen in the image given in Figure 3.11. Figure 3.12 shows the output datasheet from a Olympus 5 MHz 64-element phased array, used for most of this work. Table 3.3 shows the same characterisation in table form.



Figure 3.11. Phased array characterisation hardware

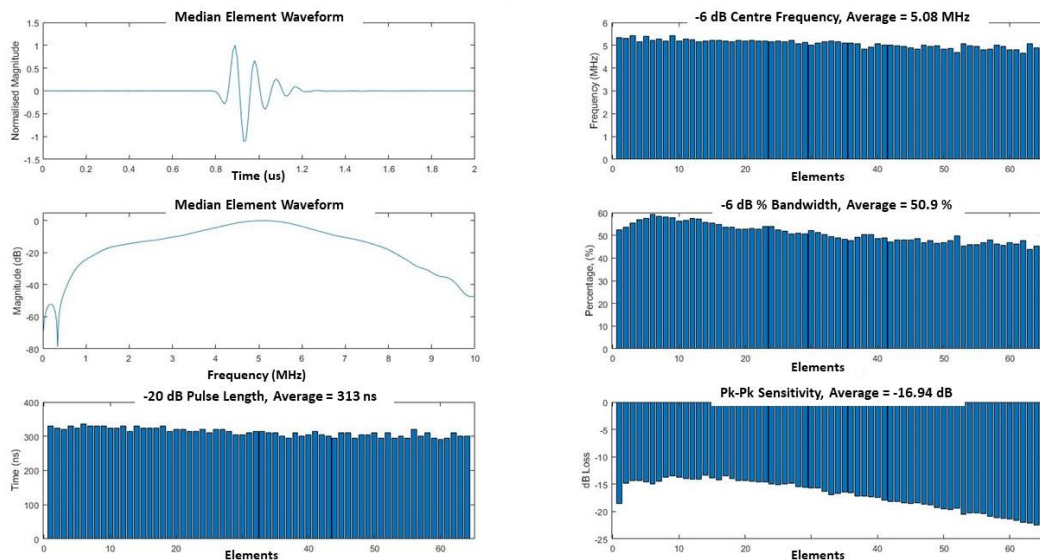


Figure 3.12. Output datasheet for an Olympus 64-element, 5 MHz probe

Parameter	Value			
	Average	Max	Min	Standard Deviation
Pulse Length -20 dB (ns)	313	335	290	12
Pulse Length -30 dB (ns)	415	585	345	78
Centre Frequency (MHz)	5.08	5.44	4.64	0.17
Bandwidth (%)	50.9	43.9	59.3	4.1%
Sensitivity (dB)	-16.9	-22.4	-13.4	2.7
Crosstalk (adjacent) (dB)	-5.1	-3.7	-11.3	4.4
Crosstalk (2nd adjacent) (dB)	-7.1	-3.4	-13.0	4.7

Table 3.3. All output data from phased array characterisation tool in table form. Olympus 64-element, 5 MHz probe.

3.2.2.5 Summary

This section has introduced a phased array characterisation tool, explained the parameters under investigation and presented the results when applied to the Olympus 5 MHz wheel probe phased array, used throughout research reported on in this thesis. The information supplied in the manufacturer's datasheet has been confirmed, in terms on centre frequency, pulse, length, sensitivity etc, as has the satisfactory performance of all elements on the array. This is valuable as it allows for both comparison between arrays as well as a form of performance-monitoring over time or extensive use.

3.2.3 Data Processing

3.2.3.1 Introduction

Raw data is in the form 3D matrix. This is formed of the array axis, scanning axis and number of samples. For each scanning position and array aperture, the ultrasonic pulse echo response is recorded as an RF A-scan. This is in the form of a 8-bit, time series, encoded with the robot's position at time of acquisition. Data presentation can thereby be referred to the physical inspection environment, defect identification and localisation performed in terms of the robotic coordinate system.

As is often the case, the envelope is calculated by means of the Hilbert transform [128]. Scans can be contrast stretched so that each A-scan has normalised values to span a range of 0-1. Any saturated points then show up as ones. A Savitzky-Golay Filter (SGF), is a method of curve fitting to smooth the data and remove noise. This filter applies a polynomial of chosen order to a specific window size, a subsection of points on each A-scan. In the cases where this is used, a polynomial of order two, cubic, is fitted to every 11 individual data points. All these post-processing operations are optional, depending on their necessity to resolve images and identify defects.

In addition to examples of A and B-scans from defective panels, several different C-scan modalities are presented. The method by which these are generated from each A-scan can be visualised in Figure 3.13. An amplitude C-scan uses the maximum value taken within a specific depth on each A-scan. The corresponding ToF C-scan is a plot of the location of this value, converted to a depth using the sample frequency and bulk velocity, and allowing the location of defects to be identified. In addition to

these, two other imaging methodologies are also generated. Either using their known location or by detection of first and last major peaks in each scan, the front and back wall signals are identified. Both the 'damage echo image' and 'back wall amplitude image' are based on the location of these [76]. The back wall amplitude image is a C-scan with the gate adjusted to span only the back wall region. The damage echo image removes front and back wall peaks and images only the signals received from the internal section of the composite. This is effectively like an amplitude C-scan but the gate spans the whole interior section of the sample. This can be done either by simply truncating the scan, by say 1 mm either side of the front and backwall, or by subtracting a known reference signal of a clean section of sample from each A-scan. The first method is very effective for defects within the central section of the material but suffers since signals corresponding to defects close to either surface may also be removed. If there is any superposition of backwall with flaw signal then this will not be picked up and the defect not found [89]. The second method is therefore preferable, but it is not without issue since the reference echo is formed from the average of many A-scans and therefore may not be perfectly suited in terms of amplitude, phase, or spectral content for that specific location. Subtraction, therefore, often leaves a small feature which can still eclipse the size of any flaw signal within the sample. In a damage echo image, there is no way of determining the depth of defects. The corresponding ToF image would then need to be used for this purpose.

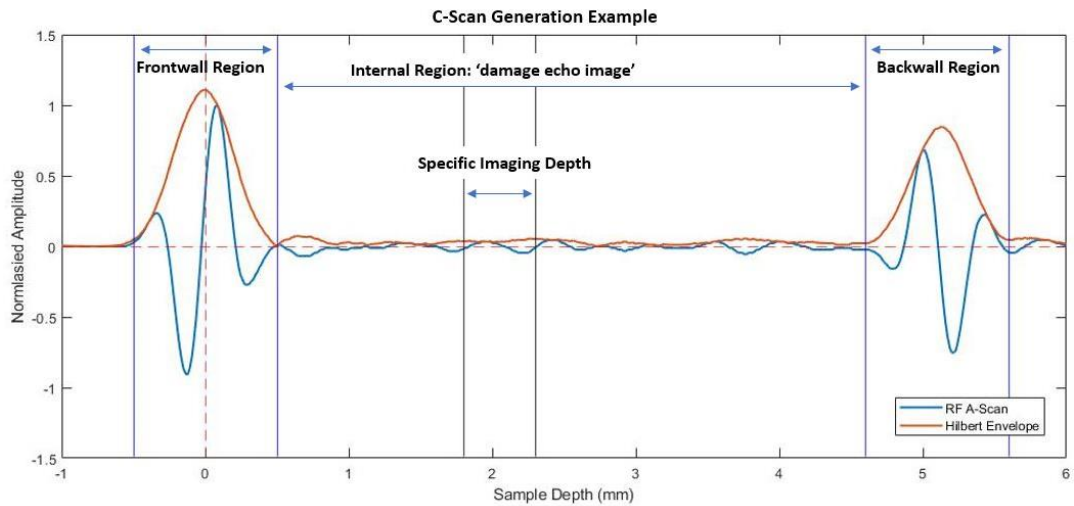


Figure 3.13. Example A-scan highlighting which region is used for each type of C-scan.

Examples of these data presentation methods are shown for a defect-free CFRP panel, those with artificial defects and finally several rejected parts from the manufacturing procedure in section 3.4.1, section 3.4.2 and section 3.4.3. Summary tables of defect sizing are also presented in the same sections. All scan types for every sample would result in far too many individual figures with a high level of repeated images and redundancy in the data. The data presented are aimed to show the range of scans and effectiveness of the inspection method.

3.2.3.2 Defect Sizing

The -6 dB drop technique is a common tool in ultrasound inspection for feature sizing [129]. The size of a defect is defined using the spatial points where the amplitude has dropped past the -6 dB (50%) point, as compared to the maximum defect response amplitude [130][131]. However, the flaw response in the real world is far from an ideal Gaussian bell meaning this technique can sometimes undersize a defect [132]. Depending on application, or probe frequency, a -12 dB or -6 dB drop method may be the most appropriate [132]. Defect sizing reported in these results uses the -6 dB method since the flaw response tends to be clear and have adequate SNR with the background noise, from the composites' internal structure, comparatively low.

3.2.3.3 Gating Procedure

To account for delay line variations, raw A-scans are corrected to remove variation in front wall position. Within the first 20 % of the acquisition length, the maximum value and location of the Hilbert envelope is located. This is taken to be the zero point of sample depth and every individual A-scan is time-shifted so that these peaks coincide. The corrected A-scan is trimmed to allow for a total imaging depth of 6 mm. The effects of coupling variation, insufficient tyre compression or slight surface irregularities are thereby removed. This procedure is exemplified in Figure 3.14.

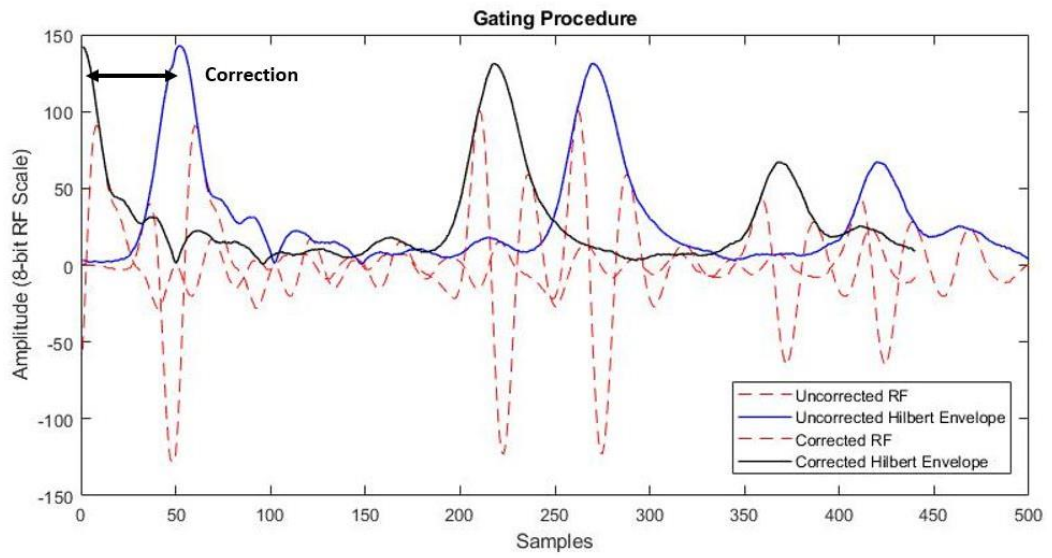


Figure 3.14. Example RF and corrected A-scans demonstrating the gating procedure.

3.2.4 Ultrasonic NDT Modelling

3.2.4.1 Introduction

Modern manufacturing techniques, and the composite materials used in a wide range of industries, are becoming increasingly complex. Reliable computer modelling is essential when analysing the effectiveness of a given NDT inspection scenario. These models aid in the design, validation, and implementation stages. Entire procedures can be simulated by modelling the generation, propagation, and interaction of ultrasonic waves with a test specimen [133]. Probability of Detection (PoD) curves are a common way of establishing the limits of a given inspection and there is a now a trend toward using ones generated using simulation software [134]. Broadly speaking, the process of modelling an ultrasonic composite inspection can be split into three parts [135][70]:

1. A model of the source is used to simulate a realistic pulse of ultrasound. The input signal is often simplified to a pressure load.
2. A layer model to allow the stacking of multiple plies for determination of its impulse response to normal-incidence ultrasound.
3. Material properties of constituents used in the composite layup need to be determined so that the equivalent ones of the final one can be found.

The source of the load or input signal in a model is usually the ultrasonic transducer. These are often represented mathematically using the Huygens principle. The surface is treated as a series of point or line sources, the waves spreading out radially from each. Every infinitesimal point of the wave front can then be viewed as another point

source and thus the propagation mapped. Using this principle, the focussing ability and beam spread of the sound can be analysed. Sound propagation through any structure can be considered as a transfer function affecting all the frequency components of the input signal. One needs to consider: the output source, attenuation, beam-spread, time-delay, reflection, and transmission of any features encountered and the transmission and reception characteristics of the transducers. All these can then be combined to form the basis for ultrasonic wave modelling [135]. Reflection and transmission coefficients in complex exponentials form allow for this to be applied many times and thus the response from a multi-layered, composite structure analysed [136].

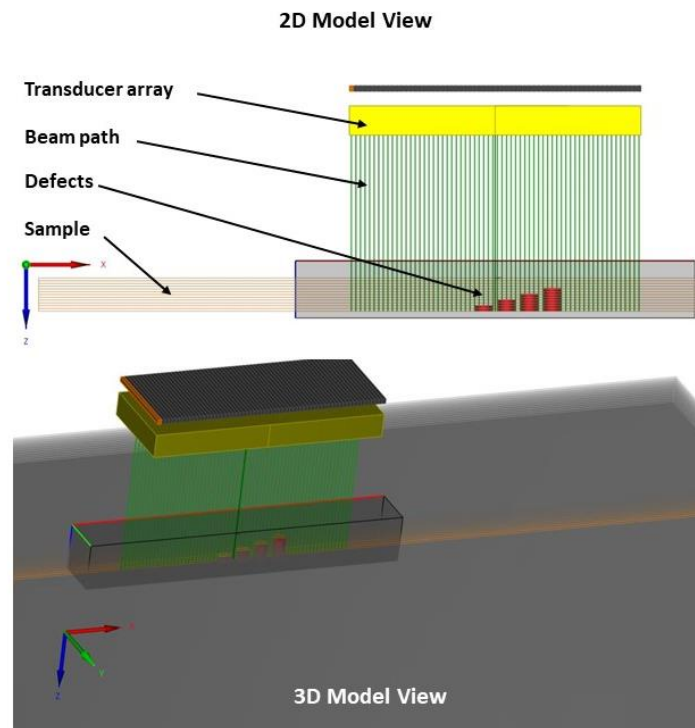
The third step concerns the material properties. A composite material is formed of two materials with different properties to form a new one with the desired ones. The inhomogeneities in composites create frequency dependent effects to the ultrasound propagation which need to be considered when the incident wave is not modelled merely as a pressure wave.

There are a multitude of different possible modelling techniques: numerical, analytical, ray tracing, boundary element, finite difference, element, and integration models. There are advantages and disadvantages in terms of computing power, accuracy and relevance to a given inspection techniques. Hybrid models can be used to minimize the drawbacks of each distinct model type.

3.2.4.2 CIVA

Throughout this research the CIVA software package is used. This is based on a combination of ray tracing and FEM analysis. A range of different samples, transducer arrays and firing sequences can be generated in the model with CIVA accurately modelling sample geometry, parameters of a composite material's constituent parts, and the interaction of such a material with an ultrasonic phased array transducer.

The version used for this work includes the optional FIDEL add-on for inspection simulation of composite materials [137]. This allows the user to insert specific parameters such as, fibre density, thickness as well as resin density and speed of sound, before performing a sample homogenization. Homogenization starts at the ply level, before considering the number of layers and their orientation. This stage is simplified for a pultruded CRRP sample, as studied here. It is in effect one, much thicker, unidirectional ply. Figure 3.15 shows screenshots of the model defined in the CIVA environment alongside examples of the probe configuration and composite material windows.



Phased array and composite material definition within CIVA

Probe Id: 1 Transmission/Reception

Operating mode: 1 Transmission/Reception

Probe type: Immersion

Crystal shape: Focusing Signal Case

Crystal shape: Pattern Linear phased array

Phased array Whole aperture

Incident dimension: 51.1 mm

Elevation: 20 mm

Grid and gap

Number of elements: 64

Gap between elements: 0.1 mm

Dimensions of elements

Element width: 0.7 mm

100% 0° 90° Top Bottom

Specimen

File

Geometry Material Additional components

- Volume #1 Laminated composite
 - Ply :: Single ply composite
 - Fiber :: Transversely isotropic
 - Matrix :: Isotropic

Name Carbon Fibre

Type Laminated composite

Layer-level homogenization

Description Homogenized

Name	Thickness (mm)	Angle /Z (deg)
Ply n° 0	0.483	0
Ply n° 1	0.483	0
Ply n° 2	0.483	0
Ply n° 3	0.483	0
Ply n° 4	0.483	0
Ply n° 5	0.483	0

Algorithm HLS

Slowness surfaces

2D curves

Figure 3.15. Example of CIVA model view as well as ultrasonic phased array probe composite material parametrisation.

It is thereby possible to generate data from a simulation of any experimental set-up and phased array operational mode used in this as well as subsequent chapters. Results are beneficial in understanding the underlying principles and compared to those obtained from experimental data.

3.2.4.3 CIVA Modelling of this Set-Up

Artificial datasets are produced using CIVA simulations are obtained from a model based on the experimental set-up described in the Chapter 3, Section 3.3. Defects of various sizes, within a composites sample, can be added in this model. CIVA then produces a dataset free of noise or sample defects. These data can be exported for post-processing to account for the effects of probe speed and varying PRF values on the producible C-scans. Background and signal noise can be added at chosen magnitudes and distributions to simulate coupling inconsistencies or other experimental errors which cannot be computer modelled. This work serves as a useful insight into the factors to consider before experimental inspections are carried out. Key simulation parameters used are detailed in Table 3.4.

Parameter	Value
Calculation Type	3D
Longitudinal-Wave	Considered
Shear-Wave	Not Considered
Inspection Type	Direct
Probe	5 MHz, Phased Array, Immersion

Table 3.4. Simulation parameters used to produce simulated data using CIVA.

3.3 Practical Set-Up

This section introduces the basic components of the initial inspection set-up, justifies their use, and details underlying principles. KUKA robots manipulate an Olympus phased array wheel probe as a tool and incorporate a Force-Torque (FT) sensor. Using a PEAK LTPA Phased Array Controller (PAC), high-speed data acquisition with specifically tailored focal laws, is achieved. Hardware is interfaced using NI LabVIEW with image reconstruction, analysis, and defect characterisation performed either in MATLAB as post-processing or within the LabVIEW environment. Main components of the set-up can be visualised in Figure 3.17 with a section of CFRP sample also shown. Figure 3.16 gives a system diagram illustrating the connections between hardware components, described in sections 3.3.1 to 3.3.4. This is shown alongside an image of the experimental set-up.

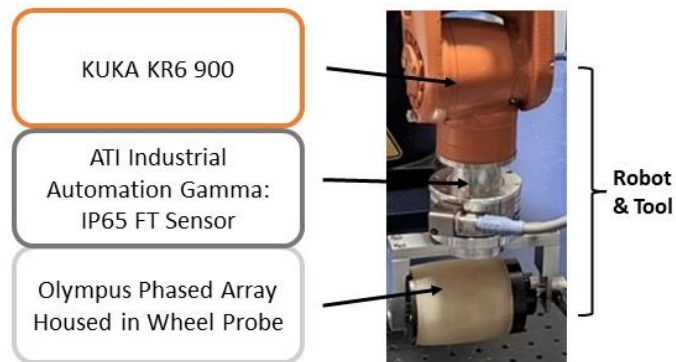
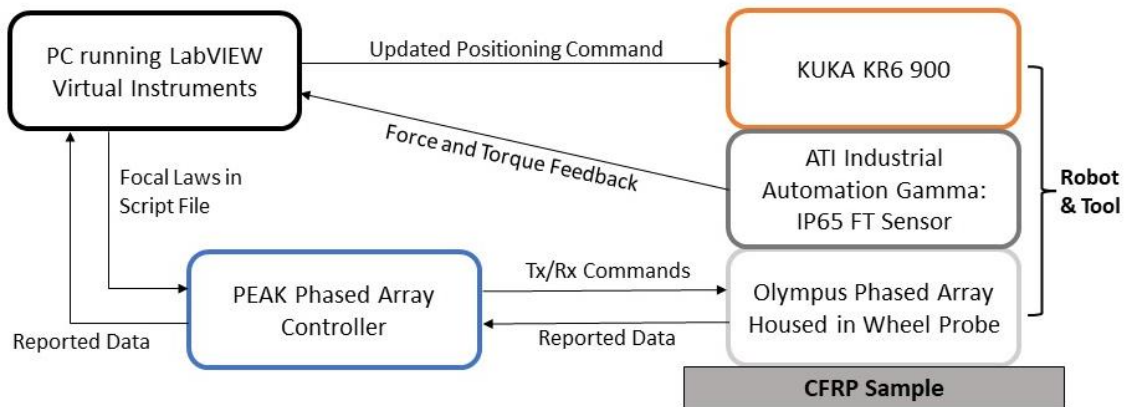


Figure 3.16. System block diagram illustrating the connections between each of the practical component referred to an image of the experimental set-up.

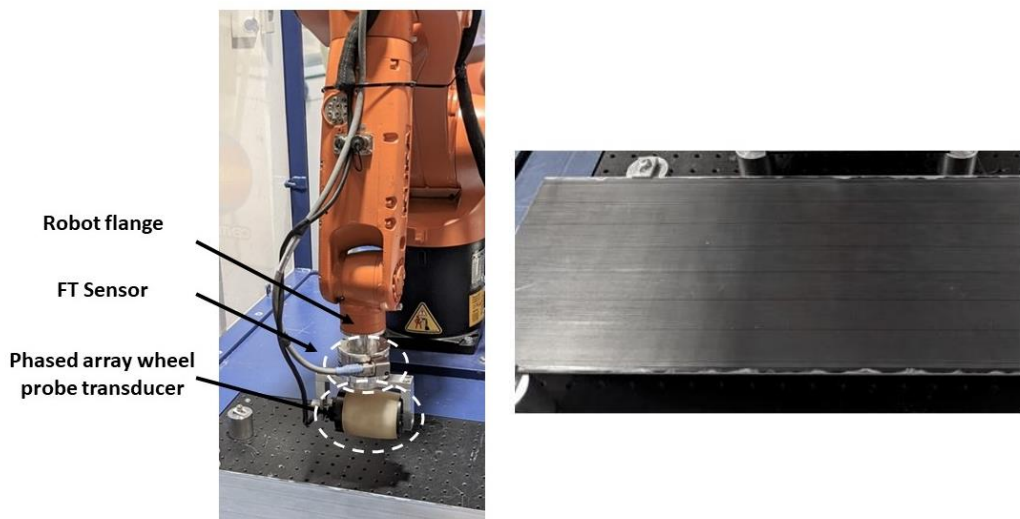


Figure 3.17. Images of the probe and associated hardware attached to the KR6 robot flange. The second image shows a clean section of the pultruded sample

3.3.1 KUKA Robotics and Force-Torque Sensor

A KUKA 6-axis robot is used to generate and execute the desired inspection path. Movement of the tool, in all six degrees of freedom is facilitated either through the KUKA user interface or LabVIEW-based control. Scanning paths are computed and executed using a KUKA KR6 R900 with a maximum load and reach of 6.7 kg and 900 mm respectively. Using robotics, the tool home position and scan start position can be chosen and programs controlling the motion, for different tools, home positions and scan path parameters can be edited offline. A KR6 allows for the high speeds, up to 2 ms^{-1} , required when investigating the limits of scanning speed phased array operation. Industrial robots are equipped with position and velocity sensors to allow them to follow programmed paths [61]. The FT sensor, model: ATI Industrial Automation Gamma IP65, allows the system to react to external influences, vital for robots when used in industrial applications. For example, a desired force on an object can be maintained during motion [138]. Ethernet connections are used since real-time communications are required to update the robot position based on live FT feedback. The FT allows for a chosen force to be exerted in a certain axis and this to be maintained as the programmed path is carried out. Such an application is known as 'sensor-guided' and allows for reliable coupling between a transducer wheel probe and sample under ultrasonic inspection as in [56]. For instance, 30 N can be consistently applied as the scan progresses. The z-position of the robot updated based on the force-torque reading fed back into the Robot Sensor Interface (RSI) and any variations in sample height, or errors in robot path, compensated for. The pressure applied to the sample is monitored and robot positioning takes place in increments of

4 ms, based on user-determined limits and set-points of force and torque. Alongside this, visualisation and analysis of the measured force and torques in real time is achieved through the KUKA developed RSI. Images of both robot and FT sensor utilised are shown in Figure 3.18.

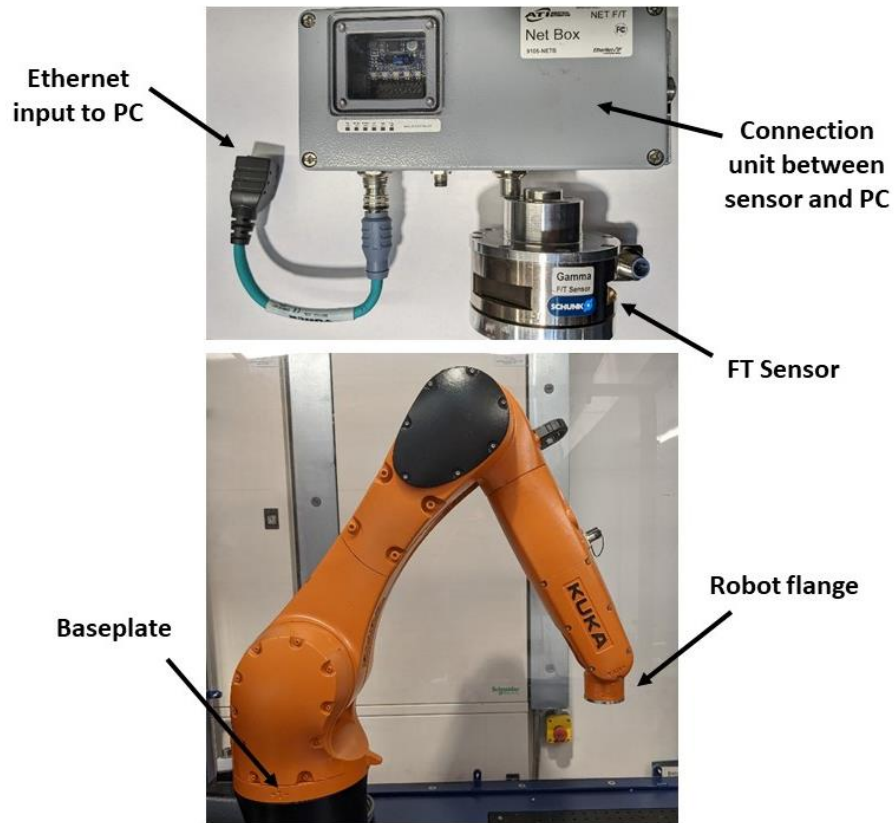


Figure 3.18. Example images of KUKA KR6 robot and Shunk FT sensor used throughout.

3.3.2 Olympus Phased Array Wheel Probe

For this body of work, PAUT is carried out using an Olympus 5 MHz, 64-element array housed within an impedance-matched, water-filled, rubber tyre. The phased array transducer housed within has element width and height of 0.7 and 10.0 mm respectively. The 0.8 mm pitch gives a 0.1 mm gap and 64 elements, permit a maximum coverage of 51.2 mm. Components of this wheel probe can be seen in Figure 3.19, and with the device full assembled shown in Figure 3.20.

Such a transducer configuration has significant advantages over a more traditional liquid coupling inspection which can lead to inaccurate part positioning due to the stand-off variability [56]. Even if these are negated, it can be challenging to maintain constant coupling, free from bubbles or turbulence. A wheel probe inspection set up can overcome rough sample surfaces and inconsistent coupling. It also removes the need for pumping equipment or tanks and the risk of water ingress, which can impact the part's performance in terms of fatigue strength and compromise the bond strength in joints [56]. Despite this, one of the drawbacks are the high attenuation and spectral filtering properties of the rubber polymer, used for the wheel's tyre. Reducing the frequency or averaging over a greater transmission aperture have been reported to reduce attenuation as well as the impact of the frequency downshift observed during polymer-transmission [139]. However, such approaches can compromise both resolution and acquisition rate. One successful solution reported is the application of Golay-coded excitation to increase SNR, when such probes are used for FMC and TFM imaging [139].

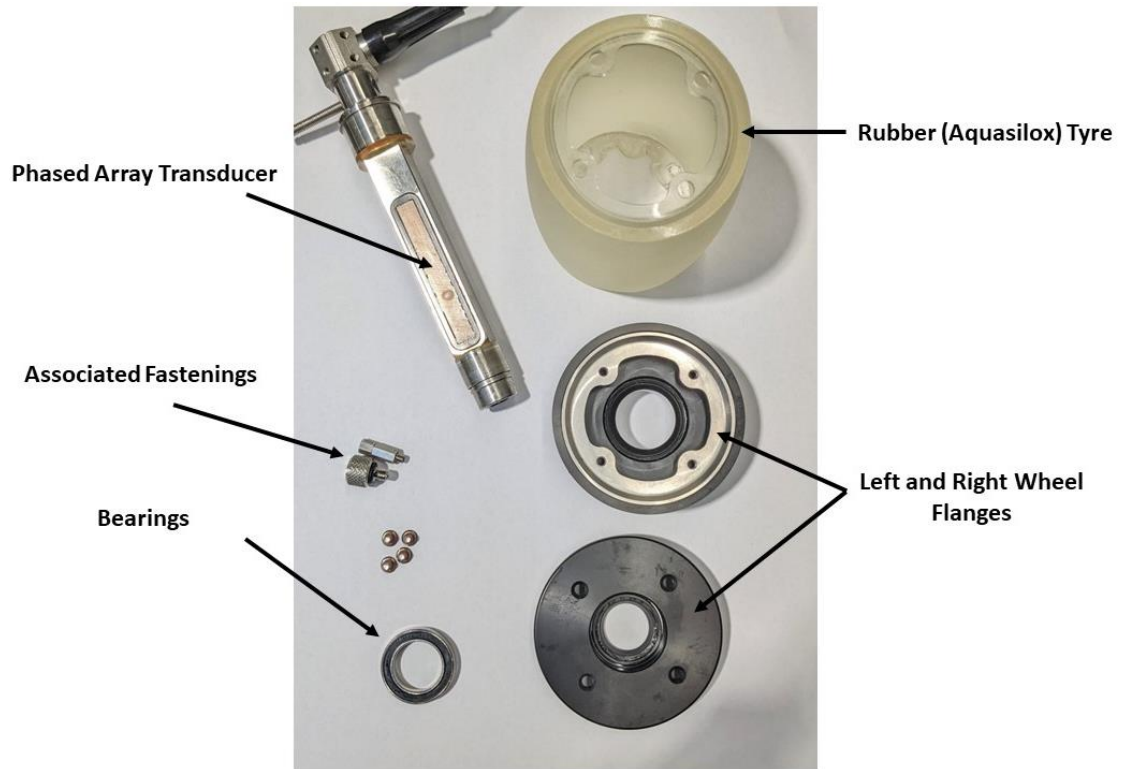


Figure 3.19. Labelled image of disassembled phased array ultrasonic wheel probe.

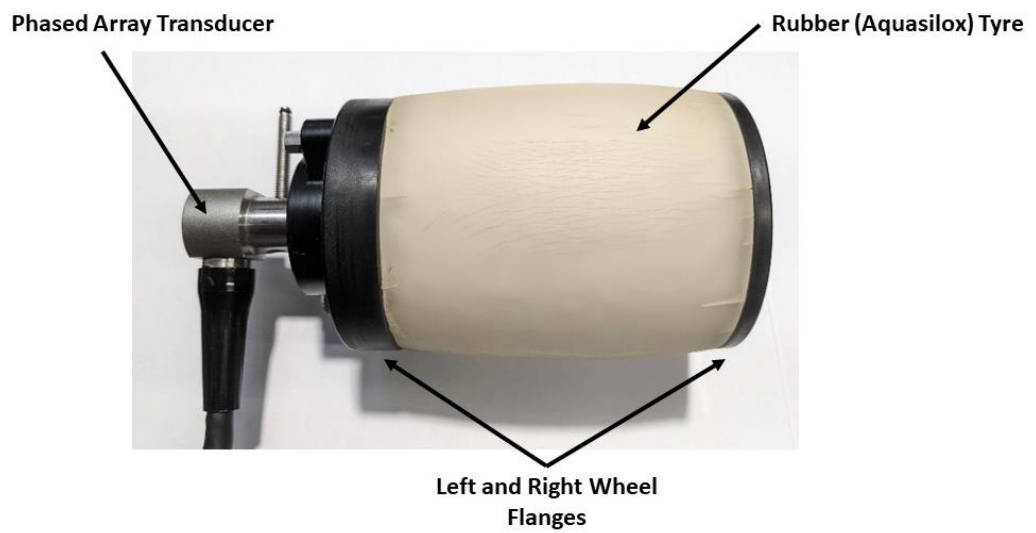


Figure 3.20. Image of the fully assembled wheel probe.

3.3.3 Phased Array Data Acquisition

Various phased array controllers are available to purchase commercially. One example is the LTPA, manufactured by Peak NDT and shown in Figure 3.21, supporting 64 channels on both transmit and receive and data acquisition rates of up to 120 MB/s using high-speed ethernet connections [125]. The device allows for in-situ monitoring, and has high data output, therefore making it ideal for this application. Since the end goal of the research is to incorporate a NDT set-up into the SGRE production line, it makes sense, from the outset, to use only equipment commercially available and not that exclusively for research purposes. Initially, this is limited to a maximum PRF of 20 kHz, shown to be more than adequate for the imaging resolution and scanning speeds required. However, with a custom firmware update, these can be increased to the 55 kHz to potentially facilitate much higher values. Focal laws are written with a software called ArrayGen and communicated to the LTPA using NI LabVIEW.



Figure 3.21. Examples of PAC units as manufactured by PEAK NDT.

As explained in section 3.2.1.3, the delay line length limits the maximum PRF. In this inspection, a given thickness of water will allow for a maximum sample thickness of twice this value. This is due to the bulk velocity in CFRP being roughly twice that in water. 3070 ms^{-1} and 1480 ms^{-1} respectively. Since the wheel probe has a 25 mm delay line, up to 50 mm of sample could theoretically be inspected.

Allowing for a necessary gated acquisition window of 45-50 μs , calculated using the thicknesses and bulk velocities of the wheel probe, a maximum PRF of 18-20 kHz is possible. Higher values would require a shorter delay line and thus only a thinner sample could be inspected. Since the sample is planar and comparatively thin, there is potential in this work to increase scanning speed and utilise higher PRFs than would be possible with thicker, more complex samples. In example, since the panel has a thickness of 5.1 mm, a much shorter delay-line could be used. Using 3 mm of water, giving 6 mm maximum inspection thickness, permits a maximum PRF of 83 kHz, or 67 kHz if a 20 % time-gap between firing is included. Higher resolutions and higher scanning rates could then be achieved. In practice, this would require a custom designed probe and wedge along with a PAC firmware update but in theory of such an inspection set-up is feasible. As an aside, when considering this much shorter delay line, it is important to check the location of the near/far field transition for the transducer array.

3.3.4 LabVIEW Integration

All the components necessary for the inspection can be linked together in the NI LabVIEW environment. Script files defining the phased array focal laws can be exported to the LTPA via this environment and thus all the components in the practical set-up are integrated and communicate with each other through one platform. This allows for control of robot movement, data acquisition and initial processing along with any feedback loops to be carried out. Finalised imaging and data analysis, using MATLAB functions written for the application, can be executed in isolation, or linked to LabVIEW using the 'Mathscript' module. Figure 3.22 shows the front control panels of LabVIEW virtual instruments (VI) used for both robot motion control as well as phased array data acquisition.

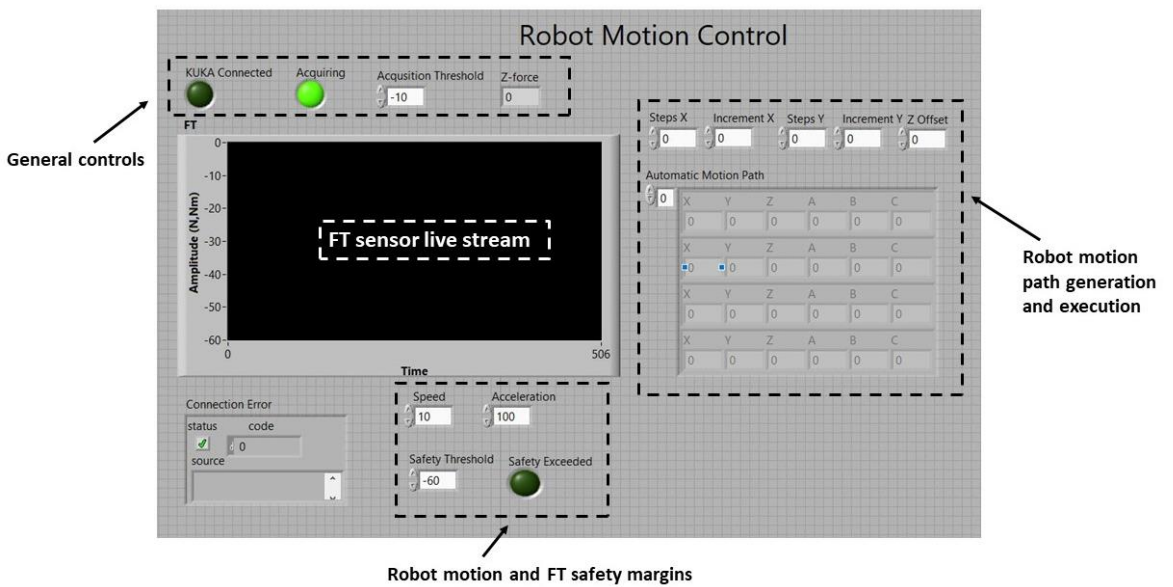
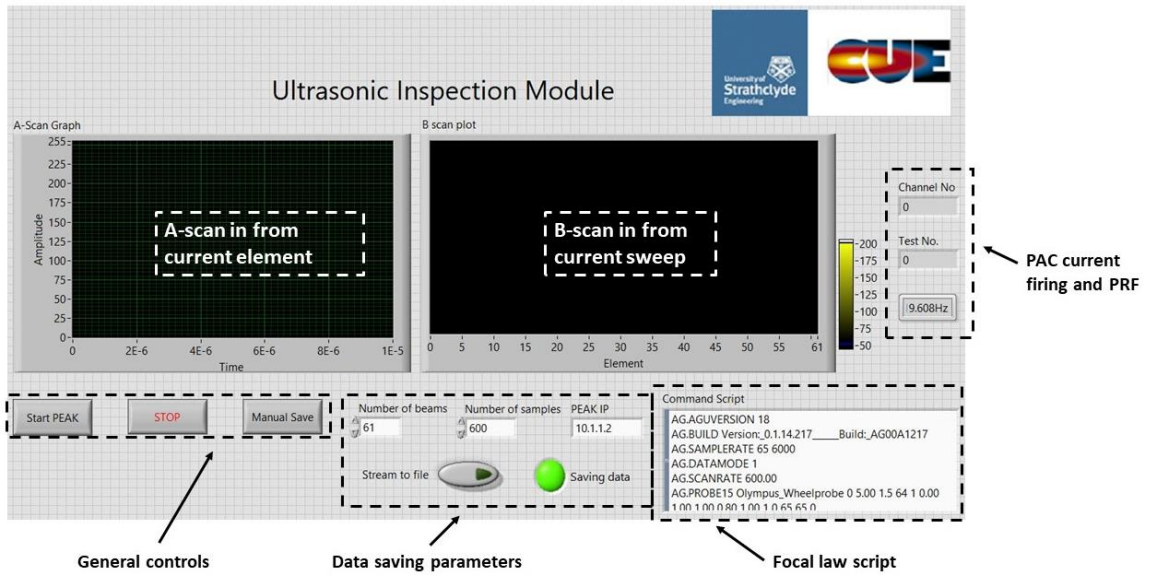

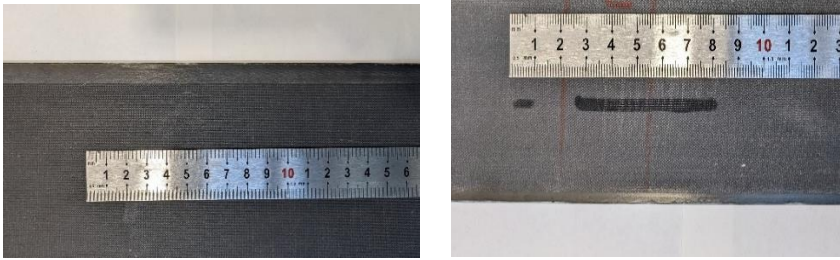


Figure 3.22. Annotated VI controls used for robot path execution and array control

3.3.5 Samples

3.3.5.1 Pultruded CFRP Panels

As described in Chapter 2, section 2.1.4, there is a necessity to inspect these blade subcomponents before they are incorporated into the glass fibre moulding process. Several defects and features which can be present in such pultruded panels are shown in Table 3.5. Images are taken from samples received from this projects' industrial partner, SGRE. Section 3.4 reports on the results of ultrasound inspection carried out on such panels before section 3.5 proposes an in-process inspection system, allowing ultrasonic NDT to be integrated into this CFRP uncoiling process.

Defect Type	Example Images
Fibre knots	
Delamination	<p data-bbox="675 1384 1262 1417">Not surface visible, UT inspection essential</p> 

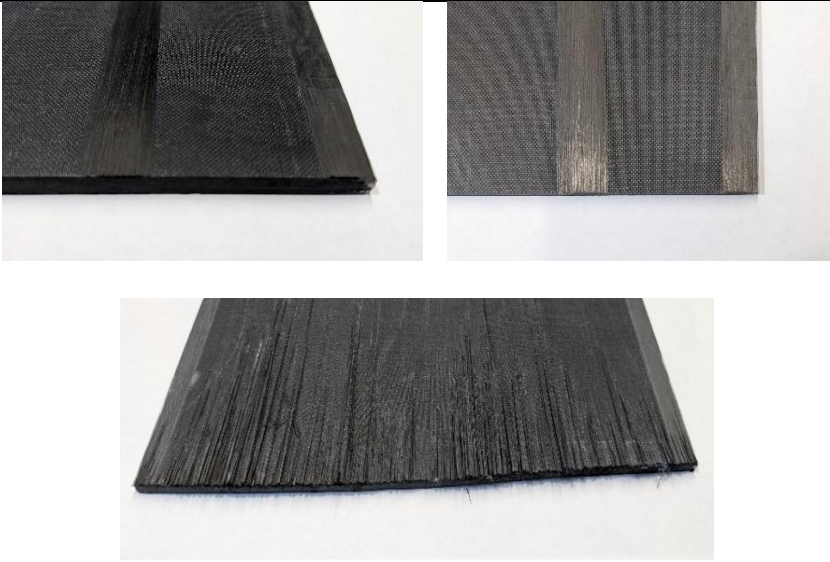
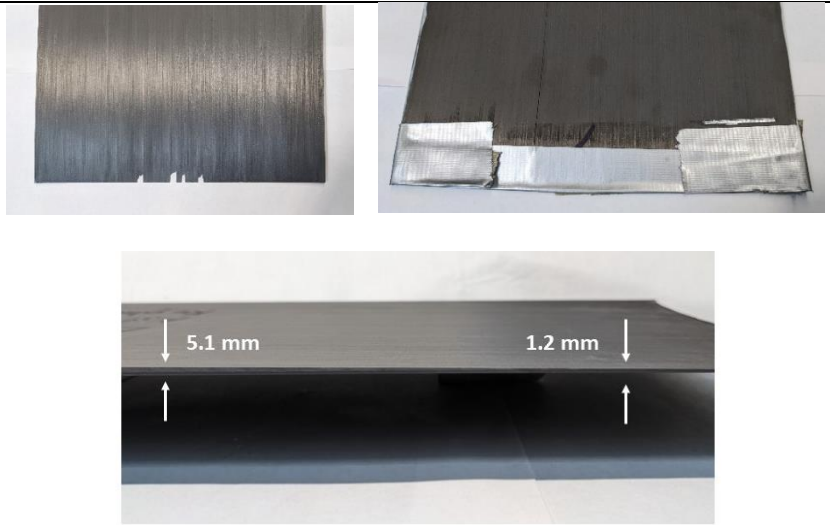
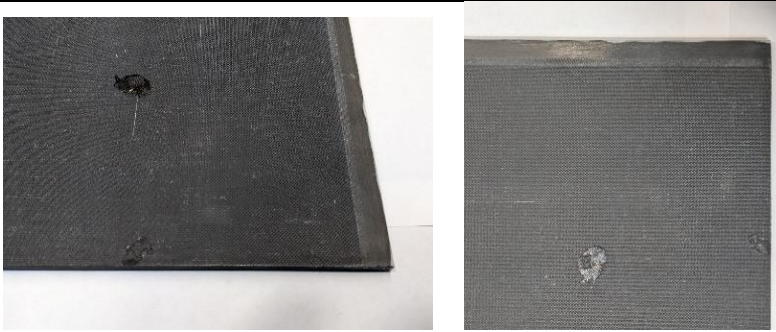
<p>Frayed Fibres</p>	
<p>Thickness Changes</p>	
<p>Resin Drop</p>	
<p>Resin Pool</p>	<p>Not surface visible, UT inspection essential</p>

Table 3.5. Potential defects within CFRP panels

3.3.5.2 Defect-free Samples

These samples are flat and planar with a thickness of 5.1 mm and ranging between 195.5 and 200.5 mm. Their length varies in the range of 500 to 1500 mm. The CFRP has FVFs values of 60-70 % and a fibre diameter of 0.007 mm, within an epoxy matrix. Several defect-free samples, shown in Figure 3.23, are used for initial inspections, for familiarization of the acquisition hardware and software.



Figure 3.23. Image of a defect-free pultruded CFRP sample

CFRP typically has bulk velocity around 3000 ms^{-1} across the fibres with values up to three times that, observed in the fibre direction [140][141]. Phased array approaches that utilise unfocussed sub-apertures, set to a few elements, are shown to yield high quality scan, both in previous works and in this research [55][119]. Within an isotropic material, metal alloy for example, each aperture would need to be focussed on a depth to prevent excessive beam-spread resulting in a low received SNR.

3.3.5.3 Artificial Defect Samples

It is also necessary to machine artificial defects into one of the undefective panels to test and optimise the imaging and defect detection methods applied. These are in the form of flat-bottomed holes and slots, of various diameters and depths, creating local variations in the panel thickness and changing the location of the backwall echo. Figure 3.24 and Figure 3.25 illustrate the layout and dimensions of these artificial defects and shows images of front and back-surface after machining.

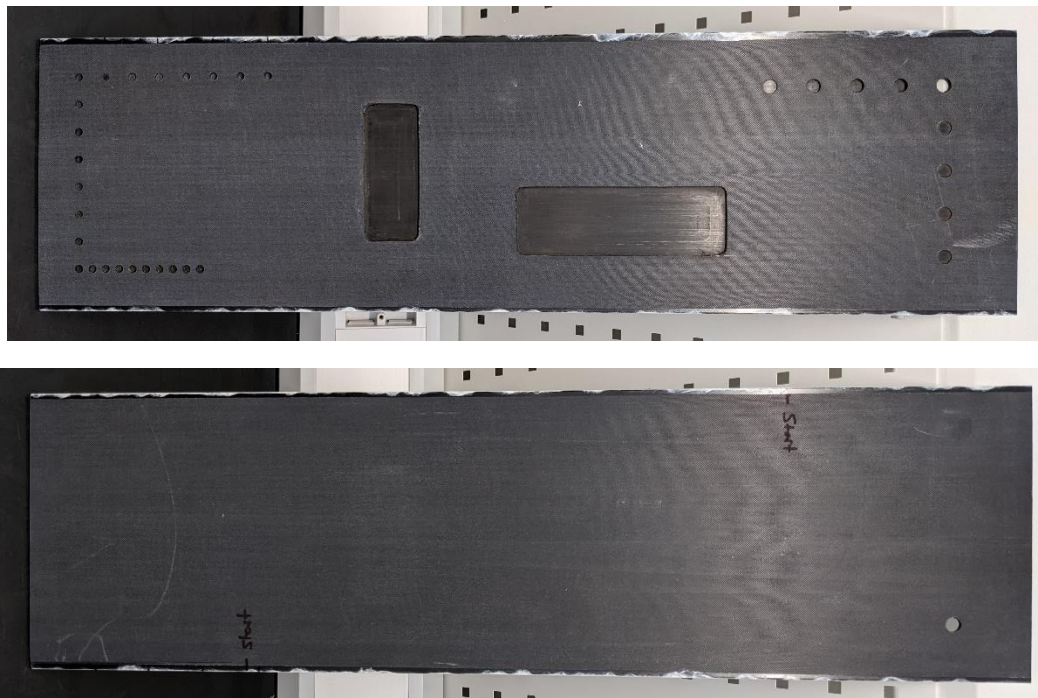


Figure 3.24. Images of a pultruded CFRP sample with artificial defects machined.

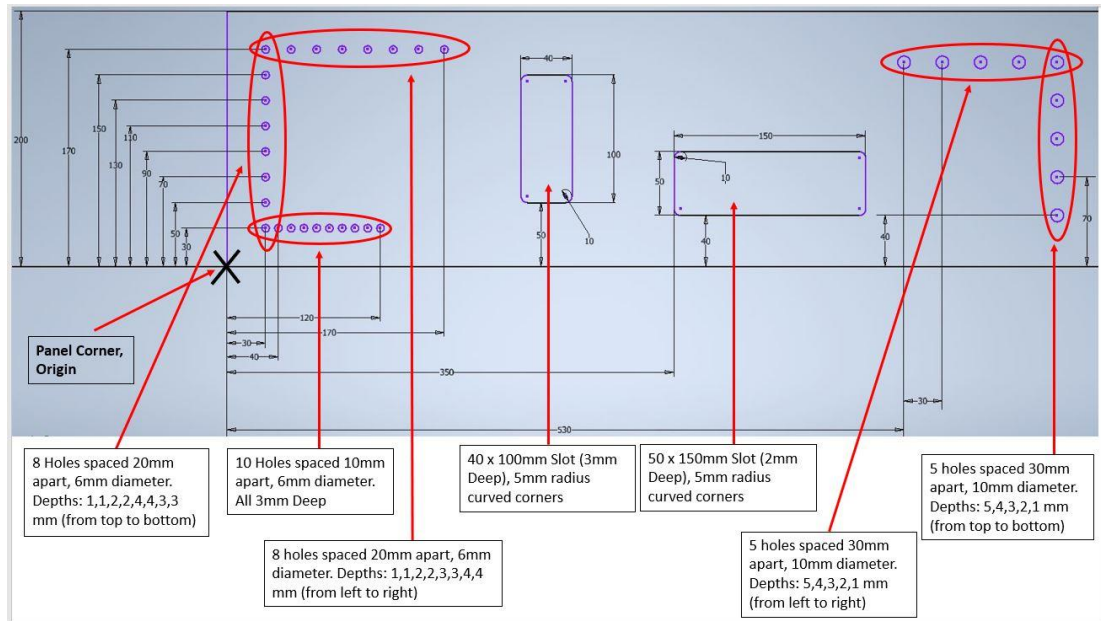


Figure 3.25. Dimensions and positions of artificial defects in CFRP panel.

3.3.5.4 Defective Samples

Five ‘real-world’ defective panels, rejected materials from the manufacturing environment, are also inspected. Initial visual inspection shows thickness changes, ply, fibre breakage and other anomalies pictured in Table 3.5. Such features can be viewed and characterised by ultrasound inspection, reported in the section 3.3.5.4. The potential presence of internal defects, delaminations and resin pools, make UT inspection essential. Figure 3.26 and Figure 3.27 show photographs of two of these samples before ultrasonic NDT is carried out.

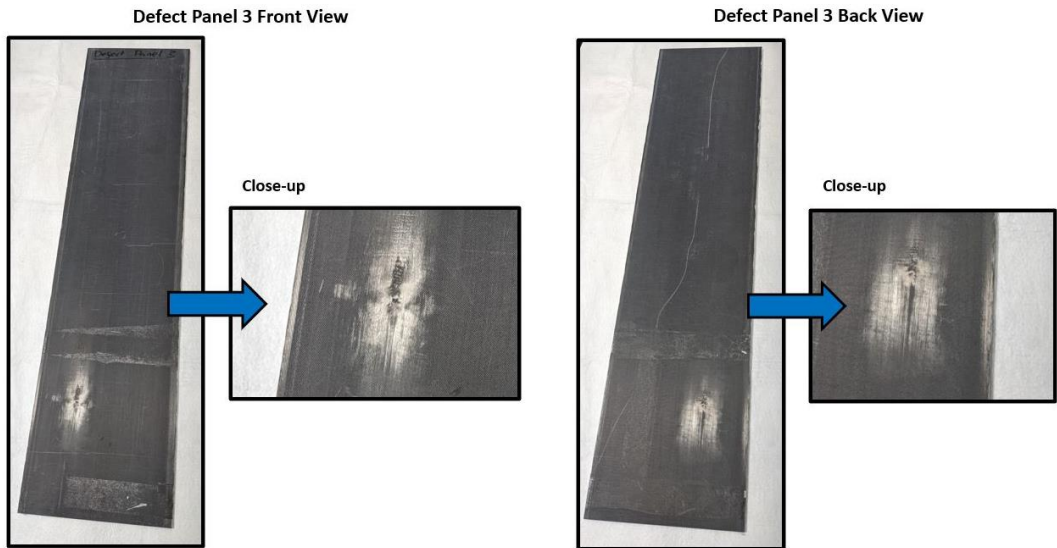


Figure 3.26. Defect panel 3 photographs with defects highlighted.

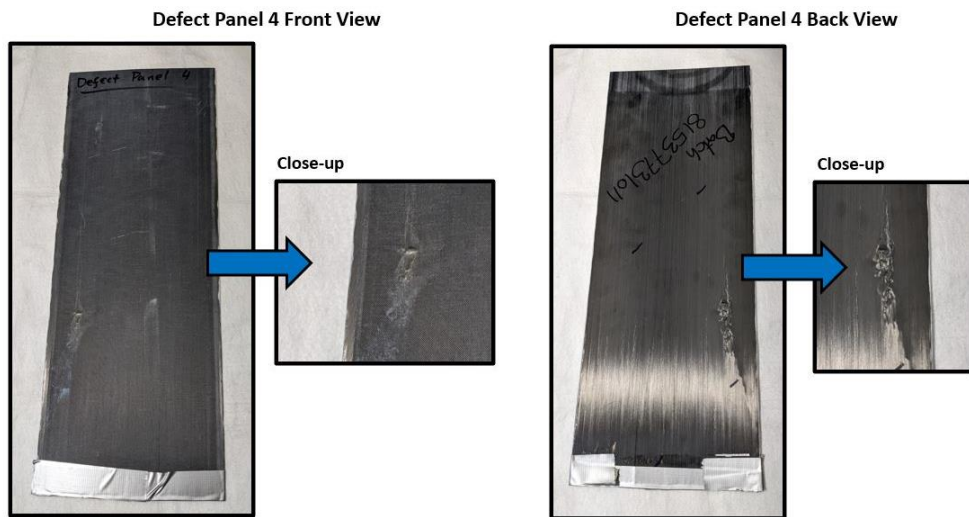


Figure 3.27. Defect Panel 4 photographs with defects highlighted.

3.4 Results and Discussion

3.4.1 Defect-free Panel Scans

A and B-scans for a clean CFRP panel are shown in Figure 3.28. The ToF data from a C-scan gives the panel thickness as 5.1 mm. Such scans are shown in the following sections for both a panel with artificial defects and the rejected samples. Inspection was performed with the parameters given in Table 3.6, Scenario 1 from Table 3.1.

Initial measurements determine the speed of sound of the pultruded samples to be in the range of $2880 - 2950 \text{ ms}^{-1}$, normal to the fibres with an average attenuation value across the array elements of 0.66 dBmm^{-1} in the same orientation. This calculation is based upon the ratio of the amplitudes taken from first and second backwall echoes, and the sample thickness as measured with callipers [142].

Inspection Parameter	Value
PRF	7.6 kHz
Scan speed	100 mms^{-1}
Channels	61, (4-element linear imaging)
Receiver Gain	30 dB
Predicted scan axis resolution	0.8 mm
Experimental scan axis resolution	0.81 mm

Table 3.6. Inspection parameters used to generate scans of a clean CFRP panel.

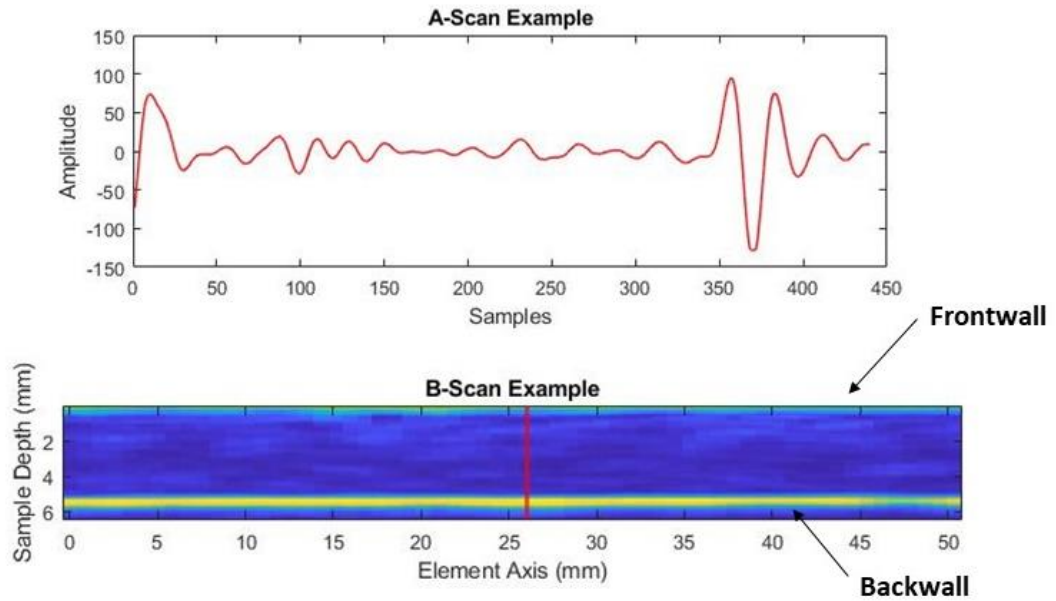


Figure 3.28. Example of A, B-scan taken from a clean pultruded CFRP panel. The A-scan is located at the indicated position on the B-scan.

3.4.2 Artificial Defect Panel Scans

The procedure is repeated for a sample with artificial defects in it. Inspection parameters are the same as in the previous section, shown in Table 3.6. An example A-scan and B-scan, taken across the holes, is shown in Figure 3.29. The validity of the -6 dB hole sizing method can be seen in the results presented in Table 3.7 using the amplitude profile shown in Figure 3.30.

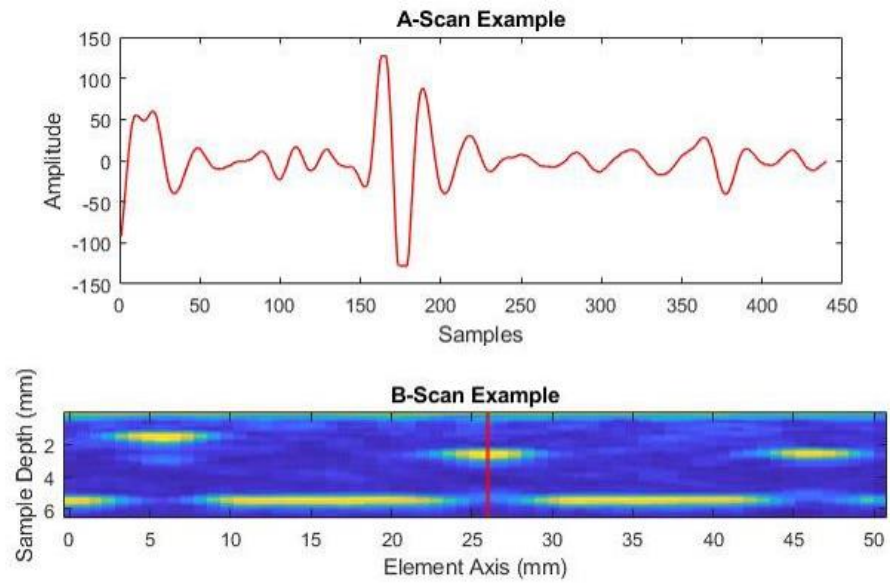


Figure 3.29. A and B-scans taken at a hole position from the artificial defect panel. The A-scan is taken from the indicated position on the B-scan.

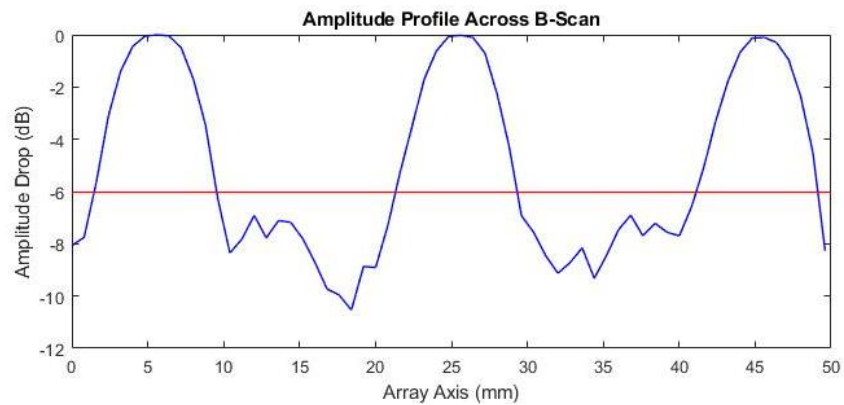


Figure 3.30. Amplitude profile taken from the internal section of the sample across the B-scan. Used for 6 dB hole sizing.

Artificial Defect Size	-6 dB Sizing Result (mm)
3 adjacent 10 mm holes	8.8, 9.4, 8.9
3 adjacent 6 mm holes	5.5, 5.6, 6.2

Table 3.7. Results of sizing algorithm applied to machined 6 and 10-mm holes.

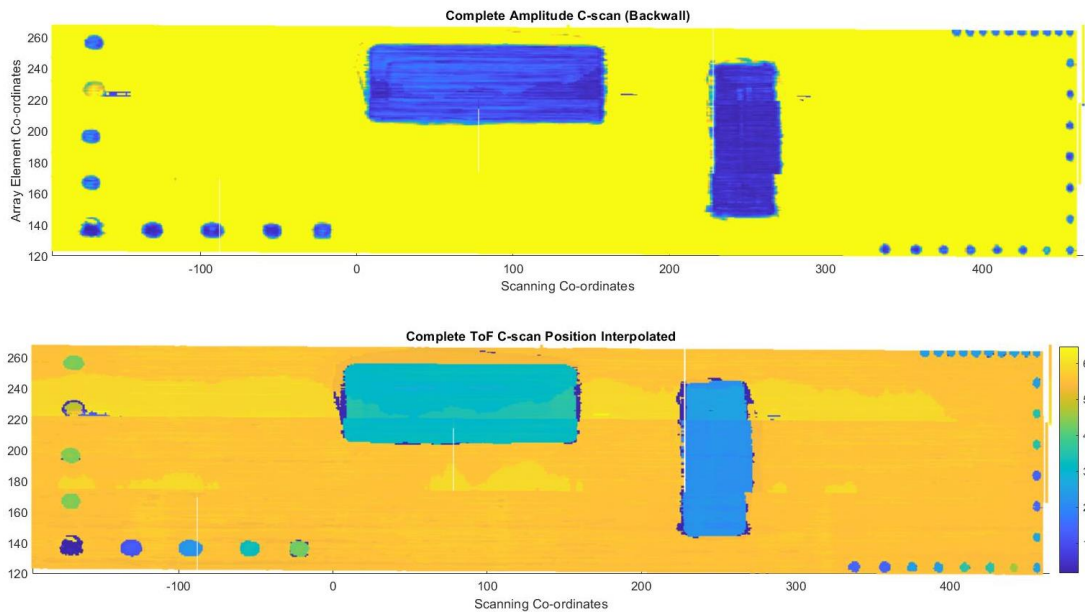


Figure 3.31. C-Scans taken from a section of the artificial defect panel.

3.4.3 Defective Panel Scans

Results from four separate panels are now presented. Defect Panel 3 has clear surface damage, imaged in Figure 3.26. In addition, the internal damage is located and characterised in defect panels 1,2 and 3 showing the strength of this inspection technique. The ToF scan from Defect Panel 4 is a good example of this data giving an accurate thickness profile, Figure 3.35. This sample has a tapered end section as well as surface defects. B and C-scans imaging the region of interest in panels 1 and 3 are shown in Figure 3.32 to Figure 3.34. The 6 dB sizing technique, applied to one defect, is shown in the schematic in Figure 3.36. Finally, a summary table of defect sizes is given in Table 3.8.

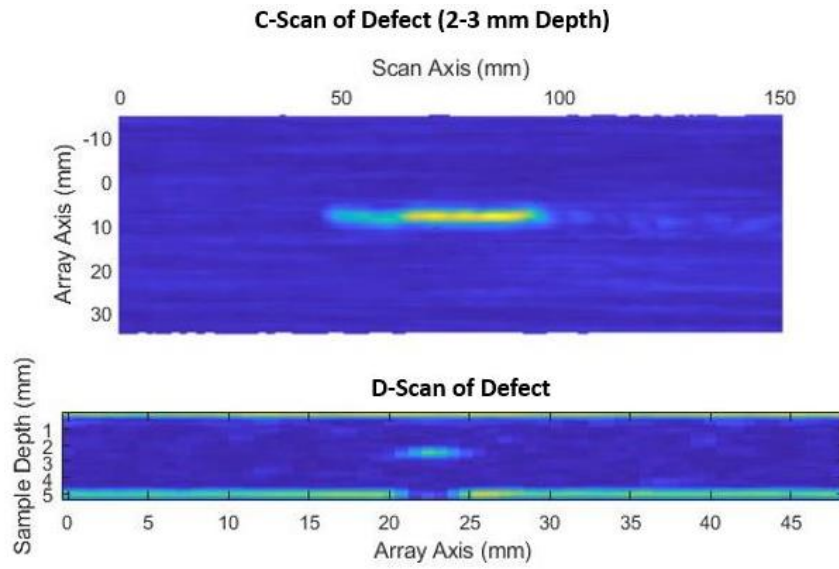


Figure 3.32. B and C-scans taken for the RoI in Defect Panel 1.

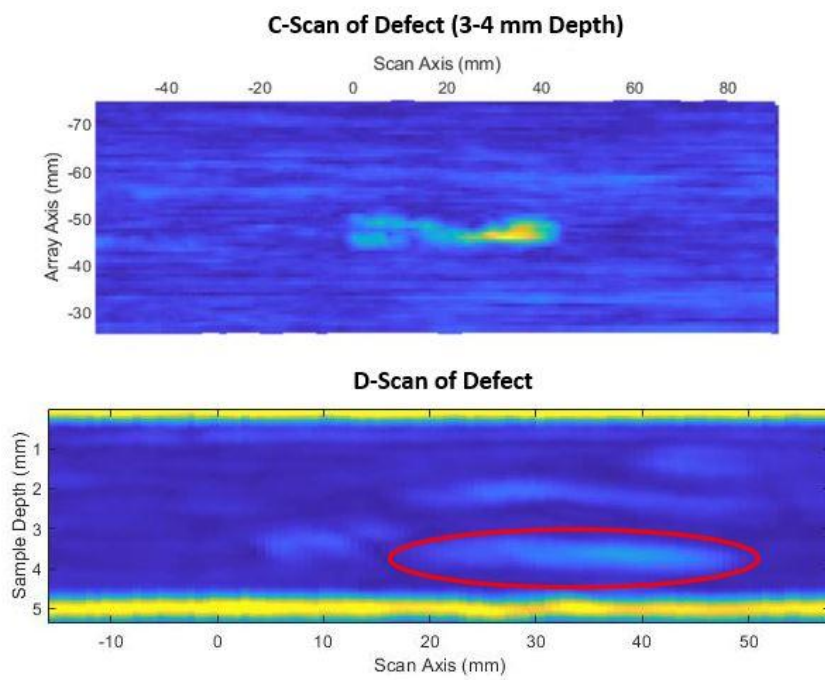


Figure 3.33. B and C-scans taken for the RoI in Defect Panel 2.

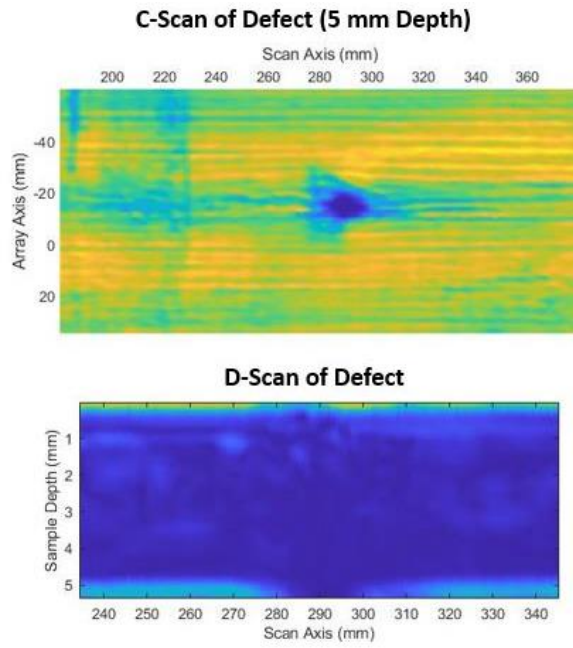


Figure 3.34. B and C-scans taken for the ROI in Defect Panel 3.

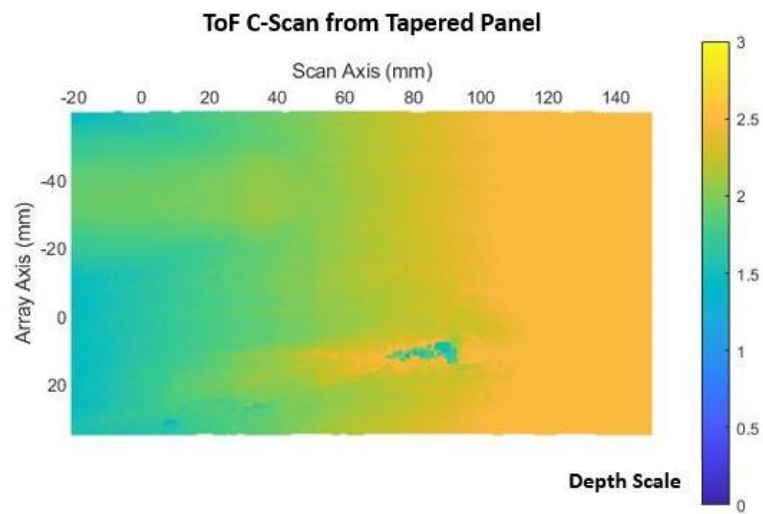


Figure 3.35. ToF C-scan taken from Defect Panel 4.

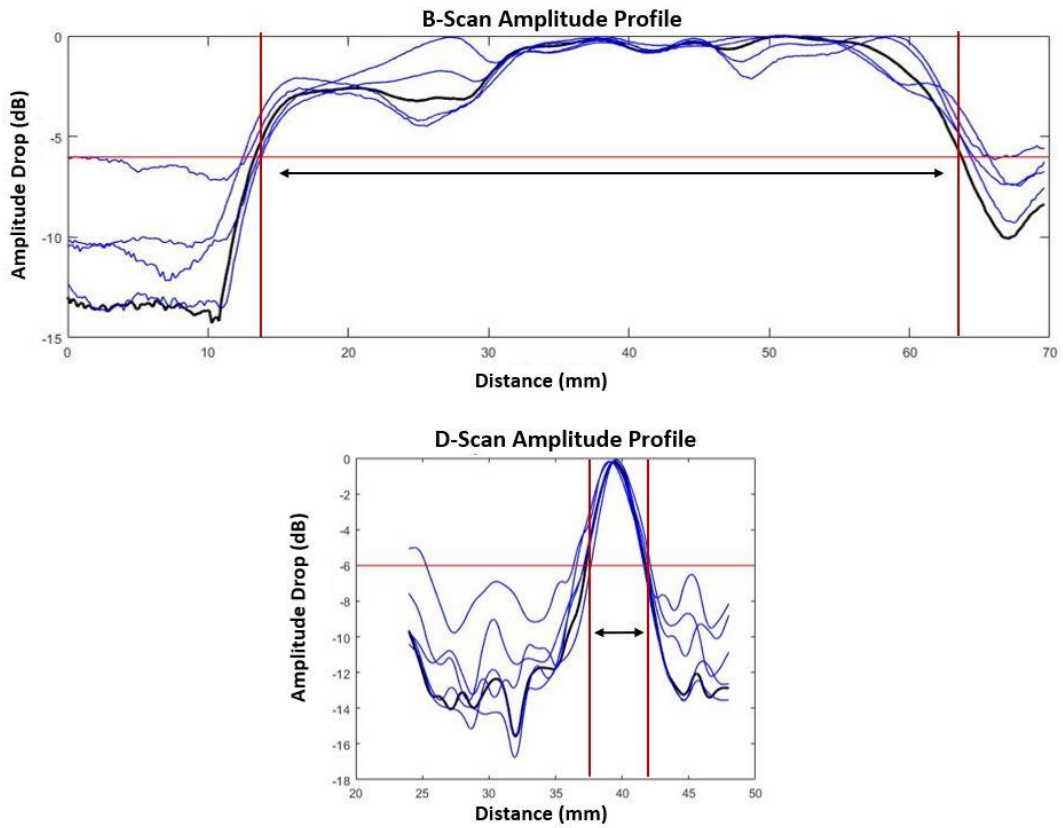


Figure 3.36. 6 dB sizing technique, across five lateral positions, applied to an internal defect found in Defect Panel 1.

Sample	-6 dB Sizing Result (mm)	Depth (mm)	Probable Defect-type
Defect Panel 1	5 x 52	2.2 - 2.9	Delamination
Defect Panel 2	7 x 28	3.5 - 4.1	Long Resin Pool
Defect Panel 3	18 x 25	5.1 - 6.0	Fibre Knot

Table 3.8. Summary table of defect sizes found in Defect Panels 1-3.

3.4.4 Practical Limitations

To establish the limitations of the robot scanning set-up, several investigations are carried out. These quantify the robustness of the phased array wheel probe inspection and will be important when such hardware is applied in a manufacturing environment. Probe alignment, coupling forces and sample edge effects are looked at. Throughout these the artificial defect sample is used and the impact on hole sizing is investigated.

3.4.4.1 Probe Alignment

The effects of transducer pitch and roll, with respect to the sample surface, are investigated. Pitch is defined a rotation around the array axis, with roll around the scan axis. This can be visualised in Figure 3.37.

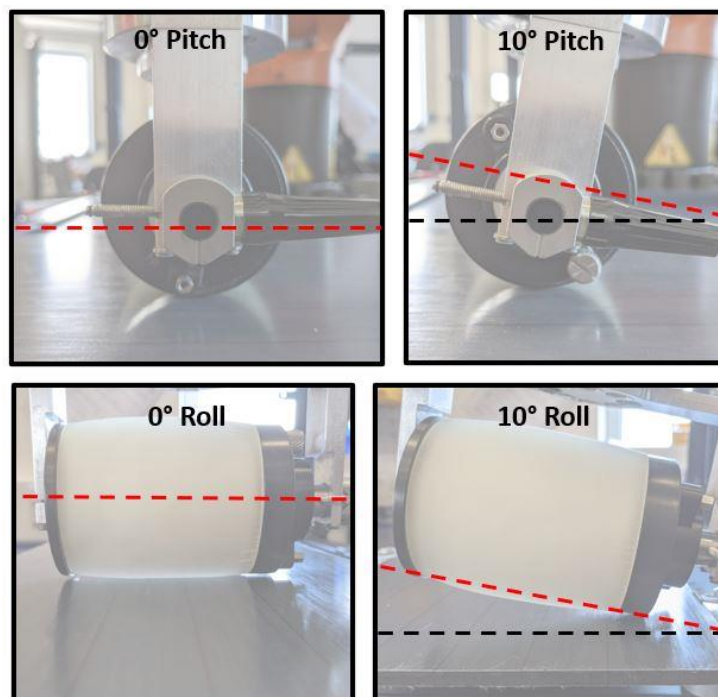


Figure 3.37. Schematic defining pitch and roll axis for the wheel probe

When considering phased array inspection, too great a pitch or roll angle will result in the sound not returning to transducer element used to transmit it. This limit, in both axes, is dependent on the phased array pitch, height as well as the geometry of the delay line and sample, shown in Table 3.9. The schematic in Figure 3.38 best shows with the maximum pitch and roll angle, calculated by trigonometry, with a lateral distance shifted beyond half the pitch or height considered unacceptable for imaging. For example, it is found that a returning sound beam will ‘miss’ receiving elements beyond pitch and roll angles of 4.5° and 1.3° , respectively, for this inspection set-up. The limit of roll is less due to the smaller size of each element in this dimension and a lack of compliance of rubber to sample. A larger probe tyre with more downwards force would improve this margin for error. Finally, the effect of probe movement in the scanning axis is negligible, when compared to these effects of poor alignment.

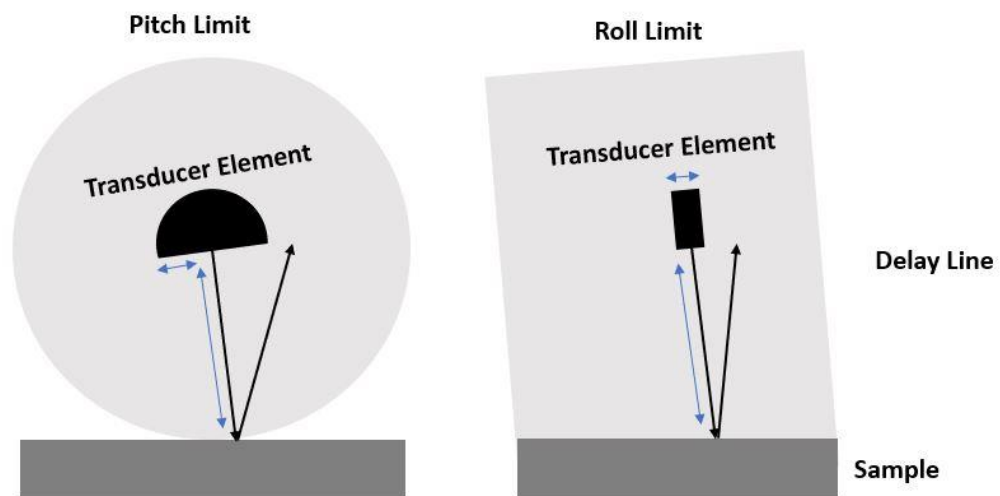


Figure 3.38. Schematic demonstrating the pitch and roll limits for ultrasonic wheel probe phased array imaging

Parameter	Value (mm) (°)
Delay Line	25
Array Pitch	0.8
Array Height	10
Maximum Roll	1.3
Maximum Pitch	4.5

Table 3.9. Relevant parameters for maximum permissible pitch and roll.

A series of 10 mm holes, at depths of 1-4 mm, machined into the artificial defects panel, are inspected with the pitch varied in 1-degree increments from -5 to +5 degrees. The resultant C-scans can be seen in Figure 3.39, with hole sizing and A-scan amplitude values presented in Table 3.10. For each pitch angle the average backwall peak to peak amplitude is recorded. The value taken in each A-scan can be seen in Figure 3.40. This is compared to that at normal incidence, 0-degree pitch, and expressed as a dB drop. Increasing pitch angle thereby also reduces the SNR in each A-scan used for imaging. ToF also increases with increasing pitch angle since the effective thickness of the sample is greater at non-normal incidence. When varying the roll angle, Figure 3.41, lack of coupling and rubber compliance to the sample quickly degrade the image beyond 1° from optimal alignment. Throughout these results, the image degrades well before the theoretical limits in Table 3.9. Lack of compliance to the sample, and inadequate SNR are the causes of this. Based on the C-scans presented, acceptable pitch and roll are set 2° and 1°, respectively. This upper limit does not cause any practical problems since the KUKA robotics employed allow for an angular positioning accuracy of $\pm 0.1^\circ$ [143]. The plane of the array

face can be held parallel to the sample in both orientations with an accuracy much finer than any pitch and roll angles that would create imaging difficulties.

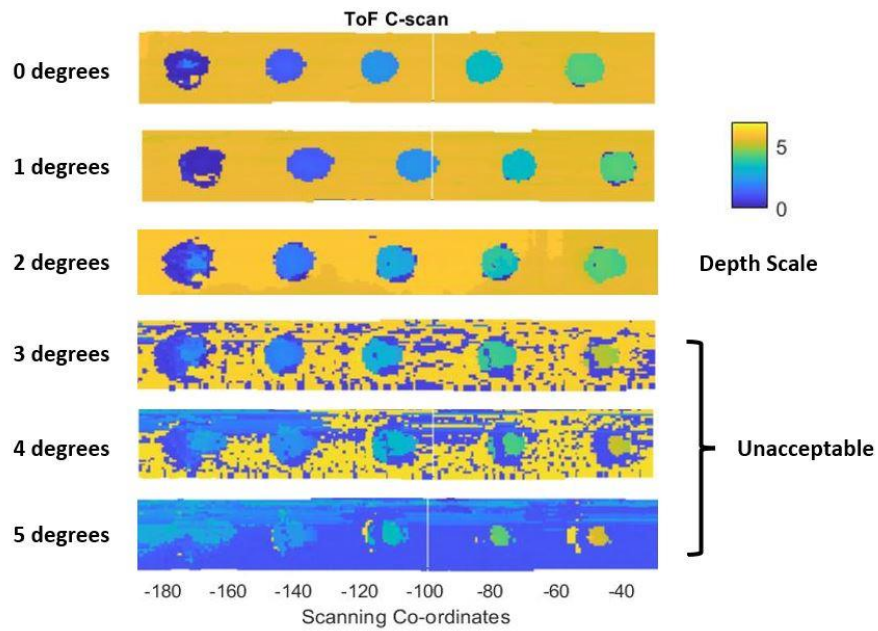


Figure 3.39. Impact of pitch angle on C-scans of 10 mm artificial defect holes.

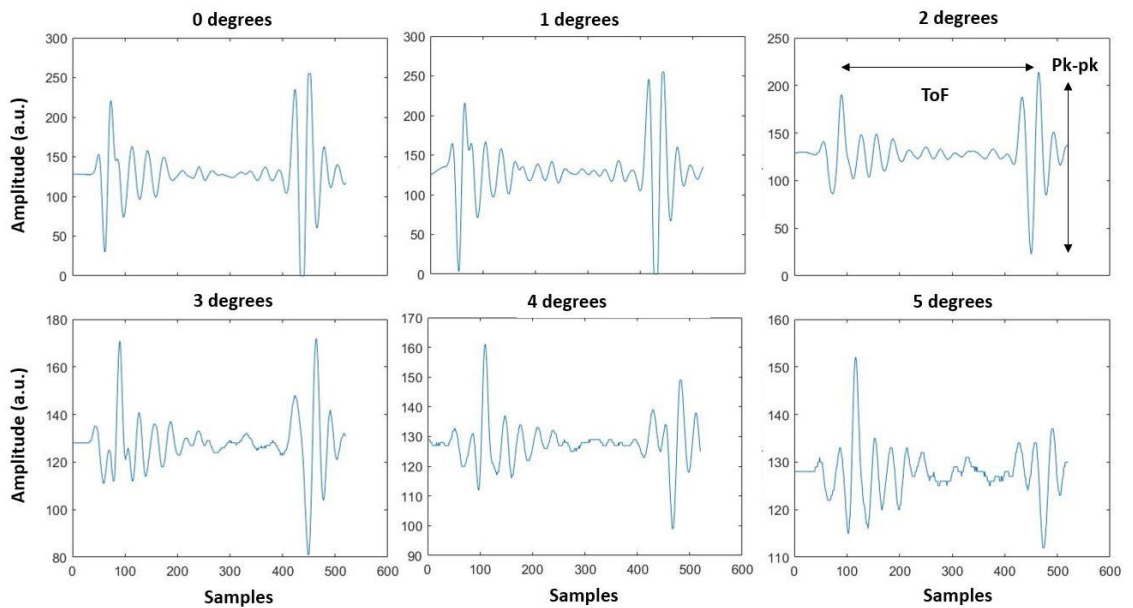


Figure 3.40. Effect on increasing pitch angle on ToF and backwall amplitude in each A-scan.

Pitch Angle (°)	Size (Array x Scan axis) (mm)	Backwall Amplitude Decay (dB)	Backwall Amplitude Decay (%)
0	11 x 12	0 (reference value)	0
1	10 x 14	-0.1	-1.6
2	12 x 16	-1.9	-19.5
3	N/A	-9.7	-67.2
4	N/A	-14.9	-82.0
5	N/A	-19.2	-89.1

Table 3.10. Effect of pitch on hole sizing and backwall signal amplitude.

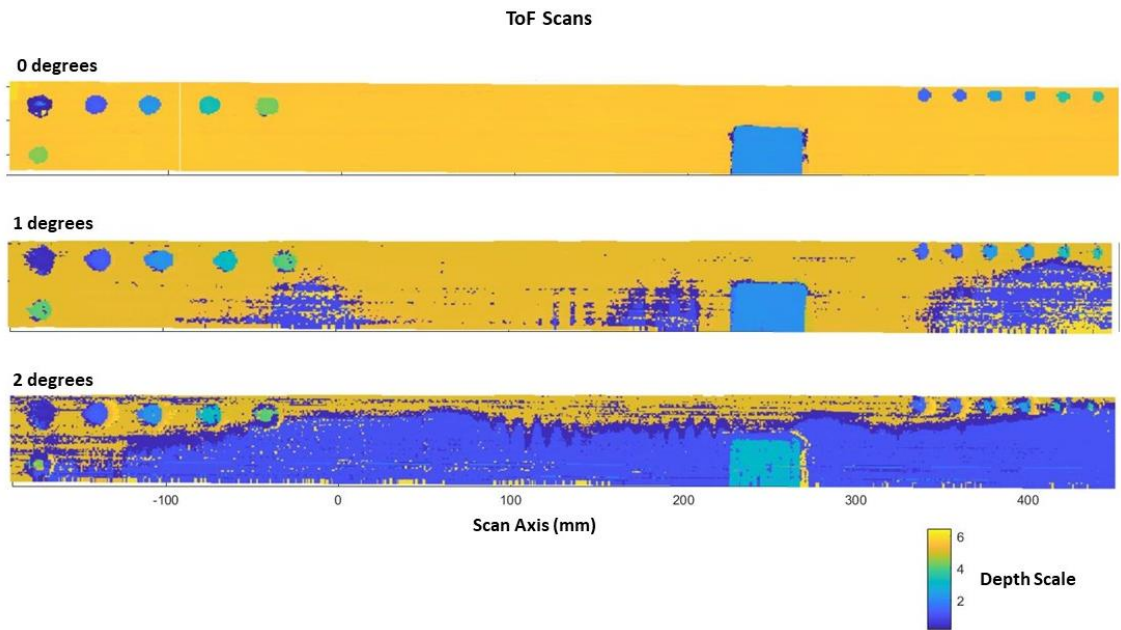


Figure 3.41. Impact of roll angle on the artificial defect sample C-scans.

3.4.4.2 Force Variation

The current hardware incorporates a FT sensor. Forces and torques experienced at the robot flange can be viewed in real time and/or used to correct the robotic position as the inspection progresses. This allows for an investigation into the effects of force variation into resultant C-scans to be carried out. Thereby the limits of this practical consideration can be quantified, as the alignment was in the previous section. Forces in the range 5-30 N are applied and the C-scan images, shown in Figure 3.42, analysed. All data were acquired at a scanning speed of 100 mms^{-1} and 7.6 kHz PRF. Both 25 and 30 N produce near identical images. However, 30 N is preferable for more reliable inspection at higher speed where any force variation can be greater and not as quickly corrected for. The only anomaly are a few dry patches on the scan taken at 25 and 20 N. These can be addressed through a better method to keep the tyre damp and are not relevant to the force investigation. At 20 N a clear image can be observed. It is though, advantageous to increase the force and introduce some safety margin. Unreliable coupling and insufficient rubber deformation become obvious below 20 N. In the 15 N scan the backwall response is present but further away since the rubber is not sufficiently compressed and therefore the gating procedure is incorrectly applied. At 10 N and 5 N, not all phased array elements are coupling into sample. Gating issues are therefore exacerbated, and the acquisition length no longer captures the backwall. The tyre not being sufficiently compressed makes the delay line longer. In addition to the pitch and roll criteria, these results mean a minimum force of 25 N is chosen.

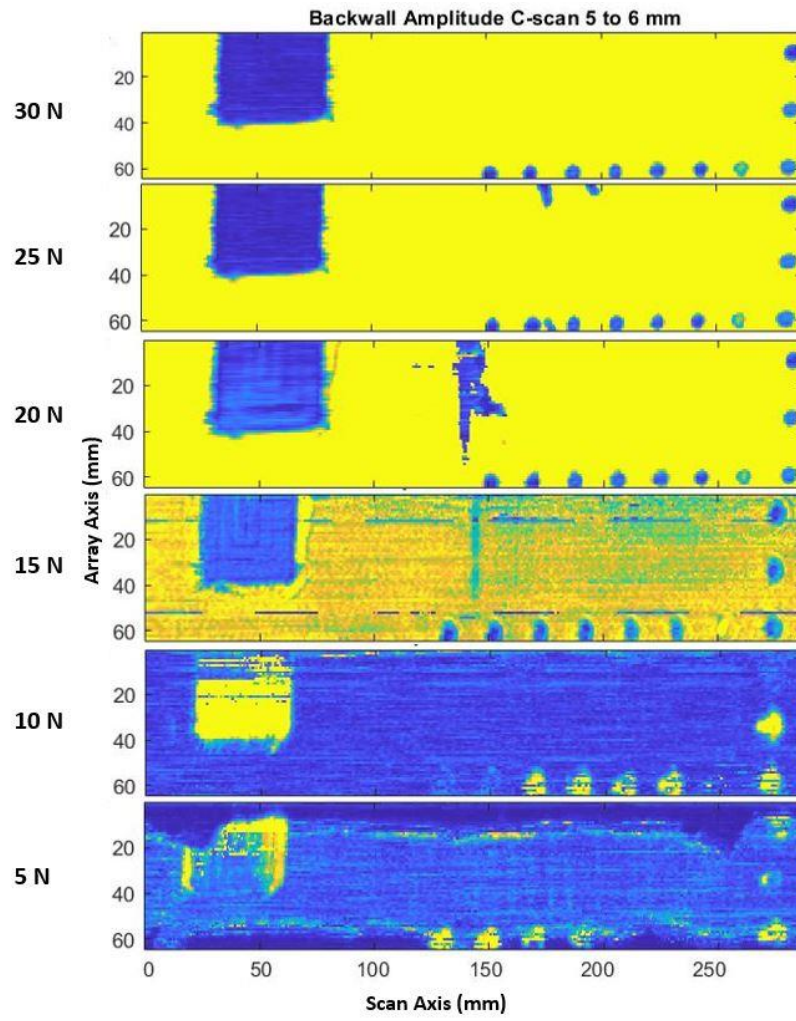


Figure 3.42. Impact of force variation on artificial defect sample C-scans.

3.4.4.3 Edge Effects

Finally, the effect the wheel probe covering the edge of the sample are looked at. A section of the tyre is not in contact with the sample, overlapping the side of panel, as shown in Figure 3.43.

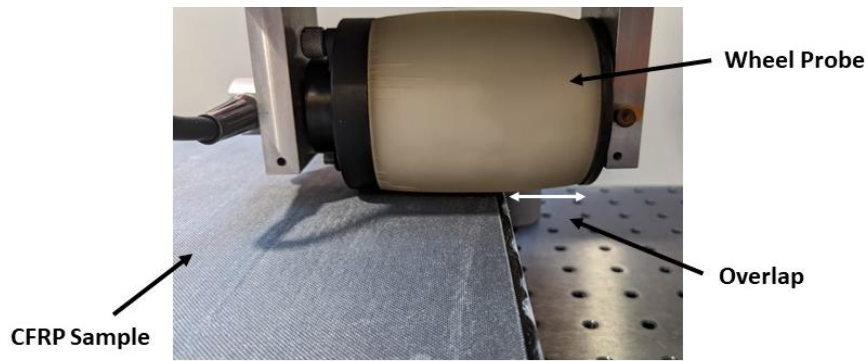


Figure 3.43. Wheel probe and transducer overlapping the side of the sample.

Several C-scans are shown in Figure 3.44, but no undesired imaging effects observed. This is encouraging since it demonstrates the robustness of the inspection system and probe overlap not an issue to accommodate when factory implementation is considered in the second part of Chapter 3.

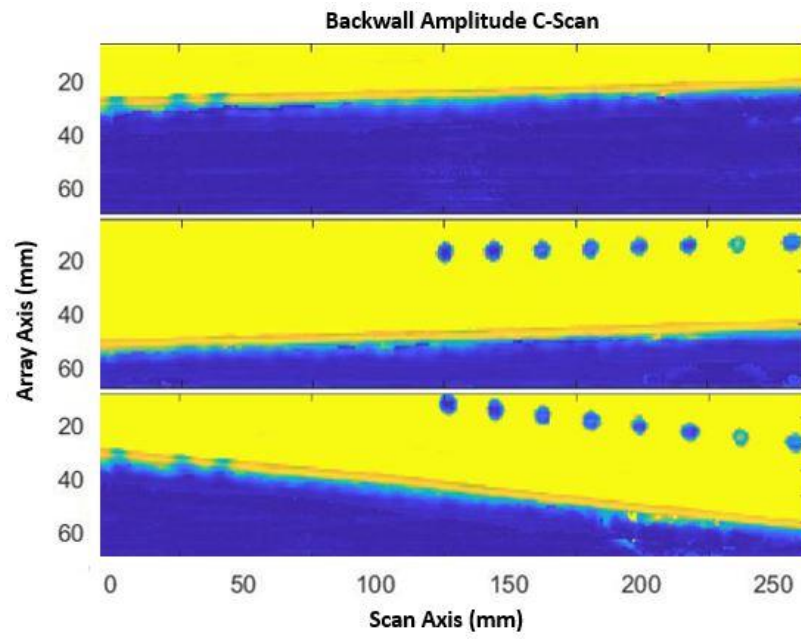


Figure 3.44. Impact of tyre overlap on artificial defect sample C-scans.

3.5 In-process Ultrasonic Inspection System

3.5.1 Introduction

The use of robotic scanning for such simple geometry components does, however, add an unnecessary level of complexity as well as high capital costs. A simpler, more robust, inspection set-up is now proposed. This takes the form of a custom-designed aluminium frame supporting a series of rollers with the phased-array wheel probe held in a fixed position. The FT sensor, and its feedback into the robotic positioning system, are therefore also redundant. This inspection set-up can be modified to accommodate a custom wheel probe and array and thus allow for full panel width coverage. Such a device is discussed in the future work section.

3.5.2 Components

An in-process ultrasonic inspection system is designed in the AutoCAD inventor environment and manufactured by a University of Strathclyde based workshop. Dimensions can be seen in Figure 3.45, with the inspection system in Figure 3.46.

Key components are as follows:

- Aluminium frame
- Supporting rollers with inbuilt bearings
- Olympus 5 MHz phased array wheel probe
- PEAK NDT phased array controller
- Encoder wheel for PAC integration through NI LabVIEW

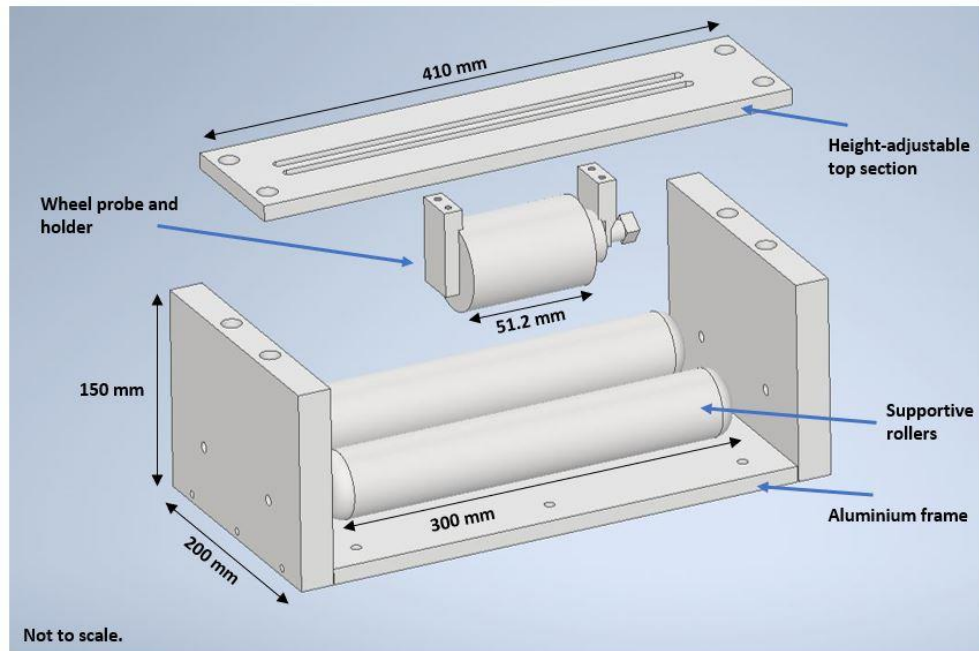


Figure 3.45. AutoCAD assembly of an ultrasonic inspection system design.

3.5.2.1 Frame

A simple box construction supports the rollers below the sample and allows for the phased array wheel probe to be height-adjusted onto the upper surface of the CFRP panel. The aluminium used on the bottom, sides and top is of 25 mm and 15 mm thicknesses, respectively.

3.5.2.2 Supporting Rollers

Two supporting rollers, with inbuilt bearings support the panel as it moves through the inspection system. These are manufactured by 'Interroll' and available off-the-shelf through RS Components, part number: 17X3JAALAE

3.5.2.3 Olympus Phased Array Wheel Probe

The same 5 MHz Olympus PA, housed within a rubber wheel is mounted to the top plate of the frame. Specifications and dimensions are as described in the first half of Chapter 3. The probe is mounted midway between the supporting rollers and clamped down using the threaded mounts on the frame. This ensures good compliance between the rubber and sample and adequate force for ultrasound coupling. Despite the FT sensor no longer being included, the rubber delay line is fully compressed onto the sample and the top section clamped down using threaded rods. The force is estimated at 50 N and well beyond the 25 N defined as a minimum value from Section 3.4.4.2 . Since there is no component directly below the phased array, a strong backwall reflection from the CFRP-air interface is guaranteed.

3.5.2.4 Phased Array Data Acquisition

Again, the PEAK LTPA, allows for 64 channels to be controlled on transmission and reception and data acquisition rates of up to 120 MB/s using high-speed ethernet connections [125]. Since the end-goal is to incorporate a NDT set-up into the SGRE production line it makes sense to utilise commercially available equipment and not that exclusively for research purposes. The focal laws triggered on the array facilitate simple linear imaging. There is no need for any FMC or MA acquisition at this stage. Therefore, hardware demands on the phased array controller call for a high number of total channels with a comparatively lower number of these to be individually addressed on reception and transmission. A PEAK LTPA may typically have a 64:64 or 64:32 modality. The linear imaging applied here only uses a 4 or 8-element

aperture. Since the inspection system offers potential for a much wider phased array, covering the entire panel width, a 256:16 or 256:8 modality may become necessary. Such a configuration would have to be custom designed by PEAK. However, since the demands in terms of reception channels, are less than many off-the-shelf options, this has the potential to come at a reduced cost. Initially, the PAC can operate at a maximum PRF of 20 kHz. However, with a custom firmware update, this could be increased to the 55 kHz to facilitate higher scanning speeds and resolutions. At current pull-through rates, PRF values well within this limit yield adequate resolutions, as shown in section 3.2.1.8.

3.5.2.5 Encoder and LabView Integration

To relate the UT data back the physical location it was acquired at, some form of data-encoding is necessary. For these inspections, an encoder is mounted to one of the supporting rollers to monitor the distance and speed moved by the panel. The model used is a Baumer Electric CH-8500, Frauenfeld and has a resolution of 1000 steps per revolution. Using the 40 mm diameter wheel a 0.3 mm scan axis resolution is achievable. This device connects to the PEAK unit and allows for integration through the LabVIEW environment. Encoder operation can either be active or passive. Passively, the LTPA will continuously fire the focal laws at a given PRF, taking the encoder position for each sweep of array. This would lead to a variation in resolution if the pull-through speed is not constant. The other mode of operation sees the LabVIEW virtual instrument constantly checking the encoder position and only firing the phased array when a positional change is observed. Again, this position is

3.5.3 Samples

In addition to the five defective panels referred to in the first half of this Chapter 3, an additional eight rejected sample are obtained from the industrial partner. Thereby, a total of 13 samples can be inspected, with any defects found characterised through A, B and C-scan analysis. Figure 3.48 to Figure 3.50 show several photographs, additional to ones in the first half this chapter, of these samples with surface defects highlighted.

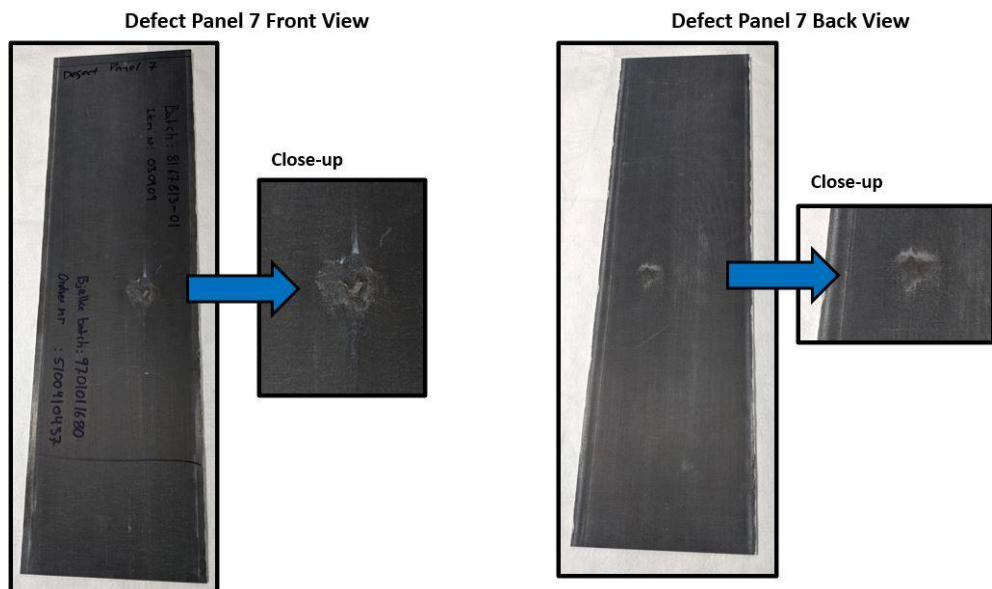


Figure 3.48. Defect panel 7 with surface defect indications highlighted.

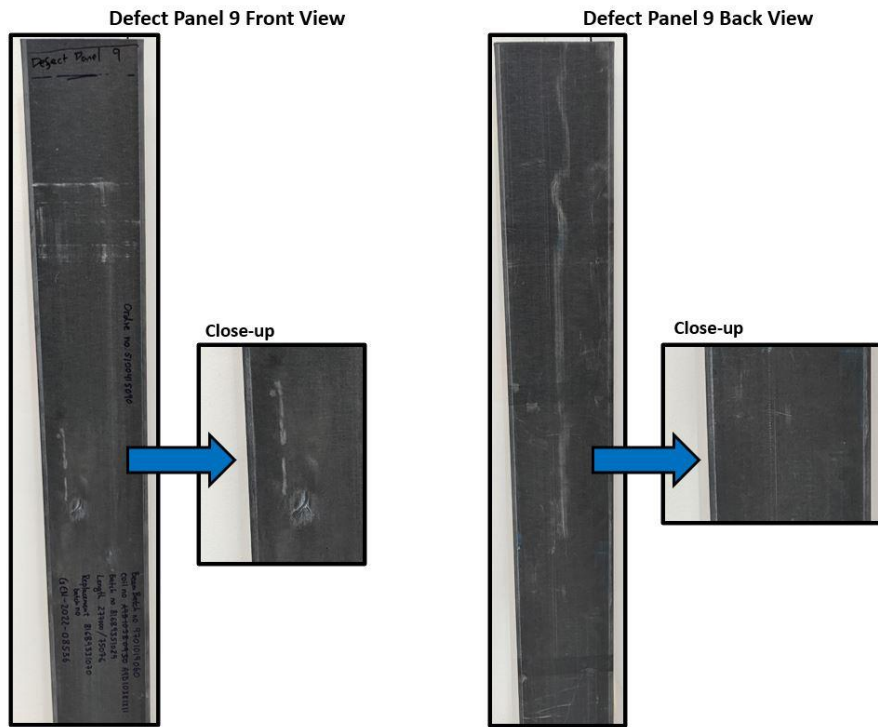


Figure 3.49. Defect panel 9 with surface defect indications highlighted

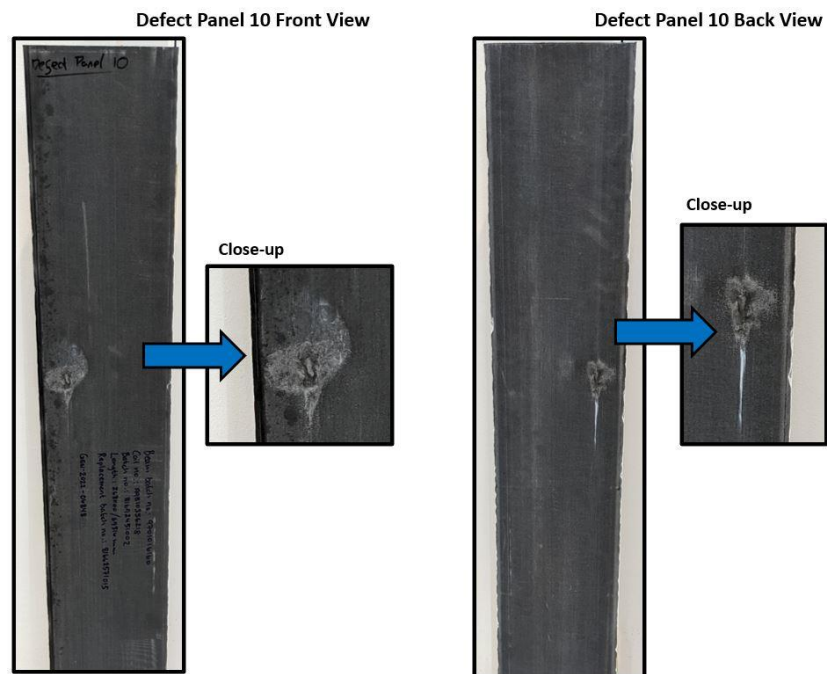


Figure 3.50. Defect panel 10 with surface defect indications highlighted

3.5.4 Inspection Procedure

Industrial requirements on such an inspection call for a scanning rate of 100 mm/s. There is the potential for this to increase to 200 mm/s in the future. To demonstrate the robustness of the encoder-triggered phased array inspection panels are moved through the inspection system by hand. Any variation in speed accounted for in the final images since more data is captured at higher pull through speeds, and less at slower ones, thus maintaining a consistent pixel size. The current phased array wheel probe, now employing a 4-element sub-aperture for linear imaging, has a coverage of 48.8 mm. This is the result of the 0.8 mm element pitch multiplied by 61 channels, as given by Equation 3.1. To cover the entire panel width of around 200 mm, five inspection passes are performed with the probe in shifted positions, measured as shown in Figure 3.46. These datasets are then stitched together in post-processing to give C-scans of the entire panel. Overlaps between, and positioning of each, scan pass are detailed in Figure 3.51, Figure 3.52 and Table 3.11.

Parameter	Value
Edge Overlap pass 1	11.2 - 12.8 mm (14-16 elements)
Edge Overlap pass 5	2.3 - 4.8 mm (4-6 elements)
Scan Overlap 1-4	9, 9, 9, 4 mm
Start/end gap	95 mm

Table 3.11. Table detailing the probe positioning with the inspection system.

Since the Baumer encoder has a 1000-step angular resolution, and a 40 mm encoder wheel gives a step-size relating to 0.3 mm of sample movement, LabVIEW code is modified to fire on every third step, achieving as close to square pixels as possible with current hardware. Resultant images have a resolution on 0.8 mm x 0.9 mm (array pitch x three encoder steps).

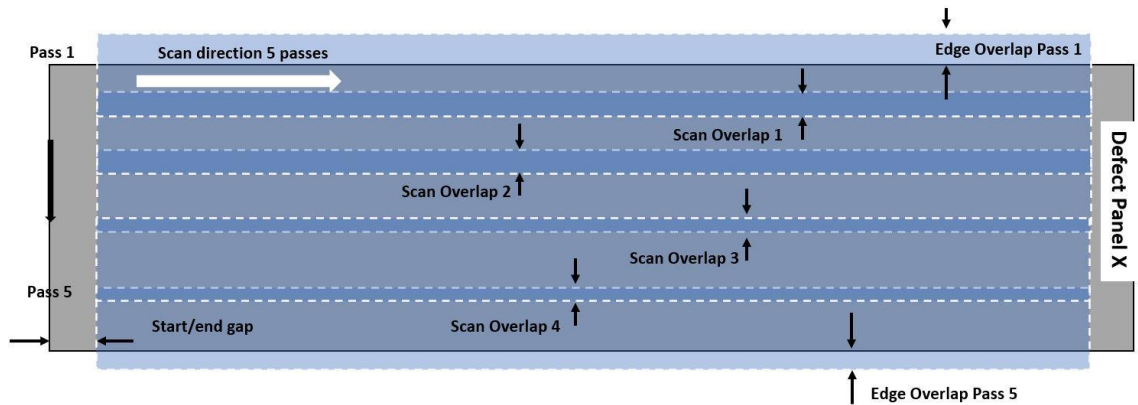


Figure 3.51. Schematic detailing positions of scan passes in relation to sample.

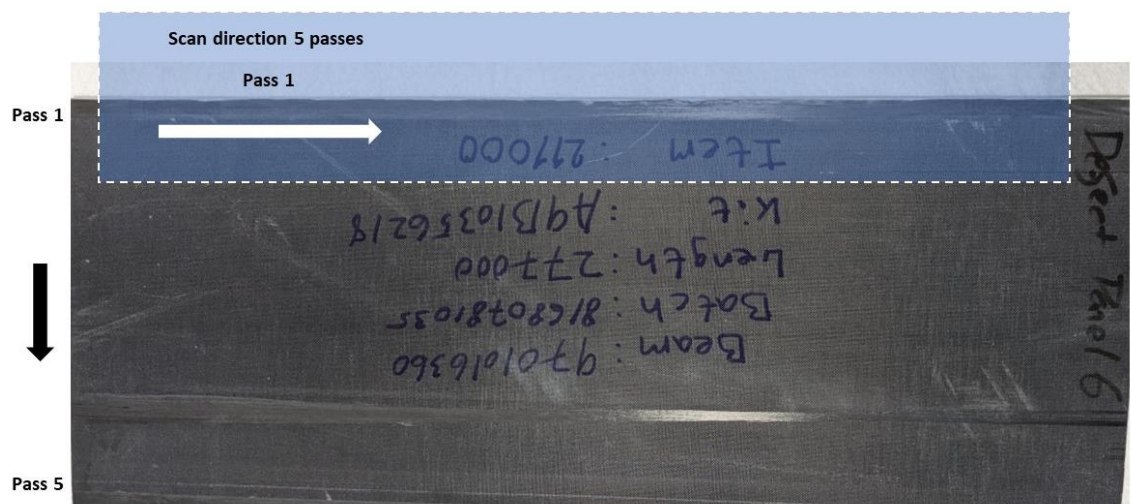


Figure 3.52. Image detailing example of scan pass 1 in relation to sample.

3.5.5 Results and Discussion

As in the results presented in section 3.4, A, B and C-scans are now generated from the data acquired using the inspection system. Defect characterisation is now performed using the encoded position information and phased array pitch size. Defect Panel 7, 10 and 11 are presented here as examples. C-scans from each can be seen in Figure 3.53, Figure 3.54 and Figure 3.55, with the results of defect sizing summarised in Table 3.12. Since several flaws are visible in the scans, the characterised defect has been circled on each C-scan. It must be noted at this point that 13 panels all with several flaws, leads to large amounts of data, potential presentation, and characterisation methods. There is a high level of repetition, and the effectiveness of the in-process ultrasonic inspection system can be seen in the subset of results shown here.

Panel	-6 dB Sizing Result (mm)	Depth (mm)	Type of Defect
Defect Panel 7	7 x 63	1.6 - 2.7	Longitudinal Resin Pool
Defect Panel 10	25 x 16	5.0 – 6.0	Fibre Knot
Defect Panel 11	4 x 138	1.6 - 2.4	Longitudinal Resin Pool

Table 3.12. Summary table of defect sizes found in Defect Panels 7, 10 and 11.

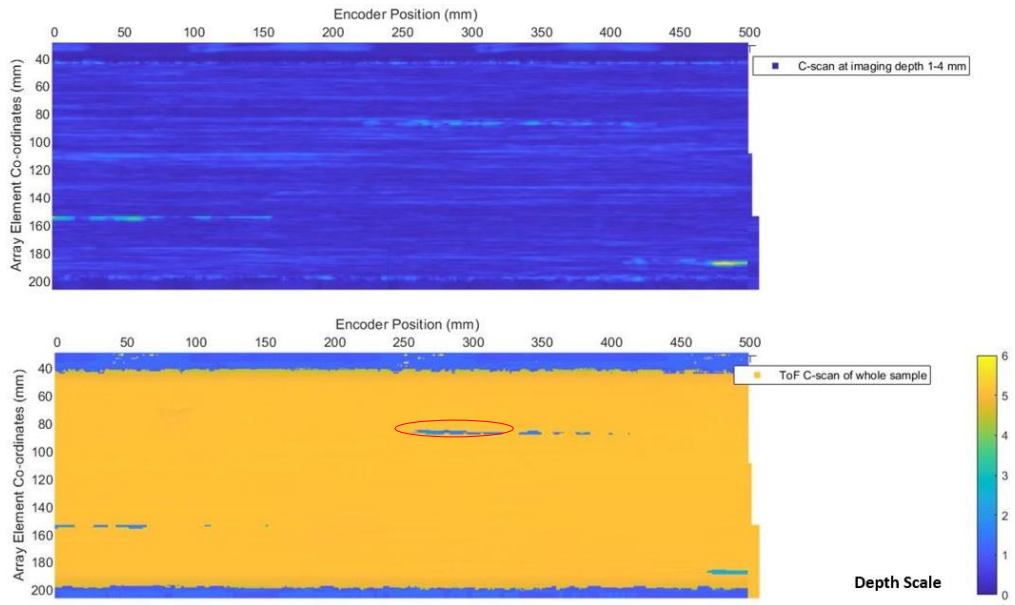


Figure 3.53. Defect Panel 7, amplitude, and ToF C-scan

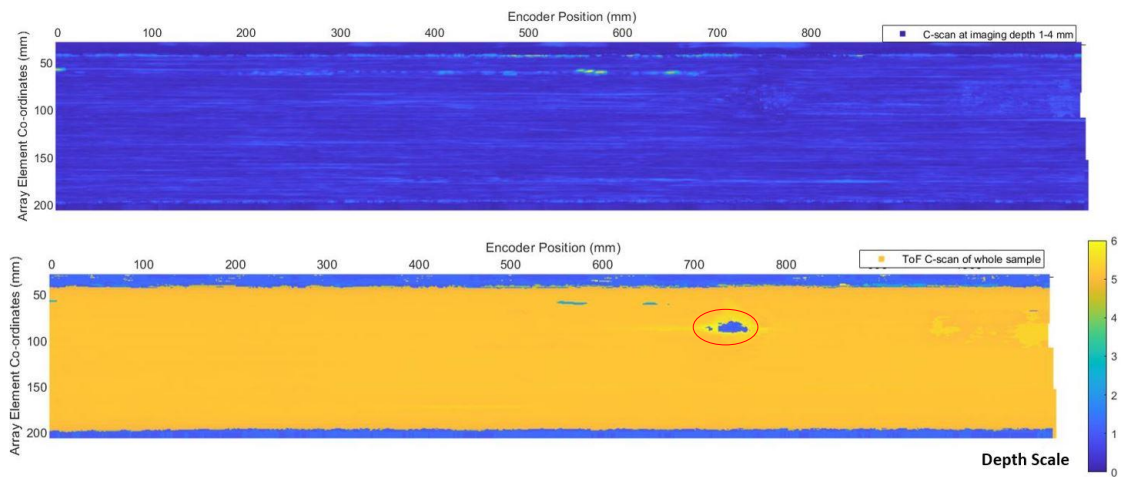


Figure 3.54. Defect Panel 10, amplitude, and ToF C-scan

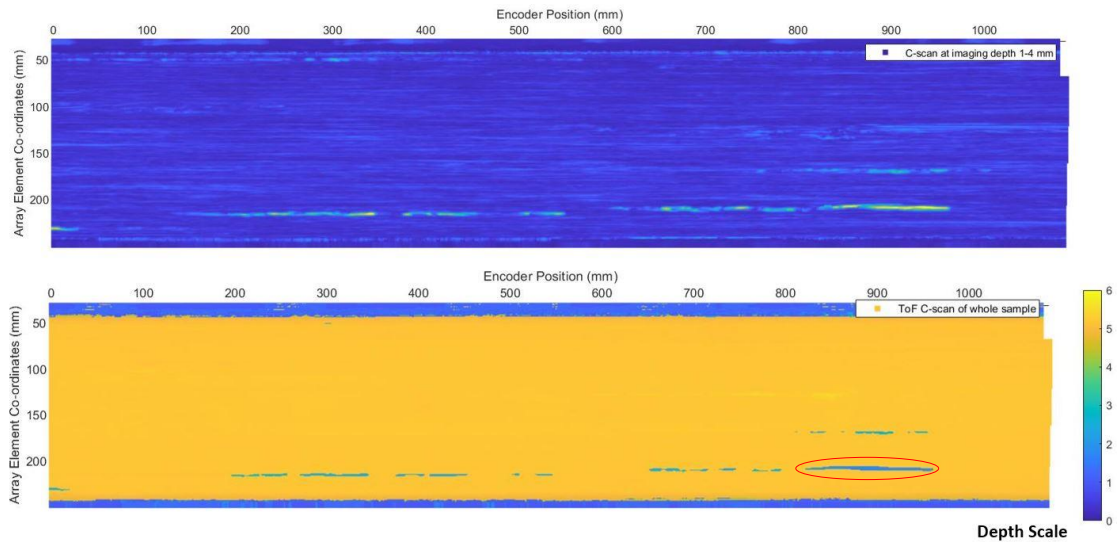


Figure 3.55. Defect Panel 11, amplitude, and ToF C-scan

3.5.6 Future Work

The main consideration is the implementation of the in-process ultrasonic inspection and defect characterisation system within a factory environment. Based on the results presented here, the general design idea is to be maintained. The ability of a phased array wheel probe to effectively image the internal structure of CFRP panels, as well as identify internal reflectors indicating defects, and measure any sudden thickness changes has been demonstrated. Within a manufacturing environment performing several scans of each panel with the probe mechanically shifted to facilitate full coverage is impractical. A wheel probe configuration with a minimum of 200 mm of active transducer width is necessary. One is therefore presented with choices regarding the number of individual probes, their operation through PAC units as well as considerations in terms of redundancy and complexity of the set-up in its entirety. Table 3.13 summarises the technical and commercial advantages and disadvantages.

Configuration	Single Probe	4 Olympus Probes
Technical Advantages	<ul style="list-style-type: none"> • Mechanical simplicity • Inspection imaging simplicity • Robustness 	<ul style="list-style-type: none"> • Readily available, off-the shelf components
Technical Disadvantages	<ul style="list-style-type: none"> • Both the wheel and transducer would need to be manufactured specifically for this application 	<ul style="list-style-type: none"> • Multiple cables. • Requirement for force torque sensors to ensure coupling consistency.
Commercial Advantages	<ul style="list-style-type: none"> • Reduced cost of fewer parts 	<ul style="list-style-type: none"> • Lower individual costs
Commercial Disadvantages	<ul style="list-style-type: none"> • Greater individual costs. • Custom made probe would take longer to manufacture 	<ul style="list-style-type: none"> • Due to number of individual components total cost exceeds that of simpler set-ups

Table 3.13. Summary of technical and commercial considerations in choosing an inspection configuration.

On balance, a single probe housing a custom array and triggered using a single PAC unit is considered most suitable. Robustness and simplicity are the main factors driving this decision along with the set-up allowing for simpler imaging and defect detection and localisation to be implemented. A single array allows for the same linear imaging scheme used previously to be implemented. There is no image-alignment or stitching of separate array outputs to contend with. A schematic of such a potential inspection set up can be seen in Figure 3.56.

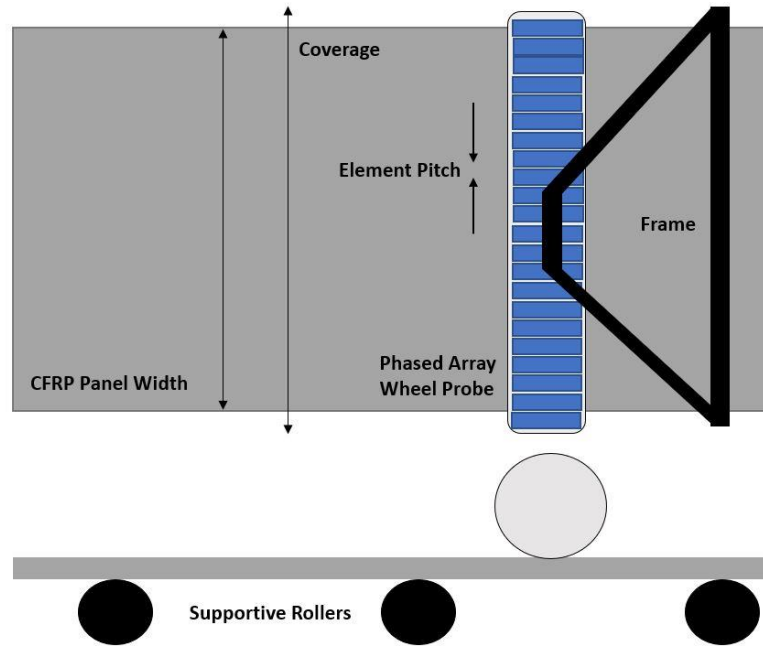


Figure 3.56. Schematic of proposed single array and wheel probe set-up.

Based on the same equations, Equation 3.2 to Equation 3.5, as the calculation tool presented for the robotic inspection parameters, Chapter 3, section 3.2.1.8, several different scenarios involving varying PRF, pull-through speeds and phased array imaging configurations are presented in Table 3.14. As in section 3.2.1.8, a screenshot of this calculator can be seen in Figure 3.57. Table 3.14 validates that the target speed of 100 mms^{-1} allows for adequate resolution at modest PRF values. This inspection configuration has sufficient headroom to accommodate a doubling in pull-through speed whilst still supporting a resolution fine enough to hit a 3 mm defect three times. When considering various phased array pitch sizes, the effect on achievable imaging performance much be considered, particularly the impact of grating lobes as the pitch increases [144].

Wheel Probe Inspection Configuration					
INPUTS					
Inspection Set-Up			Array Specifications		
Panel Width	200		Number of Elements	128	
Number of Probes	1		Pitch	1	
			Element Step Size	1	
PRF	20000		Active Aperture Size	4	
Scan Speed	100				
OUTPUTS					
Inspection Coverage		PAC Requirements		Resolutions	
Coverage per Probe	128 mm	Channels per Probe	125	FPS	160
Total Coverage	128 mm	Total Channels Required	125	Array Axis	1.0 mm
				Scanning Axis	0.6 mm

Figure 3.57. Screenshot, highlighting inputs and outputs of an Excel-based tool used to demonstrate achievable resolution for different custom probe configuration.

Scenario	Pitch (mm)	Channels	Pull-Through Speed (mms ⁻¹)	PRF (kHz)	Resolution (array x scan axis)
1	0.8	256	100	32	0.8 x 0.8
2	1.5	144	100	9.2	1.5 x 1.5
3	2	128	100	6.2	2.0 x 2.0

Table 3.14. Hypothetical inspection scenarios for a custom wheel probe facilitating wider than 200 mm coverage.

Based on the experience of manufacturers of phased arrays and PACs, an approximate breakdown of the costs involved in factory implementation of an roller inspection system incorporating a custom wheel probe has been compiled. Table 3.15 illustrates this. A conservative estimate would but the total capital cost of such a device at £160k.

Component	Approximate Cost
256-element, 1 mm pitch, phased array	£12k
256/128 channel phased array controller	£130k
Custom-made tyre	£8k
Array housing within tyre	£5k
Inspection system frame	£3k

Table 3.15. Estimates of component costs for a custom phased array wheel probe.

3.6 Conclusion

This chapter has shown the effectiveness of a robot phased array inspection in performing ultrasonic NDT of pultruded CFRP used in wind turbine construction. Basic components used have been described and their use justified. Key to this work is the ultrasonic phased array housed within a water-filled wheel probe. A characterisation tool used to parameterise the device has been presented and applied. In terms of practical inspection, the effects of various parameters on the achievable resolution have been quantified. The limits of coupling force and probe alignment, in this practical set, have been found as a minimum of 25 N and no more than 1 and 2 degrees respective roll and pitch angle. The successes of the wheel probe scanning approach led to the design and testing of an in-house, in-process ultrasonic inspection system for factory implementation. Simpler, and more robust in its design, this has been used to carry out inspections on numerous rejected samples, provided by the industrial partner. To make such a set-up more suited to the production line the design of a custom wheel probe has been outlined and costed.

4 Adaptive MA Beamforming

4.1 Introduction

This chapter reports on an adaptive and novel method ultrasonic phased array testing. Multi-aperture (MA) beamforming is used, with the exact configuration in which individual elements are activated to transmit and receive ultrasound optimised for the application. MA beamforming has previously been shown to increase frame rates, and hence inspection speeds, when compared to traditional linear beamforming, in both NDT as well as medical applications. The concept and process are verified and validated using C-scans taken from the same CFRP sample used in previous chapters.

4.1.1 Linear Scanning and MA Beamforming

The operation of PAUT traditionally involves what is known as linear scanning. One aperture, consisting of a single or group of elements, is excited by each pulse of the phased array. The active aperture in each pulse steps along the array in a linear fashion with many positions contributing to each frame. This leads to a low frame rate, the PRF divided by the number of pulses constructing each frame. This PRF is also subject to limitations set by PAC hardware and software as well as experimental parameters, such as the depth and bulk velocity of delay line and sample.

By contrast, MA beamforming involves excitation of multiple groups of elements to transmit several beams simultaneously, each in a different location along the array, thereby increasing the frame rate. The difference between these two methods is best

understood visually, as shown in Figure 4.1. Crosstalk between elements, as well as artefacts from nearby beams, will degrade lateral resolution. This overlap of beams is the main concern when applying MA beamforming. Therefore, it is common practice to include a gap of elements between apertures [145]. Increasing aperture spacing reduces the beam-contamination at the expense of reduced frame rate [55]. Obviously, the number of parallel apertures is limited by the number of elements that can be simultaneously handled by the PAC, both on transmission and reception.

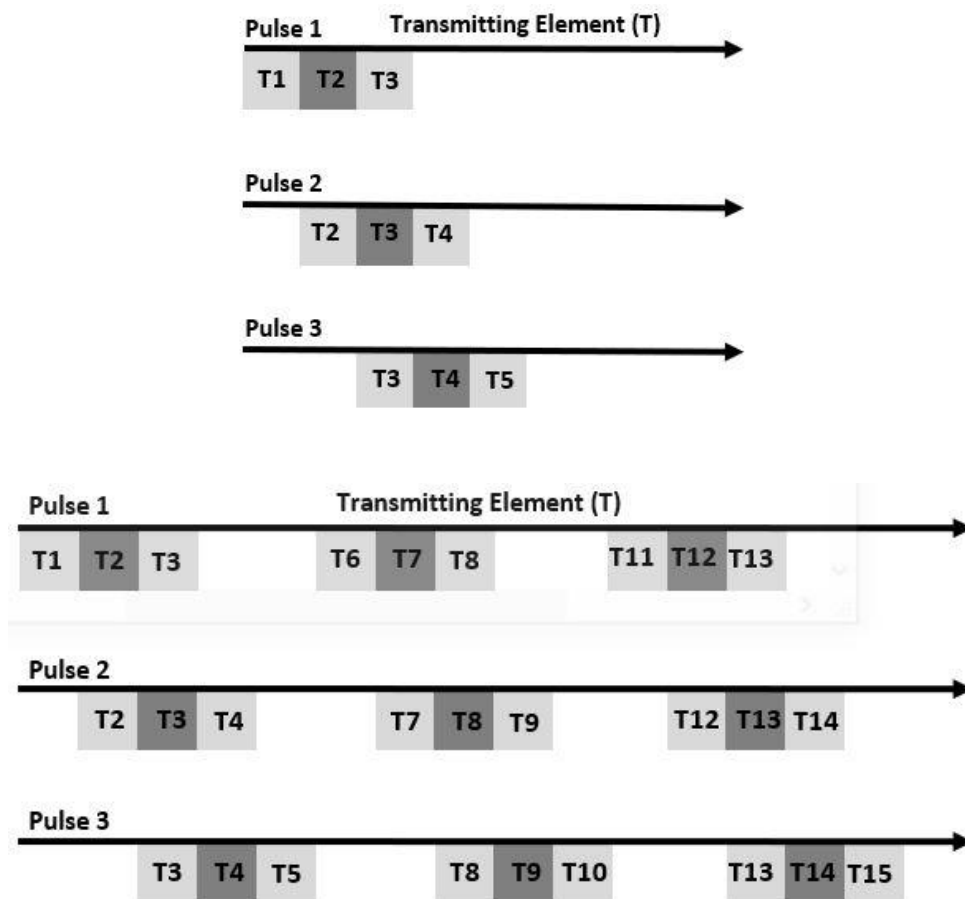


Figure 4.1. Schematic contrasting linear (top) to MA (bottom) beamforming for the first three pulses. In this example the aperture, step and MA gap size are three, one and two elements respectively.

MA beamforming offers the possibility of increasing the frame rate, and scanning speeds, under the same PRF [145][146]. High SNR can be preserved when there is limited beam-contamination. The use of multiple transmission elements has also been shown to increase inspection speeds in an FMC configuration. Increases of a factor of eight were reported in [119]. However, no scheme for adapting the aperture size and spacing, specifically to the inspection sample and target defect size, and thus keeping contamination to a quantifiable and acceptable level has been reported.

It must be noted that MA beamforming is most suitable in applications where the sample is planar. In this case, beam contamination between adjacent apertures is minimal and can be quantified. The lack of curved surfaces and use of a thin sample leads to limited issues regarding refraction and attenuation respectively. This allows for several apertures to be triggered simultaneously with the minimum necessary gap quantified using calibration data. Should a more complex sample be inspected, where adequate image quality rather than scanning speed is the main challenge, then other imaging methods are more appropriate. These include plane wave imaging, or the use of post-processing algorithms performed on FMC data. An example would be the total focussing method (TFM) where full FMC data is used, along with the sample geometry, to synthetically focus every point on the image.

Several additional considerations must be taken when comparing MA aperture beamforming to linear. During MA imaging, transducers receive a more complex backwall signal since the reflection from the bottom surface originating from the neighbouring aperture is also partly received. As the gap increases this effect reduces. Similarly, the acquisition length may have to be increased so that all the points from

the transmitted waveform are still received. Receiver gain may also need to be reduced to avoid saturation due to the increased total energy coupled into the sample [145][146].

4.1.2 MA in Medicine

The medical field employs a similar concept. Here, the simultaneous use of several pulses is known as Multi-Line Transmission (MLT) [147]. Frame rate increases are of benefit when imaging fast moving organs [148][149]. Examples of MLT are found in cardiac imaging since the characteristics of interest exhibited by the heart will typically change on much shorter timescales than, for example, the liver or kidneys [150][151]. As in NDT, the main limitation is beam-contamination and the potential for image artifacts. Several techniques for tackling this issue have been reported including Golay coding or the use of covariance matrices [152][153][154]. As in NDT, these techniques are applied either to the excitation pulses or in post-processing algorithms and not directly linked to the ultrasonic characteristics of the sample.

4.1.3 Defect Sizing Techniques

The -6 dB drop technique is a common tool in ultrasound inspection for feature sizing [129]. The size of a defect is defined using the spatial points where the amplitude has dropped past the -6 dB (50 %) point, as compared to the maximum defect response amplitude [130][131]. However, since the flaw response in the real world is far from an ideal curve, this technique can sometimes undersize a defect [132].

4.2 Autonomous Multi-Aperture Theory

The core concept allows for adaptive MA beamforming, whereby the optimum MA gap is based on the defect response decay, obtained by moving the receiving (R) element away from the transmitting (T) one. FMC datasets collected from the calibration sample are in the form of a 3D matrix corresponding to a time-sequence for every transmit and receive element combination. The resultant matrix is defined by T rows and R columns with the third dimension containing the number of samples in each time-sequence. Linear B-scans, with various apertures sizes and focal points, can be reconstructed from this FMC data and calibration defects characterized based on the amplitude of the ultrasound echo. These are obtained from the diagonal of the matrix. The aperture size on transmission and reception corresponds to the number of summed rows and columns respectively, as shown in Figure 4.2. Hole sizing is based on the -6 dB sizing method used with the extracted B-scans. Once a defect has been sized, the A-scan corresponding to the edge of the feature can be found. This is from a specific array element, the starting point for the MA algorithm and corresponds to T_iR_j , where $i=j$. The A-scans from this point all the way to $T_iR_{(j\pm n)}$ are analysed, taking the amplitude of the defect response within a time-window defined by the sample geometry and path length taken by the sound. The variable 'n' is set to allow for the received amplitude to have decayed sufficiently below the threshold value. Upon a shift of 'n' elements the signal amplitude is typically less than 10 % of that found at T_iR_j . Responses from both the right and left-hand side of the feature are considered, with a user-defined number of different starting elements allowing for averaging.

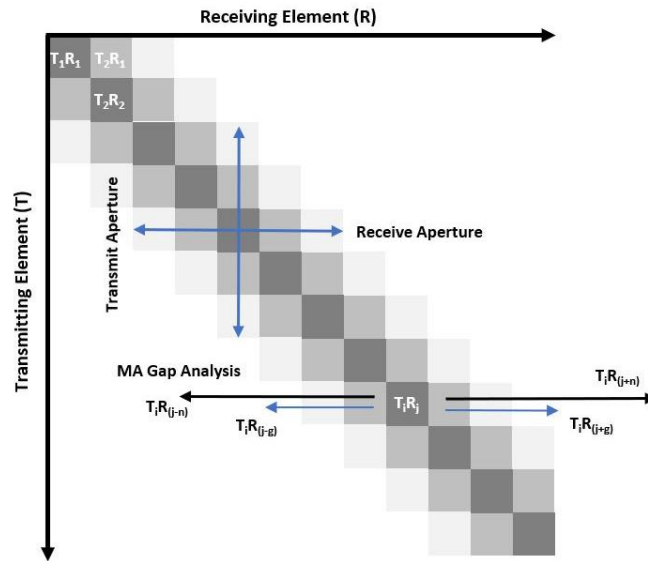


Figure 4.2. Schematic of FMC matrix to illustrate algorithm procedure.

The defect response amplitude will drop past a user-defined value at $T_iR_{(j+g)}$, where ‘g’ defines the minimum MA gap ($g < n$) and thus the maximum number of apertures triggered simultaneously. Necessary gaps are rounded up to the nearest element since it is not possible to fire a non-integer element number. Frame rates and resolutions are predicted and verified with B and C-scan images used to confirm that the MA focal laws produce an image in which a critical defect size can still be identified. In the results presented, the critical defect size is defined by the industry partner’s requirement of 3 mm. Therefore, the MA focal laws are chosen based on this calibration dataset and is autonomous and adaptive to the inspection sample. A flowchart best summarises this procedure and is shown in Figure 4.3.

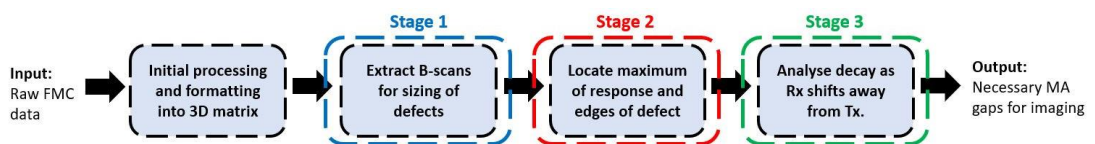


Figure 4.3. Flow chart describing the autonomous and adaptive MA algorithm.

4.3 Experimental Procedure

4.3.1 Hardware

The same hardware, described in Chapter 3, Section 3.3, is used both to acquire calibration data as well as carry out mock inspections for validation purposes using the final algorithm output. Again, hardware and software are interfaced within one LabVIEW environment, allowing ultrasonic data acquisition and robotic position to be handled using a single application. An image of the practical set-up, attached to the robot flange is shown in Figure 4.4.

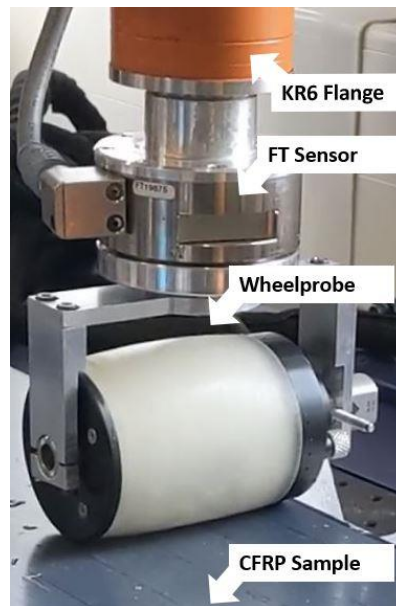


Figure 4.4. Image of the of the probe and associated hardware attached to the KR6 robot flange.

4.3.2 Resolution Definitions

Throughout this work, C-scan image resolution is defined as the average spacing between A-scans, each forming one pixel, in either axis. The scanning resolution is in the axis of the mechanical movement of the probe and a consequence of the number of channels, PRF and scan speed. These are further limited by the dimensions of the delay line, and depth of material. The array resolution is dependent on the phased array pitch and aperture step size. The algorithm designed to implement the autonomous MA concept operates on the FMC data acquired with the probe stationary and hole sizing results therefore refer to this array axis, unless otherwise stated. Since array and scan resolution are linked by the PRF of the controller, a reduction in the number of pulses required for one frame, increases the scan axis resolution. This is the key benefit of MA beamforming, since PRF is not wasted by sweeping the entire array using only a single aperture, as in linear beamforming.

4.3.3 Inspection Scenarios

Three inspection scenarios demonstrate the validity of this work. Scenario A applies classical linear beamforming demonstrating how the highest resolution can be achieved at low speed. This is the low speed, high resolution, reference scan. The same focal laws are used in Scenario B, but acquisition at higher speed leads to a far coarser spatial resolution. Scenario B is the high speed, and therefore reduced resolution, case. Inspection parameters used in scenarios A and B are detailed in Table 4.1.

Inspection Parameter	Scenario A (Reference scan)	Scenario B (High speed)
Parallel Apertures	1	1
Scan Speed	3.3 mms ⁻¹	22.1 mms ⁻¹
Theoretical Resolution in Scan Axis	0.8 mm	5.4 mm

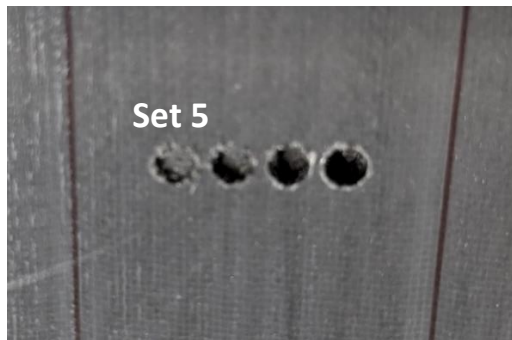
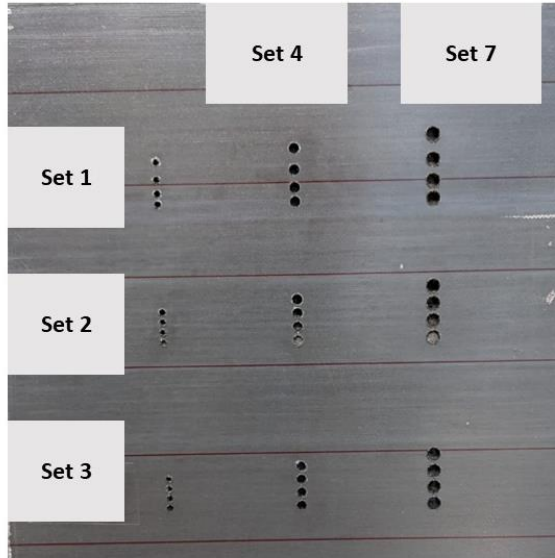
Table 4.1. Summary of inspection parameters relating to the first two scanning scenarios.

MA beamforming offers higher frame rates by simultaneous triggering of several apertures on the phased array. Firing all 64 elements simultaneously and obtaining 64 separate A-scans gives the maximum frame rate with one pulse per frame. This is known as ‘paintbrush’ transmission and has been shown to increase inspection rates albeit at reduced resolutions [120]. In such an acquisition strategy the frame rate is equal to the PRF and it can be simulated from FMC calibration data for hole sizing [120]. Despite the maximum energy coupled into the sample, the beam contamination leads to oversizing of defects or mischaracterisation since their responses bleed together. It has been demonstrated that such an inspection greatly overestimates the -6 dB size. The proposed adaptive and autonomous MA concept enables the optimum transmission and reception parameters, based on the ultrasonic propagation characteristics of the sample under inspection and minimum defect size, to be identified and applied in a third scenario: Scenario C. Focal laws facilitating the highest frame rate are used in this case and thereby a best-of both-worlds approach between scenario A and B is found giving both high scan speed and resolution.

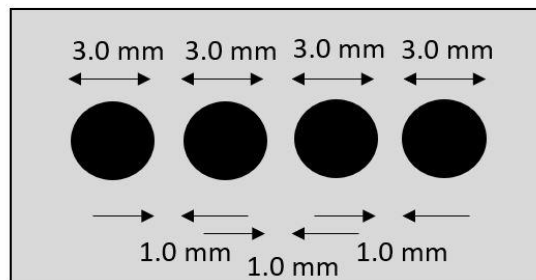
4.4 Calibration and Validation Samples

A calibration sample containing artificial defects, in the form of sets of series of four flat-bottomed holes is used to generate the reference FMC dataset. This calibration sample is shown in Figure 4.5. Defects are in sets with a variation in the depth, diameter or spacing. The calibration sample has been designed and machined specifically for the application in terms of the target defect size and spacing. It is thereby possible to suit the MA adaptive algorithm based on requirement. The industrial application presented in this paper currently requires an inspection accurate enough to confidently resolve individual defects of 3.0 mm, in their largest dimension, throughout the sample thickness and therefore the adaptive, autonomous MA concept uses a calibration set containing 3 mm defects spaced 1 mm apart at depths of 1-4 mm. This is calibration set 5 in Figure 4.5. Should a greater or lesser accuracy be called for, this can be implemented with FMC data from a relevant calibration defect set or sample and is thereby adaptive to each inspection requirement.

The calibration sample is a part of the same CFRP panel used in the validation section. A force of 30 N is applied to ensure good coupling, using a water film. Z-position is updated, based on force-torque feedback. The optimum receiver gain of 30 dB, as used in section 3.4.1, allows adequate SNR without any saturation from the shallowest defects. For experimental validity, these and A-scan gating are optimised for the acquisition of the calibration FMC datasets and then held constant throughout.



Calibration Defect Set 5, Plan View



Cross-Sectional View

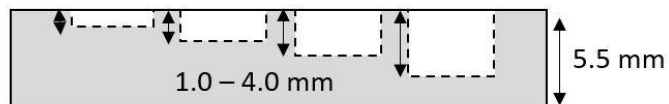


Figure 4.5. Image and specifications of calibration sample used to collect FMC data.

4.5 Results and Discussion

The algorithm flowchart, Figure 4.3, has the main stages highlighted for reference in the following paragraphs. The results presented are obtained working with data from calibration set 5, a defect size of 3.0 mm, spaced 1.0 mm apart and at depths ranging from 1.0 - 4.0 mm. Throughout the following imaging and defect characterisation sections a sub-aperture of four is used in both linear scanning and MA beamforming. This is chosen as the optimum point between lower SNRs, observed when firing one or two elements, and the detrimental effects of the defect-response being smeared over too large a proportion of the array, which is the case when employing six or even eight elements in each pulse. A four element sub-aperture allows 61 beams per frame, one complete sweep of the 64-element phased array as shown previously in Figure 4.1, and now illustrated by Equation 4.1 with the total elements, $N=64$, aperture size $A=4$, step size $S=1$, resulting in the number of beams or channels, $C=61$. A four-element aperture is held constant and used in the MA beamforming so that results obtained can be reliably compared to linear scanning, without the impact of changing aperture size.

$$C = \frac{(N - A)}{S} + 1$$

Equation 4.1

4.5.1 Sizing and Location of Calibration Defects

A -6 dB (50 %) change in amplitude, referred to the maximum in each defect, is chosen to be most suitable sizing technique based on results presented in 3.4. The size is determined by the beams either side of the peak response once the amplitude drops below 50 % of this peak. From the data collected and shown in Table 4.2, this method typically only oversized by around 15 %, compared to the known physical size. This is due to the aperture of four approach as detailed above, added to FMC data in post processing. Comparatively low SNRs, obtained from the composite panel, made the -12 dB (25 %) sizing method unsuitable. The magnitude of the ultrasonic response from non-defective sections often exceeded 25 % of the peak defect-value, meaning the data contained insufficient dynamic range to employ this technique. Next, the location of maximum defect response at each of the four depths is identified. The A-scan corresponding to the edge of the defect is located, again by the -6 dB method. This refers to the point where the backwall signal magnitude exceeds that of the defect. An element corresponding to the start and end of each defect is identified in the second stage, algorithm flowchart, Figure 4.3.

Hole Diameter (mm)	Hole Depth (mm)	Hole Sizing, FMC (Aperture 4) (mm)
3.0	1.0	3.5
3.0	2.0	3.3
3.0	3.0	3.6
3.0	4.0	3.7

Table 4.2. Results of defect sizing for calibration set 5 using FMC data and an artificial aperture of four.

4.5.2 MA Gap Determination

Analysis of data contained across the rows of the FMC matrix allows for the optimum gap size to be identified. By incrementally moving the receiving element away from the transmitting one the amplitude decay at which distance a new aperture could be fired in a MA scheme is selected. This is stage three, algorithm flowchart Figure 4.3, of the autonomous MA concept. The necessary gap, shown in, Table 4.3 is an average value from either side of each flat-bottomed hole. The responses, starting with edge elements, chosen by the -6 dB hole sizing technique, are analysed (as shown in Figure 4.6). Since element number is a discrete variable and has been interpolated to identify a distance on the array at which the response has decayed below -6dB, the response originating from elements either side of the identified must also be analysed with a mean value used for final MA gap determination. This procedure accounts for the step-like variation in amplitude caused by discrete phased elements. Again, it is not possible to take a value from a non-integer element number so the responses from either side must also be considered.

The curves, shown in Figure 4.6, correspond to the amplitude decay observed by moving from T_iR_j to $T_iR_{(j+n)}$, at a given location. The starting point, T_iR_j , is transmission/reception over the edge of the defect. This procedure is carried out either side of the defect and at every defect depth, the attenuation curve formed comparing responses across receiving elements for the same depth. Since the absolute values of response of each depth are not considered, with each curve normalised to the maximum found at that depth, no significant correlation between defect depth and amplitude spatial decay curve is expected. The amplitude decay is determined only

by the attenuation within the CFRP and inspection geometry, thus allowing the MA gap to be chosen based on the characteristics of the sample. Discrepancies between the curves are due to coupling and element response variations across the array. These are present since the probe is in a fixed position whilst FMC calibration data is acquired. To confirm this, several more FMC data sets are acquired with the probe moved along the array axis by ± 2 mm, to ensure different elements are used to generate the curves. Averages are calculated to show that there is no discernible trend. Each decay gives a necessary gap or five or six independent of defect depth.

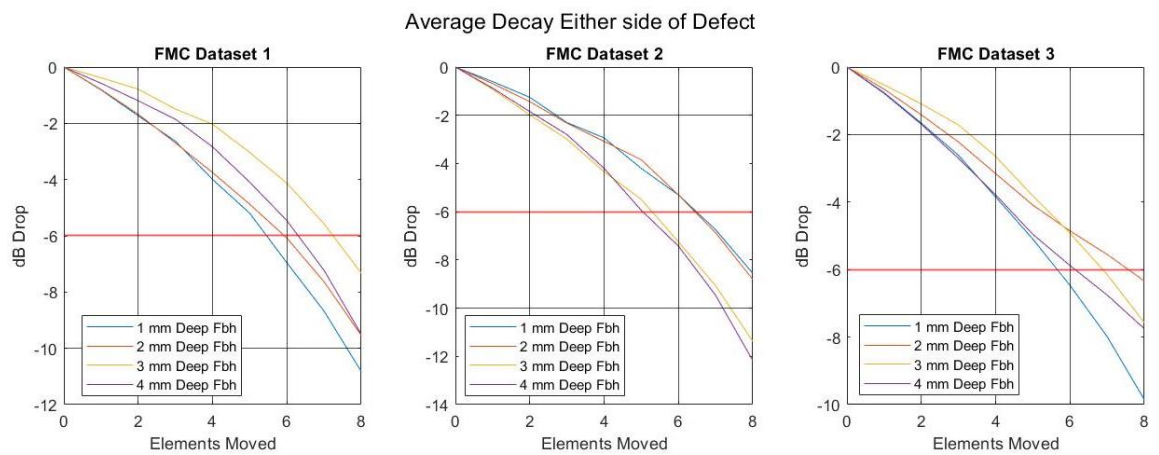


Figure 4.6. Decay curves observed by shifting receiving element incrementally away from the edge of each defect in calibration set 5. Data are obtained from three separate FMC acquisitions scanning four separate defects.

Hole Diameter (mm)	Hole Depth (mm)	Necessary MA Gap (FMC dataset 1)	Necessary MA Gap (FMC dataset 2)	Necessary MA Gap (FMC dataset 3)
3.0	1.0	5	5	5
3.0	2.0	5	5	5
3.0	3.0	6	5	5
3.0	4.0	5	5	6

Table 4.3. Algorithm-determined distance necessary to observe -6 dB drop in defect response magnitude and resultant necessary gap for MA beamforming.

The autonomous MA inspection concept chooses a necessary gap of five elements, based on the average array distance allowing a -6 dB drop and the known element pitch of 0.8 mm, and produces the corresponding focal laws. This can be seen from the results in Table 4.3. Calculating a mean value across columns 3-5 gives a value of 5.17. Since an integer number of elements must be used, the algorithm selects 5 as the optimum MA gap. With the four-element aperture approach, this allows for seven simultaneous apertures, and nine pulses (the first two shown in Figure 4.7) of the 64-element array to complete a full sweep and acquire one frame. The focal laws can then be written into the PAC for the validation section where outputs from the autonomous MA concept are validated using C-scans from a validation sample. An increase in inspection speed, when compared to a linear four-aperture sweep, by a factor of $61/9 = 6.7$ is made possible with no degradation in hole-sizing or defect detection capability.

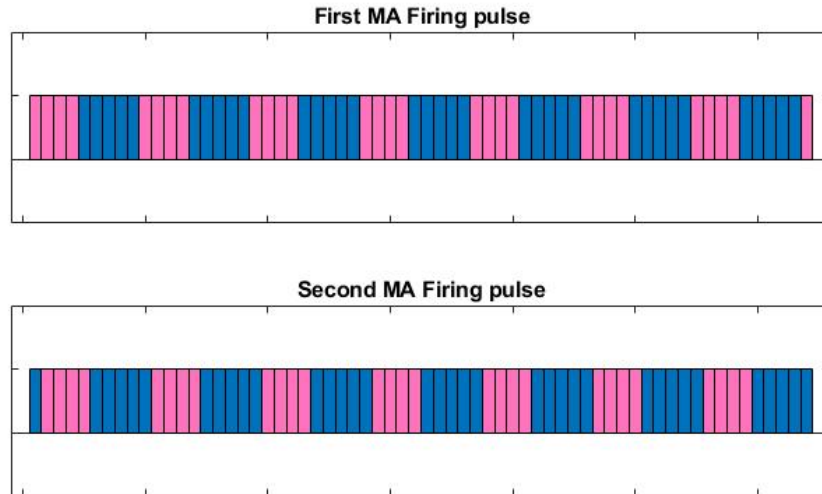


Figure 4.7. Schematic of focal laws written with algorithm-determined MA gap. Only the first two pulses of the necessary nine are shown.

To further enforce the chosen MA firing scheme a table of defect sizing for the calibration holes, scanned under each inspection scenario as well as the original FMC dataset, is generated (as shown in

Table 4.5). Scenario B is the same as Scenario A since scanning speed does not affect resolution in array axis and the hole sizing will yield identical results, provided the probe is in the same position when pulsed and covering the centre of the defects. B-scans obtained are also included to demonstrate image quality. Two variations on Scenario C, using a MA gap deliberately chosen to be either too small or too large (as shown in Table 4.4), emphasize the choice made by the autonomous MA concept. These cases exhibit firstly increased beam interference in the decreased gap case and secondly wasted PRF since more pulses than necessary are utilised to sweep across the entire array, in the increased gap case. Focal law parameters, B-scans and corresponding defect sizing are shown in Figure 4.4.

MA Firing /Parameter	Scenario C (Autonomous MA gap of 5 elements)	Scenario C (Decreased gap of 3 elements)	Scenario C (Increased gap of 7 elements)
MA Gap	5	3	7
Aperture Size	4	4	4
Simultaneous Apertures	7	9	6
Pulses per Sweep	9	7	11
Speed Increase compared to Linear Beamforming	6.7	8.7	5.5

Table 4.4. Summary of MA focal laws chosen by algorithm as well as ones with a gap two elements too large and too small.

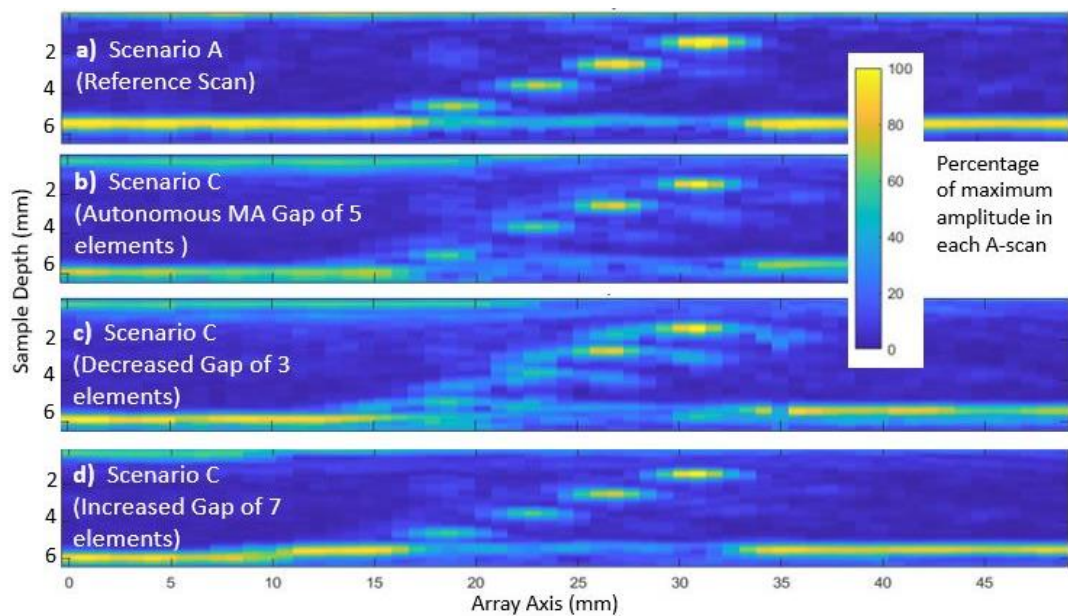


Figure 4.8. B-scans obtained with both a linear and three MA beamforming cases. The focal law parameters in each are as follows. a) Linear firing with a four-element aperture. b) MA firing with a gap of five elements chosen by the adaptive MA algorithm as the optimum size. c) MA firing with a decreased gap of three elements, chosen to be too small to prevent beam contamination. d) MA firing with an increased gap of seven elements, chosen to be unnecessarily large and thus wasting PRF for the same imaging quality. The results of defect sizing performed on each are presented in Table 5.5.'

Sizing results are typically within less than 0.5 mm, when comparing a linear sweep, applied experimentally in inspection scenario A, to one simulated using FMC calibration data (as shown in

Table 4.5). This is to be expected since within a FMC matrix is contained all the data which can be obtained using a given focal law. Validity of the proposed autonomous MA concept can be confirmed by the sizes found by Scenario C. These values are again within 0.5 mm of those found in the initial linear scan. Scenario B is not shown here but the same sizing is found provided the probe is positioned above the holes when firing. There is no difference between A and B in terms of beamforming, or array axis resolution, only in the movement speed. Using too small a gap oversized the holes significantly due to contamination between parallel beams. The reason for this is the significant echo received by an adjacent firing aperture from the same defect since the gap is not large enough to allow for a -6 dB decay from the edge of the feature. They are, however, not oversized to the same extent as in a paintbrush sweep applied to FMC data, where the entire array is pulsed. In effect, the benefit of spaced multi-apertures can already be seen, in comparison to paintbrush excitation, but the focal laws are not yet optimised.

When a gap larger than that determined using the adaptive MA concept is applied no additional advantage is seen in the imaging. The MA gap is already sufficiently large to accurately resolve the holes. In this case the defect response between adjacent apertures will have decayed well beyond the -6 dB point which was used to define the optimum gap within the algorithm. Therefore, values here are again very similar to scenario C (autonomous MA concept). The drawback here lies in the number of

pulses required per frame, which is two higher than in the optimised case. The potential speed improvement, at the same resolution, is therefore less, $61/11 = 5.5$ compared to $61/9 = 6.7$. One is effectively wasting PRF for the same image quality.

Hole Diameter (mm)	Hole Depth (mm)	Scenario A (Reference)	FMC (Ap. 4)	FMC (Paint)	Scce. C (Auto. MA)	Scce. C (Decreased gap)	Scce. C (Increased gap)
3.0	1.0	2.9	3.5	4.5	3.1	3.8	3.1
3.0	2.0	3.4	3.3	4.8	3.2	4.0	3.4
3.0	3.0	3.3	3.6	4.9	3.1	4.3	3.2
3.0	4.0	3.9	3.7	5.0	3.6	5.6	3.8
Average		3.4	3.5	4.8	3.3	4.4	3.4

Table 4.5. Hole-sizing of calibration data set 5 with FMC, linear and MA beamformed data, both autonomous MA gap as well as increased and decreased.

4.5.3 Validation Scans

To further demonstrate the validity of the chosen focal laws for both linear scanning as well as MA beamforming a mock inspection of an entire pultruded CFRP sample is performed. This highlights the effectiveness of the autonomous MA concept, and the inspection speed or resolution increases it facilitates. A three-pass raster with a 300 mm scan length is carried out, covering an area of 0.044 m^2 . The sample contains a series of 3.0 mm holes with a minimum spacing of 1.0 mm, shown in Figure 4.9.

This allows the proposed MA concept to be tested by imaging the same defect dimensions as in the calibration sample. Again, all three scenarios use a four-element

aperture to show the benefit of MA beamforming in comparison to a linear sweep with other parameters held constant. The C-scans generated by this mock inspection, along with defect sizing carried out on the data, can be seen in Figure 4.10 and Figure 4.11, respectively.



Figure 4.9. Sample containing a series of 3 mm holes, used for the validation.

Before proceeding, a point must be raised regarding data transfer rates and hardware limitations when implementing MA beamforming. The simultaneous acquisition of A-scans from nearly half the phased array elements is required since seven simultaneous apertures of size four are fired. Current acquisition hardware and software limits permit approximately a 7 kHz refresh rate whilst using linear beamforming, acquiring one A-scan per pulse. The multi-fold increase in data volume means that the speed increases, made possible by MA beamforming, must be demonstrated at a much lower PRF than would be the case in linear scanning. In these validation results, the near seven-fold scanning speed increase is shown at a PRF of 250 Hz, scanning at 3.3 and 22.1 mms^{-1} . These comparatively low speeds are

necessary to accommodate the lower PRF and continue to allow for adequate resolution.

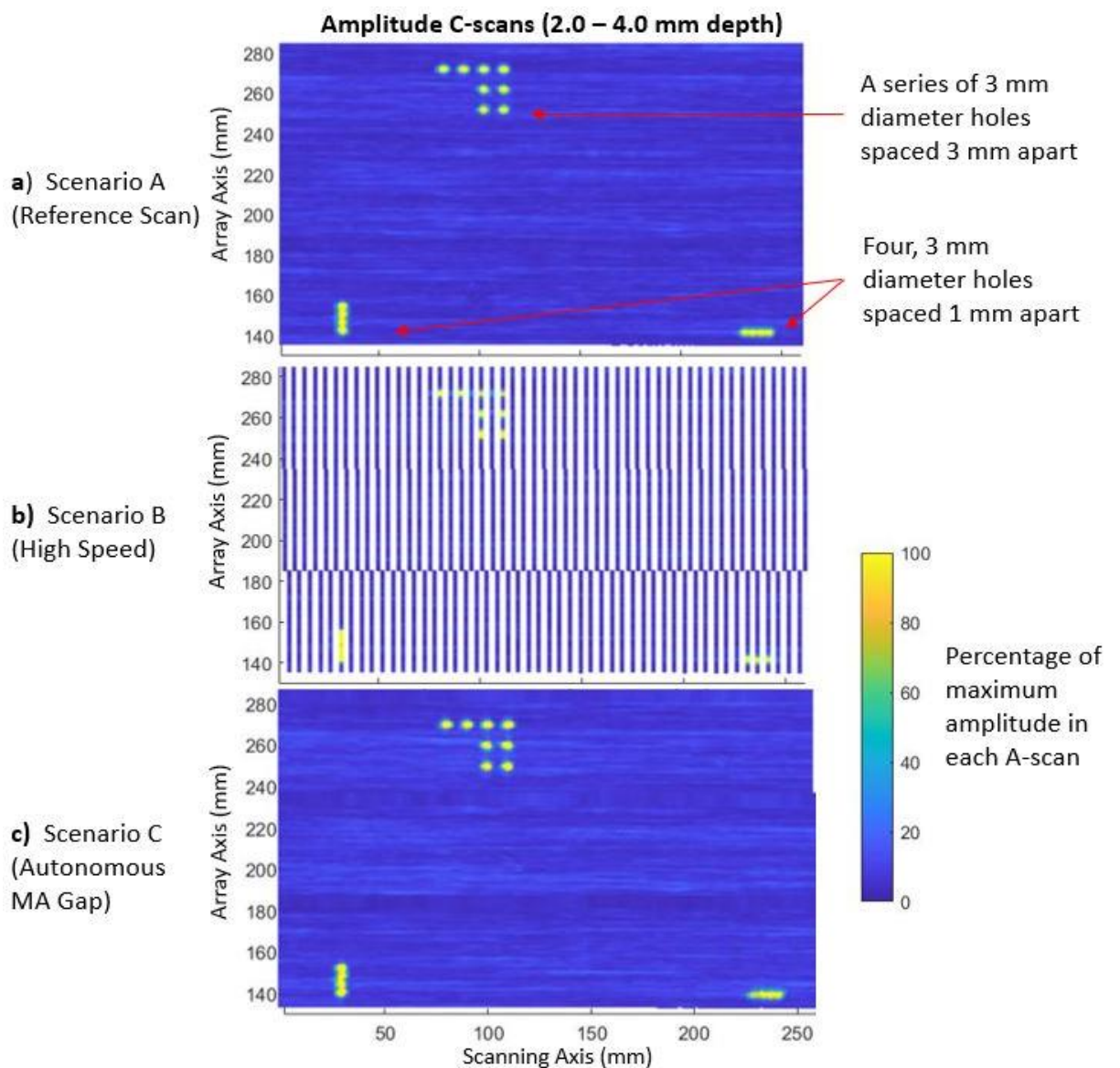


Figure 4.10. Validation C-scans from scenarios A-C. The inspection parameters for each image are as follows. a) The reference case, low speed using linear scanning. b) The high-speed case, using the same focal laws but a much higher scanning speed than in 'a'. c) Finally, the MA firing case with gap chosen by the autonomous MA algorithm. Both high resolution and reliable defect sizing is achieved at high scanning speed. The results of defect sizing for each scenario are presented in Figure 12.

Inspection Parameter	Scenario A (Reference)	Scenario B (High speed)	Scenario C (Autonomous MA)
PRF	250 Hz	250 Hz	250 Hz
Parallel Apertures	1	1	7
Scan Speed	3.3 mms ⁻¹	22.1 mms ⁻¹	22.1 mms ⁻¹
Theoretical Resolution in Scan Axis	0.8 mm	5.4 mm	0.8 mm
Actual Resolution in Scan Axis	0.9 mm	5.2 mm	0.8 mm

Table 4.6. Resolution comparisons and inspection parameters for each scenario.

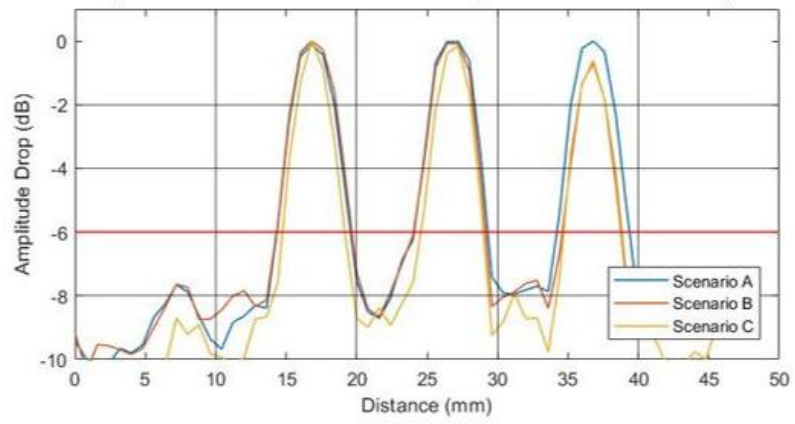
The adaptive MA scenario C yields the same resolution as reference scenario A but at a scanning speed nearly seven times greater. This comes at no degradation to defect sizing or identification ability and thereby validates the methodology of this work. Amplitude profiles (as shown in Figure 4.11) further enforce the results from hole-sizing (as shown in

Table 4.5). They are, however, created using data from the validation panel and a full three-pass raster with each inspection scenario and thus more impactful. Curves have been shifted along the x-axis, so the start of the defect corresponds to the same positions. The key comparison is Scenario A to C. Curve shapes and decay values are near-identical reinforcing the fact that there is minimal beam contamination between adjacent apertures and the correct gap chosen by the proposed autonomous MA concept. This has now shown to be the case in stationary B-scan imaging, seen in the previous section, as well as the mock inspection. A 6.7-fold frame rate increase has therefore been achieved with no detectable decrease in imaging or defect sizing.

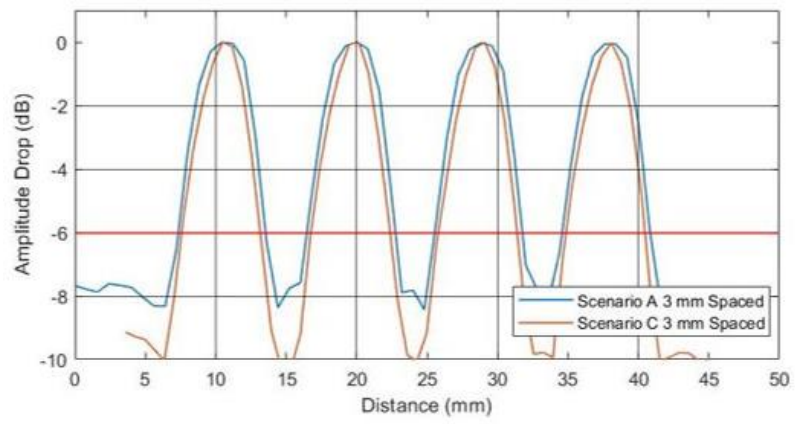
Again, Scenario B gives the same data provided the probe is above the defect when pulsed since array axis resolution is unaffected and all elements still used. This can, however, become an issue since the scan axis resolution in scenario B exceeds the defect size and therefore a defect can be missed.

Amplitude profiles in the scan direction follow the same trend with scenarios A and C near-indistinguishable. This also highlights that fact that square pixels have been achieved in the C-scans. Resolution in the array axis is determined by the element pitch of 0.8 mm with the chosen PRF and frame rate giving the same value in the scan axis. Scenario B is omitted since the higher scanning speed creates inadequate resolution in this axis to produce a similar plot.

Amplitude Profile Across 3.0 mm Spaced Defects in Array Axis



Amplitude Profile Across 3.0 mm Spaced Defects in Scan Axis



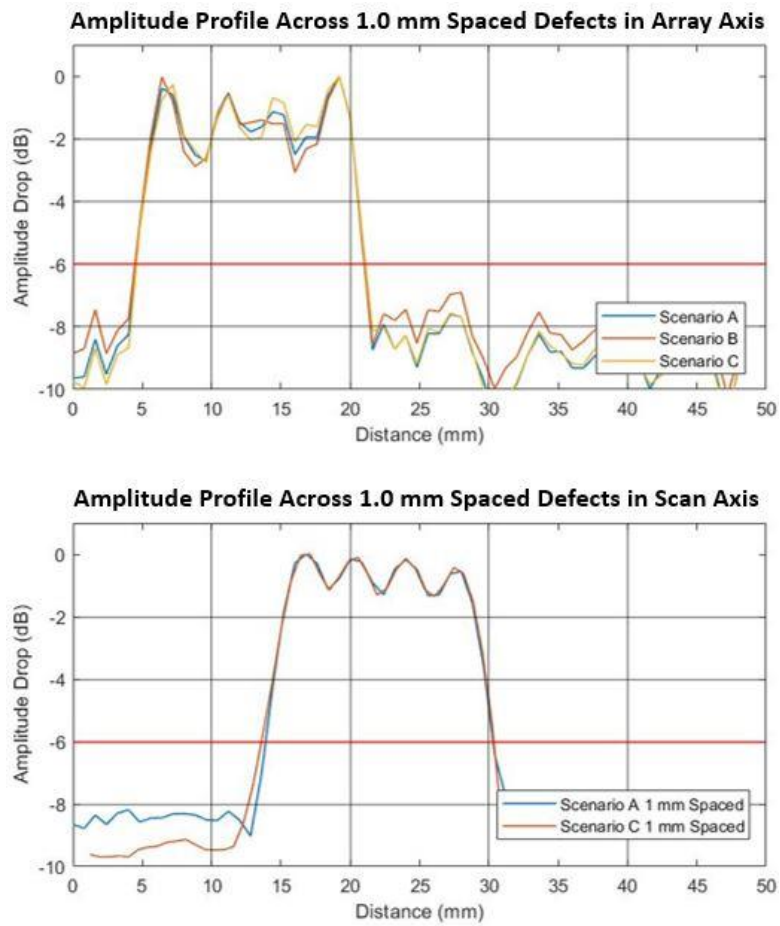


Figure 4.11. Comparison of amplitude profiles in both axis for 1.0 mm and 3.0 mm spaced holes in the validation panel using each inspection scenario.

4.5.4 PAC Firmware Update

As previously mentioned, the current operation of the PAC results in the MA beamforming theory only applied at comparatively low scanning speeds. The upper limits set by current data rates and refresh rates has led to the frame rate and resolutions advances, made possible by the method, only demonstratable at a PRF of 250 Hz, scanning at 3.3 and 22.1 mms^{-1} . This section will serve to add further explanation and outline the firmware update which will allow for the advantages of MA beamforming to be seen at the speeds necessary for manufacturing environment integration.

The transducer array is triggered by a series of PEAK NDT text commands, sent to the device via NI LabVIEW. Familiarization with the command references manual allows one to edit focal laws and adjust common inspection parameters so to suit the operation of the phased array to the current application [155]. The ‘select amplitude reporting mode’ command, AMP(S), allows the user to select the amplitude and time base data from each test to be reported back to the device and subsequently saved. The two options relevant to the application discussed in this chapter are AMPS 3 or AMPS 13. These permit for either one summed A-scan from all channels in the test, or for individual A-scans, from each channel in the focal law, to be reported and saved. AMPS 3 is used for linear beamforming since only one A-scan is required per test, the aperture being swept across the array incrementally. The same mode applied to MA beamforming results in all sub-apertures being summed to one amplitude-time series, only one A-scan saved, and the use of several apertures thereby erased. Therefore AMPS 13 must be applied so that all channels individually report. The

summing of separate sub-apertures is then performed in post-processing using all the individual amplitude time-series. The schematic shown in Figure 4.12 best illustrates the use of each amplitude reporting mode applied both to linear and MA beamforming.

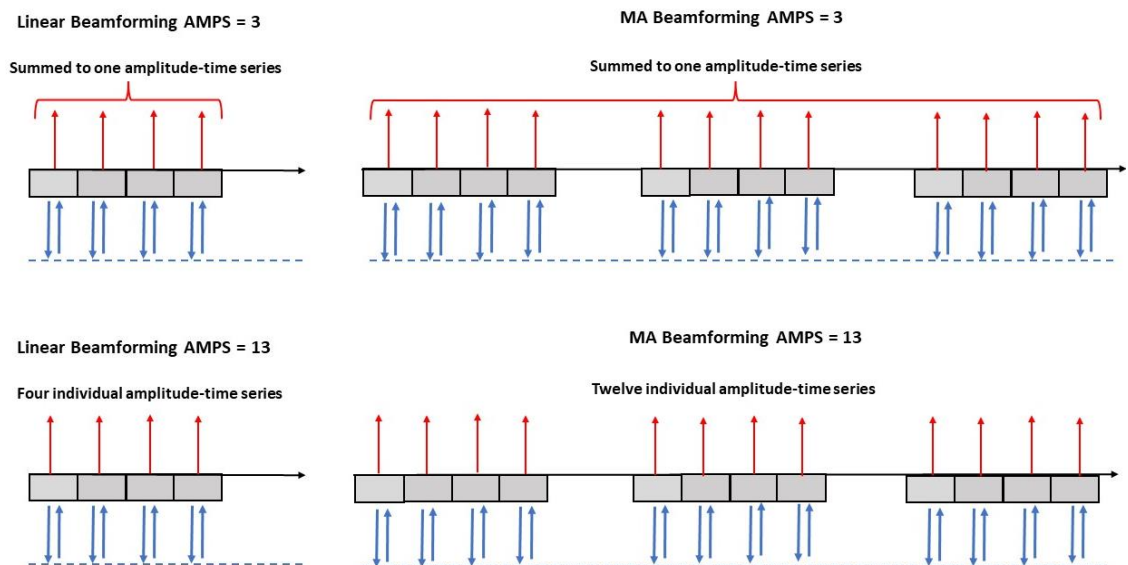


Figure 4.12. Schematic detailing the saving methodology applied during AMPS 3 and 13 commands, applied to both linear and MA beamforming.

The result of this limitation is that all individual A-scans must be recorded and processed through the LabVIEW acquisition procedure and several times more data, than is ultimately necessary, is processed. This is the underlying reason why the MA beamforming improvement to frame rate, scanning speed and resolution has only been presented as much lower PRF values giving much slower scanning speeds. To tackle this, a hybrid saving methodology, shown in Figure 4.13, would be necessary. In this hybrid approach, summing would only be performed on each sub-aperture, not across the entire array and the use of multiple simultaneous transmission retained.

In combination with a higher data rate link and optimised saving methodology within LabVIEW, such a firmware update would then allow for the same MA beamforming scanning speed increase to be demonstrated from, say, $100 - 670 \text{ mms}^{-1}$.

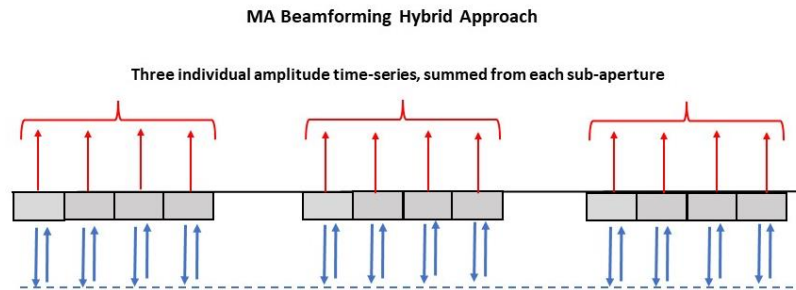


Figure 4.13. Schematic detailing the desired hybrid saving methodology to optimise the PAC operation for MA beamforming

4.6 Conclusions and Future Work

The presented MA beamforming concept offers a method to increase inspection frame rates and hence inspection speed, all while maintaining imaging spatial resolution. An adaptive autonomous MA inspection methodology and concept, that optimises the gaps between apertures to the sample in question, has been developed, tested, and validated. For this, FMC data from a calibration panel was used. The highest frame rate achievable, whilst still being able to reliably identify the critical defect size was identified.

Scenarios A and B demonstrated linear beamforming using scan speeds of 3.3 and 22.0 mms^{-1} and resulting in scan-axis resolutions of 0.8 mm and 5.4 mm respectively. In Scenario C, the optimised MA beamforming approach allowed for a 6.7-fold increase in frame rate and yield a resolution of 0.8 mm at a 22.0 mms^{-1} scan speed. This scenario offered both the best resolution and highest scan speed using MA beamforming. Similar resolution was only achieved using linear beamforming in Scenario A at a far lesser inspection speed. Defect sizing results and C-scans of entire panels validated the choice of focal laws, MA gaps and therefore the validity of the algorithm.

Results have been presented for the inspection of a CFRP panel used in wind turbine blade construction. However, the method is flexible and adaptable to samples of different thicknesses, ultrasonic propagation properties and critical defect sizes. The work is significant in highlighting the potential for MA beamforming to progress the performance of repeatable high speed robotic and automated NDT inspection activities. The application of this MA method to GFRP blade sections would,

however, pose significant challenges. Modern wind turbine blades possess geometrically complex shapes due to the continuously changing aerofoil sections between root and tip. UT inspection of such components needs to tackle coupling issues, refraction of sound within the sample, and the high levels of attenuation in GFRP. Any future work, expanding the application of this MA method, would need to address these. As detailed in the introduction, work presented here focusses on blade sub-components. These CFRP panels are used to form a structural beam, within the glass fibre, and are thin, plate-like, structures. From an ultrasound inspection point of view, they exhibit far preferable characteristics.

Another avenue for future work is the use of higher speed, optical data links as well as optimised saving structures to enable the frame rate and resolution increases to be applied at much greater scanning speeds. Currently, results have only been demonstrated at comparatively low values. As discussed, this is a hardware limitation with the current data-transfer rate shown to be close to that permitted by the hardware at one's disposal for this body of work.

The theory proven is sound and from an ultrasonic inspection point of view there is no reason that the speed increase cannot be executed at a 100 mms^{-1} starting point. The same focal laws would then allow for up to 670 mms^{-1} inspection speed utilising more efficient data transfer and processing. These values make the technology beneficial in a manufacturing environment as a powerful tool to address NDT bottlenecks.

5 FVF Screening and Fibre Directionality

5.1 Introduction

The FVF of a composite plays a key role in determining the final strength and stiffness of a part as well as influencing the ultrasonic bulk velocity. In this chapter, a novel screening technique for FVF, based on the angular dependence of the sound velocity with respect to the composite fibre direction, is presented. Following on from this, the work is extended with the aim of using the same anisotropy curves to determine the dominant fibre direction. The method is introduced and validated by inspection of the same composite panels reported on in previous chapters. The work offers significant potential in terms of factory implementation of NDT procedures to ensure final parts satisfy standards and certification by ensuring any FVF inconsistencies are identified as early in the manufacturing process as possible.

Whilst ultrasound inspection is a well-established NDT technique, the application to composite imaging presents significant challenges stemming from the inherent anisotropy of the material. If this is not considered, then defects can be missed, or their location incorrectly identified [156][157]. The velocity has a strong dependence on the angle made with the composite plies and therefore imaging algorithms must be modified to include the directional-dependent velocity profile [34].

5.1.1 Composite Material Structure and FVF Definition

A fibre reinforced polymer composite is formed by the combination of load-bearing fibres and a resin matrix, holding these in a fixed structure. These fibres can be glass, carbon, or natural materials such as hemp or cotton, often arranged in layers with alternating orientation so that the final material's elastic properties are constant in at least one plane. It is important to distinguish between the fibre volume fraction and porosity level. The fibre volume fraction is the percentage of the composite taken up by the fibres and typically in the range of 50-70 %. From a geometric analysis, FVFs higher than 90 % are impossible, due to the gaps occupied by resin, even when the fibres are arranged in a t sequence, achieving the maximum FVF. A square stacking would give a maximum of 78 %. Both these cases are illustrated in Figure 5.1. In practice even this is difficult to achieve with values higher than 70 % not commonly found in unidirectional fibre composites [32].

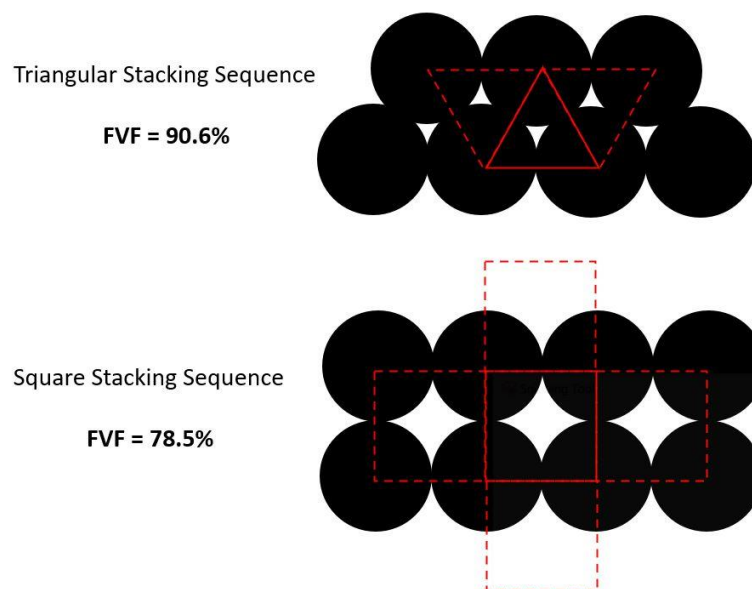


Figure 5.1. Schematic detailing a cross-sectional view of a composite showing fibres and the geometry calculations yielding the maximum FVFs.

The practically achievable FVF is also dependent on the fibre architecture as well as the method of manufacture, principally the pressure applied during the curing process, with typical CFRP laminates having FVFs around 60 %. Investigations of achievable FVF for both woven and unidirectional fibres using no consolidation pressure, vacuum infusing and high-pressure autoclave treatment, found that only with unidirectional fibres, in the form of plies or simple pultrusion, and 5-7 bar autoclave infusion could FVFs in the 60-80 % range be achieved [158].

In an ideal composite, the other part will only be the resin material. However, air trapped, as a result as the layup and curing process can result in voids and porosity. Porosity is therefore defined as the void volume fraction, typically ranging from 0-5 %. This can take a variety of forms depending on the characteristic size of the feature. A porosity value of 2 % is seen as an acceptable threshold in the aerospace sector as well as a range of other applications [159]. Porosity values below 4 % has been found to have a negligible effect on the strength of fibre reinforced composites [160]. Beyond this, a high void content indicates that the resin has not thoroughly embedded the fibres and the mechanical properties are thus detrimentally affected due to inadequate adhesion between layers [161]. Porosity can lead to fibre fractures and large areas of porosity, actual voids, can be the source of crack initiation and consequent delaminations [162].

5.1.2 FVF Effect on Properties

FVF, level of porosity, as well as the fibre orientation and layup architecture are key in determining the mechanical properties of carbon composites [158][163][164]. The rule-of-mixtures may also be used to determine the density of composite and other properties such as Poisson's ratio, strength, thermal and electrical conductivities in the fibre direction, provided the sample is unidirectional [165]. Effect of FVF on stiffness and strength, fracture toughness, typical damage mechanisms, as well as their evolution, are detailed in [158][166][167][168][169].

A FVF of 60-70 % in CFRP has been shown to result in optimal mechanical properties [170]. This was demonstrated for an automotive application in the design of a composite suspension in [158]. Increasing the FVF from 40 % to 70 %, yielded a linear relationship between tensile properties. A greater FVF, within this range, giving a greater strength in the final composite material since the fibre strength is greater than that of the matrix material. However, beyond 70 % there was decrease in the strength owing to insufficient resin to wet the fibres producing a more brittle part [158]. The upshot of this could be delaminations and kissing dis-bonds within the material as a consequence of shear stress developed between the lamina [158]. It was found that a FVF in the range of 60-70 % struck an optimum point.

5.1.3 Conventional FVF Measurement

FVF is commonly determined through destructive means. This can be achieved by measuring the weight of a small sample before and after burning the resin away by acid digestion [161]. The sample is exposed to a highly oxidising acid at elevated temperature until the resin matrix is completely dissolved. FVF determination is then a case of weighing the remaining fibres and expressing this a proportion of the total composite volume [171][172]. The most common chemistry used for composites of this type are polyesters, vinyl esters, polyurethane, and epoxies. These substances are usually very inert towards most solvents making chemical digestion difficult.

The industry standard, ASTM D3171-22, to determine FVF is based on this method [173]. After digestion, ignition, or carbonization, by one of eight procedures, the fibres are essentially unaffected. This allows for calculation of both weight and volume of both constituents. Using the composite density compared to these volume fractions also yields the void content and the level of porosity as a percentage [174]. The standard details a second method applicable only to laminate materials of known fibre area weight, and calculates reinforcement or matrix content using the thickness of the laminate [173].

Conventional FVF measurement is a form of destructive testing and comes with inherent drawbacks. Firstly, it is time-consuming, and therefore unfeasible to integrate seamlessly into a manufacturing workflow. Resin burn-off takes one day of preparation before the testing can be carried out. Acid digestion is an even longer process and typically takes two days until only the composite fibres remain. Both methods involve hazardous chemicals, bringing with them additional safety concerns

and procedures. For glass fibres, digestion can be performed in one step. However destructive FVF measurement of carbon fibre composites requires two distinct stages. Step one is carried out within an inert atmosphere where the matrix is degraded to carbon ash. The second step, performed in air, is to remove this residual ash. Regardless of which method chosen, it is challenging to take additives or fillers into account. FVF can only be determined precisely if the exact content of these is known. Alternatives exist and are described in [163][175][176][177]. These include optical microscopy and the use of carbonization instead of acid digestion. The result of carbonization is the same, in that only the fibres remain for weight and volume determination. Optical microscopy-based techniques allow for the FVF to be determined by image analysis but again this is a destructive technique, involving cutting up a section of sample. These methods are also time consuming, and in most cases, only take a small sample size into account, thereby reducing confidence levels across a larger component. Finally, and also based on the rule of mixtures and knowledge of the two constituent components, the FVF can be determined through Archimedes principle provided the exact volume can be determined using a 3D scan technique [177].

5.2 Ultrasonic FVF Measurement Theory

A brief introduction to the sample and ultrasonic inspection hardware is now given. This is necessary at this stage to clarify the parameters referred to in the ultrasonic FVF measurement theory. A more thorough description of CFRP panels inspected and experimental set-up is given later after the measurement theory is detailed. A CFRP sample, from the previously described turbine construction process is used to demonstrate this theory. PAUT is carried out using a self-contained water-delay line and dry coupling medium to transmit ultrasound into the sample. Figure 5.2, shows a schematic of the inspection set up, the parameters of which are referred to in the following paragraphs. The mathematical theory behind the proposed approach for ultrasonic determination of FVF, is based on a ray propagation model of this practical set-up. The model is applicable to any phased array inspection comprising a delay line, coupling and sample with known thicknesses and ultrasound velocities, with the example shown here for the application presented in this chapter.

Similar examples of such models, used to analyse ultrasound data, can be found in literature and applied, for example, to calculate the thickness of a corrosion layer formed after prolonged exposure of the composite in a corrosive environment in [178]. A calculation is based on sample geometry, probe separation and varying sound velocities. Similarly, a ray propagation model is used along with pulse echo and through transmission data to determine the velocity anisotropy in [34]. The proposed FVF estimation approach presented here, differs from [34], in that only one phased array is used, with the transmission and reception apertures acting as the separate transducers. Also, three layers of material are considered and the velocity as

a function of angle in the third layer, the CFRP, is calculated. This angular variation is created by increasing the gap between transmission and reception apertures on the phased array as shown in Figure 5.2.

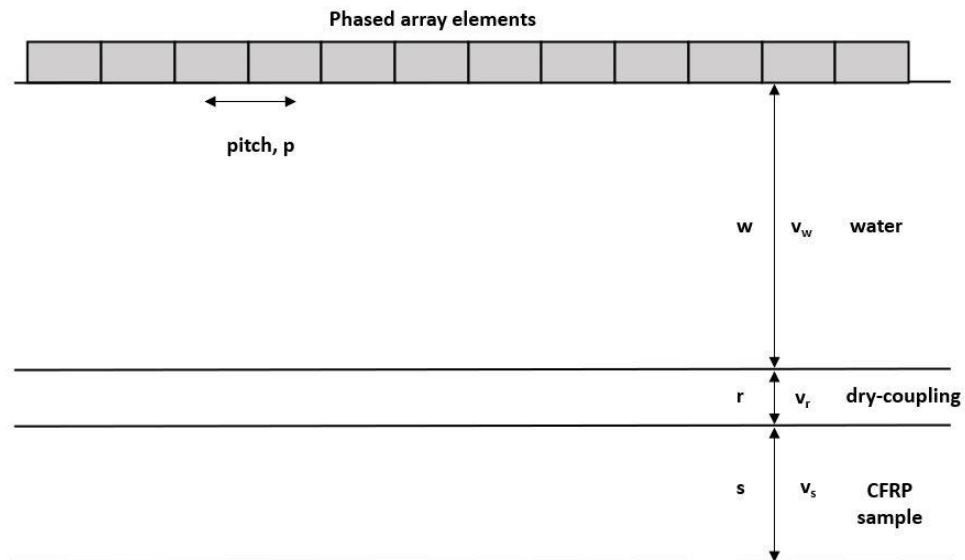


Figure 5.2. Schematic of the phased array inspection set-up.

Two separate acoustic paths corresponding to front and back wall echoes are modelled and analysed. The minimum distance, shortest propagation time, is assumed for both. Firstly, the propagation angles and distances are calculated using Snell's law, Equation 5.1, as well as the known bulk ultrasonic velocity in the delay line, dry-coupling medium, and sample under inspection at normal incidence. Figure 5.3. illustrates the parameters of relevance from the experimental set-up. The values of these, detailed in Table 5.1. must be known as must the panel thickness. Since the velocity influences the ray propagation angles, by Snell's law, which in turn are used to calculate the velocity as a function of angle to the plies, the thickness used at the start of the algorithm cannot be dependent on the velocity output. It must be obtained

from a separate measurement and used as an input. At each interface Snell's law (Equation 5.2) applies, with refraction angle at interface one being the incident angle at interface two, see Figure 5.4.

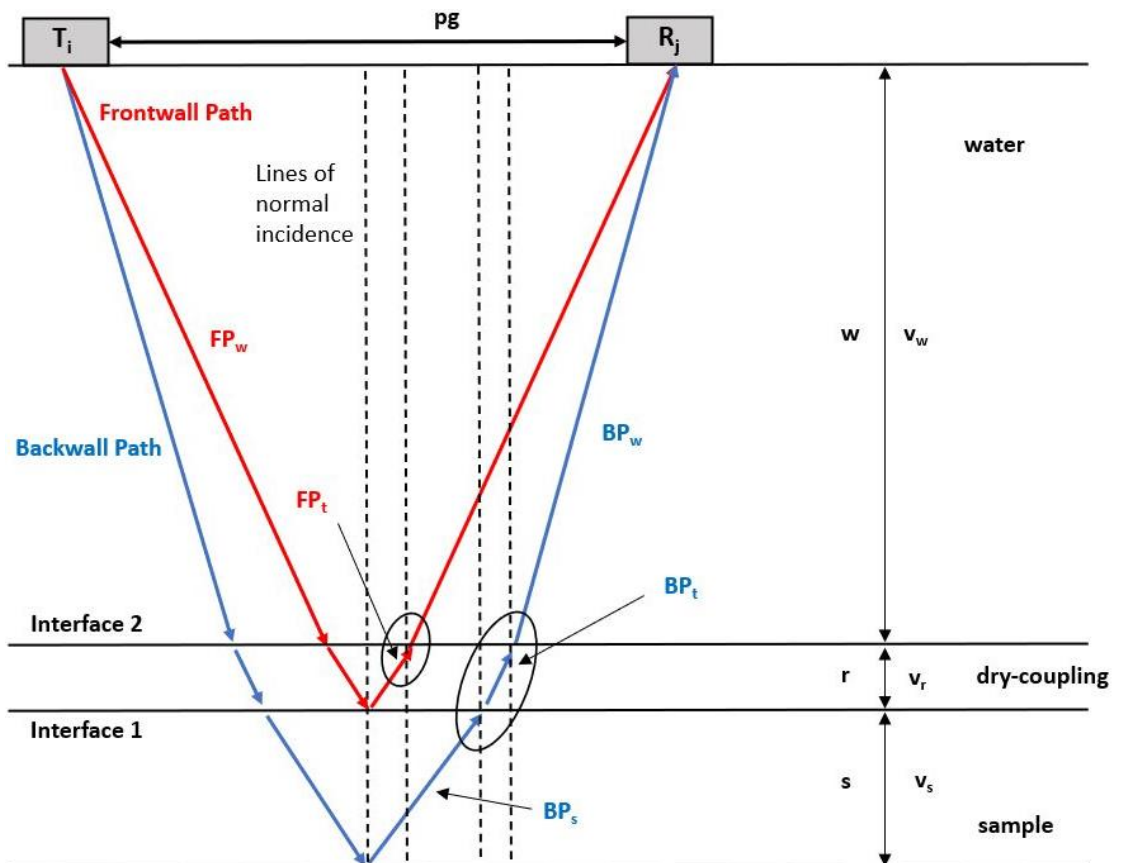


Figure 5.3. Schematic illustrating the geometry of wheel probe and sample in a cross-sectional view. The interfaces analysed using Snell's law, for both ray propagation paths, are circled, and expanded.

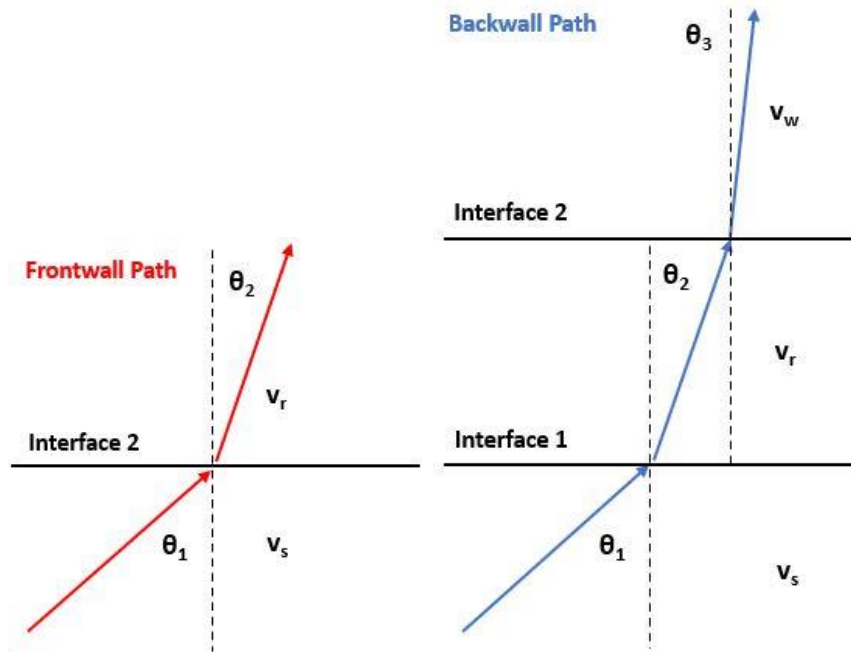


Figure 5.4. Schematic illustrating Snell's Law for both propagation paths.

$$\frac{\sin\theta_1}{v_1} = \frac{\sin\theta_2}{v_2}$$

Equation 5.1

It must be noted here that the angles are not the same in the above paths since they refer to different acoustic paths. The axial distance moved across the array is then given by Equation 5.2.

$$d_{axial} = \frac{pg}{2} = s \tan\theta_1 + r \tan\theta_2 + w \tan\theta_3$$

Equation 5.2

Where s, r and t are the thickness of sample, dry-coupling medium, and water delay line, respectively. The angles θ_1 , θ_2 and θ_3 in each medium are defined with respect to the normal. The physical distance along the array, between transmission and

reception elements, is twice d_{axial} and calculated from the number of elements between transmission and reception, g , and the phased array pitch, p .

This calculation is carried out for both the front and backwall propagation path thus yielding different angles. These, along with the thickness of delay line and sample give an expression for the angles of incidence and refraction as function of the distance shifted across the phased array for both the front and backwall echo. The whole procedure is repeated for every transmission and reception combination making up a full FMC matrix.

Next, the time delays corresponding to each step of these propagation path can be computed using the inspection geometry and speed of sound, Equation 5.3 to Equation 5.7. Variable names are defined such that FP_w and BP_c correspond to the time delay corresponding to the front wall path in water and backwall path in coupling respectively. It must be noted that angles are not the same in the front wall and backwall path.

$$FP_c = \frac{r}{v_r \cos \theta_1}$$

Equation 5.3

$$FP_w = \frac{w}{v_w \cos \theta_2}$$

Equation 5.4

$$BP_c = \frac{r}{v_r \cos \theta_2}$$

Equation 5.5

$$BP_w = \frac{w}{v_w \cos \theta_3}$$

Equation 5.6

$$BP_s = \frac{s}{v_s \cos \theta_1}$$

Equation 5.7

Individual A-scans are extracted from a FMC matrix, the general structure of which is shown in Figure 5.5.

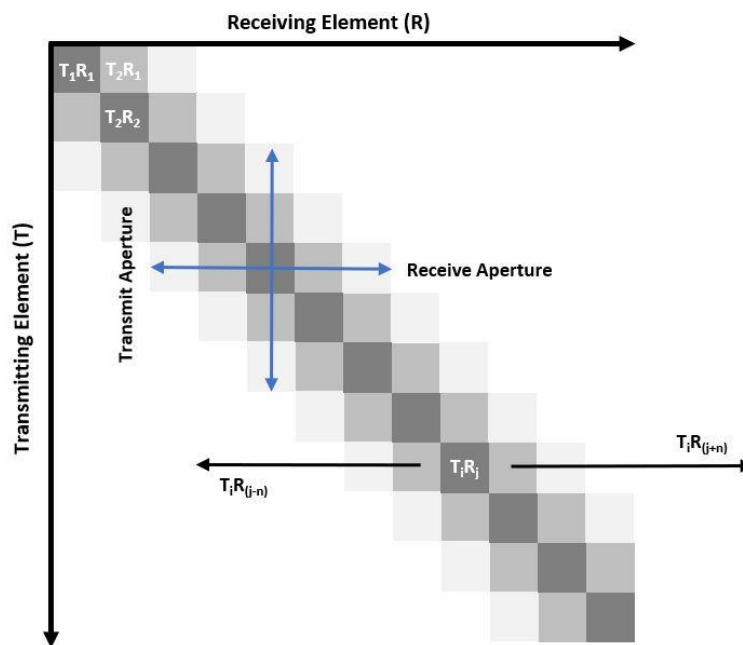


Figure 5.5. FMC definition showing the structure of matrix containing A-scans from every possible transmit and receive combination. The angular variation is achieved by investigating the effect of shifting the reception element whilst transmission is constant.

The time delay, ' Δt ', between front and backwall echo is given by Equation 5.8 and illustrated in Figure 5.6. As is common practice with ToF calculation in various imaging algorithms the arrival time is determined from the Hilbert peak, thereby accounting for both phase and amplitude variation, not the merely RF waveform. Beyond the 1st critical angle, shear wave peaks are recorded alongside longitudinal ones, on each A-scan. The correct front and backwall peak, corresponding to longitudinal waves, must be identified based on amplitude and location relative to the maximums in each scan. Using the propagation path and time delay between front and backwall echo, the speed of sound at angular incidence in the sample, v_s , is isolated. Combining Equation 5.3 to Equation 5.7 with Equation 5.9 yields Equation 5.10. Repeating this procedure across the range of axial distances, A-scan traces in a FMC dataset corresponding to $T_i R_{j \pm 25}$, the velocity in the sample as a function of angle shifted from normal propagation is calculated.

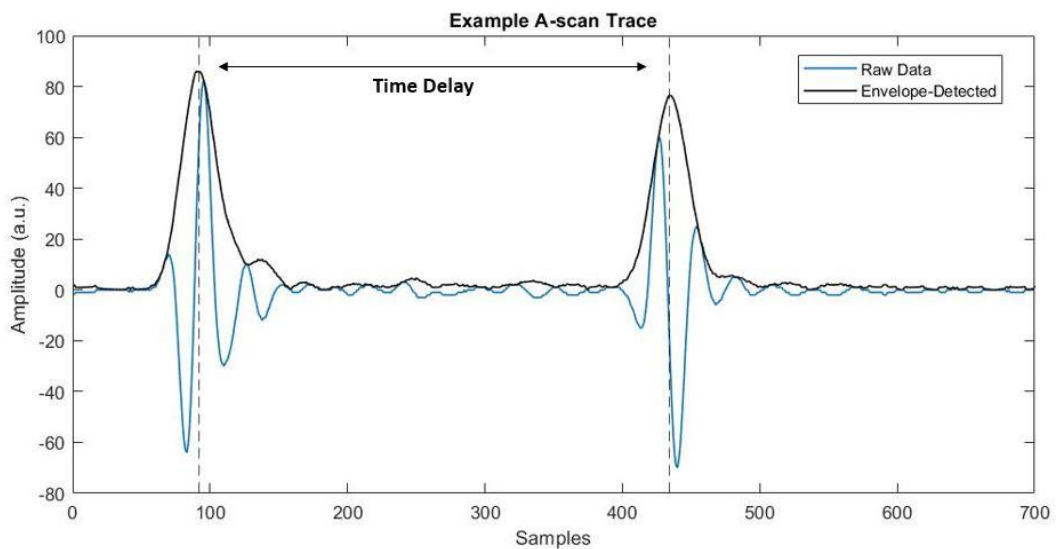


Figure 5.6. Example A-scan, highlighting the delay between front and backwall response as well as the envelope-detected using the Hilbert Transform.

$$\Delta t = \frac{(pos_{back} - pos_{front})}{sampling}$$

Equation 5.8

$$\frac{\Delta t}{2} = (BP_s + BP_c + BP_w) - (FP_c + FP_w)$$

Equation 5.9

$$v_s = \left(\frac{\cos\theta_1}{s} \left(\frac{\Delta t}{2} + \frac{r}{v_r \cos\theta_1} + \frac{w}{v_w \cos\theta_2} - \frac{r}{v_r \cos\theta_2} - \frac{w}{v_w \cos\theta_3} \right) \right)^{-1}$$

Equation 5.10

5.3 Experimental Hardware

More specific parameters of the sample, inspection geometry and phased array are necessary to give quantitative results to the FVF measurement theory. These samples are flat and planar pultruded CFRP with a thickness of 5.1 mm and width of 195.5 to 200.5 mm, the same as used throughout Chapters 3 and 4.

The CFRP panels have FVFs in the range of 60-70 %. Exact values are obtained from the supplier, SGRE whom conducted both in-house tests, using acid digestion, as well as a third-party FVF measurement. This was carried out by the IMA 'Materialforschung und Anwendungstechnik' in Dresden and in accordance with standards ASTM D3171, Method 1, Procedure B [173][179]. Three separate FVF samples are used in this work with FVFs of 60.5, 66.3 and 69.9 %. These values will be referred to as the known values in subsequent sections of this chapter.

The same experimental hardware as utilised in Chapter 3, section 3.3 and Chapter 4, section 4.3.1, is again used for this work. That is, phased array ultrasonic testing is carried out using an Olympus 5 MHz, 64-element array with pitch and height of 0.8 and 10.0 mm respectively. The fibre diameter of the CFRP sample is approximately 0.007 mm, surrounded by the resin matrix. The resultant wavelength from a 5 MHz probe in the composite material is 0.6 mm. This is a difference of three order of magnitude with the material heterogeneity on a scale much smaller than the inspection wavelength.

The array is controlled by a PEAK LTPA phased array controller supporting 64 channels on both transmit and receive. The self-contained water delay line and

acoustically optimised coupling medium removes the need for liquid coupling, pumping equipment, or immersion tanks, often used in ultrasonic inspection. The risk of water ingress into the sample is thereby negated. Hardware and software are interfaced within the LabVIEW environment. Previous publications have demonstrated the effectiveness of similar set-ups when applied to PAUT of composite aerospace components [56][119]. Table 5.1 detailing thicknesses and sound velocities referred to in Figure 5.2.

Inspection Parameter	Value
Pitch, p	0.8 mm
Water delay line thickness, w	24 mm
Dry-coupling thickness, r	1 mm
CFRP sample, s	5.0 – 5.3 mm
Velocity in water, v_w	1480 ms^{-1}
Velocity in dry coupling, v_r	1560 ms^{-1}
Velocity in sample, v_s	Determined by Model

Table 5.1. Numerical values of necessary inspection parameters.

To distinguish between panels of different FVFs, using the described ray propagation method, the phased array must be parallel to the fibre orientation. Since angular variation is achieved by increasing the gap between transmission and reception apertures, this must be orientated along the fibre direction, as shown in Figure 5.7. It is necessary for the sound to travel along, not across, the fibres so that increasing their

number by increasing FVF causes an increase in velocity measured. The FVF affects the rate of change of velocity as a function of the angle made to fibres. Since the sample is of pultruded CFRP, essentially only containing one ply, all fibres are orientated in the same axis, thus simplifying the inspection.

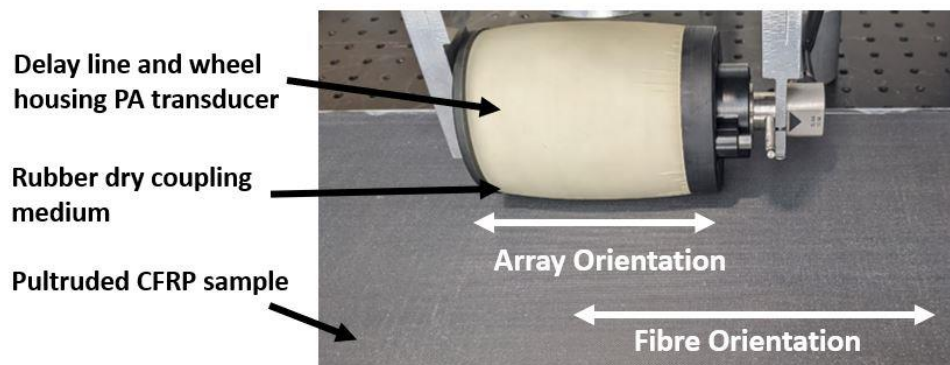


Figure 5.7. Image showing the experimental hardware and CFRP sample used, highlighting the necessary array and fibre orientation

5.4 Ray Tracing Simulations

To confirm the validity of the FVF determination method, and to generate data to compare experimental results to, several computer simulations are also carried out. For this, the CIVA software package is utilised which is based on a combination of ray tracing and FEM analysis. The version used for this work includes the optional FIDEL add-on for inspection simulation of composite materials [137]. This allows the user to insert specific parameters such as fibre density, thickness as well as the resin density and speed of sound, before performing a sample homogenization. Homogenization starts at the ply level, before the number of layers and their

orientation is considered. This stage is simplified for a pultruded CRRP sample, as studied here. It is in effect one, much thicker, unidirectional ply.

Using this software package, it is possible to generate data from a simulation of the described experimental set-up. CIV4 can accurately model the sample geometry, the parameters of a composite material's constituent parts, and the interaction of such a material with an ultrasonic phased array transducer. Simulated FMC data is used in the FVF determination method, to generate curves of velocity as a function of propagation angle in the sample. These results are shown, and compared to those obtained from experimental data, in the following sections.

5.5 Results and Discussion

5.5.1 Glass Block Validation

The theory presented previously has yielded a final expression by which the velocity in the sample can be calculated as a function of propagation angle, Equation 5.10. Throughout these sections this is used to characterise the FVF of known and blind CFRP samples.

However, firstly, a validation based on FMC data acquired from a isotropic glass calibration block, with a thickness of 50 mm, is carried out. It is expected that this isotropic sample should generate a straight-line plot of velocity as a function of propagation angle and validate the ray propagation model. Experimental data, acquired by PAUT, is compared to an equivalent CIVA simulation in Figure 5.8.

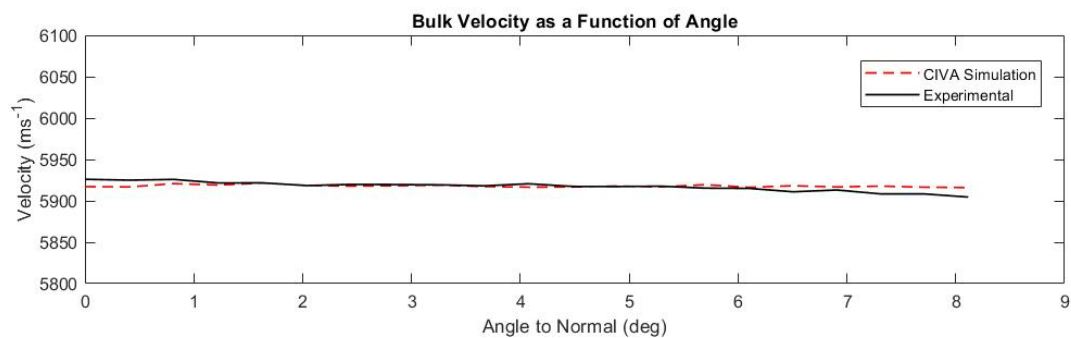


Figure 5.8. Validation of method using FMC data acquired from a isotropic material, a glass calibration block. Experimental data and CIVA simulated data are plotted on the same axis.

Since the level of anisotropy within CFRP panels is used to distinguish between varying FVFs and therefore validation of the model using an isotropic sample is an important first stage. Using a 50 mm glass block the sound velocity across a range of

angles, by varying transmission and reception elements, was computed. As shown in Figure 5.8, a straight-line plot of velocity as a function of propagation angle with a constant value of 5930 ms^{-1} , can be seen. Any slight variation can be attributed to small thickness or purity changes in the sample, ambient temperature variations and the measurement of the ToF values using the envelope method. Simulation data from CIVA gave a slightly lesser value of 5920 ms^{-1} with no variation due to the ideal inspection made possible in a computer model. This confirms the isotropic nature of the sample and the validity of the ray tracing algorithm for the next stages of the work. The angular range here is much smaller than in subsequent sections regarding the CFRP panels. This is due to the geometry of the inspection set-up shown in Figure 5.2. The isotropic glass block has a thickness of 50 mm whilst the CFRP panels, 5 mm. All other array and delay line values are identical and thus the same physical gap between transmission and reception element results in an angular range of 0 - 8 degrees in the glass and 0 - 31 degrees in the CFRP sample.

5.5.2 CFRP Panel Characterisation

Next, three CFRP panels, with FVFs of 60.5, 66.3 and 69.9 % are inspected. These are the calibration samples to which blind tests can then be compared. Again, FMC data is acquired experimentally from each and compared to CIVA simulation. The increase in velocity, relative to that found at normal incidence, for each panel is shown in Figure 5.9. Normal incidence velocities for FVFs of 60.5, 66.3 and 69.9 % and found to be 2877, 2914 and 2958 ms^{-1} respectively.

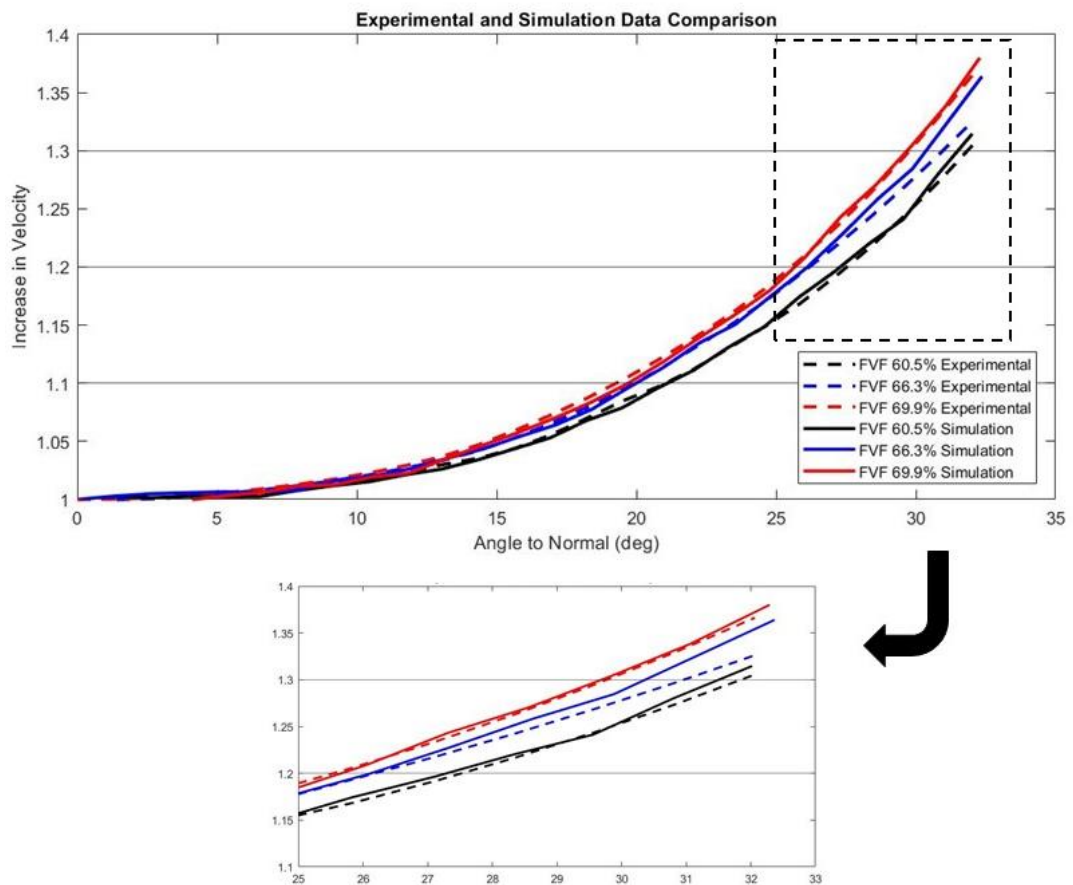


Figure 5.9. Comparison of relative velocity as a function of angle to normal incidence. Three FVFs are plotted along with data from CIVA simulation. The increase in velocity is normalised and expressed as increase relative to that seen at normal interface.

5.5.3 FVF Investigations

Robustness of the signal processing methods and inspection procedure would be the first things to address when advancing this work. Instead of a manual measurement, ultrasonic determination of thickness could be used. The velocity calculation algorithm would need to be adapted to solve the resultant closed form equations. Since all results reported use stationary ultrasonic testing challenges faced applying FVF determination to a moving scan are also to be considered. A more robust determination of the front and backwall peak location, to handle inconsistencies in amplitude and ToF stemming from the probe movement, would be necessary. One potential method could apply an optimised TVG to each A-scan as well as across the reception elements in the FMC matrix.

Fibre directionality investigations by the same methodology have shown positive initial results. However, for this technique to become an inspection tool, used to determine fibre disorientation or lay-up sequence error, significantly more work would need be carried out in terms of A-scan gating and peak identification from specific depths.

5.5.4 Repeatability of Results

The experimental procedure used to generate Figure 5.9 is now repeated. For each calibration panel, several datasets are acquired at different locations on the sample. Each FMC dataset is acquired with the probe stationary and processed to generate a plot of velocity as a function of angle made to the fibres. The repeatability of the trend, seen in Figure 5.9, is clear in the curves for each FVF shown in Figure 5.10.

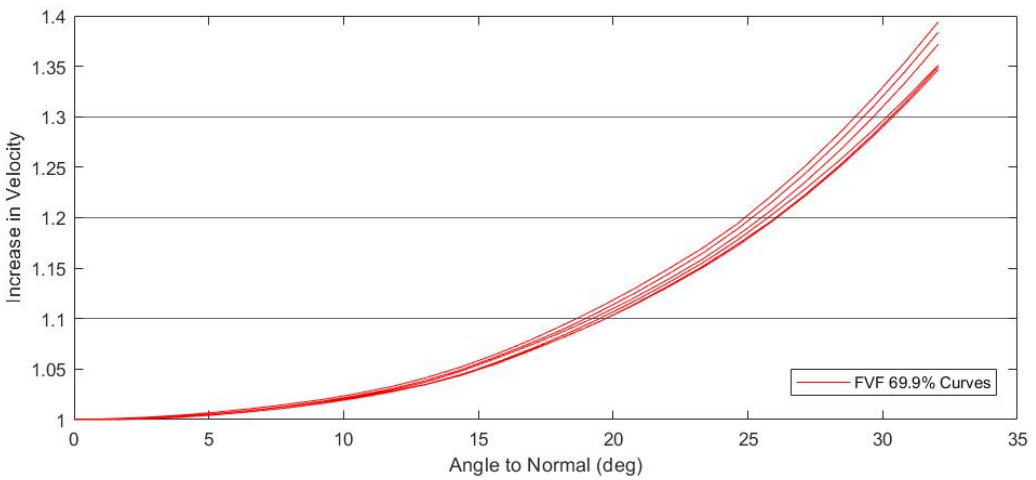
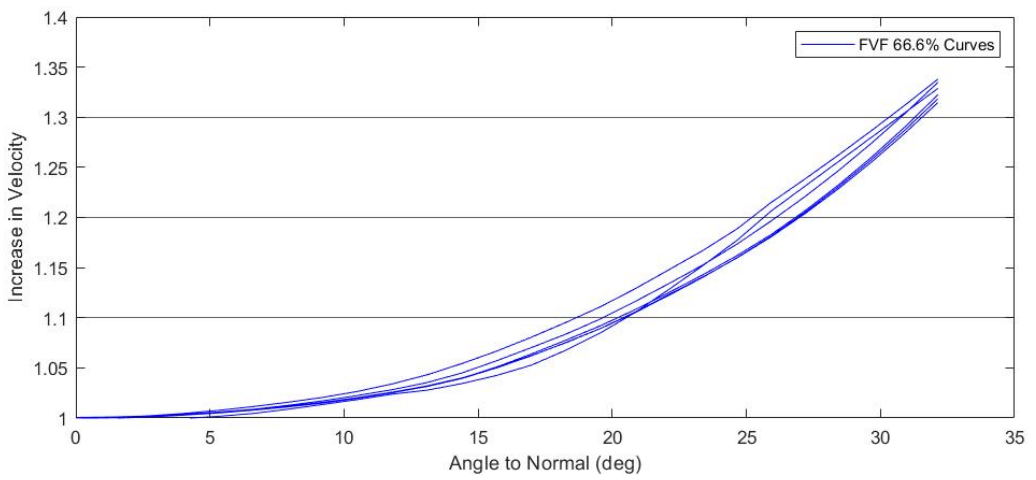
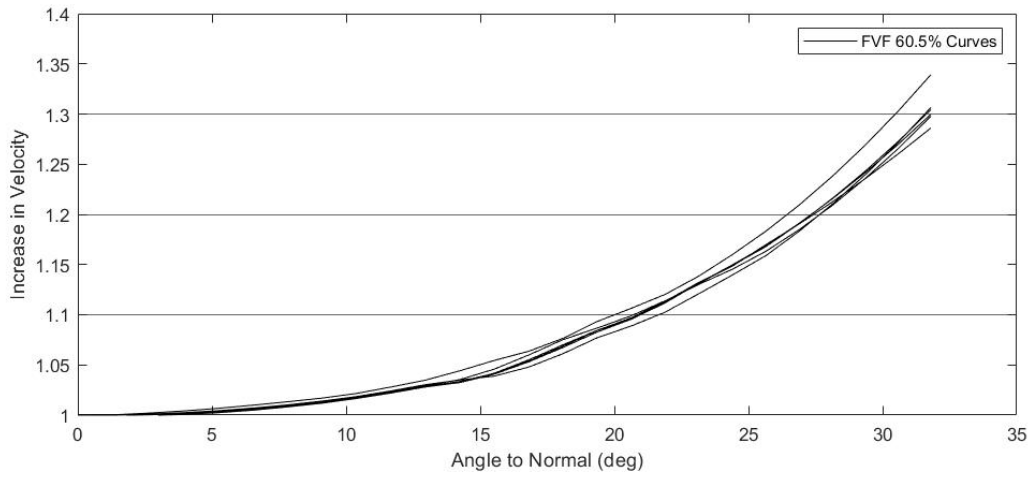


Figure 5.10. Relative velocity curves generated for six FMC datasets taken from each FVF panel.

5.5.5 Generation of Screening Curves

For each FVF value, an average curve is generated using the FMC datasets. Alongside this, upper and lower limits, accounting for the standard deviation across the data, are also calculated. These limits are used as the screening limits for FVF inspection in later sections of this chapter. Average values and screening curves are shown in Figure 5.11.

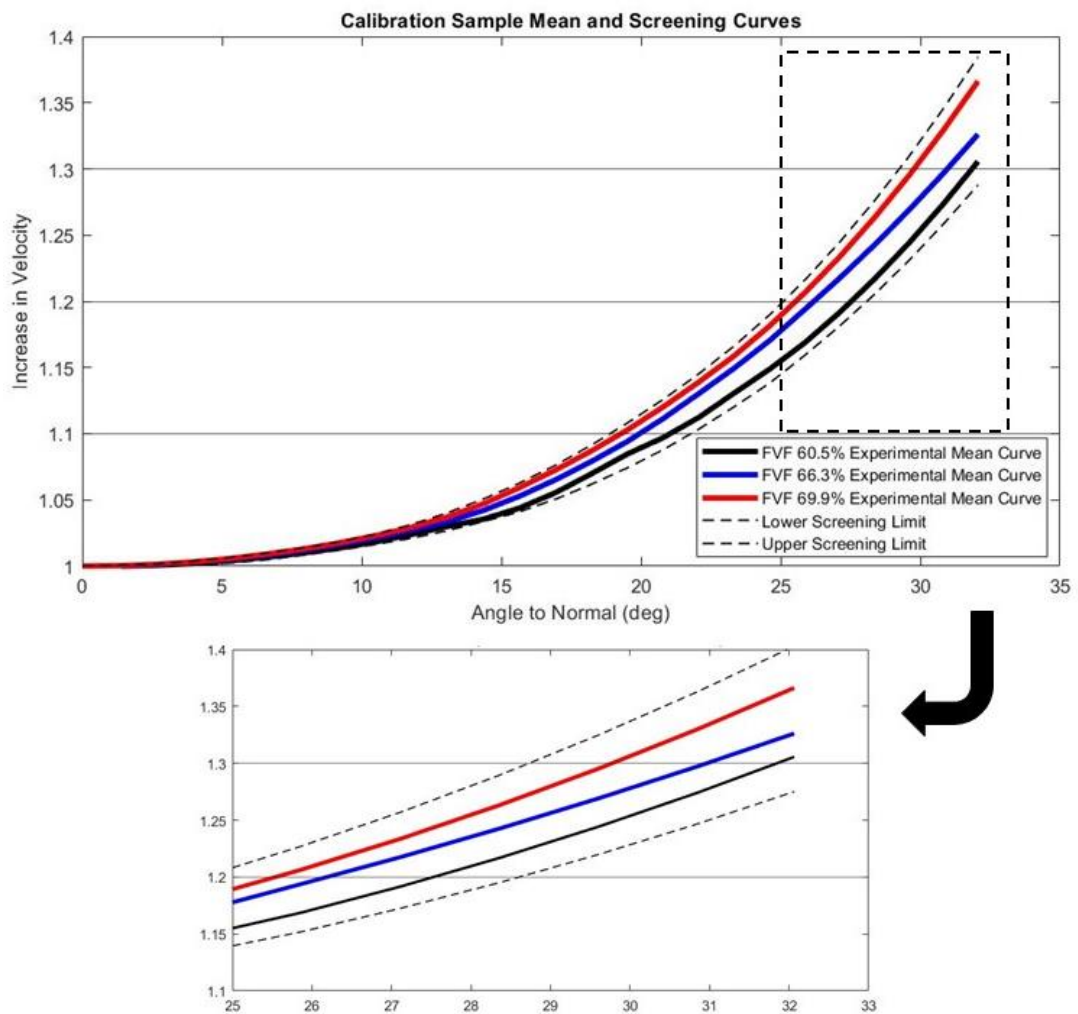


Figure 5.11. Average curves generated from multiple FMC datasets. Lower and upper screening curves are formed based on the standard deviation from the mean for each FVF.

5.5.6 Blind Tests

Following the generation of the screening curves, shown in Figure 5.11, a blind test was carried out on a sample of slightly increased thickness, and again specified FVF of 60.5 %. The purpose of this step is to prove the validity of the method on different sample geometries and show that the velocity as a function of propagation angle is independent of sample thickness. Figure 5.12. shows the velocity as a function of propagation angle, for this blind test, compared to both the screening curves and the upper and lower limits. The plot closely follows the 60.5 % calibration one and is within the lower limit.

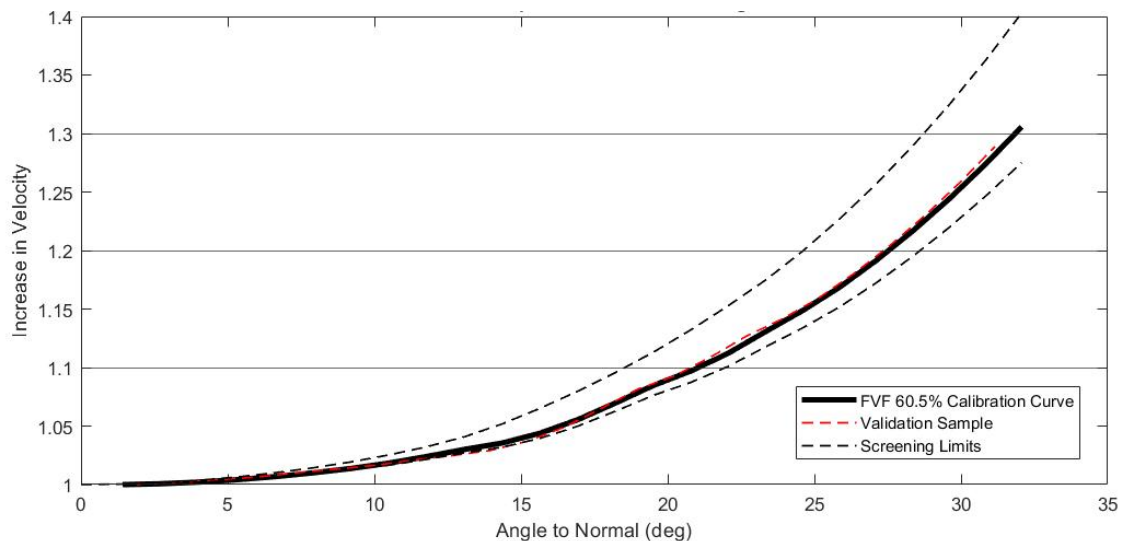


Figure 5.12. Validation of method using FMC from a separate FVF 60.5% panel compared to the screening curves as well as the FVF 60.5% calibration panel.

The same calculation, applied to CFRP panels of varying FVFs, has shown, firstly the anisotropic nature of CFRP in that the velocity changes as a function of propagation angle. Secondly, the extent of this effect varies with the FVF. Thereby,

rate of velocity increase as a function of propagation angle proves to be a reliable method of distinguishing between the FVF. The lower FVF samples having a velocity which increases less rapidly as the propagation angle steepens.

Since the clear trend shows up after averaging separate acquisitions at different locations on each sample the method is best suited as a screening process to ensure the FVF falls in the desired range of 60-70 %, rather than a precise determination of FVF. This must be kept in mind when considering the results presented here, where one can be certain that the panel is defect free and that the FVF is well within the screening limits.

The effectiveness of the CIVA package is also clear when applied to composite ultrasound inspection. Using sample parameters such as the individual fibre thickness, density as well as sound velocity and density in the epoxy resin, CIVA can generate a highly accurate representation of the experimental composite. The results from each FVF model closely follow the curves generated experimentally. Again, any variation is due to experimental procedure and the accuracy with which the ToF between front and back wall echo can be measured using the sampling frequency. Sampling at 100 MHz is chosen so that the temporal position of front and backwall echo are known to an accuracy of 10^{-8} s giving an accuracy in the velocity of approximately 0.6 % for the sample thickness of 5.1 mm.

When considering the range of angles across which the velocity is computed, attenuation becomes a key issue. Results presented here use a maximum gap between transmission and reception element of 25. Beyond this point the amplitude of the backwall falls into the range of the noise floor. The minimal amplitude, received in a

backwall reflection is shown in the following A-scans, Figure 5.13, acquired using first elements $T_{10}R_{15}$ and secondly $T_{10}R_{35}$. This results in a total angular variation of up to 31 degrees based on the geometry of the inspection set-up shown in Figure 5.3 and emphasized in Figure 5.14.

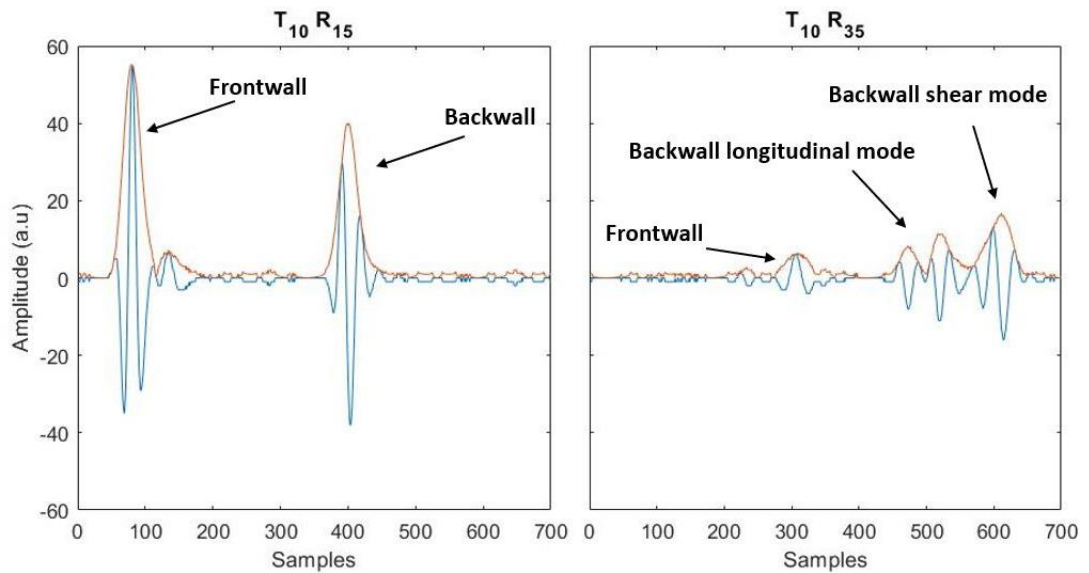


Figure 5.13. Example A-scans from $T_{10}R_{15}$ and $T_{10}R_{35}$, highlighting the amplitude of echoes and thus the increased attenuation as propagation angle and distance are increase.

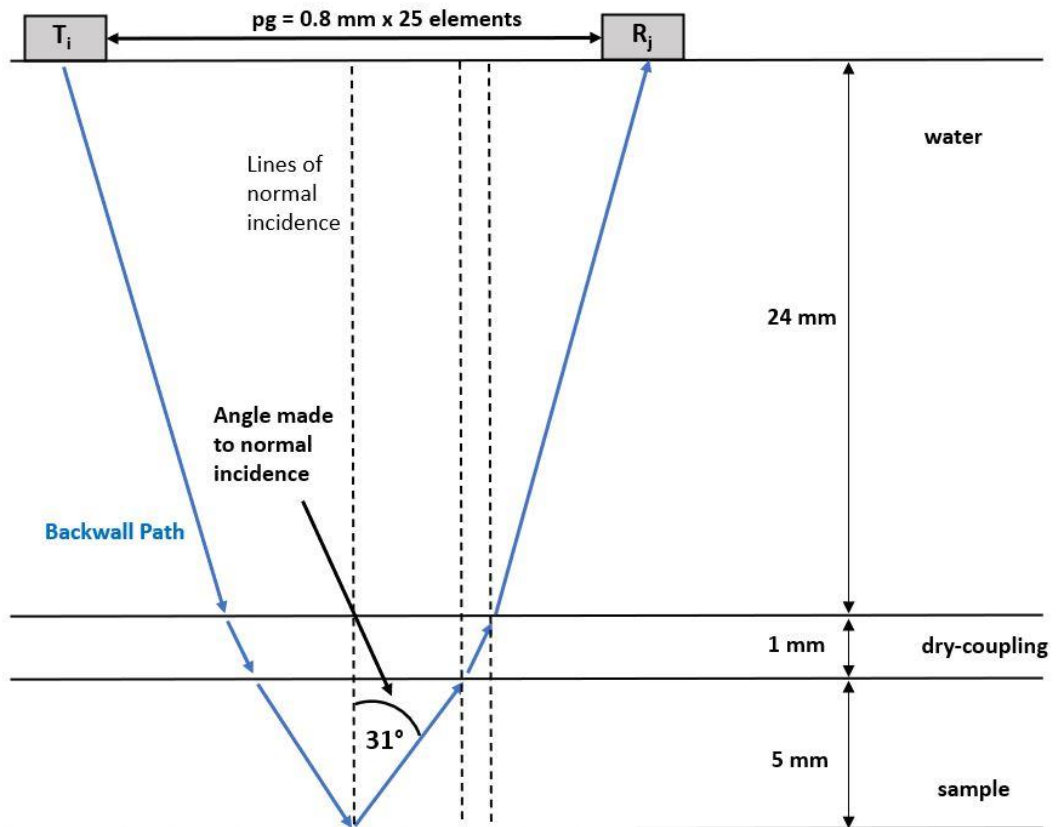


Figure 5.14. Geometry of inspection set giving the maximum propagation angle in the sample when transmission and reception elements are 25 apart.

In future, TVG could be applied to each A-scan to account for the increased attenuation of the backwall. Also, a similar correction could be added when acquiring the FMC dataset. Higher gain values would be necessary, the further the acquisition shifts away from the FMC diagonal, where transmission and reception is on the same element. The sound will have to travel through a greater thickness of sample. The level of TVG necessary across a FMC dataset could also yield information on the FVF due to the variation in attenuation observed. Such steps would allow velocity, as a function of angle curves, to be extended beyond the values presented here.

5.6 T/R Reduction Concept

Ultrasonic inspections using phased arrays are commonly performed using linear imaging, as shown in Figure 5.15.

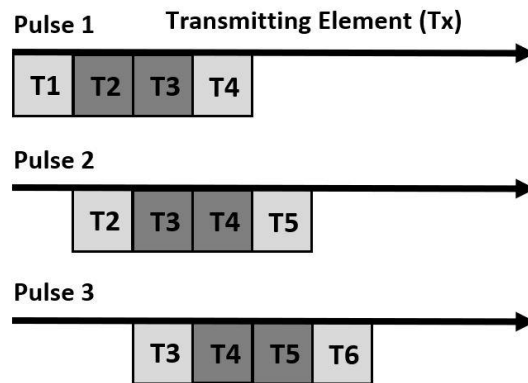


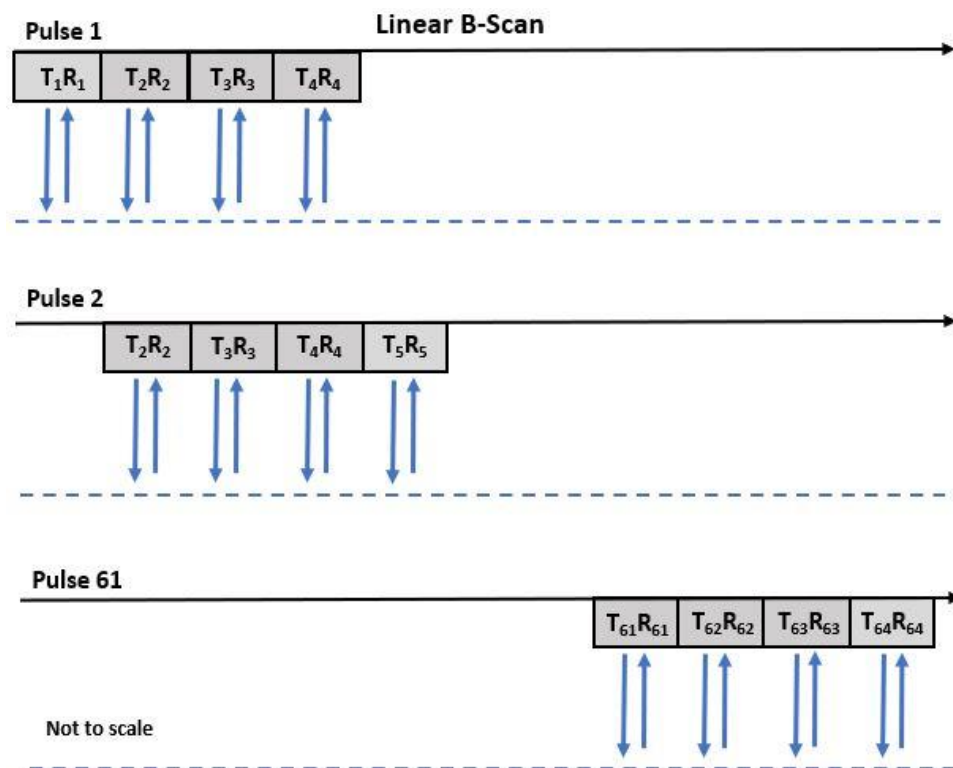
Figure 5.15. Schematic showing the active elements utilised in the first three pulses of a four-element linear scan. A 64-element array would require 61 pulses of this aperture size for complete one sweep.

In this imaging modality the frame rate is defined as the number of frames or sweeps of the phased array, performed each second. Each sweep of the array generates one B-scan. C-scans are then formed using a series of B-scans acquired as the array is physically moved across the sample. Frame rate is therefore key in determining either the resolution, or maximum scan speed achievable in ultrasonic C-scans.

This section proposes a method by which the previously detailed FVF determination can be integrated into linear imaging. This allows the user to obtain, firstly, an ultrasonic scan, from which any defects within the component can be detected and characterised, and secondly, a validation that the FVF falls within the desired range. A reduction in the necessary transmission and reception elements, used to determine

FVF, is proposed. This is necessary since acquiring a full FMC dataset alongside each linear sweep would drastically reduce the frame rate since all elements on the PA are individually triggered.

Four transmit and receive combinations, at three propagation angles from the known geometry, are selected (as shown in Table 5.2). These are used to significantly sub-sample the velocity curve at three angles. Angles are chosen to be well spaced and large enough to fall in the region of the curve where the FVF changes causes divergence in velocity as a function of propagation angle. Thereby, FVF can be screened using an additional twelve pulses, preserving the frame rate so that the screening procedure can be incorporated into linear imaging without adversely affecting the final resolution. Figure 5.16, illustrates the phased array elements used in linear imaging as well as the additional ones used for FVF screening.



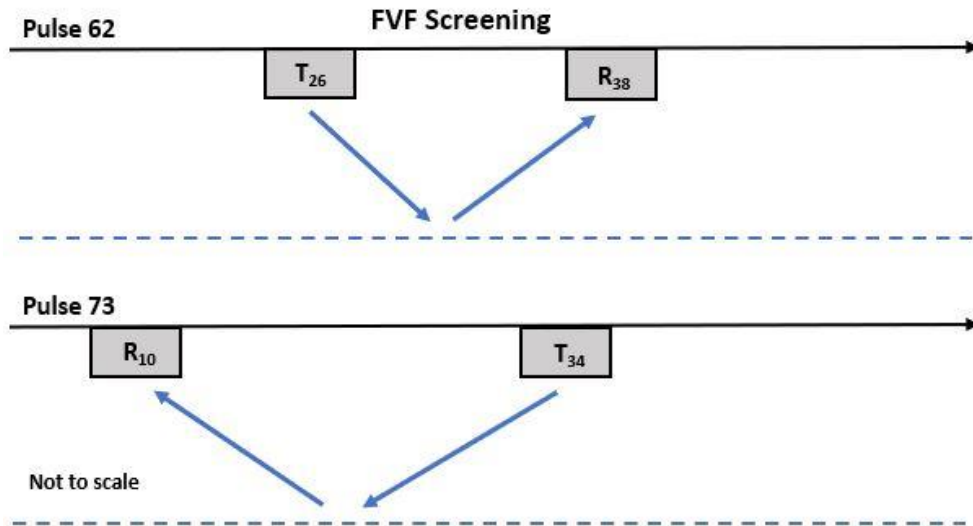


Figure 5.16. Schematic illustrating the transmission and reception elements used for firstly a linear B-scan, and secondly to capture the additional data required for FVF screening.

Table 5.2. shows the elements used for transmission and reception, used to subsample the velocity curve, and the propagation angles they generate. In example $T_{26}R_{38, 14}$, refers to transmission on element 26, reception on 38 then 14. The gap between transmission and reception elements is 12. Propagation angle relative to normal interface, from the inspection geometry, is 15.7 degrees.

The 64-element array, operated with a 4-element sub aperture, requires 61 pulses per frame in linear imaging. Incorporating the FVF screening, 12 additional beams are fired in each sweep, bringing the total to 73. This is a mere 15 % reduction in frame rate compared to standard linear imaging.

PA Pulses	Transition\Reception Combinations	Gap between Transmission and Reception	Propagation Angle to Normal (deg)
62-67	T ₂₆ R _{38, 14} T ₂₆ R _{44, 8} T ₂₆ R _{50, 2}	12, 18, 24	15.7, 23.3, 30.8
68-73	T ₃₄ R _{46, 22} T ₃₄ R _{52, 16} T ₃₄ R _{58, 10}	12, 18, 24	15.7, 23.3, 30.8

Table 5.2. Schematic illustrating transmission and reception elements, as well the beam angle they generate, used for the additional twelve PA pulses.

The effective velocity obtained from each additional pulse is averaged for each angle to the plies to give one value at each of the three chosen angles. It is then a simple case of confirming that these datapoints fall within the pre-determined screening curves, which have been generated from FMC data. An additional step allows for the interpolation of the calibration curves, for each known FVF, and therefore the inspection data can be used to obtain an approximate FVF value alongside a ultrasonic image generated from linear imaging.

5.7 FVF Determination with Linear Imaging

The final section of this chapter combines linear imaging and FVF determination. This carried out on three blind samples as a mock inspection procedure, applying the previous work as a screening process. Example scans from the linear phased array imaging can be seen in Figure 5.17. CFRP panels are defect-free and thus only the front and backwall are visible in the ultrasound images acquired from the inspection. Results from the velocity at the given angles, generated by firing elements shown in Table 5.2, are plotted as crosses alongside the calibration curves in Figure 5.18. A FVF value, using a spline interpolation, for each is shown in Table 5.3. These results are compared to known values as obtained by acid digestions and carried out by these third party. The method proves effective in the 1-2 % discrepancy between the experimental and known values. Despite the experimental results given to same 0.1 % accuracy as the theoretical ones, this is beyond what can be reasonably expected of this. At this point an accuracy of 2 % is a conservative estimation of the fidelity of the ultrasound FVF with more work on quantifying still to be performed.

Known FVF (%)	Interpolated FVF (%)	Percentage Error (%)
60.5	61.1	1.0
66.3	66.1	0.3
69.9	68.3	2.3

Table 5.3. Comparison of known FVF values to those approximated from the inspection implementation along with a percentage error.

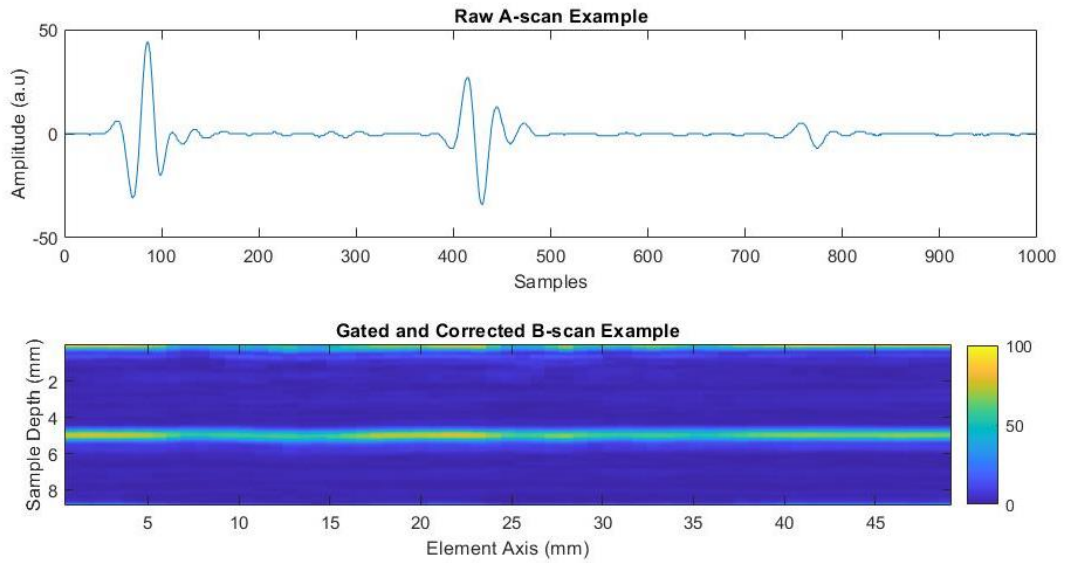


Figure 5.17. Example A and B-scans obtained during phased-array inspection of defect-free samples alongside FVF screening implementation.

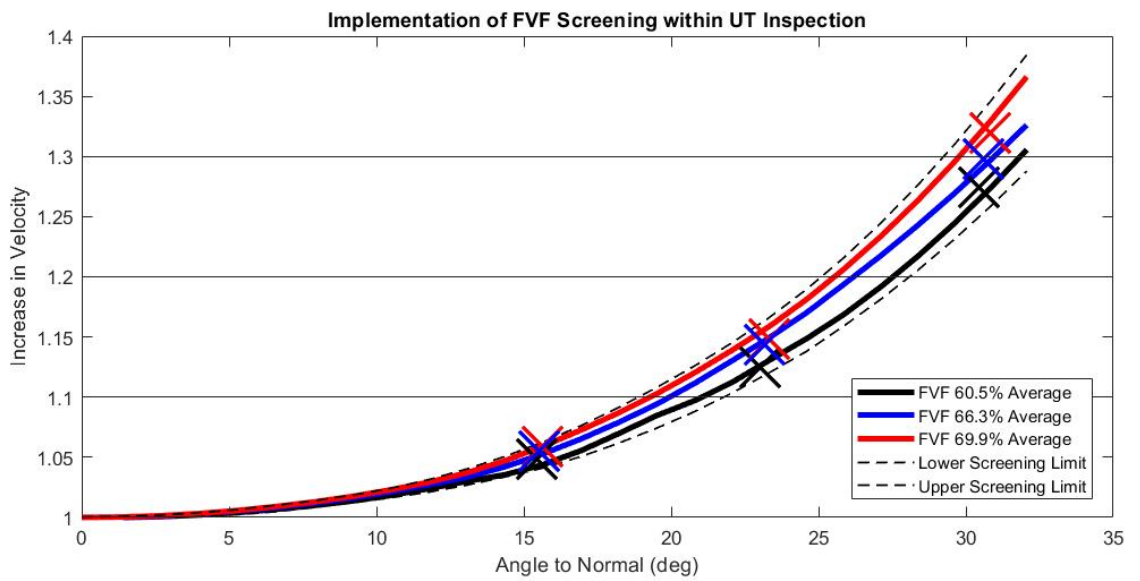


Figure 5.18. Inspection implementation. Screening curves and average curves for each FVF calibration sample plotted alongside the point values of effective velocity increase at specific angles from the inspection.

5.8 Fibre Directionality

5.8.1 Theory

The ray tracing model presented has been effective in utilising FMC datasets to quantify the anisotropy within CFRP panels and thus distinguish between various FVF values. As highlighted in Figure 5.7, the assumed orientation of the fibres, with respect to the array axis, is crucial in maximising the observed velocity increase. Wheel probe and transducer array are orientated parallel to the fibres so that the propagation angle within the sample yields the greatest velocity increase, when compared to normal incidence, and divergence between FVF values is maximised. An image of this initial orientation is shown in Figure 5.19. This idea is now extended with the aim of using the same anisotropy curves to determine the dominant fibre direction. For clarification, Figure 5.20 presents a schematic defining both the probe rotation and sample propagation angle, referred to in the text.

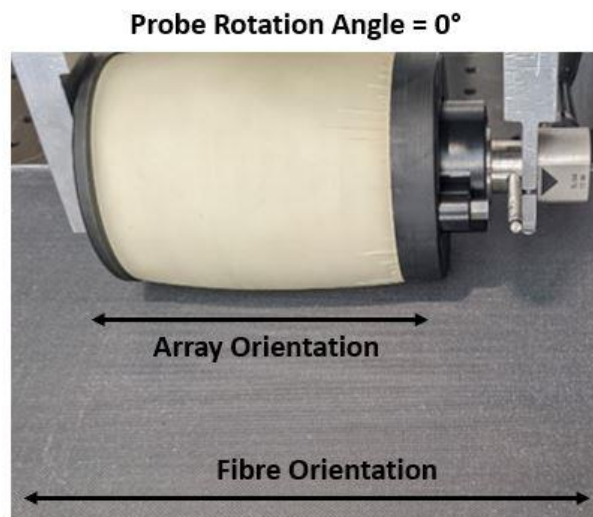


Figure 5.19. Image showing probe rotation angle at zero degrees. The array and fibre orientation are parallel.

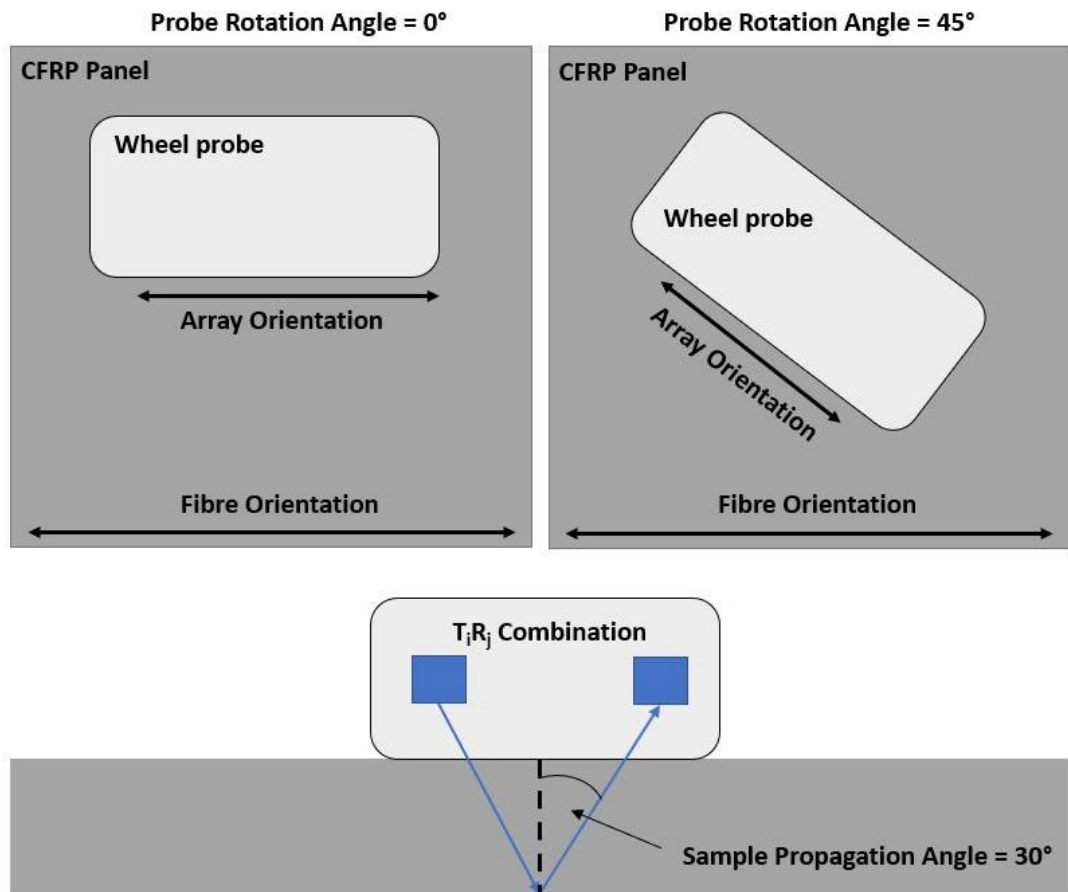


Figure 5.20. Schematic highlighting angles and orientations regarding fibre directionality work.

By rotating the probe, a full 360 degrees, and obtaining an FMC at each angular increment a plot of sample propagation angle versus velocity for each probe rotation angle can be generated. The steepest of these curves will correspond to the array positioned parallel to the fibres, the sound travelling purely along the fibres at much greater velocity. By contrast, when the array is orthogonal to the dominant fibre direction variation in the sample propagation angle, data should show no velocity increase. In this case, sound is travelling across the fibres, the material structure is

homogenous in this axis, and the internal structure ‘looks’ the same at normal incidence as it does at an angular incidence, generated by a T_iR_j variation.

It must be noted that at the start of this section of work the fibre orientation is assumed to be along the length of the panels. This is a reasonable assumption since these are single ply, pultruded, samples. This orientation is only confirmed by the results as a proof of concept. The theory is intended to be extended to determine fibre orientation in a blind test, where there could be significant variation resulting in mechanical performance degradation, or when a composite contains several plies in a lay-up sequence.

5.8.2 Initial Results and Discussion

FMC datasets are acquired for an entire rotation of the transducer with respect to the fibre orientation, in 5-degree increments. This step size is chosen as the best balance between data fidelity and inspection practicality. The procedure is repeated for the same three FVF samples as used the previous screening work. Both the impact of array orientation, with respect to the fibres as well as increased FVF can be seen in the resultant velocity data. Post-processing of FMC data is necessary to produce final curves. This starts with peak identification algorithms applied to each A-scan across a range of transmit and reception elements. The flowchart in Figure 5.21 highlights the steps taken in this work.

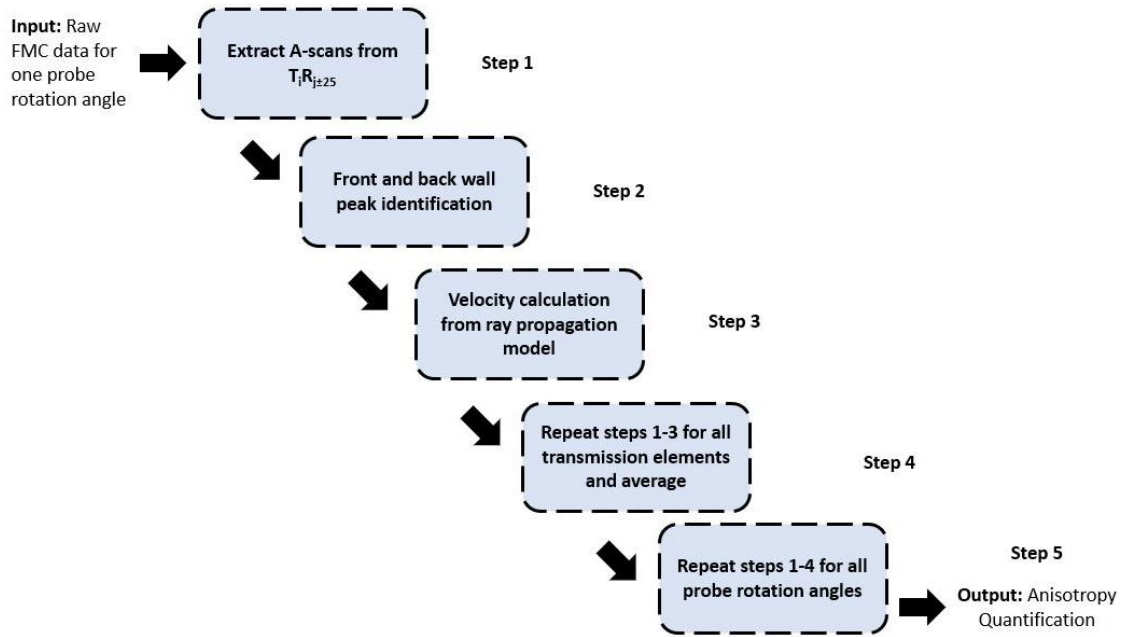


Figure 5.21. Schematic highlighting post-processing steps to yield anisotropy quantification from FMC data.

Figure 5.23 shows a subsection of the effective velocity, calculated from FMC data and using the same ray propagation model as in Figure 5.3, for probe rotation angle of 0 to 90 degrees in 5-degree increments. The general trend of these curves, reverses from 90 to 180, repeats from 180 to 270 and reverses again from 270 to 360 degrees. Plotting specific velocity increases at a chosen sample propagation angles yields a sinusoidal trend of probe rotation angle versus effective velocity increase. These curves for all three FVFs are shown in Figure 5.24 at various sample propagation angles. To highlight the trend the values are summed over a range of sample propagation angles, as shown in Figure 5.23.

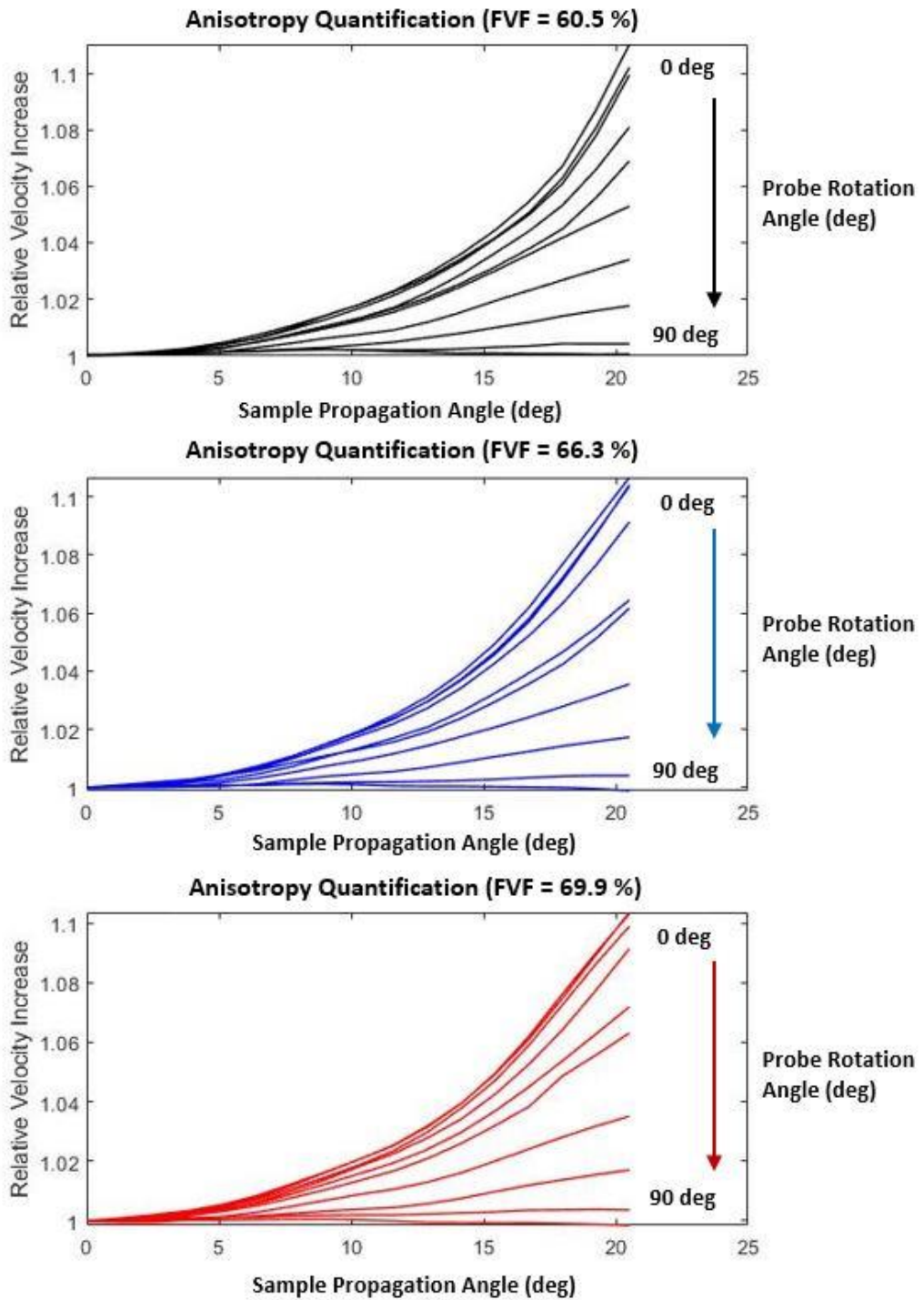


Figure 5.22. Increased in velocity as a function of sample propagation angle for a 0-90 range of probe rotation angles. Plots for FVF = 60.5, 66.3 and 69.9 % are shown.

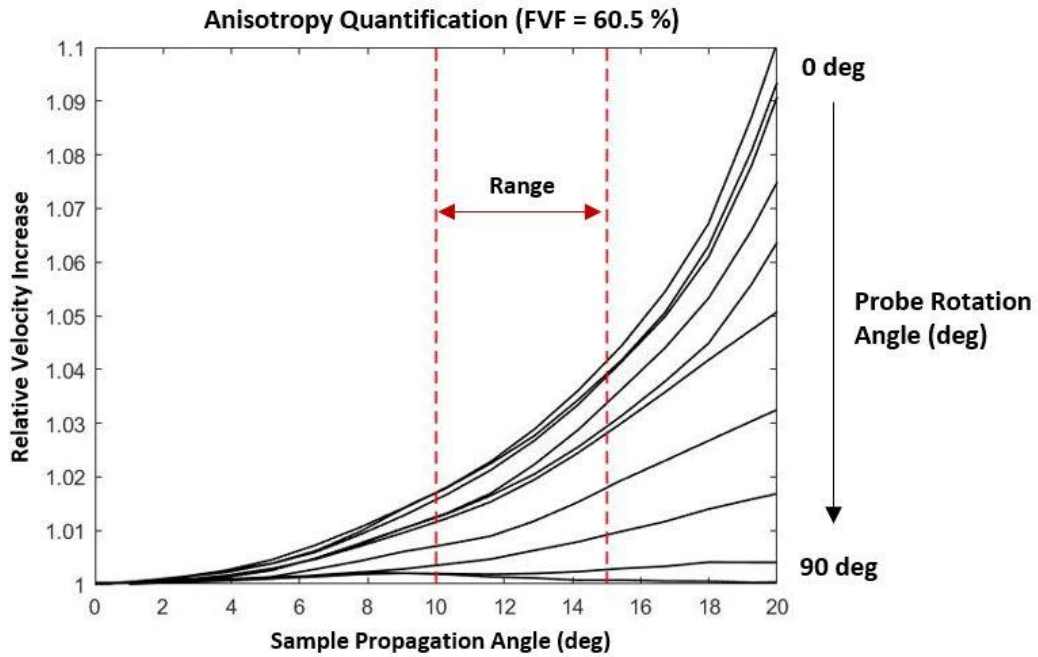


Figure 5.23. Anisotropy quantification graph highlighting a subsection of sample propagation angles used to generate curves.

These initial results act to validate the anisotropy quantification as a method of FVF determination. The importance of probe orientation with respect to fibre orientation is crucial in FVF determination since it allows for an increase in velocity to be seen at increased sample propagation angles. Figure 5.24 shows no relative velocity increase when probe and fibres are at 90 and 270 degrees to each other. This confirms the isotropy of the CFRP along this axis. By contrast the maximum increase in velocity is seen at 0, 180 and 360, when array and fibres are parallel, and the velocity increase is due to sound travelling along the fibres. Figure 5.24 plots this variation as seen at sample propagation angles of 10-15 degrees. In this range, divergence between different FVF is not as pronounced and thus differences can only be seen clearly at the peak values. Plotting a similar curve using data from beyond 20 degrees

sample propagation angle would split the curves apart further. However, challenges are encountered with peak identification and mode conversion resulting in a comparatively 'messy' received A-scan. Alongside a few other suggestions, this issue is discussed in the future work.

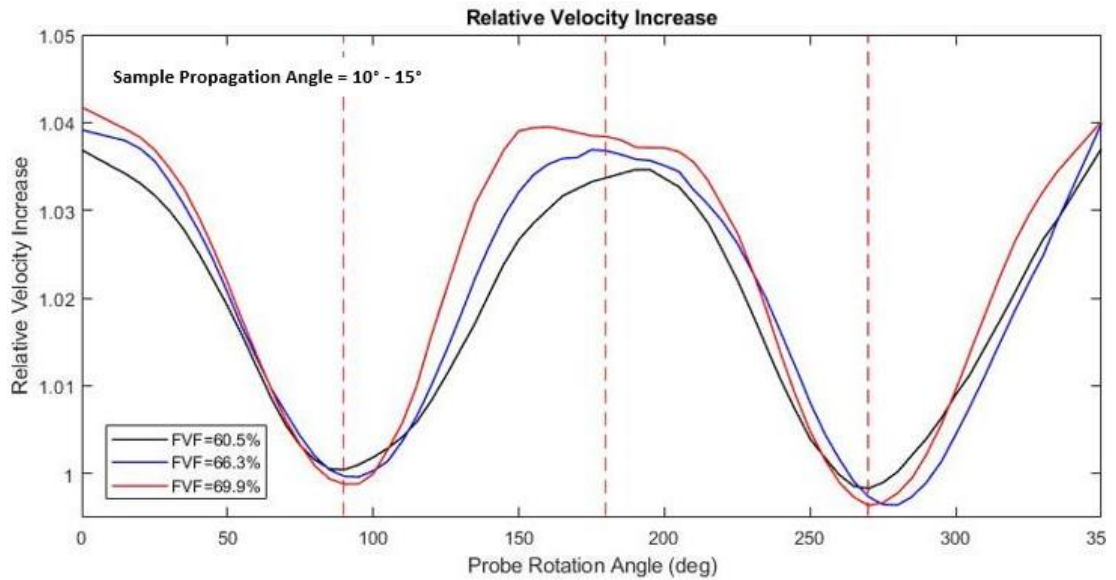


Figure 5.24. Effective velocity increase across the full rotation of probe rotation angle at a subsection of sample propagation angles. Curves are generated for three FVF values.

5.9 Future Work

Throughout the results and discussion sections, the effectiveness of the ray tracing model applied to FMC datasets, acquired through ultrasonic phased array testing, has been demonstrated. Therefore, the method presented here has been proven to be successful in FVF determination of pultruded CFRP panels. To further increase robustness as well as take steps to effectively incorporate the work into a manufacturing process, there are several avenues for future work.

To calculate the ray propagation angles in the model, the panel thickness must be obtained by manual measurement. This is currently performed using callipers and thus the accuracy is within 0.1 mm. Using a ultrasonic determination of thickness would result in closed form equations with the velocity output influencing the initial thickness value. One possibility for future work would be to either modify the algorithm to solve closed loop equations or for the thickness to be acquired from say, a 3D laser scanned model of the sample.

The inspection implementation has only been shown to give both accurate ultrasonic images and FVF determination when the phased array probe and sample are in a fixed position. Within a manufacturing environment, to characterise entire sections of sample, either the probe or sample would need to move so that 2D ultrasonic scans can be generated. The use of phased arrays, housed within water-filled rubber tyres, is an attractive possibility for such future work. Bespoke wheel probes, and phased arrays, for a variety of NDT applications have been reported in [180]. Such a device could be custom designed to facilitate both linear imaging as well as FVF screening, using the method reported in this paper. The inspection procedure would require

determination of the front and backwall peak location, robust enough to handle inconsistencies in amplitude and ToF stemming from the probe movement. The longitudinal wave peak would still need to be reliably isolated from the shear wave ones when handling A-scans beyond the 1st critical angle. The method currently used for peak identification is not robust enough to handle data acquired from a moving probe and would therefore need to be refined.

In terms of the directionality determination, the first step would be blind tests of panels with varying orientation. If it is possible to determine the dominant direction by comparison of scans to calibration dataset, then the idea could be extended. Following on from this more complex CFRP sample, with several layers and more complex layup sequences could be inspected. Each A-scan would then need to be gated accordingly so that the response from a specific layer is isolated. The variation of these 'sections' of A-scan, as the probe rotation angle is changed, could yield information on the dominant fibre direction in each ply and thus how well a given lay-up sequence has been executed.

5.10 Conclusions

A novel FVF screening technique based on analysis of a ray propagation model in combination FMC data, acquired from an ultrasonic PA, has been presented. The validity of this is confirmed using both a isotropic glass block as well as simulation data from CIVA software with an additional composites package.

The angular dependence of the sound velocity with respect to the composite fibre direction is shown to be a reliable parameter to distinguish between FVF values in the desired 60-70 % range. Screening curves generated from calibration data are used to approximate the FVF of three separate blind samples. A discrepancy of no more than 2.3 % in the worst case, and less than 1 % in the best, is found between the known FVF values and those calculated using the methodology presented.

Expansion of the methodology for fibre directionality determination has given positive initial results. It has been possible to confirm the dominant fibre orientation in each of the three FVF panels. Since this was known before and the CFRP is pultruded, these results serve merely as a validation of the anisotropy quantification concept.

There is significant scope in terms of future work to allow demonstrated principles to be reliably and robustly applied to a moving inspection and thereby integrated into a manufacturing environment. The benefit in the proposed form of FVF testing is multi-faceted. Firstly, there is value in the much faster feedback provided, when compared to conventional measurements. This is still the case even when precise ultrasonic measurement and extensive data analysis procedures necessary, are considered. It is

possible to produce more data, in a shorter period, for quality assurance. The non-destructive nature of ultrasonic measurement is also inherently safer for operators. Finally, a lower cost of testing is achieved due to the significantly shortened preparation and test time. Results shown will be beneficial to the manufacturing process with the potential to ensure that final components satisfy manufacturing standards and is a powerful tool in guaranteeing that FVF consistency is maintained.

6 Concluding Chapter

6.1 Conclusions

The objective of this research was focussed on the development of new NDT methodologies for implementation in large scale wind turbine blade manufacturing. To that end, each of the three chapters, forming the body of this thesis, contribute to a specific aspect of ultrasonic testing of composites. Throughout the project, there has been close collaboration between the University based team and industrial partner SGRE. The research has great potential to be effectively implemented in a manufacturing environment with overall benefits to the industry.

Existing hardware and robotic ultrasonic inspection techniques were applied to perform small scale inspections of CFRP samples. The effectiveness of this equipment and design of data analysis and imaging algorithms, has been shown by the range of scans and defect characterisation presented in Chapter 3. The robustness of this set-up was investigated in terms of limits on scanning speed, probe alignment and coupling force whilst still allowing target defect sizes to be identified. These results paved the way for design of an in-process ultrasonic inspection system, targeted at production line integration. Several rejected CFRP components were obtained from SGRE, and the inspection system was shown to be a reliable means of identifying flaws within these. To implement such a set-up on a production line a wheel probe and array allowing for full panel width coverage is necessary. A range of configurations were considered before a final set-up was justified, costed, and pitched.

Whilst multi-aperture beamforming is an existing technique applied in NDT as well as medical ultrasound, the adaptive application to these CFRP panels is novel. After a discussion of the underlying concepts, permitting frame rate, inspection and resolution increases an adaptive and autonomous algorithm was presented. This was used to determine optimal focal laws for the sample in question as well as a critical defect size. The validity of the approach was shown through three separate inspection scenarios using firstly low and high-speed scanning with linear beamforming. MA beamforming is used in the third of these scenarios, combining high scanning speed and resolution. A 6.7-fold increase in scanning speed with no degradation in resolution or defect sizing accuracy was reported. This is highest frame rate achievable, whilst still being able to reliably identify the critical defect size, as identified by the adaptive and autonomous algorithm. The concept was tested by the mock inspection of CFRP panel under each of these scenarios. The resolutions seen in the final C-scans and results of defect sizing algorithms applied, validate the MA beamforming method.

A literature review shows the importance of a composite's FVF in determining the mechanical properties of a component. Whilst determining strength and stiffness, this parameter also influences the ultrasonic bulk velocity. This link was exploited in the third major contribution reported in this thesis. Within a manufacturing environment it is crucial to identify any significant FVF variations as early as possible, to ensure final parts satisfy standards and certifications. Therefore, a novel screening technique for FVF, based on the angular dependence of the sound velocity with respect to the composite fibre direction has been presented. The validity of this approach confirmed

using both an isotropic glass block as well as simulation data from CIVA software with additional composites package. FMC data acquired from a PA ultrasonic probe is used to generate calibration data then employed to estimate the FVF of samples in blind tests. Experimental results showed FVF values determined by this method are typically within 2 % of reference ones having be determined by a third party using more conventional testing methods. An initial investigation into this work as a potential tool to determine fibre directionality has also been carried out. As with the previous two sections, the research offers significant potential in terms of factory implementation of NDT procedures but it still at the initial research stage, with many more lab-based investigations to be carried out.

6.2 Future Work

Future work related to this thesis, can again be split into sections relating to the previous chapters. Each is at a different technology readiness level and thus next steps range from further laboratory testing for the lowest TRL, FVF work, to funding applications taking projects from the research to industrial environment, for the in-process ultrasonic inspection system. In addition to this a few initial ideas relating to GFRP inspection are discussed.

6.2.1 In-process Ultrasonic Inspection System

Key to the success of both robotic and inspection system scanning is the ultrasonic phased array housed within a water-filled wheel probe. To suit production line requirements a roller probe with a minimum active transducer coverage of 200 mm is necessary. Technical and commercial advantages and disadvantages of a variety of configuration have been presented and a single custom probe decided upon. The next step in this section of the work will involve the manufacture and initial testing of such a device.

6.2.2 Adaptive MA Beamforming

The most important next step in this work concerns the PEAK firmware update described in Section 4.5.4 to optimise the PAC for MA operation. Optimised saving using only the data from the desired channels as well as performing the summing of separate element responses, in the correct MA configuration, at the point of reception,

rather than in post processing, would streamline the entire inspection procedure. Alongside the use of higher speed data links, the frame rate and resolution increases made possible by the MA method could then be applied to at much higher speeds. With a linear imaging scan velocity starting at 100 mms^{-1} , the same focal laws would then allow for an increase up to 670 mms^{-1} , and thereby make the technology hugely beneficial in a manufacturing environment as a powerful tool to address NDT bottlenecks.

6.2.3 Ultrasonic FVF Determination

Robustness of the signal processing methods and inspection procedure would be the first things to address when advancing this work. Instead of a manual measurement, ultrasonic determination of thickness could be used. The velocity calculation algorithm would need to be adapted to solve the resultant closed form equations. Since all results reported use stationary ultrasonic testing challenges faced applying FVF determination to a moving scan are also to be considered. A more robust determination of the front and backwall peak location, to handle inconsistencies in amplitude and ToF stemming from the probe movement, would be necessary. One potential method could apply an optimised TVG to each A-scan as well as across the reception elements in the FMC matrix.

Fibre directionality investigations by the same methodology have shown positive initial results. However, for this technique to become an inspection tool, used to determine fibre disorientation or lay-up sequence error, significantly more work

would need be carried out in terms of A-scan gating and peak identification from specific depths.

6.2.4 Advanced Defect Identification

As described in the literature review in Chapter 2, machine learning and pattern recognition techniques can be employed to allow for large volumes of inspection data to be quickly analysed and checked for defects based on characteristic features. This has the potential to reduce the analysis and defect detection bottlenecks caused by vast quantities of data acquired in modern NDT techniques. Defect detection and data processing methods, employed throughout the work presented in this thesis fall short in their complexity of what can be described as machine learning with the emphasis on robustness and implementation. Future work could therefore investigate such techniques, identify the most suitable, and integrate them with the inspection procedures and practical hardware described in this thesis.

6.2.5 GFRP Inspection

All ultrasonic inspection was carried out on pultruded CFRP panels. Chapter 3 outlined initial robotic inspections before presenting an inspection system for factory implementation with no scans performed using GFRP samples. Since the vast majority of the wind turbine blade structure is still composed of this composite, there is huge potential to expand the principles presented and apply them to GFRP sections. This will bring with it additional challenges, due to difficulties experienced during

ultrasonic testing of GFRP. These include higher attenuation values a less ordered lay-up structure. Additionally, whilst the CFRP panels are thin, planar, and therefore comparatively simple to inspect, GFRP is used to form aerofoil sections and is much thicker, with a complex curved geometry. The application of simple linear imaging, or the MA method, to GFRP blade sections would need to address the resultant coupling issues, refraction of sound within the sample, and lower SNR levels in received data. A starting point for this avenue of future work could be CIVA simulation of GFRP inspection with models resembling wind turbine blades. The additional CIVA FIDEL composites package would be key and help to justify, for example, the use of a certain probe frequency, pitch, and element configuration. Initially, this could take the form of consultation work for wind turbine blade manufacturers. Next, a similar workflow, to that used in this PhD, could be followed with small GFRP samples tested within a research environment before scaling-up and factory implementation. This would allow for knowledge of the GFRP structure, how it behaves under ultrasound inspection with defect identification and characterisation, to be acquired before more practical considerations are taken.

6.3 General Overview

The exponential growth in demand for wind energy installations has been driven by commitments to net-zero targets put in place by many governments over the course of the last decade. Manufacturers have responded to such pressures by increasing both the size of individual turbines as well as the numbers they construct. Such rapid scaling-up has meant there is also increased demand on NDT procedures, which have played a role since the advent of the industry, to reliably identify material defects and integrate into the manufacturing workflow without generating bottlenecks. The work presented is in response to this and concerns future ultrasonic NDT techniques relating to in-process inspection, novel phased array operation and data analysis methodologies. These advances are of benefit within the manufacturing environment, leading to overall improvements in wind energy production.

6.4 References

- [1] J. Lee and F. Zhao, "Global Wind Report 2021," *Glob. Wind Energy Council*, p. 75, 2021.
- [2] Patel, "IPCC Summary for Policy Makers 2018," pp. 9–25, 2019.
- [3] H. Hans-O. Pörtner, Debra C. Roberts, *Climate Change 2022 - Impacts, Adaptation and Vulnerability - Summary for Policymakers*. 2022.
- [4] "Climate Action Tracker." [Online]. Available: <https://climateactiontracker.org/global/temperatures/>.
- [5] M. S. Chowdhury *et al.*, "Current trends and prospects of tidal energy technology," *Environ. Dev. Sustain.*, vol. 23, no. 6, pp. 8179–8194, 2021, doi: 10.1007/s10668-020-01013-4.
- [6] A. B. S. Bahaj, M. Mahdy, A. S. Alghamdi, and D. J. Richards, "New approach to determine the Importance Index for developing offshore wind energy potential sites: Supported by UK and Arabian Peninsula case studies," *Renew. Energy*, vol. 152, pp. 441–457, 2020, doi: 10.1016/j.renene.2019.12.070.
- [7] D. Lugo-laguna, A. Arcos-Vargas, and F. Nuñez-herandez, "A european assessment of the solar energy cost: Key factors and optimal technology," *Sustain.*, vol. 13, no. 6, pp. 1–25, 2021, doi: 10.3390/su13063238.
- [8] "Office for National Statistics: Wind Energy in The UK," 2021.
- [9] WindEurope, "Offshore Wind in Europe: Key trends and statistics," 2020.
- [10] R. Smith and H. V. Manufacturing, "Report from the Workshop on NDT and SHM Requirements for Wind Turbines 13-14 February 2019 Workshop on NDT and SHM Requirements for Wind Turbines," no. February, 2019.
- [11] E. Sesto and N. H. Lipman, "Wind energy in Europe, 2021 Statistics," 2021.
- [12] M. A. Drewry and G. A. Georgiou, "A review of NDT techniques for wind turbines," *Insight Non-Destructive Test. Cond. Monit.*, vol. 49, no. 3, pp. 137–141, 2007, doi: 10.1784/insi.2007.49.3.137.
- [13] "Wind Atlas Europe." [Online]. Available: <http://www.windatlas.dk/Europe/>.
- [14] "SG 8.0-167 DD. Product Brochure." Siemens Gamesa Renewable Energy, pp. 1–2.
- [15] "Siemens Gamesa launches 10 MW offshore wind turbine," *SGRE Newsroom*, 2019.
- [16] RenewableCube, "Wind Energy 2021," 2021. .
- [17] C. West, "Contracts for Difference Allocation Round 4," 2022.
- [18] M. M. Vanegas-Cantarero, S. Pennock, T. Bloise-Thomaz, H. Jeffrey, and M. J. Dickson, "Beyond LCOE: A multi-criteria evaluation framework for offshore renewable energy projects," *Renew. Sustain. Energy Rev.*, vol. 161, no. July 2021, p. 112307, 2022, doi: 10.1016/j.rser.2022.112307.
- [19] W. Shen *et al.*, "A comprehensive review of variable renewable energy levelized cost of electricity," *Renew. Sustain. Energy Rev.*, vol. 133, no. March, p. 110301, 2020, doi: 10.1016/j.rser.2020.110301.
- [20] S. Evans, "Record-low price for UK offshore wind is four times cheaper than gas," 2022.
- [21] Lazard, "Levelized Cost of Energy v10," *Lazard.Com*, no. November, pp. 0–21, 2017.
- [22] M. Albadi, "On Techno-economic Evaluation of Wind-based DG," University of Waterloo, 2016.
- [23] G. A. M. Van Kuik, "The Lanchester-Betz-Joukowsky limit," *Wind Energy*, vol. 10, no. 3, pp. 289–291, 2007, doi: 10.1002/we.218.
- [24] X. W. Deng, N. Wu, K. Yang, and W. L. Chan, "Integrated design framework of next-generation 85-m wind turbine blade: Modelling, aeroelasticity and optimization," *Compos. Part B Eng.*, vol. 159, no. August 2018, pp. 53–61, 2019, doi: 10.1016/j.compositesb.2018.09.028.
- [25] L. Freris, *Inherit the Wind*. 1992.
- [26] I. Amenabar, A. Mendikute, A. López-Arraiza, M. Lizaranzu, and J. Aurrekoetxea, "Comparison and analysis of non-destructive testing techniques suitable for delamination inspection in wind turbine blades," *Compos. Part B Eng.*, vol. 42, no. 5, pp. 1298–1305, 2011, doi: 10.1016/j.compositesb.2011.01.025.
- [27] V. A. Raišutis R, Jasiunienė E, Šlīteris R, "The review of non-destructive testing techniques suitable for inspect manufacturing of the wind turbine blades," vol. 63, no. 1, pp. 63(1):26–30, 2008.

- [28] A. Fahr, "Ultrasonic C-scan inspection of composite materials," *Eng. J. Qatar Univ.*, vol. 5, no. February, pp. 201–222, 1992.
- [29] J. J. Bender, S. R. Hallett, and E. Lindgaard, "Investigation of the effect of wrinkle features on wind turbine blade sub-structure strength," *Composite Structures*, vol. 218, pp. 39–49, 2019, doi: 10.1016/j.compstruct.2019.03.026.
- [30] P. Colombi and C. Poggi, "An experimental, analytical and numerical study of the static behavior of steel beams reinforced by pultruded CFRP strips," *Compos. Part B Eng.*, vol. 37, no. 1, pp. 64–73, 2006, doi: 10.1016/j.compositesb.2005.03.002.
- [31] J. Vyas and R. J. Kazys, "A review on nondestructive techniques and characteristics of composite materials for the aerospace system," *MATEC Web Conf.*, vol. 233, 2018, doi: 10.1051/mateconf/201823300003.
- [32] D. K. Rajak, D. D. Pagar, R. Kumar, and C. I. Pruncu, "Recent progress of reinforcement materials: A comprehensive overview of composite materials," *J. Mater. Res. Technol.*, vol. 8, no. 6, pp. 6354–6374, 2019, doi: 10.1016/j.jmrt.2019.09.068.
- [33] B. Shue, A. Moreira, and G. Flowers, "Review of recent developments in composite material for aerospace applications," *Proc. ASME Des. Eng. Tech. Conf.*, vol. 1, no. PARTS A AND B, pp. 811–819, 2009, doi: 10.1115/DETC2009-87847.
- [34] C. Li, D. Pain, P. D. Wilcox, and B. W. Drinkwater, "Imaging composite material using ultrasonic arrays," *NDT E Int.*, vol. 53, pp. 8–17, 2013, doi: 10.1016/j.ndteint.2012.07.006.
- [35] J. Hale, "Boeing 787 From Ground Up," *Boeing Comer. Aeromagazine*, p. 9, 2012.
- [36] A. S. Mahmood, J. Summerscales, and M. N. James, "Resin-Rich Volumes (RRV) and the Performance of Fibre-Reinforced Composites: A Review," *J. Compos. Sci.*, vol. 6, no. 2, pp. 1–16, 2022, doi: 10.3390/jcs6020053.
- [37] R. Fuentes *et al.*, "Autonomous ultrasonic inspection using Bayesian optimisation and robust outlier analysis," *Mech. Syst. Signal Process.*, vol. 145, p. 106897, 2020, doi: 10.1016/j.ymssp.2020.106897.
- [38] B. Wang, S. Zhong, T. L. Lee, K. S. Fancey, and J. Mi, "Non-destructive testing and evaluation of composite materials/structures: A state-of-the-art review," *Adv. Mech. Eng.*, vol. 12, no. 4, pp. 1–28, 2020, doi: 10.1177/1687814020913761.
- [39] K. A. Tiwari and R. Raisutis, "Comparative Analysis of Non-Contact Ultrasonic Methods for Defect Estimation of Composites in Remote Areas," *CBU Int. Conf. Proc.*, vol. 4, pp. 846–851, 2016, doi: 10.12955/cbup.v4.863.
- [40] Ł. Doliński, M. Krawczuk, and A. Zak, "Detection of Delamination in Laminate Wind Turbine Blades Using One-Dimensional Wavelet Analysis of Modal Responses," *Shock Vib.*, vol. 2018, 2018, doi: 10.1155/2018/4507879.
- [41] J. Ye *et al.*, "A multi-scale model for studying failure mechanisms of composite wind turbine blades," *Compos. Struct.*, vol. 212, no. December 2018, pp. 220–229, 2019, doi: 10.1016/j.compstruct.2019.01.031.
- [42] A. Benammar, R. Draï, and A. Guessoum, "Detection of delamination defects in CFRP materials using ultrasonic signal processing," *Ultrasonics*, vol. 48, no. 8, pp. 731–738, 2008, doi: 10.1016/j.ultras.2008.04.005.
- [43] A. Katunin, K. Dragan, and M. Dziendzikowski, "Damage identification in aircraft composite structures: A case study using various non-destructive testing techniques," *Compos. Struct.*, vol. 127, pp. 1–9, 2015, doi: 10.1016/j.compstruct.2015.02.080.
- [44] J. S. Chou, C. K. Chiu, I. K. Huang, and K. N. Chi, "Failure analysis of wind turbine blade under critical wind loads," *Eng. Fail. Anal.*, vol. 27, pp. 99–118, 2013, doi: 10.1016/j.engfailanal.2012.08.002.
- [45] "Caithness Windfarms Accident Statistics," 2019. [Online]. Available: <http://www.caithnesswindfarms.co.uk/AccidentStatistics.htm>.
- [46] "British Institute of Non-Destructive Testing," 2022. [Online]. Available: <https://www.bindt.org/education-and-training/>.
- [47] R. W. Martin, A. Sabato, A. Schoenberg, R. H. Giles, and C. Niezrecki, "Comparison of nondestructive testing techniques for the inspection of wind turbine blades' spar caps," *Wind Energy*, vol. 21, no. 11, pp. 980–996, 2018, doi: 10.1002/we.2208.
- [48] A. Jüngert, "Damage Detection in Wind Turbine Blades using two Different Acoustic Techniques," *7th fib PhD Symp. Stuttgart, Ger.*, no. December, pp. 1–10, 2008.
- [49] C. Mineo, "Automated NDT Inspection for Large and Complex Geometries of Composite Materials," University of Strathclyde, 2015.
- [50] R. Mohammadkhani, L. Z. Fragonara, P. M. Janardhan, I. Petrunin, A. Tsourdos, and I. Gray, "Ultrasonic phased array imaging technology for the inspection of aerospace composite structures," *2019 IEEE Int. Work. Metrol.*

AeroSpace, Metroaerosp. 2019 - Proc., pp. 203–208, 2019, doi: 10.1109/MetroAeroSpace.2019.8869635.

- [51] P. J. Schilling, B. P. R. Karedla, A. K. Tatiparthi, M. A. Verges, and P. D. Herrington, “X-ray computed microtomography of internal damage in fiber reinforced polymer matrix composites,” *Compos. Sci. Technol.*, vol. 65, no. 14, pp. 2071–2078, 2005, doi: 10.1016/j.compscitech.2005.05.014.
- [52] R. A. Smith, L. J. Nelson, M. J. Mienczakowski, and R. E. Challis, “Automated non-destructive analysis and advanced 3d defect characterisation from ultrasonic scans of composites,” *ICCM Int. Conf. Compos. Mater.*, vol. 51, no. 2, pp. 82–87, 2009.
- [53] M. F. Mahmod, E. A. Bakar, and A. R. Othman, “Defect Detection of Fiberglass Composite Laminates (FGCL) with Ultrasonic A-Scan Signal Measurement,” *IOP Conf. Ser. Mater. Sci. Eng.*, vol. 114, no. 1, 2016, doi: 10.1088/1757-899X/114/1/012106.
- [54] BINDT, “Ultrasonic Flaw Detection.” [Online]. Available: <https://www.bindt.org/What-is-NDT/Ultrasonic-flaw-detection/>. [Accessed: 12-Feb-2020].
- [55] C. Mineo *et al.*, “Robotic geometric and volumetric inspection of high value and large scale aircraft wings,” *2019 IEEE Int. Work. Metrol. AeroSpace, Metroaerosp. 2019 - Proc.*, pp. 82–86, 2019, doi: 10.1109/MetroAeroSpace.2019.8869667.
- [56] C. Mineo *et al.*, “Flexible integration of robotics, ultrasonics and metrology for the inspection of aerospace components,” *AIP Conf. Proc.*, vol. 1806, no. February, 2017, doi: 10.1063/1.4974567.
- [57] B. Wright, I. Cooper, P. I. Nicholson, C. Mineo, and S. G. Pierce, “PAUT inspection of complex shaped composite materials through 6 DOFs robotic manipulators,” *NDT 2014 - 53rd Annu. Conf. Br. Inst. Non-Destructive Test.*, no. June 2018, 2014.
- [58] E. Cuevas, M. López, and M. García, “Ultrasonic Techniques and Industrial Robots : Natural Evolution of Inspection Systems Ultrasonic Techniques and Industrial Robots : Natural Evolution of Inspection Systems,” *Symp. - NDT*, no. September 2015, pp. 1–12, 2012.
- [59] I. Cooper, P. I. Nicholson, D. Yan, B. Wright, and C. Mineo, “Development of a fast inspection system for aerospace composite materials - the IntACom project,” in *5th International Symposium on NDT in Aerospace*, 2013, no. November, pp. 13–15.
- [60] C. N. Macleod, G. Dobie, S. G. Pierce, R. Summan, and M. Morozov, “Machining-Based Coverage Path Planning for Automated Structural Inspection,” *IEEE Trans. Autom. Sci. Eng.*, vol. 15, no. 1, pp. 202–213, 2016, doi: 10.1109/tase.2016.2601880.
- [61] J. Riise, C. Mineo, S. G. Pierce, P. I. Nicholson, and I. Cooper, “Adapting robot paths for automated NDT of complex structures using ultrasonic alignment,” *AIP Conf. Proc.*, vol. 2102, no. May, 2019, doi: 10.1063/1.5099756.
- [62] R. Raišutis, E. Jasinien, and E. Žukauskas, “Ultrasonic NDT of wind turbine blades using guided waves,” *Ultrasound. ISSN1392-2114. Kaunas Technol.*, vol. 63, no. 1, pp. 7–11, 2008.
- [63] K. A. Tiwari and R. Raišutis, “Post-processing of ultrasonic signals for the analysis of defects in wind turbine blade using guided waves,” *J. Strain Anal. Eng. Des.*, vol. 53, no. 8, pp. 546–555, 2018, doi: 10.1177/0309324718772668.
- [64] P. Laugier and G. Haïat, “Introduction to the Physics of Ultrasound,” in *Bone Quantitative Ultrasound*, P. Laugier and G. Haïat, Eds. Dordrecht: Springer Netherlands, 2011, pp. 29–45.
- [65] Olympus, “Olympus Phased Array Tutorial.” [Online]. Available: <https://www.olympus-ims.com/en/ndt-tutorials/phased-array/>. [Accessed: 06-Feb-2020].
- [66] P. Louvriot, A. Tachattahte, and D. Garnier, “Robotised UT Transmission NDT of Composite Complex Shaped Parts,” *4th Int. Symp. NDT Aerosp.*, pp. 1–8, 2012.
- [67] L. Séguin-Charbonneau, J. Walter, L. D. Thérout, L. Scheed, A. Beausoleil, and B. Masson, “Automated defect detection for ultrasonic inspection of CFRP aircraft components,” *NDT E Int.*, vol. 122, no. February, 2021, doi: 10.1016/j.ndteint.2021.102478.
- [68] B. W. Drinkwater and P. D. Wilcox, “Ultrasonic arrays for non-destructive evaluation: A review,” *NDT E Int.*, vol. 39, no. 7, pp. 525–541, 2006, doi: 10.1016/j.ndteint.2006.03.006.
- [69] M. Moles and A. Lamarre, “Ultrasonic Phased Arrays,” *Adv. Mater. Process.*, vol. 165, no. 3, 2007.
- [70] C. Holmes, B. W. Drinkwater, and P. D. Wilcox, “Post-processing of the full matrix of ultrasonic transmit-receive array data for non-destructive evaluation,” *NDT E Int.*, vol. 38, no. 8, pp. 701–711, 2005, doi: 10.1016/j.ndteint.2005.04.002.
- [71] J. Zhang, B. W. Drinkwater, and P. D. Wilcox, “Comparison of ultrasonic array imaging algorithms for non-destructive evaluation,” *AIP Conf. Proc.*, vol. 1511, no. 8, pp. 825–832, 2013, doi: 10.1063/1.4789130.

- [72] R. Gongzhang, "New Algorithms for Enhancing Ultrasonic NDE of Difficult Materials," University of Strathclyde, 2017.
- [73] T. E. Gómez, F. M. De Espinosa, and I. A. Csic, "Fabrication and Characterisation of silica aerogel films for air-coupled piezoelectric transducers in the megahertz range," *IEEE Ultrason. Symp.*, vol. 00, no. c, pp. 1107–1110, 2002, doi: 10.1109/ULTSYM.2002.1192487.
- [74] S. P. Kelly, G. Hayward, and T. E. G. Alvarez-Arenas, "Characterization and assessment of an integrated matching layer for air-coupled ultrasonic applications," *IEEE Trans. Ultrason. Ferroelectr. Freq. Control*, vol. 51, no. 10, pp. 1314–1323, 2004, doi: 10.1109/TUFFC.2004.1350960.
- [75] Nuffieldbioethics, "Nuffield Prenatal Scans." [Online]. Available: <https://www.nuffieldbioethics.org/topics/beginning-of-life/non-invasive-prenatal-testing>.
- [76] A. Hauffe, F. Hähnel, and K. Wolf, "Comparison of algorithms to quantify the damaged area in CFRP ultrasonic scans," *Compos. Struct.*, vol. 235, no. November 2019, 2020, doi: 10.1016/j.compstruct.2019.111791.
- [77] T. D'Orazio, M. Leo, A. Distante, C. Guaragnella, V. Pianese, and G. Cavaccini, "Automatic ultrasonic inspection for internal defect detection in composite materials," *NDT E Int.*, vol. 41, no. 2, pp. 145–154, 2008, doi: 10.1016/j.ndteint.2007.08.001.
- [78] T. Hasiotis, E. Badogiannis, and N. G. Tsouvalis, "Application of ultrasonic C-scan techniques for tracing defects in laminated composite materials," *Stroj. Vestnik/Journal Mech. Eng.*, vol. 57, no. 3, pp. 192–203, 2011, doi: 10.5545/sv-jme.2010.170.
- [79] R. L. T. Bevan, J. Zhang, N. Budyn, A. J. Croxford, and P. D. Wilcox, "Experimental Quantification of Noise in Linear Ultrasonic Imaging," *IEEE Trans. Ultrason. Ferroelectr. Freq. Control*, vol. 66, no. 1, pp. 79–90, 2019, doi: 10.1109/TUFFC.2018.2874720.
- [80] R. L. T. Bevan, N. Budyn, J. Zhang, A. J. Croxford, S. Kitazawa, and P. D. Wilcox, "Data fusion of multi-view ultrasonic imaging for characterisation of large defects," *IEEE Trans. Ultrason. Ferroelectr. Freq. Control*, vol. 3010, no. c, pp. 1–1, 2020, doi: 10.1109/tuffc.2020.3004982.
- [81] R. Gongzhang, M. Li, T. Lardner, and A. Gachagan, "Robust defect detection in ultrasonic nondestructive evaluation (NDE) of difficult materials," *IEEE Int. Ultrason. Symp. IUS*, pp. 467–470, 2012, doi: 10.1109/ULTSYM.2012.0116.
- [82] K. A. Tiwari, R. Raisutis, and V. Samaitis, "Signal processing methods to improve the Signal-to-noise ratio (SNR) in ultrasonic non-destructive testing of wind turbine blade," *Procedia Struct. Integr.*, vol. 5, pp. 1184–1191, 2017, doi: 10.1016/j.prostr.2017.07.036.
- [83] R. H. Herrera, R. Orozco, and M. Rodriguez, "Wavelet-based deconvolution of ultrasonic signals in nondestructive evaluation," *J. Zhejiang Univ. Sci.*, vol. 7, no. 10, pp. 1748–1756, 2006, doi: 10.1631/jzus.2006.A1748.
- [84] R. Kažys, O. Tumšys, and D. Pagodinas, "Ultrasonic detection of defects in strongly attenuating structures using the Hilbert-Huang transform," *NDT E Int.*, vol. 41, no. 6, pp. 457–466, 2008, doi: 10.1016/j.ndteint.2008.03.006.
- [85] R. B. Tayong, M. J. Mienczakowski, and R. A. Smith, "3D ultrasound characterization of woven composites," *AIP Conf. Proc.*, vol. 1949, pp. 1–11, 2018, doi: 10.1063/1.5031603.
- [86] L. J. Nelson and R. A. Smith, "Fibre direction and stacking sequence measurement in carbon fibre composites using Radon transforms of ultrasonic data," *Compos. Part A Appl. Sci. Manuf.*, vol. 118, no. December, pp. 1–8, 2019, doi: 10.1016/j.compositesa.2018.12.009.
- [87] R. Fuentes, C. Mineo, S. G. Pierce, K. Worden, and E. J. Cross, "A probabilistic compressive sensing framework with applications to ultrasound signal processing," *Mech. Syst. Signal Process.*, vol. 117, pp. 383–402, 2019, doi: 10.1016/j.ymsp.2018.07.036.
- [88] R. Fuentes, C. Mineo, and K. Worden, "Compressive Sensing for Direct Time of Flight Estimation in Ultrasound-based NDT," *Int. Work. SHM*, 2017.
- [89] B. Masson, "A novel automatic defect detection method for the ultrasonic inspection of aircraft of composite parts," *46th Annu. Rev. Prog. Quant. NDE*, pp. 1–3, 2019.
- [90] F. P. G. Márquez, A. A. Jimenez, and C. Q. G. Muñoz, "Non-destructive testing of wind turbines using ultrasonic waves," in *Non-Destructive Testing and Condition Monitoring Techniques for Renewable Energy Industrial Assets*, Elsevier Ltd., 2020, pp. 91–101.
- [91] K. Chandrasekhar, N. Stevanovic, E. J. Cross, N. Dervilis, and K. Worden, "Damage detection in operational wind turbine blades using a new approach based on machine learning," *Renew. Energy*, vol. 168, pp. 1249–1264, 2021, doi: 10.1016/j.renene.2020.12.119.
- [92] T. Lardner, G. West, G. Dobie, and A. Gachagan, "Automated sizing and classification of defects in CANDU pressure tubes," *Nucl. Eng. Des.*, vol. 325, no. September, pp. 25–32, 2017, doi: 10.1016/j.nucengdes.2017.09.029.

- [93] P. Zacharis, G. West, G. Dobie, T. Lardner, and A. Gachagan, "Data-driven analysis of ultrasonic inspection data of pressure tubes," *Nucl. Technol.*, vol. 202, no. 2–3, pp. 153–160, 2018, doi: 10.1080/00295450.2017.1421803.
- [94] M. E. Ibrahim, R. A. Smith, and C. H. Wang, "Ultrasonic detection and sizing of compressed cracks in glass- and carbon-fibre reinforced plastic composites," *NDT E Int.*, vol. 92, no. June, pp. 111–121, 2017, doi: 10.1016/j.ndteint.2017.08.004.
- [95] R. A. Smith, L. J. Nelson, M. J. Mienczakowski, and P. D. Wilcox, "Ultrasonic tracking of ply drops in composite laminates," *AIP Conf. Proc.*, vol. 1706, pp. 1–10, 2016, doi: 10.1063/1.4940505.
- [96] R. A. Smith, L. J. Nelson, M. J. Mienczakowski, and P. D. Wilcox, "Ultrasonic Analytic-Signal Responses from Polymer-Matrix Composite Laminates," *IEEE Trans. Ultrason. Ferroelectr. Freq. Control*, vol. 65, no. 2, pp. 231–243, 2018, doi: 10.1109/TUFFC.2017.2774776.
- [97] T. Koskinen, J. Kuutti, I. Virkkunen, and J. Rinta-aho, "Online nonlinear ultrasound imaging of crack closure during thermal fatigue loading," *NDT E Int.*, vol. 123, no. July, p. 102510, 2021, doi: 10.1016/j.ndteint.2021.102510.
- [98] M. Wood, P. Charlton, and D. Yan, "Ultrasonic evaluation of artificial kissing bonds in CFRP composites," *e-Journal Nondestruct. Test.*, vol. 19, no. 12, pp. 1–10, 2014.
- [99] BINDT, "Report from the Workshop on NDT and SHM Requirements for Wind Turbines," *Rep. from Work. NDT SHM Requir. Wind Turbines*, no. February, 2019.
- [100] Y. Du, S. Zhou, X. Jing, Y. Peng, H. Wu, and N. Kwok, "Damage detection techniques for wind turbine blades: A review," *Mech. Syst. Signal Process.*, vol. 141, p. 106445, 2020, doi: 10.1016/j.ymsp.2019.106445.
- [101] D. Li, S. C. M. Ho, G. Song, L. Ren, and H. Li, "A review of damage detection methods for wind turbine blades," *Smart Mater. Struct.*, vol. 24, no. 3, p. 33001, 2015, doi: 10.1088/0964-1726/24/3/033001.
- [102] K. Chandrasekhar, N. Stevanovic, M. Corbetta, N. Dervilis, and K. Worden, "On the structural health monitoring of operational wind turbine blades," *Struct. Heal. Monit. 2017 Real-Time Mater. State Aware. Data-Driven Saf. Assur. - Proc. 11th Int. Work. Struct. Heal. Monit. IWSHM 2017*, vol. 2, no. September 2019, pp. 2522–2529, 2017, doi: 10.12783/shm2017/14151.
- [103] K. Chandrasekhar, N. Stevanovic, E. J. Cross, N. Dervilis, and K. Worden, "Gaussian processes for structural health monitoring of wind turbine blades," *Struct. Heal. Monit. 2019 Enabling Intell. Life-Cycle Heal. Manag. Ind. Internet Things - Proc. 12th Int. Work. Struct. Heal. Monit.*, vol. 2, no. September, pp. 2710–2717, 2019, doi: 10.12783/shm2019/32419.
- [104] M. Haywood-Alexander, N. Dervilis, K. Worden, G. Dobie, and T. J. Rogers, "Informative Bayesian tools for damage localisation by decomposition of Lamb wave signals," *J. Sound Vib.*, vol. 535, no. May, p. 117063, 2022, doi: 10.1016/j.jsv.2022.117063.
- [105] M. Haywood-Alexander, N. Dervilis, K. Worden, E. J. Cross, R. S. Mills, and T. J. Rogers, "Structured machine learning tools for modelling characteristics of guided waves," *Mech. Syst. Signal Process.*, vol. 156, p. 107628, 2021, doi: 10.1016/j.ymsp.2021.107628.
- [106] P. Kaewniam, M. Cao, N. Faisal, D. Li, and E. Manoach, "Recent advances in damage detection of wind turbine blades: A state-of-the-art review," *Renew. Sustain. Energy Rev.*, vol. 167, no. June, p. 112723, 2022, doi: 10.1016/j.rser.2022.112723.
- [107] R. Yang, Y. He, and H. Zhang, "Progress and trends in nondestructive testing and evaluation for wind turbine composite blade," *Renew. Sustain. Energy Rev.*, vol. 60, pp. 1225–1250, 2016, doi: 10.1016/j.rser.2016.02.026.
- [108] J. M. Farley, "EFNDT Guidelines on the overall NDT quality system in Europe," in *17th World Conference on Nondestructive Testing*, 2008, pp. 25–28.
- [109] SGRE, "NDT Procedure Comparison," no. May, 2020.
- [110] ASTM, "ASTM Ultrasonic NDT Standards." [Online]. Available: <https://www.astm.org/Standards/nondestructive-testing-standards.html#E07.06>.
- [111] B. Zhou, T. T. Tian, G. Zhu, J. B. Zhao, and D. H. Liu, "An ultrasonic testing method for wall thickness of turbine blades," *Meas. J. Int. Meas. Confed.*, vol. 198, no. May, p. 111357, 2022, doi: 10.1016/j.measurement.2022.111357.
- [112] E. Jasiūnienė *et al.*, "Ultrasonic NDT of wind turbine blades using contact pulse-echo immersion testing with moving water container," *Ultragarsas (Ultrasound)*, vol. 63, no. 3, pp. 28–32, 2008, doi: 10.5755/J01.U.63.3.17075.
- [113] J. Cheng, C. He, Y. Lyu, Y. Zheng, L. Xie, and L. Wu, "Ultrasonic inspection of the surface crack for the main shaft of a wind turbine from the end face," *NDT E Int.*, vol. 114, no. July 2019, p. 102283, 2020, doi: 10.1016/j.ndteint.2020.102283.
- [114] Statista, "Newly Installed Capacity Worldwide." [Online]. Available:

<https://www.statista.com/statistics/515731/newly-installed-capacity-of-gamesa-worldwide/>.

- [115] SGRE, “Financial Statements and Management Report,” 2021.
- [116] ForceTechnologies, “P-scan – Automatic Ultrasonic Inspection,” 2015.
- [117] ForceTechnologies, “P-scan Probes.” [Online]. Available: <https://p-scan.com/scanners-probes/phased-array-probe-specs/>.
- [118] Olympus, “EVIDENT NDT Solutions.” [Online]. Available: <https://www.olympus-ims.com/en/ndt-instruments/>.
- [119] C. Mineo *et al.*, “Fast ultrasonic phased array inspection of complex geometries delivered through robotic manipulators and high speed data acquisition instrumentation,” *IEEE Int. Ultrason. Symp. IUS*, vol. 2016-Novem, pp. 1–4, 2016, doi: 10.1109/ULTSYM.2016.7728746.
- [120] C. Mineo *et al.*, “Fast ultrasonic phased array inspection of complex geometries delivered through robotic manipulators and high speed data acquisition instrumentation,” *IEEE Int. Ultrason. Symp. IUS*, vol. 2016-Novem, pp. 16–19, 2016, doi: 10.1109/ULTSYM.2016.7728746.
- [121] Olympus, “Probe test data sheet,” 2018.
- [122] S. Mosey, M. Sutcliffe, M. Weston, B. Knight-Gregson, and D. Liaptsis, “Development and implementation of calibration process for Full Matrix Capture,” *NDT 2014 - 53rd Annu. Conf. Br. Inst. Non-Destructive Test.*, no. March 2016, 2014.
- [123] M. Ingram, A. Gachagan, A. Nordon, A. J. Mulholland, and M. Hegarty, “Calibration of ultrasonic hardware for enhanced total focusing method imaging,” *Insight Non-Destructive Test. Cond. Monit.*, vol. 62, no. 7, pp. 408–415, 2020, doi: 10.1784/insi.2020.62.7.408.
- [124] M. Ingram, “Exploring the Application of Ultrasonic Phased Arrays for Industrial Process Analysis,” University of Strathclyde, 2019.
- [125] PEAK, “Products: LTPA.” [Online]. Available: <https://www.peakndt.com/products/ltpa/>. [Accessed: 06-Feb-2020].
- [126] Olympus, “Testing and Documentation,” 2007.
- [127] I. S. Domínguez, P. A. Contla, E. M. Hernández, and M. A. von Krüger, “Efeitos de crosstalk causados pela geometria de elementos piezoelétricos na matriz de transdutores ultrassônicos,” *Rev. Bras. Eng. Biomed.*, vol. 27, no. 2, pp. 90–97, 2011, doi: 10.4322/rbeb.2011.008.
- [128] T. Stepinski and F. Lingvall, “Automatic Defect Characterisation in Ultrasonic NDT.”
- [129] M. V. Felice and Z. Fan, “Sizing of flaws using ultrasonic bulk wave testing: A review,” *Ultrasonics*, vol. 88, pp. 26–42, 2018, doi: 10.1016/j.ultras.2018.03.003.
- [130] BSI, “Standards Publication Non-destructive testing — Ultrasonic testing — Examination for discontinuities perpendicular to the surface,” 2014.
- [131] BSI, “Standards Publication Non-destructive testing — Ultrasonic testing — Characterization and sizing of discontinuities (ISO,” 2014.
- [132] P. Ciorau, “Comparison between -6dB and -12dB amplitude drop techniques for length sizing.”
- [133] J. Dobson, A. Gachagan, R. O’Leary, A. Tweedie, and G. Harvey, “Finite element analysis of ultrasonic CFRP laminate inspection,” *55th Annu. Conf. Br. Inst. Non-Destructive Testing, NDT 2016*, pp. 522–533, 2016.
- [134] H. A. Bloxham, A. Velichko, and P. D. Wilcox, “Establishing the Limits of Validity of the Superposition of Experimental and Analytical Ultrasonic Responses for Simulating Imaging Data,” *IEEE Trans. Ultrason. Ferroelectr. Freq. Control*, vol. 66, no. 1, pp. 101–108, 2019, doi: 10.1109/TUFFC.2018.2875781.
- [135] J. M. Dobson, “An integrated framework for finite element modelling of ultrasonic inspections of carbon fibre reinforced polymer components,” 2019.
- [136] R. A. Smith, “Use of 3D ultrasound data sets to map the localised properties of fibre-reinforced composites . PhD thesis , University of Nottingham .,” 2010.
- [137] CIVA NDE, “CIVA 2020 User Manual,” 2020.
- [138] J. Loske and R. Biesenbach, “Force-torque sensor integration in industrial robot control,” *2014 15th Int. Work. Res. Educ. Mechatronics, REM 2014*, no. January 2016, 2014, doi: 10.1109/REM.2014.6920241.
- [139] D. Lines *et al.*, “Using Coded Excitation to maintain Signal to Noise for FMC+TFM on Attenuating Materials,” *IEEE Int. Ultrason. Symp. IUS*, vol. 2019-Octob, pp. 635–638, 2019, doi: 10.1109/ULTSYM.2019.8925564.

- [140] C. S. Alexander, "Dynamic response of a carbon fiber -epoxy composite subject to planar impact," *ECCM 2012 - Compos. Venice, Proc. 15th Eur. Conf. Compos. Mater.*, no. June, pp. 24–28, 2012.
- [141] A. M. Dorado and D. G. Moore, "Composite Material Characterization using Acoustic Wave Speed Measurements," *ASNT Annu. Conf. held Salt Lake, UT*, pp. 1–5, 2015.
- [142] B. Zoofan, "Measuring the Attenuation Coefficient of Ultrasonic Beams in Materials.pdf," 2017.
- [143] KUKA, "KUKA.RobotSensorInterface 4.0 Manual," 2009.
- [144] P. D. Wilcox and J. Zhang, "Quantification of the Effect of Array Element Pitch on Imaging Performance," *IEEE Trans. Ultrason. Ferroelectr. Freq. Control*, vol. 65, no. 4, pp. 600–616, 2018, doi: 10.1109/TUFFC.2018.2794627.
- [145] R. Su, C. Mineo, C. N. Macleod, S. G. Pierce, and A. Gachagan, "Multi-aperture beamforming for automated large structure inspection using ultrasonic phased arrays," *AIP Conf. Proc.*, vol. 2102, no. May, 2019, doi: 10.1063/1.5099837.
- [146] R. Su, C. Mineo, C. N. Macleod, S. G. Pierce, and A. Gachagan, "Golay Coded Multi-Aperture Beamforming using Ultrasonic Phased Arrays," 2018.
- [147] T. G. Bjåstad, "High frame rate ultrasound imaging using parallel beamforming," Norwegian University of Science and Technology, 2009.
- [148] O. S. B. S. Vedula, G. Zurakhov, and A. Bronstein, *High Frame-Rate Cardiac Ultrasound Imaging with Deep Learning*, vol. 1. Springer International Publishing, 2018.
- [149] E. Boni *et al.*, "Architecture of an Ultrasound System for Continuous Real-Time High Frame Rate Imaging," *IEEE Trans. Ultrason. Ferroelectr. Freq. Control*, vol. 64, no. 9, pp. 1276–1284, 2017, doi: 10.1109/TUFFC.2017.2727980.
- [150] Y. Wang, T. Su, and S. Zhang, "Multi-line acquisition with delay multiply and sum beamforming in phased array ultrasound imaging, validation of simulation and in vitro," *Ultrasonics*, vol. 96, no. February, pp. 123–131, 2019, doi: 10.1016/j.ultras.2019.02.004.
- [151] S. A. Nyrnes, S. Fadnes, M. S. Wigen, L. Mertens, and L. Lovstakken, "Blood Speckle-Tracking Based on High-Frame Rate Ultrasound Imaging in Pediatric Cardiology," *J. Am. Soc. Echocardiogr.*, vol. 33, no. 4, pp. 493–503.e5, 2020, doi: 10.1016/j.echo.2019.11.003.
- [152] Y. M. Benane, B. Nicolas, D. Bujoreanu, C. Cachard, and O. Basset, "An enhanced chirp modulated Golay code for ultrasound diverging wave compounding," *Eur. Signal Process. Conf.*, vol. 2018-Septe, pp. 81–85, 2018, doi: 10.23919/EUSIPCO.2018.8553055.
- [153] B. H. Kim and T. K. Song, "Multiple transmit focusing using modified orthogonal Golay Codes for small scale systems," *Proc. IEEE Ultrason. Symp.*, vol. 2, no. April 2019, pp. 1574–1577, 2003, doi: 10.1109/ultsym.2003.1293208.
- [154] A. C. Jensen and A. Austeng, "An approach to multibeam covariance matrices for adaptive beamforming in ultrasonography," *IEEE Trans. Ultrason. Ferroelectr. Freq. Control*, vol. 59, no. 6, pp. 1139–1148, 2012, doi: 10.1109/TUFFC.2012.2304.
- [155] PEAK, "Micropulse Command Reference Manual," 2017.
- [156] C. Ménard, S. Robert, R. Miorelli, and D. Lesselier, "Optimization algorithms for ultrasonic array imaging in homogeneous anisotropic steel components with unknown properties," *NDT E Int.*, vol. 116, 2020, doi: 10.1016/j.ndteint.2020.102327.
- [157] H. Cao, S. Guo, S. Zhang, Y. Xie, and W. Feng, "Ray tracing method for ultrasonic array imaging of CFRP corner part using homogenization method," *NDT E Int.*, vol. 122, no. June, p. 102493, 2021, doi: 10.1016/j.ndteint.2021.102493.
- [158] M. I. Ali and J. Anjaneyulu, "Effect of fiber-matrix volume fraction and fiber orientation on the design of composite suspension system," *IOP Conf. Ser. Mater. Sci. Eng.*, vol. 455, no. 1, 2018, doi: 10.1088/1757-899X/455/1/012104.
- [159] E. A. Birt and R. A. Smith, "A review of NDE methods for porosity measurement in fibre-reinforced polymer composites," *Insight Non-Destructive Test. Cond. Monit.*, vol. 46, no. 11, pp. 681–686, 2004, doi: 10.1784/insi.46.11.681.52280.
- [160] D. U. Shah, P. J. Schubel, P. Licence, and M. J. Clifford, "Determining the minimum, critical and maximum fibre content for twisted yarn reinforced plant fibre composites," *Compos. Sci. Technol.*, vol. 72, no. 15, pp. 1909–1917, 2012, doi: 10.1016/j.compscitech.2012.08.005.
- [161] F. Abdalla, M. Megat, M. Sapuan, and S. Bb, "Determination of Volume Fraction Values Of Filament Wound Glass and Carbon Fiber Reinforced Composites," *ARPJ Eng Appl Sci*, vol. 3, no. 4, pp. 7–11, 2008.

- [162] S. Tehranchi and H. Saidpour, "Determination of void distribution and fibre volume fraction in filament wound composites."
- [163] Q. Wang, H. Ning, U. Vaidya, S. Pillay, and L. A. Nolen, "Development of a carbonization-in-nitrogen method for measuring the fiber content of carbon fiber reinforced thermoset composites," *Composites Part A: Applied Science and Manufacturing*, vol. 73, pp. 80–84, 2015, doi: 10.1016/j.compositesa.2015.02.025.
- [164] H. Kim, G. Kim, S. Lee, G. Choe, T. Noguchi, and J. Nam, "Direct tensile behavior of amorphous metallic fiber-reinforced cementitious composites: Effect of fiber length, fiber volume fraction, and strain rate," *Compos. Part B Eng.*, vol. 177, no. July, p. 107430, 2019, doi: 10.1016/j.compositesb.2019.107430.
- [165] H. Rahmani, S. H. M. Najafi, A. Ashori, and M. Golriz, "Elastic properties of carbon fibre-reinforced epoxy composites," *Polym. Polym. Compos.*, vol. 23, no. 7, pp. 475–481, 2015, doi: 10.1177/096739111502300706.
- [166] J. H. Chen, E. Schulz, J. Bohse, and G. Hinrichsen, "Effect of fibre content on the interlaminar fracture toughness of unidirectional glass-fibre/polyamide composite," *Compos. Part A Appl. Sci. Manuf.*, vol. 30, no. 6, pp. 747–755, 1999, doi: 10.1016/S1359-835X(98)00188-2.
- [167] O. I. Okoli and G. F. Smith, "Failure modes of fibre reinforced composites: The effects of strain rate and fibre content," *J. Mater. Sci.*, vol. 33, no. 22, pp. 5415–5422, 1998, doi: 10.1023/A:1004406618845.
- [168] E. Belmonte, M. De Monte, C. J. Hoffmann, and M. Quaresimin, "Damage initiation and evolution in short fiber reinforced polyamide under fatigue loading: Influence of fiber volume fraction," *Compos. Part B Eng.*, vol. 113, pp. 331–341, 2017, doi: 10.1016/j.compositesb.2017.01.023.
- [169] M. Kardos, E. Körner, D. Penumadu, and N. Modler, "The influence of fiber volume fraction and fiber length on the evolution of pore content and the paintability of sheet molding compounds," *Compos. Part B Eng.*, vol. 185, no. January, p. 107760, 2020, doi: 10.1016/j.compositesb.2020.107760.
- [170] A. Esnaola, I. Tena, J. Aurrekoetxea, I. Gallego, and I. Ulacia, "Effect of fibre volume fraction on energy absorption capabilities of E-glass/polyester automotive crash structures," *Compos. Part B Eng.*, vol. 85, pp. 1–7, 2016, doi: 10.1016/j.compositesb.2015.09.007.
- [171] D. Grund, M. Orlishausen, and I. Taha, "Determination of fiber volume fraction of carbon fiber-reinforced polymer using thermogravimetric methods," *Polym. Test.*, vol. 75, no. March, pp. 358–366, 2019, doi: 10.1016/j.polymertesting.2019.02.031.
- [172] M. A. A. Mohsin, L. Iannucci, and E. S. Greenhalgh, "Fibre-volume-fraction measurement of carbon fibre reinforced thermoplastic composites using thermogravimetric analysis," *Heliyon*, vol. 5, no. 1, p. e01132, 2019, doi: 10.1016/j.heliyon.2019.e01132.
- [173] *ASTM D3171-22: Standard Test Methods for Constituent Content of Composite Materials*. 2012.
- [174] E. Cilley, D. Roylance, and S. N., "Methods of fibre and void measurement in graphite epoxy composites," 1974.
- [175] M. C. Waterbury and L. T. Drzal, "Determination of Fiber Volume Fractions by Optical Numeric Volume Fraction Analysis," *J. Reinf. Plast. Compos.*, vol. 8, no. 6, pp. 627–636, 1989, doi: 10.1177/073168448900800605.
- [176] H. W. He, W. Huang, and F. Gao, "Comparison of four methods for determining fiber content of carbon fiber/epoxy composites," *Int. J. Polym. Anal. Charact.*, vol. 21, no. 3, pp. 251–258, 2016, doi: 10.1080/1023666X.2016.1139395.
- [177] R. Zbončák, V. Votrubec, and M. Švec, "The alternative procedures of fiber volume ratio determination of long-fiber carbon - Epoxy composites," *Manuf. Technol.*, vol. 18, no. 1, pp. 160–164, 2018, doi: 10.21062/ujep/71.2018/a/1213-2489/MT/18/1/160.
- [178] M. Kusano, S. Takizawa, T. Sakai, Y. Arao, and M. Kubouchi, "Simultaneous sound velocity and thickness measurement by the ultrasonic pitch-catch method for corrosion-layer-forming polymeric materials," *Ultrasonics*, vol. 82, pp. 178–187, 2018, doi: 10.1016/j.ultras.2017.08.001.
- [179] IMA, "Materialforschung und Anwendungstechnik Dresden." [Online]. Available: <https://www.ima-dresden.de/>.
- [180] R. K. W. Vithanage *et al.*, "A Phased Array Ultrasound Roller Probe for Automated in-Process/Interpass Inspection of Multipass Welds," *IEEE Trans. Ind. Electron.*, vol. 68, no. 12, pp. 12781–12790, 2021, doi: 10.1109/TIE.2020.3042112.